

TSUNAMI HYDRODYNAMICS IN COASTAL ZONES

A THESIS SUBMITTED TO  
THE GRADUATE SCHOOL OF NATURAL AND APPLIED SCIENCES  
OF  
MIDDLE EAST TECHNICAL UNIVERSITY

BY

CEREN ÖZER

IN PARTIAL FULFILLMENT OF THE REQUIREMENTS  
FOR  
THE DEGREE OF DOCTOR OF PHILOSOPHY  
IN  
CIVIL ENGINEERING

MARCH 2012

Approval of the thesis:

**TSUNAMI HYDRODYNAMICS IN COASTAL ZONES**

submitted by **CEREN ÖZER** in partial fulfillment of the requirements for the degree of **Doctor of Philosophy in Civil Engineering Department, Middle East Technical University** by,

Prof. Dr. Canan Özgen \_\_\_\_\_  
Dean, Graduate School of **Natural and Applied Sciences**

Prof. Dr. Güney Özcebe \_\_\_\_\_  
Head of Department, **Civil Engineering**

Prof. Dr. Ahmet Cevdet Yalçiner \_\_\_\_\_  
Supervisor, **Civil Engineering Dept., METU**

**Examining Committee Members:**

Prof. Dr. Can Elmar Balas \_\_\_\_\_  
Civil Engineering Dept., Gazi University

Prof. Dr. Ahmet Cevdet Yalçiner \_\_\_\_\_  
Civil Engineering Dept., METU

Prof. Dr. Ayşen Ergin \_\_\_\_\_  
Civil Engineering Dept., METU

Prof. Dr. İsmail Aydın \_\_\_\_\_  
Civil Engineering Dept., METU

Assoc. Prof. Dr. Utku Kanoğlu \_\_\_\_\_  
Engineering Sciences Dept., METU

**Date:** \_\_\_\_\_ 23.03.2012 \_\_\_\_\_

**I hereby declare that all information in this document has been obtained and presented in accordance with academic rules and ethical conduct. I also declare that, as required by these rules and conduct, I have fully cited and referenced all material and results that are not original to this work.**

**Name, Last Name: CEREN ÖZER**

**Signature :**

# ABSTRACT

## TSUNAMI HYDRODYNAMICS IN COASTAL ZONES

Özer, Ceren

Ph.D., Department of Civil Engineering

Supervisor: Prof. Dr. Ahmet Cevdet Yalçın

March 2012, 187 pages

This study analyzes the parameter “hydrodynamic demand” that is also defined by the square of Froude Number representing the damage of tsunami waves on structures and coastlines, and other hydrodynamic parameters, i.e., the distribution of instantaneous flow depths, runup values and the direction of maximum currents, occurred during tsunami inundation by using advanced numerical modeling. The analyses are performed on regular-shaped basins with different bottom slopes and real-shaped topographies using different wave shapes, wave periods and types. Various orientation and amount of coastal and land structures are used in simulations to have results for many different cases. This study provides the opportunity to define the damage of level in residential areas and to test the performance of coastal protection structures. The behavior of tsunami hydrodynamic parameters in shallow and inundation zone is investigated and a correlation is obtained between the average maximum values of square of Froude Number with the wave characteristics and sea bottom slope. After determining hydrodynamic parameters in regular shaped basins, a case study is applied by modeling the March 11, 2011 Great East Japan Tsunami with finer resolution in nested domains. The determination of hydrodynamic parameters in inundation zone during 2011 Japan event is performed in one of the most damaged coastal city Kamaishi.

Keywords: Tsunami, inundation, runup, current velocity, water surface elevation, solitary wave, leading elevation/depression wave, March 11 2011 Great East Japan Tsunami

## ÖZ

### KIYI BÖLGELERİNDE TSUNAMİ HİDRODİNAMİĞİ

Özer, Ceren

Doktora, İnşaat Mühendisliği Bölümü  
Tez Yöneticisi : Prof. Dr. Ahmet Cevdet Yalçın

Mart 2012, 187 sayfa

Bu çalışmada, depreşim dalgalarının kıyı şeridinde ve kıyı yapılarında verdiği zararı ifade eden “hidrodinamik etki düzeyi” parametresi - bir diğer ifadeyle Froude Sayısının karesi- ve anlık akım derinliği, tırmanma yükseklikleri ve en yüksek akım hızlarının yönleri gibi hidrodinamik parametreler ileri sayısal modelleme teknikleri kullanılarak analiz edilmektedir. Analizler, farklı dalga şekilleri, periyotları, yönleri ve tipleri kullanılarak; farklı taban eğimine sahip düzgün şekilli basenler ve gerçek topografyalar üzerinde gerçekleştirilmektedir. Benzetimlerde, depreşim dalgalarının yapılar üzerindeki davranışları incelenirken, farklı konum ve sayıda kıyı ve kara yapısı kullanılarak çeşitli yorumlar yapılmaktadır. Bu çalışma sayesinde, kıyılarda tsunami hasarı tesbit edilebilirken kıyı koruma yapılarının tsunami baskınları karşısındaki performansları da değerlendirilmektedir. Tsunami hidrodinamik parametrelerinin sığ suda ve baskın alanında değişimleri incelenmekte ve test basenlerinde yapılan analiz sonuçlarından yararlanılarak ortalama en yüksek Froude sayısı karesi için dalga karakteristikleri ve taban eğimiyle ilişkili bir korelasyon ortaya çıkarılmaktadır. Test basenindeki analizler sayesinde baskın alanında tsunami hidrodinamik parametrelerinin davranışları anlaşıldıktan sonra, 11 Mart 2011 Büyük Doğu Japonya Tsunamisi ele alınarak bir durum çalışması yapılmakta ve baskın alanında tsunami parametrelerinin değişimleri incelenmektedir. Bu çalışma için 2011 Japonya tsunamisinde en büyük hasar alan şehirlerden biri olan Kamaishi seçilmiştir.

Anahtar Kelimeler: Depreşim dalgası, baskın, tırmanma, akıntı hızı, su yüzeyi yüksekliği, tek dalga, öncü yükselen/çöken dalga, 11 Mart 2011 Büyük Doğu Japonya Tsunamisi

Dedicated to *my precious family* and to the *light of my life*

## ACKNOWLEDGMENTS

I would like to express my sincere appreciation to *Prof. Dr. Ahmet Cevdet Yalçın* for his endless and very valuable supports, academic supervision, and for his heartfelt efforts to join me in such newly developed phenomenon and to provide opportunities to open up new frontiers in my researches. I would like to thank *Prof. Dr. Ayşen Ergin* and *Dr. Işıkhan Güler* for their hearty supports and great sympathy throughout my thesis, and also for their contributions to my coastal engineering education with their valuable knowledge and experiences.

My most willingly thanks are to my dear friends *Hülya Karakuş, Cüneyt Baykal, Mustafa Esen and Seçil Özdemir* for their very valuable supports, endless patience and encouragement. I want to thank my sincere friends in METU Ocean Engineering Research Center for their great efforts to amuse and encourage me even at hard times.

I dedicate my thanks to the guidance of all referred studies, which throw fresh light on my newly developed research subject.

I would like to acknowledge *Dr. Andrey Zaitsev* for his valuable collaboration and efforts in the modification of numerical code NAMI DANCE in my research. I also want to thank *Prof. Efim Pelinovsky* for his contributions shedding a light to this modification stage.

I want to thank *Prof. Dr. Costas Synolakis* for his valuable contributions and encouragement to work on new aspects of tsunamis.

I also want to acknowledge Tohoku University and Port and Research Institute (PARI) Japan for valuable supports for obtaining measurements at Kamaishi Buoy.

Words are inadequate to express my thanksgiving to my mother *Nüvit Özer*, my brother *Gökhan Özer* and my father *Ayhan Özer*, for their everlasting supports, endless love and encouragement.

I dedicate my special thanks to *Muhterem Sadettin Sözdinler* for his precious supports, encouragement and *love* in the last painstaking stages of my thesis. He knew how to make me feel like he is next to me even from far beyond the oceans.

Finally, I would like to acknowledge that this study was partly supported by the Scientific and Technological Research Council of Turkey (TÜBİTAK) Research Grant No: 108Y227, “MOdel Development and Risk Analysis for Tsunamis in the Black Sea and Mediterranean (MORAT)” and by European Commission funded research project “Tsunami Risk AND Strategies For the European Region (TRANSFER)”.

# TABLE OF CONTENTS

ABSTRACT .....	iv
ÖZ.....	v
DEDICATION.....	vi
ACKNOWLEDGMENTS .....	vii
TABLE OF CONTENTS.....	ix
LIST OF TABLES.....	xiii
LIST OF FIGURES .....	xiv
LIST OF SYMBOLS.....	xxiii
CHAPTERS	
1. INTRODUCTION.....	1
2. LITERATURE SURVEY .....	4
3. THEORETICAL BACKGROUND AND NUMERICAL SCHEME.....	18
3.1 Theoretical Background .....	18
3.2. Governing Equations of NAMI DANCE.....	24
3.2.1 Shallow Water Theory .....	24
3.2.2. Shallow Water Equations .....	29
3.3. Numerical Scheme of the Model.....	30
3.3.2. Initial Conditions in Numerical Scheme .....	33
3.4. Open Boundary Conditions.....	33
3.5. Boundary Conditions in Runup Calculations .....	35
3.6. Static Source Inputs.....	36

3.7. Stability of the Model.....	37
3.8. Conditions for Residential Areas in Inundation Zone.....	38
3.9. Derivation of Hydrodynamic Demand and the Role of Froude Number.....	38
4. VERIFICATION AND VALIDATION OF NUMERICAL CODE: NAMI DANCE.....	42
4.1 Laboratory Benchmarking - Verification of NAMI DANCE Comparing with the Experimental Results .....	43
4.2 Field Benchmarking- Verification of NAMI DANCE with Real Measurements of March 11, 2011 Great East Japan Tsunami .....	48
4.3. Verification of the Model with the Problem of Solitary Wave Runup on a Sloping Beach .....	56
4.4. Scientific and Operational Evaluation.....	62
5. MODEL APPLICATION.....	64
5.1. Model Parameters.....	64
5.1.1. The Properties of Test Basins .....	65
5.1.2. Characteristics of Inputted Wave for the Tests .....	68
5.2 Symmetry Test of the NAMI DANCE computations in Circular Bathymetry with Forced Disturbance .....	71
5.3. Investigation of Tsunami Behavior with Different Wave Characteristics on a Plain Beach.....	72
5.3.1. Calculation of Hydrodynamic Parameters on a Plain Beach .....	72
5.3.2. Runup Calculation for Single Sinusoidal Wave climbing on a Plain Beach.....	86
5.4. Investigation of Hydrodynamic Parameters for Different Basin Layout.....	89
5.4.1. Spatial Distribution of Hydrodynamic Parameters .....	93
5.4.2. Change of Hydrodynamic Parameters along the Cross-sections .....	99

5.4.3. The Wave Shape Effect on the Hydrodynamic Parameters Along the Cross-sections.....	112
5.4.4. The Wave Period Effect on the Hydrodynamic Parameters Along the Cross-sections.....	112
5.5. The Performance of Coastal Protection with Lengthwise Seawall .....	116
5.6. Investigation of Tsunami Behavior on a Plain Beach for the N-waves .....	118
5.6.1. Comparison of Runup Values for an N-wave and Sinusoidal Wave computed by NAMI DANCE.....	118
5.6.2. Comparison of NAMI DANCE Runup results for N-waves with Analytical Approaches.....	120
5.7. The Effect of Manning Coefficient on Hydrodynamic Parameters in Inundation Zone .....	122
6. CASE STUDY – INVESTIGATION OF HYDRODYNAMIC PARAMETERS DURING THE 2011 GREAT EAST JAPAN TSUNAMI IN KAMAISHI BAY .....	126
6.1. The Investigation of Hydrodynamic Parameters around the Kamaishi Breakwaters.....	130
6.2. The Effect of Kamaishi Breakwater on Hydrodynamic Parameters in Residential Area.....	134
6.3. The Investigation of Hydrodynamic Parameters in case of Full Protection of Breakwater without Overtopping.....	138
7. GENERAL EVALUATION, DISCUSSION AND CONCLUSION.....	140
7.1 General Discussion and Evaluation of the Results .....	140
7.2 Summary of the Results and Conclusion .....	147
8. SUGGESTIONS FOR FURTHER STUDIES .....	149
REFERENCES.....	151
APPENDIX A .....	160

APPENDIX B.....	162
APPENDIX C.....	173
CURRICULUM VITAE.....	185

## LIST OF TABLES

### TABLES

Table 3.1: Values of Manning’s Roughness Coefficient $n$ for Various Channel Materials (TUNAMI-N2, 2001) .....	28
Table 3.2: Roughness Coefficients for Tsunami Simulation (after Kotani et al, 1999; CAO of Japanese Government, 2004) .....	29
Table 3.3: The List of Seismic Rupture Parameters .....	36
Table 3.4: Suggestions for the Value of Drag Coefficient $C_D$ (Ozer, 2007) .....	41
Table 4.1: Relative Absolute Mean Percent Error for the Laboratory Benchmarking .....	46
Table 4.2: The computed and calculated runup values of solitary waves with different wave amplitudes on different bottom slopes .....	57
Table 5.1: The List of Test Basins with Their Properties .....	66
Table 5.2: The comparison of runup, $\overline{Fr_{\max}^2}$ and $\overline{Fr_{\max}}$ values for sinusoidal wave and N-wave .....	119
Table 5.3: The numerical and analytical runup values of N-wave on a sloping beach .....	120

## LIST OF FIGURES

### FIGURES

Figure 3.1: Increasing height and decreasing length of a tsunami on a sloping beach .....	19
Figure 3.2: Sectional view of tsunami hydrodynamic parameters in inundation zone	20
Figure 3.3: The photos taken during the post tsunami survey after 2011 Japan event by the tsunami survey team under the leadership of Prof. Yalciner between May 28 and June 2, 2011. (a) a car dragged into the first floor of a primary school in Arahama, (b) high scour of a building foundation near Sendai coasts, (c) scour of the foundation of a building near the shoreline in Kamaishi (this building is famous with one of the most well-known footage from Japan event), (d) subceeding of the shoreline in Otsutchi, (e) Miyako tsunami wall from the balcony of Mayor’s office building with a dramatic picture taken from the same point during tsunami flooding, (f) damage behind the tsunami preventing walls in Otsuchi.....	21
Figure 3.4: The cross-section of a tsunami propagating on a constant-sloped beach	26
Figure 3.5: The schematic view of staggered- leap frog scheme in time and space ...	32
Figure 3.6: Seismic rupture parameters in three-dimensional projection.....	37
Figure 3.7: Sectional View of Hydrostatic Pressure on a Coastal Structure .....	39
Figure 4.1: The bathymetry and topography of the study area in the laboratory tank (red stars show the location of tide gauges) .....	44
Figure 4.2: The profile of input wave.....	44
Figure 4.3: The offshore profile of laboratory tank (Takahashi, 1996).....	44
Figure 4.4: The comparison of experimental and numerical results at the gauge points #5, #7 and #9 .....	47

Figure 4.5: Source models for the 2011 Great East Japan Earthquake. (Left, the Tohoku University-Imamura Source (Imamura et al, 2011); Right, the Fujii-Satake Source (Koketsu et al, 2011).....	49
Figure 4.6: The computed initial water surfaces for the Great East Japan Tsunami using the tsunami sources in Figure 4.5.....	50
Figure 4.7: The wave record after the earthquake at 24 km off Kamaishi by PARI Japan.....	51
Figure 4.8: The comparison of the measured data and the computed data using both the Fujii-Satake and Imamura sources of Figures 4.1 and 4.2.....	51
Figure 4.9: Propagation modeling of Great East Japan Tsunami across the Pacific..	52
Figure 4.10: The location of the selected DART buoys and the water level fluctuations measured during March 11, 2011 Japan Tsunami .....	53
Figure 4.11: The comparison of computed results with the data measured by DART-21418 during March 11, 2011 Great East Japan Tsunami .....	53
Figure 4.12: The comparison of computed results with the data measured by DART-21401 during March 11, 2011 Great East Japan Tsunami .....	54
Figure 4.13: The comparison of computed results with the data measured by DART-21419 during March 11, 2011 Great East Japan Tsunami .....	54
Figure 4.14: The comparison of computed results with the data measured by DART-46403 during March 11, 2011 Great East Japan Tsunami.....	55
Figure 4.15: The comparison of laboratory data given in Synolakis (1986) with the computed results of NAMI DANCE according to the normalized maximum runup of solitary waves on a 1/20 slope with respect to the normalized wave height. ....	58
Figure 4.16: The comparison of different laboratory data in Synolakis (1986) with the computed results of NAMIDANCE according to the normalized maximum runup of nonbreaking solitary waves climbing up different beaches with respect to the normalized wave height.....	59

Figure 4.17: The comparison of numerical results computed by NAMIDANCE (red dots) with non-linear theory and laboratory data in Synolakis (1986) according to the climb of a solitary wave with $H/d= 0.019$ ( $H\approx 1\text{m}$ ) up a $1/20$ beach for dimensionless times $t=25, t=30, t=35, t=40$ and $t=45$ .....	60
Figure 4.18: The comparison of numerical results computed by NAMIDANCE (red dots) with non-linear theory and laboratory data in Synolakis (1986) according to the climb of a solitary wave with $H/d= 0.019$ ( $H\approx 1\text{m}$ ) up a $1/20$ beach for dimensionless times $t=50, t=55, t=60, t=65$ and $t=70$ .....	61
Figure 5.1: The top view of a sample basin with the location of structures.....	67
Figure 5.2: The 3D visualization of Representative Test Basins.....	69
Figure 5.3: The 3D view of inputted sinusoidal wave with 4m height and 48min period.....	70
Figure 5.4: The bathymetry and topography of circular test basin for the verification of NAMI DANCE calculations in every direction.....	72
Figure 5.5: The snapshots of generation and propagation of the wave in circular test basin (the plot at $t=0$ shows the initial user defined source at the middle of the basin).....	73
Figure 5.6: The plot of $\overline{Fr_{max}^2}$ values calculated for the waves with initial wave amplitude $a= 2\text{m}$ .....	75
Figure 5.7: The plot of $\overline{Fr_{max}^2}$ values calculated for the waves with initial wave amplitude $a= 3\text{m}$ .....	75
Figure 5.8: The plot of $\overline{Fr_{max}^2}$ values calculated for the waves with initial wave amplitude $a= 4\text{m}$ .....	76
Figure 5.9: The Plot of $\overline{Fr_{max}^2}$ values calculated for the waves with initial wave amplitude $a= 5\text{m}$ .....	76
Figure 5.10: The Plot of $\overline{Fr_{max}^2}$ values calculated for the waves with initial wave height $a= 6\text{m}$ .....	77

Figure 5.11: The distribution of empirical relationship in Eqn. [5.2] between  $\overline{Fr_{max}^2}$  and wave characteristics-bottom slope with respect to wave period for LEW ..... 78

Figure 5.12: The distribution of empirical relationship in Eqn. [5.2] between  $\overline{Fr_{max}^2}$  and wave characteristics-bottom slope with respect to wave amplitude for LEW .... 79

Figure 5.13: The distribution of empirical relationship in Eqn. [5.2] between  $\overline{Fr_{max}^2}$  and wave characteristics-bottom slope with respect to wave period for LDW ..... 80

Figure 5.14: The distribution of empirical relationship in Eqn. [5.2] between  $\overline{Fr_{max}^2}$  and wave characteristics-bottom slope with respect to wave amplitude for LDW .... 80

Figure 5.15: The distribution of empirical relationship in Eqn. [5.2] between  $\overline{Fr_{max}^2}$  and wave characteristics-bottom slope for LEW and LDW ..... 81

Figure 5.16: The distribution of empirical relationship in Eqn. [5.3] between  $\overline{Fr_{max}^2}$  and wave characteristics-bottom slope with respect to wave period for LEW ..... 82

Figure 5.17: The distribution of empirical relationship in Eqn. [5.3] between  $\overline{Fr_{max}^2}$  and wave characteristics-bottom slope with respect to wave amplitude for LEW .... 83

Figure 5.18: The distribution of empirical relationship in Eqn. [5.3] between  $\overline{Fr_{max}^2}$  and wave characteristics-bottom slope with respect to wave period for LDW ..... 83

Figure 5.19: The distribution of empirical relationship in Eqn. [5.3] between  $\overline{Fr_{max}^2}$  and wave characteristics-bottom slope with respect to wave amplitude for LDW .... 84

Figure 5.20: The distribution of empirical relationship in Eqn. [5.3] between  $\overline{Fr_{max}^2}$  and wave characteristics-bottom slope for LEW and LDW ..... 84

Figure 5.21: Normalized maximum runoff of sinusoidal waves climbing up different sloped beaches with respect to the wave amplitude for LEW ..... 87

Figure 5.22: Normalized maximum runoff of sinusoidal waves climbing up different sloped beaches with respect to the wave amplitude for LDW ..... 87

Figure 5.23: Normalized maximum runup of sinusoidal waves climbing up different sloped beaches with respect to the wave period for LEW .....	88
Figure 5.24: Normalized maximum runup of sinusoidal waves climbing up different sloped beaches with respect to the wave period for LDW .....	88
Figure 5.25: The cross-sections passing through the openings between the buildings on the top view of extracted bathymetry.....	90
Figure 5.26: The values of average maximum $Fr^2$ observed in each type of basins for the wave period of 3min, 24min and 48min .....	91
Figure 5.27: The values of maximum inundation distance observed in each type of basins for the wave period of 3min, 24min and 48min.....	92
Figure 5.28: The distribution of maximum water elevations for the waves propagating on the 1/20 slope with the wave amplitude of 4m and wave period of 3min.....	93
Figure 5.29: The distribution of maximum current velocities for the waves propagating on the 1/20 slope with the wave amplitude of 4m and wave period of 3min.....	94
Figure 5.30: The distribution of maximum current velocities for the waves propagating on the 1/20 slope with the wave amplitude of 4m and wave period of 24min .....	94
Figure 5.31: The distribution of maximum current velocities for the waves propagating on the 1/20 slope with the wave amplitude of 4m and wave period of 48min .....	95
Figure 5.32: The distribution of maximum flow depths for the waves propagating on the 1/20 slope with the wave amplitude of 4m and wave period of 3min.....	96
Figure 5.33: The distribution of maximum flow depths for the waves propagating on the 1/20 slope with the wave amplitude of 4m and wave period of 24min.....	96
Figure 5.34: The distribution of maximum flow depths for the waves propagating on the 1/20 slope with the wave amplitude of 4m and wave period of 48min.....	97

Figure 5.35: The distribution of maximum Froude Number square ( $Fr_{max}^2$ ) for the waves propagating on the 1/20 slope with the wave amplitude of 4m and wave period of 3min .....	98
Figure 5.36: The distribution of maximum Froude Number square ( $Fr_{max}^2$ ) for the waves propagating on the 1/20 slope with the wave amplitude of 4m and wave period of 24min .....	98
Figure 5.37: The distribution of maximum Froude Number square ( $Fr_{max}^2$ ) for the waves propagating on the 1/20 slope with the wave amplitude of 4m and wave period of 48min .....	99
Figure 5.38: The three-dimensional view of Sections A-A and G-G .....	100
Figure 5.39: The variation of hydrodynamic parameters in inundation zone through the Section A-A for the test basins 01, 02 and 03 with the simulation of waves in 4m wave amplitude with 48min period on 1/20 slope .....	101
Figure 5.40: The variation of hydrodynamic parameters in inundation zone through the Section A-A for the test basins 01, 02, 04 and 20 with the simulation of waves in 4m wave amplitude with 48min period on 1/20 slope.....	103
Figure 5.41: The variation of hydrodynamic parameters in inundation zone through the Section A-A for the test basins 01, 02, 05 and 16 with the simulation of waves in 4m wave amplitude with 48min period on 1/20 slope.....	104
Figure 5.42: The variation of hydrodynamic parameters in inundation zone through the Section A-A for the test basins 06, 17 and 22 with the simulation of waves in 4m wave amplitude with 48min period on 1/20 slope .....	105
Figure 5.43: The variation of hydrodynamic parameters in inundation zone through the Section A-A for the test basins 08, 10 and 19 with the simulation of waves in 4m wave amplitude with 48min period on 1/20 slope .....	106
Figure 5.44: The variation of hydrodynamic parameters in inundation zone through the Section A-A for the test basins 05, 07 and 16 with the simulation of waves in 4m wave amplitude with 48min period on 1/20 slope .....	108

Figure 5.45: The variation of hydrodynamic parameters in inundation zone through the Section A-A for the test basins 06, 12 and 14 with the simulation of waves in 4m wave amplitude with 48min period on 1/20 slope .....	109
Figure 5.46: The variation of hydrodynamic parameters in inundation zone through the Section D-D for the test basins 06, 12 and 14 with the simulation of waves in 4m wave amplitude with 48min period on 1/20 slope .....	110
Figure 5.47: The variation of $Fr_{max}^2$ along Sections A-A, B-B and E-E for the test basins 01, 02, 03 and 04.....	111
Figure 5.48: The comparison of hydrodynamic parameters in inundation zone through the Section A-A with the simulation of waves in 4m wave amplitude with 48min period on plain beach with 1/20 slope for LEW and LDW .....	113
Figure 5.49: The comparison of hydrodynamic parameters in inundation zone through the Section A-A with the simulation of waves in 4m wave amplitude with 48min period on residential areas in test basin-02 with 1/20 slope for LEW and LDW .....	114
Figure 5.50: The comparison of hydrodynamic parameters in inundation zone through the Section A-A with the simulation of waves in 4m wave amplitude with 48min period on fully protected residential areas in test basin-02 with 1/20 slope for LEW and LDW .....	115
Figure 5.51: The distribution of maximum $Fr^2$ values calculated for Test Basins 04 and 23.....	117
Figure 5.52: The wave profiles of sinusoidal and N-wave with the wave amplitude of 1m.....	119
Figure 5.53: The normalized maximum runup of isosceles N-wave against the asymptotic expression in Eqn [5.12] on a 1/20 sloped beach.....	121
Figure 5.54: Comparison of maximum runup of leading elevation N-wave computed by NAMI DANCE and calculated by analytical relations in Tadepalli and Synolakis (1994) and Zhao et al. (2010).....	122

Figure 5.55: The difference of maximum current velocity and $Fr^2$ on plain beach (Test Basin-01) for the spatial variety of Manning's coefficient.....	124
Figure 5.56: The difference of maximum current velocity and $Fr^2$ on unprotected residential area (Test Basin-02) for the spatial variety of Manning's coefficient .....	124
Figure 5.57: The difference of maximum current velocity and $Fr^2$ on fully protected residential area (Test Basin-17) for the spatial variety of Manning's coefficient .....	125
Figure 6.1: The Location of Kamaishi city and satellite image of Kamaishi Bay .....	127
Figure 6.2: Tsunami damage in the Kamaishi City after the event (Yalciner et al., 2012).....	127
Figure 6.3: The digitized bathymetry and topography of Kamaishi Bay and City....	128
Figure 6.4: The gauge points around the buildings at the North of Kamaishi Bay and the sections crossing the two breakwaters.....	129
Figure 6.5: The comparison of water surface elevation at the seaside and leeside of the breakwater during the simulation time .....	131
Figure 6.6: The water surface fluctuation at the top of breakwater in Section 1, 2 and 4 during simulation time.....	132
Figure 6.7: The ratio of maximum current velocity between with and without breakwater cases .....	133
Figure 6.8: The ratio of maximum $Fr^2$ between with and without breakwater cases	133
Figure 6.9: The change of current velocity during simulation time at the gauge points located through the breakwater gap for with and without breakwater cases .....	134
Figure 6.10: The water level fluctuations during the simulation time at three selected gauges for with, without and damaged breakwater cases .....	135
Figure 6.11: The change of current velocities during simulation time at three selected gauge points for with, without and damaged breakwater cases .....	136
Figure 6.12: The change of square of Froude Number during simulation time at three selected gauge points for with, without and damaged breakwater cases .....	137

Figure 6.13: The ratio of maximum current velocity between the cases of with breakwater of 20m crest height (no overtopping) and without breakwater ..... 139

Figure 6.14: The ratio of maximum  $Fr^2$  between the cases of with breakwater of 20m crest height (no overtopping) and without breakwater ..... 139

## LIST OF SYMBOLS

$A$	cross-sectional area exposed to drag force
$a$	wave amplitude
$B$	width of a cross-section exposed to waves
$b$	horizontal length of the structure perpendicular to the wave direction
$\beta$	sea bottom slope angle
$C_D$	drag coefficient for non-breaking waves
$c_{\max}$	maximum speed of tsunami
$C_n$	empirical coefficient
$\cot \beta$	sea bottom slope
$D$	flow depth
$d$	water depth at the toe of the bottom slope
$d_c$	typical (maximum) water depth
$d_s$	water depth at the location of the structure
$d_t$	time step of numerical calculation
$d_x$	grid size in x direction
$d_y$	grid size in y direction
$E$	relative absolute error
$f$	friction coefficient
$F_D$	Drag force
$Fr$	Froude number
$Fr_{\max}^2$	maximum of Froude number square
$\overline{Fr_{\max}^2}$	average of maximum of Froude number square
$g$	gravitational acceleration
$h$	water depth with respect to disturbed water level
$H$	solitary wave height

$HD$	hydrodynamic demand
$i$	number of grid node in x direction
$j$	number of grid node in y direction
$k$	number of increment in time
$LDW$	Leading Depression Wave
$LEW$	Leading Elevation Wave
$M$	discharge flux in x direction
$N$	discharge flux in y direction
$n$	Manning's coefficient
$\eta(x, y, t)$	water surface elevation with respect to the undisturbed water level
$p$	hydrostatic pressure
$Ru$	runup of solitary waves
$Ru/d$	normalized runup of solitary waves
$\rho$	density of sea water
$t$	time
$\tau_{ij}$	shear stress in $i$ direction on the $j$ normal plane
$\tau_x, \tau_y$	bottom frictions in $x$ and $y$ directions
$u, v$	depth-averaged water particle velocities in the cross-shore $x$ and long-shore $y$ directions, respectively

## CHAPTER 1

### INTRODUCTION

Tsunamis are water waves which transfer short duration energy to the entire water column in large scale as a result of earthquakes, coastal and submarine landslides, volcanic eruptions, or meteor impacts. The number of waves and polarity of the initial wave depend on the seabed motion and the following developments are explained by long wave theory (Sumer et al., 2007).

After the terrible disaster of 1896 Great Meiji tsunami in Japan caused the death of more than 22000 people, the word “tsunami” began to be used in other languages than Japanese. It was used in the meaning of *harbor wave* since tsunamis had commonly occurred as unusual waves in ports and small bays. A similar term is *tidal wave*, which is the English translation of a Greek term defining tsunamis since tsunamis mostly indicate themselves along the coastlines as surges or rapid changes in water level. Smong is another word used in Indonesia, Simuelue Island for the inundation of the sea after earthquake.

Tsunamis have extensive and destructive effects on coastal and marine structures, as well as causing loss of lives and high financial burden. They can drag huge objects and carry them even into the buildings, sour the foundation of buildings, collapse the shoreline due to liquefaction, overflow tsunami defense structures and destroy the settlements (Borrero et al, 2003). The 2004 Indian Ocean Tsunami and then more devastating one 2011 Great East Japan Tsunami were extreme events showing these extreme effects on the coastal areas (Yalciner et al, 2005; 2012; Choi et al, 2005). The reason for this devastating damage is the occurrence of extensive currents together with flow depths in inundation zone. There is so much footage taken by the eyewitnesses that could survive by escaping to the higher floors of concrete buildings

in the vicinity. The footages reveal the destructive effect and dragging capability of strong tsunami currents along the coasts.

The major impacts of tsunamis are observed mostly in the shallow water and inundation zone. Tsunami effects are studied in two categories as direct and indirect effects. Direct effects of tsunamis occur just after the tsunami arrival and cause extensive damage on coastal and inland structures such as dragging of the large structures, destruction of the buildings with accumulated shoreline debris, undercutting of foundations and pilings with the effect of erosion, and overturning of huge structures are. On the other hand, indirect effects occur sometime after the arrival of the tsunami. For instance, the oscillation of long waves in enclosed basins called resonance oscillations is an example for the indirect effect. Tsunami hazards also cause great pecuniary burden to the national economies since the structural and environmental damages are excessively costly to repair.

Structural damage caused by tsunami waves can be estimated by calculating the impact forces on the structures. The impact force focused in this study is the drag force ( $F_D$ ) that is exerted by the fluid on the solid object in the flow direction.  $F_D$  is expressed by the square of the velocity component normal to the object and to the lift force. The magnitude of  $F_D$  is adjusted by a drag coefficient  $C_D$ , depending on the shape of the solid structure exposed to the fluid effect and the Reynolds number.

The level of tsunami damage is proportional to the level of the drag force. Hence, it can be represented by a dimensionless parameter '*hydrodynamic demand*' ( $HD$ ), which is obtained by the ratio of the drag force (exerted by the flow) to the hydrostatic force on the structure. In other words,  $HD$  represents the proportionality of the drag force with respect to the hydrostatic force. This is actually the square of Froude Number, which is an instantaneous parameter occurred at any location during tsunami inundation, depending on the instantaneous values of the current velocity and the flow depth at the location. The current velocity and the flow depth change in time independently, thus the maximum value of the hydrodynamic demand also varies with time.

In this thesis, the square of Froude number ( $Fr^2$ ), which is the governing parameter of the hydrodynamic demand, is calculated in the tsunami inundation zone together

with the major tsunami hydrodynamic parameters, such as maximum water surface elevations (positive tsunami amplitudes), maximum flow depths and maximum currents, by inserting new modules to the numerical model NAMI DANCE.

One of the purposes of this thesis is to derive a correlation for the damage level by means of Froude Number square ( $Fr^2$ ) in order to investigate and determine the tsunami damage in inundation area in relation with the wave characteristics and beach slope. Another aim is to investigate the behavior of tsunami hydrodynamic parameters in case of coastal protection structures for determining damage level and tsunami prone areas in residential regions. The details of the study are described in each chapter starting from the theoretical background and numerical modeling techniques and continuing with the details of analyses.

Chapter 2 describes the literature survey carried out for this study. It gives the details of different approaches to calculating the impact forces with the related equations. In Chapter 3, the theoretical and numerical background is given. Theoretical background deals with the direct effect of tsunamis on different coastal structures, and numerical background includes equations and details of the new module inserted in numerical model NAMI DANCE in this study. Chapter 4 describes the validation and verification of NAMI DANCE through the application of benchmark problems. The benchmarking is performed by comparing the numerical results with experimental data or observed data from real tsunami events. The application of the numerical model on a regular shaped basin is given in Chapter 5, where different scenarios are used and all parameters in the model are explained in detail. The analyses are performed in two parts as on different sloped plain beaches with different wave characteristics and on the beaches with different structural layout. Chapter 6 gives a case study that applied the determination of hydrodynamic parameters and evaluation of Froude Number during the tsunami inundation in 2011 Great East Japan Tsunami at Kamaishi Bay. Chapter 7 provides a summary and general evaluation and discussion of the results. In Chapter 8, suggestions for further studies are given in the light of conclusions and discussions.

## CHAPTER 2

### LITERATURE SURVEY

High tsunami amplitudes at coasts and the resulting strong flow velocities are the main causes of impact by tsunami waves. There are two types of tsunami effects: indirect and direct effects. Indirect effects occur due to the resonance of the enclosed basins by tsunami waves. On the other hand, the direct effects, which are very extensive and disastrous, cause the dragging of the whole structures, damage in the buildings with accumulated shoreline debris, undercutting of the foundations and pilings with erosion and overturning of huge structures.

The two main parameters causing damage during tsunami inundation are water surface elevations and velocity. The approaches to determining the impact forces caused by tsunami inundation need to be clarified for the selection of type of velocity to be used. Two different types of velocities are considered for the computation of hydrodynamic demands during tsunami inundation. These velocities are current velocity and wave front velocity, which may show different behaviors. Therefore, it is essential to determine the effects of these velocities when the tsunami waves come to the shoreline and begin to threat the coastal structures and human lives.

Structural damages by tsunami waves can be estimated by calculating the impact forces on structures, the drag force in particular. Force in the direction of flow exerted by the fluid on the solid is called drag. The *drag* force  $F_D$  is generated by the square of velocity component normal to the element and normal to the lift force. The magnitude is adjusted by a drag coefficient  $C_D$ , depending on the shape of structure and Reynolds number (Sumer and Fredsøe, 1997). The drag force occurring

during tsunami inundation should be estimated in order to determine the structural damage.

Major studies have been carried out to find the drag force exerted to the coastal structures. There are different approaches to the selection of the velocity component normal to the structure surface over the flow depth. Indeed, the variation uses either flow velocity or wave front velocity in the computation of drag force. These approaches are as follows.

Yalçiner and Synolakis give a brief review of generation, propagation and coastal amplification of tsunamis (in Sumer et al. 2007). They offer a different approach to calculating the direct and indirect impact of tsunamis on marine structures. They introduce a new term called *Hydrodynamic Demand*, which refers to the normalized form of drag force by hydrostatic force. This new approach is intended to enable the researchers to evaluate the level of damage on structures. In this study drag force is calculated from

$$F_D = \frac{1}{2} C_D \rho A u^2 \quad [2.1]$$

where  $A$  is the cross-sectional area exposed to drag force,  $C_D$  is the drag coefficient which is the shape parameter and should be less than 2,  $u$  is the current velocity and  $\rho$  is the fluid density. Yalçiner and Synolakis stated that evacuation of coastal areas that are under the risk of tsunami inundation is crucial in order to prevent loss of life (in Sumer et al., 2007).

Yeh (2006) studied the tsunami forces in the runup zone considered by using the algorithm recently developed by Carrier et al. (2003). In this study, he estimated the horizontal fluid force resulting from tsunami runup/drawdown processes onto a uniformly sloping beach. The maximum force per unit width is determined by

$$F = \frac{1}{2} C_D \rho h u^2 \quad [2.2]$$

where  $C_D$  is the drag coefficient suggested as 1.0-2.0 by Arnason (2004),  $\rho$  is the fluid density,  $h$  is the total flow depth and  $u$  is the velocity of flow (in Yeh, 2006).

OCDI in “Technical Standards and Commentaries for Port and Harbor Facilities in Japan” (2002) explained the transformation of tsunami in a bay with related commentaries and technical notes. They stated that during tsunami inundation in a bay, the most important types of transformations of tsunami are the increase in wave height and flow velocity caused by the decrease in the cross-sectional area toward the end of bay and the increase in wave height induced by seiche in a bay. Based on the assumption of small amplitude waves, they suggested using Green’s equation in order to calculate the influence of the change in cross-sectional area as given below.

$$\frac{H_0}{H} = \left(\frac{B_0}{B}\right)^{1/2} \left(\frac{h_0}{h}\right)^{1/4} \quad [2.3]$$

Here,  $H$  is height of long waves for a cross section with the width  $B$  and the water depth  $h$  (m), and  $H_0$  is height of long waves for a cross section with the width  $B_0$  and the water depth  $h_0$  (m). They also specified that this equation is applicable in case of having gentle variations in both the width and the water depth and having no reflected waves moving offshore. They added that this equation does not consider the energy loss due to friction and cannot be applied to shallow water when there are reflection effects at the end of the bay.

Fujima (2009) conducted hydraulic experiments to understand the characteristics of time history of wave pressure and total force exerted onto the structures. A 2-D wave basin (length: 11 m, width: 7m and depth: 1.5m) was used with a piston device for wave generation. He performed several experiments by varying the scale of the buildings, distance from the shoreline and the stroke type of incident wave. In all cases, the incident wave broke in shallow zone and hit the vertical seawall. Current velocity was measured by propeller current meter, wave force on the structure models by load cell and wave pressure by the pressure gauges. The wave pressure on structures placed 20cm onshore were estimated. He also compared the applicability

of the data to that of the existing one. Asakura et al. (2000) proposed an empirical formula to calculate the maximum tsunami force on structures by integrating the envelope of maximum standing-wave pressures (in Fujima 2009).

The hydrostatic form of the formula for estimating tsunami force was proposed. After the evaluation of the results, Fujima (2009) suggested that the tsunami damage estimation based on only the inundation depth may be inaccurate for structures far from a shoreline since the results are either overestimated or underestimated.

Fujima (2009) also estimated the tsunami force on the structures by calculating the hydrodynamic force (drag force) on the exposed buildings. Drag force in the function of inundation depth, velocity and the drag coefficient formulated as

$$F_D = \frac{C_D}{2} \rho B (h_i u_i^2)_m$$

where  $u_i$  is the velocity at a point,  $h_i$  is the inundation depth at that point,  $\rho$  is the density of water,  $B$  is the width of the model and  $C_D$  is the drag coefficient depending on the shape of the area of the structure exposed to the waves

defined as  $C_{D3} = 1.3 + 6.3 \frac{h_{im}}{D}$ . It was indicated that since the maximum inundation

depth  $h_{im}$  and the maximum velocity  $u_{im}$  may not occur at the same time, it is preferred to estimate the maximum momentum flux.

Considering the proximity of the buildings to the shoreline and testing and comparing the results of various drag coefficients, average estimation and safety estimation depending on the distance from the shoreline was estimated to be the optimum equation for drag force. Since an inertial force is not negligible in cases of structures near the shoreline, drag coefficients were calculated as functions of  $h_{im} / D$ , where  $D$  is the distance from the shoreline. New tsunami-force estimation formulas were also proposed, the applicability of which should be checked by numerical modeling to recalculate the inundation depth and velocity (Fujima, 2009).

Numerical modeling of propagation and runup of tsunamis is widely studied by many researchers. There are different approaches in terms of the algorithms used in

numerical models. In this thesis, the analyses are performed by numerical modeling by applying valid calculation theories. It is necessary and essential to validate and verify the numerical modeling tool before analyzing the tsunami motion. Some studies including numerical modeling approaches and validation and verification of numerical models are given in the following.

Okada (1985) presents a new study focusing on the surface deformation induced by an arbitrarily oriented rectangular opening-mode dislocation which provides a quantitative work for evaluating and removing fluid-filled crack-induced noises from crustal deformation records. The *Okada* model calculates analytical solution for surface deformation due to shear and tensile faults in an elastic half-space. This model is widely used to simulate ground deformation produced by local perturbation like tectonic faults (earthquakes) or volcanic dykes (magmatic intrusion). It computes the displacements, tilts and strains at the free-surface using the inputs as the rectangular fault geometry (length, width, depth, strike, dip) and 3-component dislocation amplitude (rake, slip and open).

Okada (1985) summarizes useful expressions for the analysis of static field changes associated with earthquake and also for the modeling of deformations caused by fluid-driven crack sources. He highlights that the advanced efforts invested for the formulation of a more realistic earth model include i) earth curvature, ii) surface topography, iii) crust layering, iv) lateral inhomogeneity, and v) obliquely layered medium. Despite these advanced approaches, the analyses of actual observations mostly follow the simplest assumption of an isotropic homogeneous half-space and the simplest source configuration.

Shuto (1991) compared the numerical results of three long wave theories in deep water to discuss the dispersion effects on tsunami propagation: linear Boussinesq, Boussinesq and linear long wave. He stated that the linear Boussinesq and Boussinesq equations almost coincide with the true solution (given by linear surface wave theory), suggesting that the nonlinear term is not important in deep water propagation of tsunamis. The researcher concluded that using coarser grid sizes gives

better solution of numerical dispersion than that of higher-order model with the same grid size and that of even the same model at finer grid. In the model, at every time step, the solution of the Poisson equation gives the dispersion potential, then the Boussinesq equation is solved to get the wave field. For stability, time-step should be smaller. In addition, the spatial resolution should satisfy the condition that  $\Delta x \geq 1.5h$ . However, this size is too poor to observe the wave behavior on coastal lines and islands. Therefore, a modified-explicit central-difference scheme is used to solve Boussinesq and Poisson equations. Here, the current velocity term is computed from the previous time-step, and the elevation term is term-centered (averaged between two time steps). The time-step had to be reduced by 30% compared to the code without dispersion term. This change resulted in a 30% increase of total computational time.

Imamura, who described a method of setting initial and boundary conditions of the linear long wave theory, asserted that long travel distance may yield dispersion of wave components, and therefore physical dispersion term should be included, i.e. the equations of higher order approximation should be used (1995). It is stated that vectorization rate increases when the linear theory is used, even with the ordinary programming method and that the dispersion terms become important in far-field tsunamis. The linear Boussinesq equation that includes physical dispersion term is considered appropriate to express the dispersion effect.

Imamura (1996) provides other methods of tsunami numerical modeling and describes the numerical scheme of numerical model TUNAMI-N2. The governing equations, stability conditions and runup calculations are stated in detail in this thesis.

Sato (1996) reports a numerical simulation of tsunami propagation for the 1993 Southwest Hokkaido earthquake tsunami. The model is based on the Boussinesq equation, which includes the effects of frequency dispersion. Energy dissipation due to breaking at the tsunami wave front is modeled. The validity of the model was tested with the existing laboratory data of dispersive wave trains breaking on a slope. The model was then applied to the simulation of the 1993 Southwest Hokkaido

earthquake tsunami around the southern part of Okushiri Island. Comparison with the physical model demonstrates that it is the dispersion of the wave front which caused focusing of the wave energy at the narrow region on the lee side of the island, consequently increasing the tsunami height.

One of the most comprehensive studies about tsunami numerical modeling is Synolakis and Bernard (2006) which collect and summarize the approaches for tsunami numerical calculations. They emphasize the improvements in tsunami simulations by numerical modeling after the devastating 2004 Sumatra tsunami. The progress of developing tsunami inundation modeling tools is described in detail in terms of hydrodynamics. They stated their suggestions for future research in tsunami modeling as establishing validated inundation models, developing a methodology for short-duration impact forces on structures, preparing the maps for vulnerable coastal areas immediately along with paleotsunami research, refinement in the development of better relationship between deforming seafloor motions and model initialization, and more comprehensive educational efforts on tsunami hazard mitigation.

Dao and Tkalich (2007) researched into the sensitivity of the modified version of the numerical model TUNAMI-N2 considering astronomic tide, sea bottom friction, dispersion, Coriolis force, and spherical curvature by modeling the 2004 Sumatra event as tsunami scenario. The code is modified and the resulting version is called TUNAMI-N2-NUS which solve non-linear shallow water equations. However, the code uses the Boussinesq Equations when the dispersion effect is considered.

As mentioned before, the validation and verification of tsunami numerical models are essential if the results of the models will be used by decision makers in emergency planning. As being a well-prepared synthesis, Synolakis et al. (2008) discussed analytical, laboratory and field benchmark tests with which tsunami numerical models can be validated and verified. The benchmark tests are described in detail as well as their expected solutions. They also mention the scientific and operational evaluation of the model and the necessity of continuous validation and verification processes in case of new knowledge and data are acquired. It is emphasized that

operational tsunami models should be tested continuously after each tsunami event with real time data for hind casting.

Besides numerical modeling, there are plenty of studies about the analytical solutions of tsunami propagation and runup most of which are tested and compared with the results of laboratory experiments. The analytical solutions of tsunamis are reviewed and some of the studies in literature are summarized in the following.

One of the earliest studies about analytical solutions of tsunami motion is Thaker (1981) which introduced some exact solutions to the nonlinear shallow water equations. The exact solutions correspond to time-dependent motions in parabolic basins and the shoreline is assumed to move freely. Thaker provided a solution for a flood wave if the parabolic basin is reduced to a flat one (1981). In that way, it is stated that those exact solutions may be a valuable comparison test for numerical models. It is also emphasized that since the numerical integration of nonlinear shallow water equations and the required other assumptions is not easy, it is more practice to use those exact solutions.

Liu et al. (1995) investigated runup of solitary waves on a circular island. They studied the interactions of solitary waves climbing up a circular island and carried out a series of large-scale laboratory experiments with waves of different incident height-to-depth ratios and different crest lengths. They also developed a numerical model based on the two-dimensional shallow-water wave equations including runup calculations. Under certain conditions, they observed runup and wave trapping on the back side of the island by using this numerical model.

Kanoglu and Synolakis (1998) investigated long wave runup on piecewise linear topographies and developed a general solution method for determining the amplification factor of different ocean topographies consisting of linearly varying and constant-depth segments to study how spectral distributions evolve over bathymetry. They used their results to study the evolution of solitary waves.

Kanoglu (2004) solved the initial value problem of the nonlinear evolution, shoreline motion and flow velocities of long waves climbing sloping beaches analytically for different initial wave forms. He proposed that any initial wave form can first be represented in the transformation space by the linearized form of the Carrier-Greenspan transformation for the spatial variable, and then the nonlinear evolutions of these initial waveforms can be directly evaluated. After the necessary transformations, he introduced a simplified equation for the calculation of runup/rundown motion of the shoreline. This approach is applied to Gaussian and leading-depression N-wave initial forms presented by Carrier et al. (2003), and the results are compared. Kanoglu (2004) concluded that his study is simpler than that of Carrier et al. (2003) and produces identical results since his analysis does not need to solve singular elliptic integrals. He also suggested that, based on the convenience of nonlinear shallow-water wave equations for the quantitative and qualitative predictions, the method outlined in his study may be useful to assess the impact of long waves generated by seafloor displacements and to validate numerical codes.

The method described in Kanoglu (2004) is also applied to different N-wave initial forms, such as leading-depression isosceles N-wave and generalized N-wave initial forms. Tadepalli and Synolakis (1994) use a first-order theory and derive asymptotic results for the maximum runup. They stated that a class of N-shaped waves was found in their study with very interesting behavior which is said to be a new phenomenon for tsunami runup studies. Similar trends are observed in Tadepalli and Synolakis (1994) in the maximum runup results.

Tsunami damage on coastal structures is crucial that should be studied particularly. In recent years, advances in laboratory equipment, hardware and related software provide opportunity to measure and evaluate tsunami damages on structures. Among the others, Japanese studies are more prevalent as Japan experienced many vital tsunami events in history. Shuto (2009) defines four types of damages to coastal structures caused by tsunami-induced currents in Japan: (1) Erosion of soil embankments near underpasses or bridges by concentrating water current; (2) Scour and destruction of the structure toe by strong currents parallel to long structures; (3)

Erosion of soil embankments by overflowing water of tsunamis; (4) Damage of toe of quay walls due to the waterfall that occurs when water returns and hits the sea bottom during the drawdown of tsunami. He also exemplifies the effects of current velocity concentration through a railroad underpass which collapsed at Yagi and the erosion of railway embankment made of soil after 1933 Showa Great Sanriku Tsunami in Iwate Prefecture. He adds that in the 1960 Chilean Tsunami in Haji, Okinawa, and tsunami was prevented by a long soil embankment of a coastal road, but it concentrated toward the river. Then, the strong flow eroded and washed away the road embankment near the abutment of the bridge. Makiya Bridge made of reinforced concrete remained.

Furthermore, Shuto (2009) detailed the effects of tsunami-induced current in bays and harbors through the case of the gravity- type quay wall of the Konakano Fish Market in Hachinohe Harbor, which was highly influenced by the 1960 Chilean Tsunami. The harbor was built by using the mouth of the Niida River. This quay wall was damaged and some of the caissons collapsed in 2011 Great Japan Tsunami. He added that, at the entrance of the harbor, maximum ebb flow velocity was estimated as 13 m/s and the max flood flow velocity as 8 m/s. The sea bottom drastically changed as a result of this strong current. The maximum amplitude of this tsunami was about 6m. High scouring occurred at the toe of the quay wall (from -3m to -9 m). The soil and residual water pressures due to abnormal low water level damaged the caisson bases and pushed them forward. Ten-meter-long caissons were overturned or subsided. The eyewitnesses said that the quay wall collapsed during an ebb tide in about 30 minutes.

Besides, Shuto (2009) stated that several studies exist on the simulation of the bottom erosion in Kesenuma bay each having certain limitations. Overall, they seem to be inaccurate. The distribution of measured tsunami traces on land and tsunami profile recorded on tide gauge at the Kogoshio Station was simulated. What is more, Takahashi et al. (1993) indicated that there were significant differences between measured and computed current velocities (in Shuto, 2009). The computed currents are one-half to one-third of those measured in aerial photographs.

Shuto (2009) also described the effects of overflow during tsunami inundation. He provided a depiction of the embankment made of sand with dry stone revetments on the seaside which was washed away by the 1933 Showa Great Sanriku Tsunami within a period of about 10 minutes at Yagawa, Ohara village, Miyagi Prefecture. Also described was the back slope of the coastal embankment at Ozuchi, Iwate Prefecture which was highly scoured out by the 1960 Chilean Tsunami of wave period of 35-40 minutes. The overflow depth on the crest was about 50 cm, and the height of the embankment on the land side was about 2m. Furthermore, factors used to decide whether a soil embankment is damaged by an overflowing tsunami (or Factors determining the resistance of a soil embankment to the damage caused by an overflow tsunami) are embankment materials, solid protection on three surfaces protection at the toe the height of the embankment above land on the downstream side, overflow depth on the crest and overflow duration.

Furthermore, the tsunami damage on embankments is investigated. Shuto (2009) summarized that embankments not thicker than 20 cm stay undamaged by the overflowing water regardless of embankment height and those lower than 50 cm survive in any case, even if the tsunami is very large. He described why caissons collapsed during 1960 Chilean tsunami; due to the withdrawal, the water level in the harbor lowered. Then, the next wave came to overflow the top of caissons to a water depth of about 50 cm. Strongly hit by this falling water and pushed by seepage flow, the rear mound became unstable and disturbed. Therefore, the caissons were slid and overturned under a high pressure difference that had not been considered in design forces. This incident made the waterfall effect in Ofunato Port, Iwate. When the tsunami receded, the falling water hit and scoured out the toe of the sheet-pile quay wall 4m deep, decreasing the resistant passive soil-pressure at the toe. He concludes the current simulation is difficult to perform due to the verification of calculated results. Although tsunami trace heights and gauge records are available for tsunami height simulation, few reliable measured data-records exist for current velocity. Large scale hydraulic experiments need to be conducted to improve this situation. Further studies for valid and verified current simulations should be performed in the near future.

Surge front tsunami force is an important factor that governs tsunami damage; thus needs to be investigated. Arikawa (2009) studies surge front tsunami force using physical laboratory experiments. Wooden and concrete walls are examined to predict their behavior in case of failure processes in full-scale experiments under the loads of breaking tsunami. The experiments were conducted in a large wave flume, called Hydro-Geo Flume, at the Port and Airport Research Institute (PARI), Japan. The flume is 184m in length, 3.5m in width and 12m in depth. It has a piston-type wave generator capable of generating a 2.5m high tsunami.

The mechanism of land-structure destruction was investigated using a wooden wall 2.5m high and 2.7m wide. A steel frame was used behind the wooden wall as strut that prevents the wall from being washed away without damage. The wooden wall consists of 3 layers as siding board (16 m), veneer board (1cm) and a wooden column (10cmx10cm). The flexural capacity of the siding board is 10 kN/m<sup>2</sup> for a short duration. The 2.7m-wide-wall is narrower than the 3.5m-flume, so some water drained away from the gaps between the flume side walls and the model. In the experiments, the wooden wall collapsed as soon as the instant tsunami hit the wall. He tested a total of 8 concrete walls which are 2.5m high and 2.7m wide having different thicknesses ranging from 6 to 10 cm. The pressure transducers and strain gages were installed on the cross-section of the wall. The rebars with 6mm diameter were placed at 20cm intervals. The vertical pressure distribution was plotted, and it was found that the maximum impulsive pressure obtained was about 7.7 times of the hydrostatic pressure at the inundation depth in front of the wall. The tsunami pressure time histories were also plotted.

The experimental results showed that the wooden wall was fully destroyed by the tsunami of 2.5m high measured at 30m offshore. The tsunami also damaged the concrete wall, though partly, leaving a pounded hole near the bottom of the wall. The failure occurred in the form of bending or punching shear when the strength of the wall was small. The failure mode shifts from local damage to wide destruction depending on the strength of the wall. Arikawa (2009) stated that it is important to

examine the failure processes of the walls for the design consideration of the seawalls and breakwaters to resist the tsunami forces.

A new measure called tsunami fragility estimates the tsunami damage on structures and fatalities by gathering satellite remote sensing, field survey, numerical modeling and historical data analysis with GIS (Koshimura et al., 2009). It can be explained as the probability of structural damage or the fatality ratio related to the hydrodynamic parameters of tsunami inundation such as inundation depth, current velocity and drag force.

Several empirical approaches to correlating tsunami hazard and vulnerability exist (Koshimura et al., 2009). However, their findings are generally based on the inception of local aspects of tsunami damage. Therefore, it is difficult to identify the vulnerability quantitatively. To estimate vulnerability, it is necessary to consider several uncertain sources, such as hydrodynamic parameters of tsunami inundation, structural characteristics, population, land use and any other site conditions.

Suzuki and Arikawa (2010) investigated the bulk drag coefficient in rigid dense vegetation mainly by using a three dimensional numerical simulation model CADMAS-SURF/3D by incorporating Immersed Boundary Method to calculate flow around the vertical cylinder in the Cartesian grid. Large Eddy Simulation is also incorporated as a turbulence model. They firstly validated the developed model with a single cylinder in the flow field based on literature. The results obtained ( $Re=300, 3,900$  and  $8,000$ ) show good agreement with the reference data in literature. After the validation, they allotted multiple cylinders of three different densities ( $S/D=2.8, 2.0, 1.4$ ) in a numerical wave tank, and numerical simulations are conducted to investigate bulk drag coefficient. The result shows that the ratio of bulk drag coefficient to drag coefficient, which represents a reduction, is not just a function of density but a function of parameter  $2a/S$ , in which  $2a$  is stroke of the motion and  $S$  is cylinder distance.  $2a$  is less than  $S$ ; the effect of the density is neglected because the wake does not reach the other cylinders even when the density is high. On the contrary, it might affect the ratio of bulk drag coefficient to drag coefficient when the stroke of the

motion is larger than the cylinder distance even when the density is low. In general, the ratio of bulk drag coefficient to drag coefficient decreases when  $2a/S$  increases.

Coherent structures in wave boundary layers are investigated into two parts, considering either oscillatory motion or the solitary motion. Carstensen et al. (2010) studied on the oscillatory boundary layers over smooth beds including bed shear stress measurements in an oscillating water tunnel. The experiment results reveal two significant coherent flow structures; vortex tubes and turbulent spots. They also found that similar coherent flow structures exist in case of combined oscillatory flow and current. As the continued investigation, Sumer et al (2010) studied the turbulent solitary wave boundary layers by simulating solitary motion in an oscillating water tunnel. They measured bed shear stress and velocity. Their experiments show that the solitary-motion boundary layer experiences different kinds of flow regimes as the Reynolds number is increased.

It is not common to include tsunami risk while designing coastal protection structures in Turkey. However, some researchers suggest applying tsunami modeling where seismic activity is considerably essential. Ergin and Balas (2006) applied Conditional Expectations Monte Carlo simulation in the risk assessment model developed for the Esenköy Fishery Harbor in Turkey in order to determine the occurrence probability of structural damage under design conditions, including the environmental loading parameters of tsunami and storm waves, tidal range and storm surge. In this study, tsunami did not turn out to be the key design parameter when compared to storm waves for the main breakwater of the harbor; however, in places with great seismic activity, the tsunami risk should be important depending on the occurrence probability and magnitude of the tsunami.

In the light of these studies in literature, the hydrodynamic parameters are investigated during tsunami inundation with the purpose of governing and proving a reference parameter representing the level of damage on residential areas using numerical modeling method. The details of this study are given in the following sections.

## CHAPTER 3

### THEORETICAL BACKGROUND AND NUMERICAL SCHEME

This section describes the general behavior of tsunamis in deep sea, shallow water and inundation zone. The destructive effects of tsunamis are described through real tsunami events in the world. The state-of-the-art approaches to tsunami numerical modeling worldwide are also mentioned. The method of numerical modeling with the code NAMI DANCE is discussed in detail in terms of its capabilities and ad hoc modeling principles within the broader framework of these approaches. To this end, the numerical scheme of the code is explained including the details of calculations done when the waves climb the land.

#### 3.1 Theoretical Background

The process of developing tsunami inundation modeling codes needs to have high predictive value as to tsunami hydrodynamics. Throughout the history of tsunami investigations, various approaches were used to determine tsunami hydrodynamics by laboratory experiments, analytical calculations and numerical computations (Synolakis and Bernard, 2006). The tsunami numerical modeling has been continuously improved, and now it is one of the most operative tools used for the prediction of tsunami damage and establishment of mitigation strategies and tsunami defense structures (Shuto, 1991).

The tsunamis are long waves generated by impulsive disturbances at the sea bed and along the coastline, such as earthquakes, subaerial/submarine landslides, volcanic eruptions, meteorite impacts and explosions. The tsunami computations are

principally based on the long wave theory (Shuto 1991). When tsunamis are generated and begin to propagate in deep sea, they initially show a behavior that is described by linear long wave theory. While approaching to the shoreline, the tsunami wave height increases with the reduction of its velocity and wave length decreases, then the nonlinear effects become significant. The propagation behavior of a tsunami as it approaches the shoreline is illustrated in Figure 3.1.

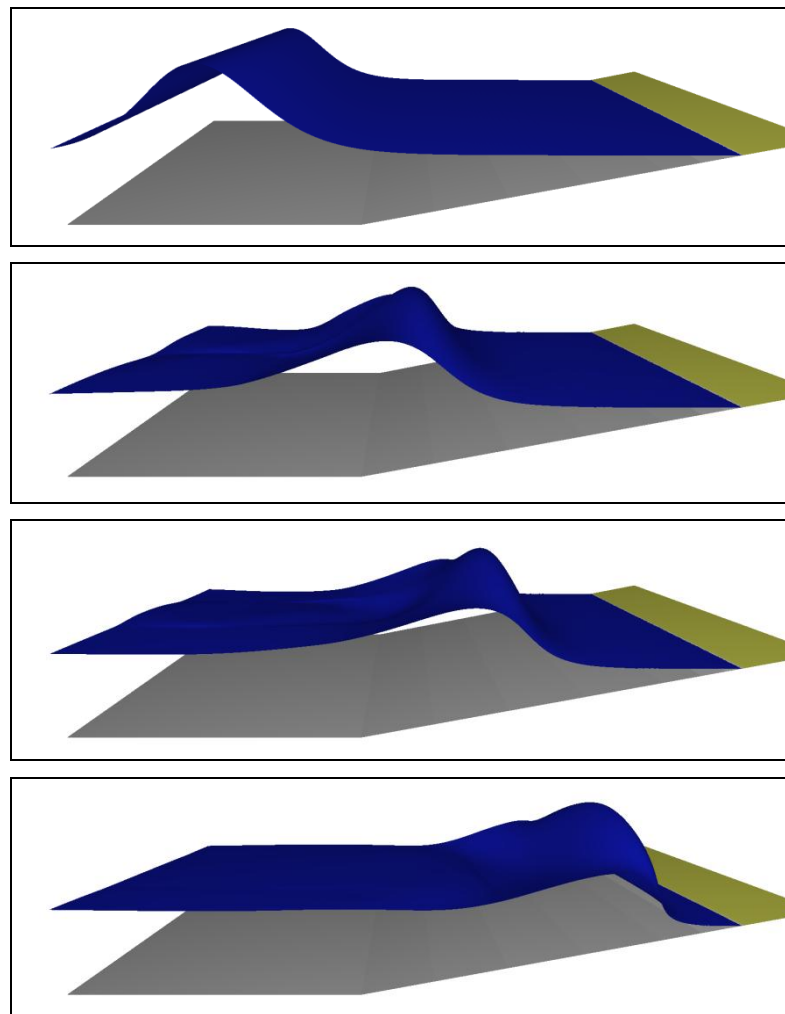


**Figure 3.1:** Increasing height and decreasing length of a tsunami on a sloping beach

When tsunamis reach to the land, the effects of hydrodynamic parameters become significant. Figure 3.2 demonstrates the sectional view of tsunami inundation zone with the hydrodynamic parameters as water surface elevation, flow depth, runup and

inundation distance. As seen from the figure, water surface elevation is specified with respect to still water level while the flow depth is stated relative to the ground level.

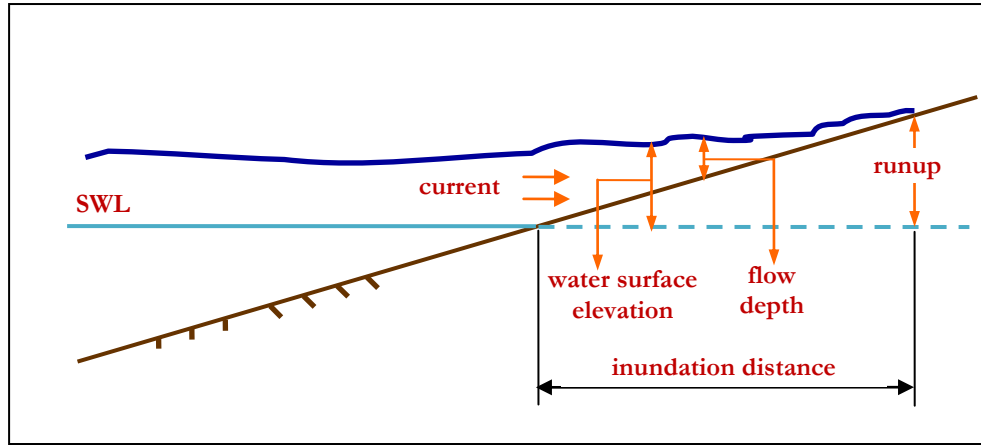


**Figure 3.2:** Sectional view of tsunami hydrodynamic parameters in inundation zone

Tsunamis have the power to show extensive and destructive effects on coastal and marine structures. The 2011 Great East Japan Tsunami was one of the most disastrous ones, affecting the East coasts of Japan to an extreme extent. The occurrence of extensive currents together with flow depths in inundation zone accounts for this devastating impact. There is much footage taken by the eyewitnesses that could survive by escaping to the higher floor of concrete buildings in the vicinity. The footages reveal the destructive effect and dragging capability of strong tsunami currents along the coasts. The photos in Figure 3.3 depict the devastating effect of the disaster along the East coasts of Japan after the tsunami. The photos are taken by the post tsunami survey team which was led by Prof. Yalciner from Middle East Technical University, Turkey and which consisted of experts from Turkey, Japan, Greece, Thailand and Peru, who visited the area between May 29 and June 3, 2011 (Yalciner et al, 2012). The photos clearly manifest that tsunamis cause extreme damage on the coasts and on the land, as well as bringing high financial burden, by dragging huge objects and carrying them even into the buildings, souring the foundation of buildings, collapsing the shoreline due to liquefaction, overflowing from tsunami defense structures and destroying the



**Figure 3.3:** The photos taken during the post tsunami survey after 2011 Japan event by the tsunami survey team under the leadership of Prof. Yalciner between May 28 and June 2, 2011. (a) a car dragged into the first floor of a primary school in Arahama, (b) high scour of a building foundation near Sendai coasts, (c) scour of the foundation of a building near the shoreline in Kamaishi (this building is famous with one of the most well-known footage from Japan event), (d) subsiding of the shoreline in Otsuchi, (e) Miyako tsunami wall from the balcony of Mayor's office building with a dramatic picture taken from the same point during tsunami flooding, (f) damage behind the tsunami preventing walls in Otsuchi.

settlements. They also cause great loss of lives. In this tsunami, for example, the number of casualties is estimated to be 17507 (Yalciner et al, 2012).

Many numerical models are used to make short-term and long-term predictions and for academic and operational purposes. Among them, the most commonly used numerical models are *COMCOT* (Liu et al, 1994; 1998), *TUNAMI-N2* (Imamura, 1996) and *MOST* (Titov and Synolakis, 1998). These three models solve Non-Linear Shallow Water Equations (NSWE) with finite difference method. There are also some other models developed by using finite-volume method such as HyFlux2 that is used in European Commission Joint Research Center (JRC) for tsunami forecasting and warning all over the world (Franchello and Krausmann, 2008). *COMCOT*, *TUNAMI-N2* and *MOST* have been validated in National Science Foundation (NSF) workshop in Catalina Island in 1995, 2004 by comparing their results with benchmark problems. The details of validation and verification processes by benchmarking are given in Chapter 4. These three codes were the only ones that can solve tsunami motions in two directions at that time (Synolakis and Bernard, 2006).

*TUNAMI-N2* was originally authored for the Tsunami Inundation Modeling Exchange (TIME) program under the umbrella of UNESCO (Goto et al., 1997; Shuto et al., 1990; Imamura, 1989) in Disaster Control Research Center, Tohoku University in Sendai, Japan.

Subsequently, the code was modified, improved and registered in USA granting copyright to Professors Imamura, Yalciner and Synolakis in 2000 (Yalciner et al, 2001; Yalciner et al, 2002; Yalciner et al, 2003; Yalciner et al, 2004; Kurkin et al, 2003; Zahibo et al, 2003; Zaitsev et al, 2002; Yalciner and Pelinovsky, 2007). The code NAMI DANCE is developed by means of the computational procedures of *TUNAMI N2* in C++ language and is presented as the user-friendly code for tsunami simulations and visualizations. The program has been applied to several tsunami events and used in more than 10 institutes worldwide (Zaitsev et al, 2008; Ozer et al, 2008, 2011; Yalciner et al, 2010, 2012).

*TUNAMI-N2* solves the tsunami motion by using explicit numerical solution of shallow water wave equations with finite-difference technique and leap frog scheme

that provides stable solution and shortens the computation time in reasonable error limits. The model develops the initial wave based on Okada (1985) calculations for co-seismic tsunamis. The user can control the shape of initial wave and dynamic inputs of the wave at a specified location in the study domain. The model is developed with FORTRAN language and can be used in Windows operating system with Visual Studio interface.

The numerical simulation model NAMI DANCE, used in this thesis, is a computational tool developed in collaboration with Ocean Engineering Research Center, Middle East Technical University, Turkey and Institute of Applied Physics, Russian Academy of Science, and Special Research Bureau for Automation of Marine Researches, Far Eastern Branch of Russian Academy of Sciences, Russia by the scientists Andrey Zaytsev, Ahmet Yalciner, Anton Chernov, Efim Pelinovsky and Andrey Kurkin, particularly for tsunami simulation and visualization (NAMI DANCE, 2011). It is developed by C++ programming language by following the staggered leap frog scheme numerical solution procedures based on the calculation principals of TUNAMI-N2 (TUNAMI-N2, 2001). The added modules of NAMI DANCE made it an improved form of TUNAMI N2 while providing direct simulations in nested domains with selective coordinate system (Cartesian and spherical) and with selective equation type (as linear or non-linear), and efficient visualization in multiprocessor environment. NAMI DANCE calculates the principal tsunami hydrodynamic parameters, namely water surface elevation, current velocities and their directions, flow depth and Froude number in selected output time intervals throughout the study domain. In addition to TUNAMI-N2, the model creates the initial wave by using not only tsunamigenic rupture parameters of earthquake but also user defined dimensions and shapes of the initial water surface disturbance. The model can make the calculations using either static source inputted as an initial wave or dynamic source (time history of water surface fluctuation) inputted from an arbitrary location. The initial tsunami source can also be inputted as water surface elevation and discharge fluxes in x and y directions throughout the domain. The model is also capable of preparing 3D plots of sea state at selected time intervals by using different camera and light positions controlled by the user, and animating the tsunami propagation and inundation in the study domain.

Furthermore, the necessary modifications were applied to the code so that it could make the calculations in a multi-processor pattern. It means that NAMI DANCE can perform its calculations by using all the processors of the executed computer. This property increases the simulation speed and reduces the process time.

Beyond these capabilities, the applications of NAMI DANCE have been improved in this study in order to calculate inundation on land more precisely as to overland currents, their directions, discharge fluxes and Froude numbers. The details of the calculations and ad hoc techniques are described in the following section.

## **3.2. Governing Equations of NAMI DANCE**

NAMI DANCE is based on the calculations of Non-Linear Shallow Water Equations (NSWE) using finite-difference technique by staggered-leap frog scheme. However, NAMI DANCE can solve linear form of Shallow Water Equations (LSWE) as well as nonlinear form of shallow water equations (NSWE) in spherical coordinates to solve the wave propagation and coastal amplification in an entire ocean. The calculation type can be selected by the user before starting the simulation. The characteristics and derivation of these equations are described in the following subsections.

### **3.2.1 Shallow Water Theory**

The Shallow Water Theory or alias Long Wave Theory is derived from the Navier-Stokes Equations, which are governed to predict the motion of all fluids (Vreugdenhil, 1994). This theory is widely used in tsunami numerical calculations according to some assumptions. In this theory, the vertical component of water particle acceleration is negligible compared to the gravitational acceleration. It means that the vertical motion of water particles does not contribute to the pressure distribution. Hence, the pressure is said to be hydrostatic.

Based on the present approximations and assumptions, the equations for conservation of mass and momentum in two-dimensional unsteady solution are as follows:

$$\frac{1}{b+\eta} \frac{\partial \eta}{\partial t} + \frac{\partial u}{\partial x} + \frac{\partial v}{\partial y} = 0 \quad [3.1]$$

$$\frac{\partial u}{\partial t} + u \frac{\partial u}{\partial x} + v \frac{\partial u}{\partial y} + \frac{1}{\rho} \frac{\partial p}{\partial x} + \frac{1}{\rho} \left( \frac{\partial \tau_{xx}}{\partial x} + \frac{\partial \tau_{xy}}{\partial y} \right) = 0 \quad [3.2]$$

$$\frac{\partial v}{\partial t} + u \frac{\partial v}{\partial x} + v \frac{\partial v}{\partial y} + \frac{1}{\rho} \frac{\partial p}{\partial y} + \frac{1}{\rho} \left( \frac{\partial \tau_{xy}}{\partial x} + \frac{\partial \tau_{yy}}{\partial y} \right) = 0 \quad [3.3]$$

$$g + \frac{1}{\rho} \frac{\partial p}{\partial z} = 0 \quad [3.4]$$

where  $x, y$  and  $z$  are the axes of Cartesian coordinate system that  $z$  is in vertical direction,  $t$  is time,  $\eta$  is water surface elevation above still water level up to free surface,  $u$  and  $v$  are the depth averaged velocities of water particles in  $x$  and  $y$  directions,  $\tau_{ij}$  is the shear stress in  $i$  direction on the  $j$  normal plane,  $g$  is gravitational acceleration and  $\rho$  is the water density.

Figure 3.4 shows the shape of a tsunami cross-section with its typical parameters propagating on a constant-sloped beach towards the shoreline. This sketch is given at this point to facilitate understanding in further derivations.

The tsunami motion is calculated by solving Eqns. [3.1], [3.2], [3.3] and [3.4] numerically by applying proper boundary conditions. The following are the dynamic and kinematic boundary conditions at the sea surface:

$$p = 0 \quad \text{at } z = \eta \quad [3.5]$$

$$w = \frac{\partial \eta}{\partial t} + u \frac{\partial \eta}{\partial x} + v \frac{\partial \eta}{\partial y} \quad \text{at } z = \eta \quad [3.6]$$

where  $w$  is the depth averaged velocities of water particles in  $z$  direction.

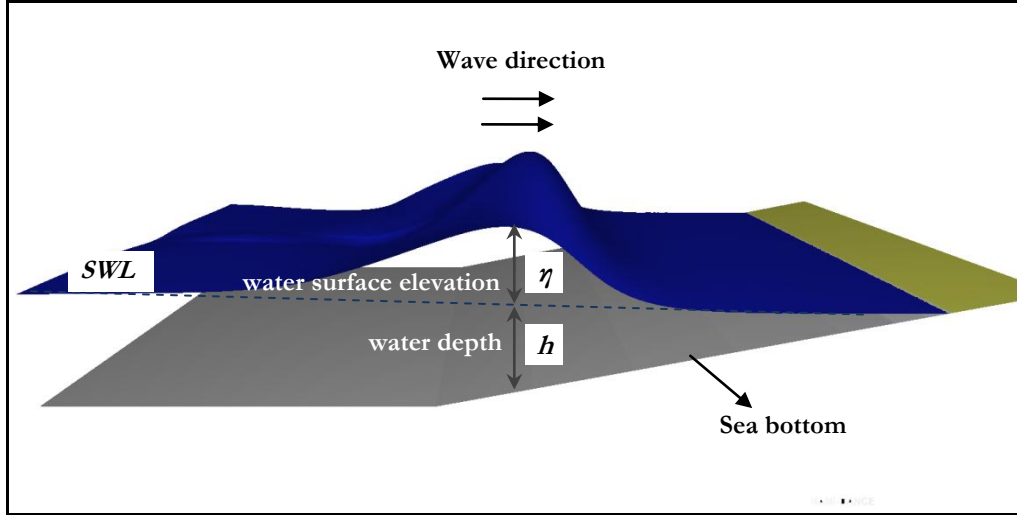


**Figure 3.4:** The cross-section of a tsunami propagating on a constant-sloped beach

The kinematic boundary condition at the impermeable sea bottom is given as

$$w = -u \frac{\partial h}{\partial x} - v \frac{\partial h}{\partial y} \quad \text{at } z = -h \quad [3.7]$$

As a result of boundary condition at the free surface and the assumption of hydrostatic pressure, the equation of momentum in  $z$ -direction is derived as in the following:

$$p = \rho g(\eta - z) \quad [3.8]$$

After applying Leibnitz Rule and using boundary conditions at the sea surface and bottom (Vreugdenhil, 1994), the two-dimensional Shallow Water Equations become

$$\frac{\partial \eta}{\partial t} + \frac{\partial M}{\partial x} + \frac{\partial N}{\partial y} = 0 \quad [3.9]$$

$$\frac{\partial M}{\partial t} + \frac{\partial}{\partial x} \left( \frac{M^2}{D} \right) + \frac{\partial}{\partial y} \left( \frac{MN}{D} \right) + gD \frac{\partial \eta}{\partial x} + \frac{\tau_x}{\rho} = A \left( \frac{\partial^2 M}{\partial x^2} + \frac{\partial^2 M}{\partial y^2} \right) \quad [3.10]$$

$$\frac{\partial N}{\partial t} + \frac{\partial}{\partial x} \left( \frac{MN}{D} \right) + \frac{\partial}{\partial y} \left( \frac{N^2}{D} \right) + gD \frac{\partial \eta}{\partial y} + \frac{\tau_y}{\rho} = A \left( \frac{\partial^2 N}{\partial x^2} + \frac{\partial^2 N}{\partial y^2} \right) \quad [3.11]$$

where  $D$  is the total water depth alias flow depth described by  $D = b + \eta$ ,  $\tau_x$  and  $\tau_y$  are the bottom shear stresses in x- and y- directions,  $A$  is the eddy viscosity which is assumed to be constant in space, and  $M$  and  $N$  are the discharge fluxes in the x- and y- directions. The solutions of Eqns. [3.9] – [3.11] are more stable comparing to Eqns. [3.1] – [3.3].

It is noted that the numerical scheme of tsunami calculations in NAMI DANCE is based on the solutions of Eqns. 3.9-3.11. The control or limitation of velocity is carried out by limiting of discharge fluxes. They are defined by

$$M = \int_{-b}^{\eta} u dz = u(b + \eta) = uD \quad [3.12]$$

$$N = \int_{-b}^{\eta} v dz = v(b + \eta) = vD \quad [3.13]$$

where  $\bar{u}$  and  $\bar{v}$  are the depth average velocities in x and y directions.

The shear stress terms are generally defined for the uniform flow with bottom friction as

$$\frac{\tau_x}{\rho} = \frac{1}{2g} \frac{f}{D^2} M \sqrt{M^2 + N^2} \quad [3.14]$$

$$\frac{\tau_y}{\rho} = \frac{1}{2g} \frac{f}{D^2} N \sqrt{M^2 + N^2} \quad [3.15]$$

where  $f$  is the friction coefficient. Manning's roughness  $n$  is preferable to dealing with the value of friction coefficient  $f$  in most of the engineering problems. Manning's coefficient  $n$  is expressed as follows:

$$n = \sqrt{\frac{fD^{1/3}}{2g}} \quad [3.16]$$

The calculations in this thesis are performed by using the value of 0.025 for Manning's roughness coefficient. However, this value depends on the calculation requirements and can be controlled by the user. The values of Manning's roughness coefficient with respect to different channel materials are given in Table 3.1 (TUNAMI-N2, 2001).

**Table 3.1:** Values of Manning's Roughness Coefficient  $n$  for Various Channel Materials (TUNAMI-N2, 2001)

Channel Material	Manning's Coefficient $n$
Neat cement, smooth metal	0.010
Rubble masonry	0.017
Smooth earth	0.018
Natural channels in good condition	0.025
Natural conditions with stones and weeds	0.035
Very poor natural channels	0.060

Another reference for Manning's coefficient values regarding different land uses is given in Table 3.2 (after Kotani et al, 1999; CAO of Japanese Government, 2004, OYO, 2007). Since these values of  $n$  for residential areas are determined in more particular assessment, this reference is taken into consideration in inundation analyses.

Then shear stress terms become

$$\frac{\tau_x}{\rho} = \frac{n^2}{D^{7/3}} M \sqrt{M^2 + N^2} \quad [3.17]$$

$$\frac{\tau_y}{\rho} = \frac{n^2}{D^{7/3}} N \sqrt{M^2 + N^2} \quad [3.18]$$

**Table 3.2:** Roughness Coefficients for Tsunami Simulation (after Kotani et al, 1999; CAO of Japanese Government, 2004)

Land Use		Roughness Coefficients
Residential site	For building site, Ordinary	Density of buildings/grid
	Lower or middle height	
	building site/dense lower	
	height building site/middle	
high-rise building site/	80□100□	0.080
commercial or business site	40-80%	0.060
	10-40%	0.040
Factory site	Factory site/ other public facility sites	0.040
Agricultural site	Paddy field, agricultural field	0.020
Forest site	Forest, mountain forest, rough forging etc.	0.030
Water body	River, pond and lake, shore, sea water	0.025
Other site	Waste land, Vacant land, Green tract of land, parks, reclaiming land, roads, golf ground etc.	0.025

### 3.2.2. Shallow Water Equations

According to the shallow water theory for the propagation of tsunamis, the horizontal eddy viscosity can be neglected since its effect can be ignored comparing with that of the bottom friction. Therefore, after substituting Eqns. [3.17] and [3.18] with Eqns. [3.9], [3.10] and [3.11] and neglecting the horizontal eddy viscosity, the following equations, named as Non-Linear Shallow water Equations (NLSW), are the fundamental equations in the calculation of tsunami propagation and inundation in NAMI DANCE.

$$\frac{\partial \eta}{\partial t} + \frac{\partial M}{\partial x} + \frac{\partial N}{\partial y} = 0 \quad [3.19]$$

$$\frac{\partial M}{\partial t} + \frac{\partial}{\partial x} \left( \frac{M^2}{D} \right) + \frac{\partial}{\partial y} \left( \frac{MN}{D} \right) + gD \frac{\partial \eta}{\partial x} + \frac{n^2}{D^{7/3}} M \sqrt{M^2 + N^2} = 0 \quad [3.20]$$

$$\frac{\partial N}{\partial t} + \frac{\partial}{\partial x} \left( \frac{MN}{D} \right) + \frac{\partial}{\partial y} \left( \frac{N^2}{D} \right) + gD \frac{\partial \eta}{\partial y} + \frac{n^2}{D^{7/3}} N \sqrt{M^2 + N^2} = 0 \quad [3.21]$$

The governing equations for tsunami propagation and coastal amplification are not limited with the Eqns. [3.19], [3.20] and [3.21]. The dispersion, linearity and

coordinate systems obtain these equations in different forms, which are given in Appendix A. NAMIDANCE provides the user with options of equations from among which he/she can select the necessary one for his/her application.

### 3.3. Numerical Scheme of the Model

NAMI DANCE solves the NSW and calculates the tsunami motion by using finite difference technique with staggered-leap frog scheme. In order to better explain the numerical scheme of the code, it makes sense to start from the linear one-dimensional long wave equation without bottom frictions which is as follows:

$$\frac{\partial \eta}{\partial t} + \frac{\partial M}{\partial x} = 0 \quad [3.22]$$

$$\frac{\partial M}{\partial t} + gD \frac{\partial \eta}{\partial x} = 0 \quad [3.23]$$

Finite difference method is used to solve Eqns. [3.22] and [3.23], which is based on the Taylor expansion series including a specified grid interval, named as  $dt$ . The forward difference scheme can be obtained from Taylor Expansion series as

$$\frac{\partial \eta(x, t)}{\partial t} = \frac{\eta(x, t + dt) - \eta(x, t)}{dt} + O(dt) \quad [3.24]$$

where  $O(dt)$  is the truncation error in the order of  $dt$ .

If  $dt$  is replaced by  $dt/2$  and  $-dt/2$ , then the scheme is obtained by the central-difference method including the second order of truncation error as shown below:

$$\frac{\partial \eta(x, t)}{\partial t} = \frac{\eta(x, t + \frac{dt}{2}) - \eta(x, t - \frac{dt}{2})}{dt} + O(dt^2) \quad [3.25]$$

It is indicated that the second order truncation error is smaller and neglected although it is more realistic to use than the first order one in the calculations.

Therefore, the central difference method is used in the numerical scheme for further calculations.

Before the numerical scheme of NAMI DANCE is explained, it is necessary to describe the staggered-leap frog scheme. The accuracy of solutions is crucial in tsunami calculations, particularly in inundation computations with finer grid sizes. The leap frog scheme is used in the computation technique in order to have more accurate results by increasing the calculation points and decreasing the truncation error.

Figure 3.5 shows the locations in space and time where the water elevation  $\eta$  and the fluxes M and N are calculated. As seen from the figure, water elevation  $\eta$  is not calculated at the same grid with the fluxes M and N both in space and time. In order to increase the accuracy, NAMI DANCE calculates the fluxes M and N in the half-time and half-space while water elevation  $\eta$  is calculated in one-time and one-space. The water depth  $h$  is also calculated at the same place and time with  $\eta$ .

After defining the staggered- leap frog scheme, the expression of Eqns. [3.22] and [3.23] by applying central difference method is given as

$$\frac{1}{dt}(\eta_i^{k+1} - \eta_i^k) + \frac{1}{dx} \left( M_{i+\frac{1}{2}}^{k+\frac{1}{2}} - M_{i-\frac{1}{2}}^{k+\frac{1}{2}} \right) + O(dx^2) = 0 \quad [3.26]$$

$$\frac{1}{dt} \left( M_{i+\frac{1}{2}}^{k+\frac{1}{2}} - M_{i+\frac{1}{2}}^{k-\frac{1}{2}} \right) + g \frac{(D_{i+1}^k + D_i^k)}{2} \frac{1}{dx} (\eta_{i+1}^k - \eta_i^k) + O(dx^2) = 0 \quad [3.27]$$

where  $dx$  is grid size in x direction,  $dt$  is the time step,  $i$  and  $j$  are the increments in x and y directions, and  $k$  is the increment in time.

It should be noted that since staggered leap-frog scheme is applied in the central difference method, the expressions  $\eta(x, t)$  and  $M(x, t)$  are not represented at the same grid location. The notation  $\eta(x, t)$  indicates  $\eta_i^k$  while the notation  $M(x, t)$

represents  $M_{i+\frac{1}{2}}^{k+\frac{1}{2}}$ .

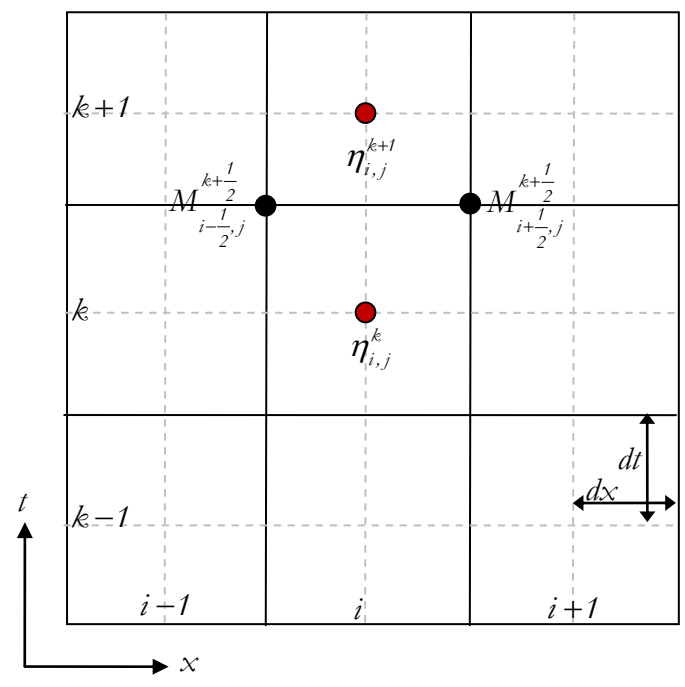
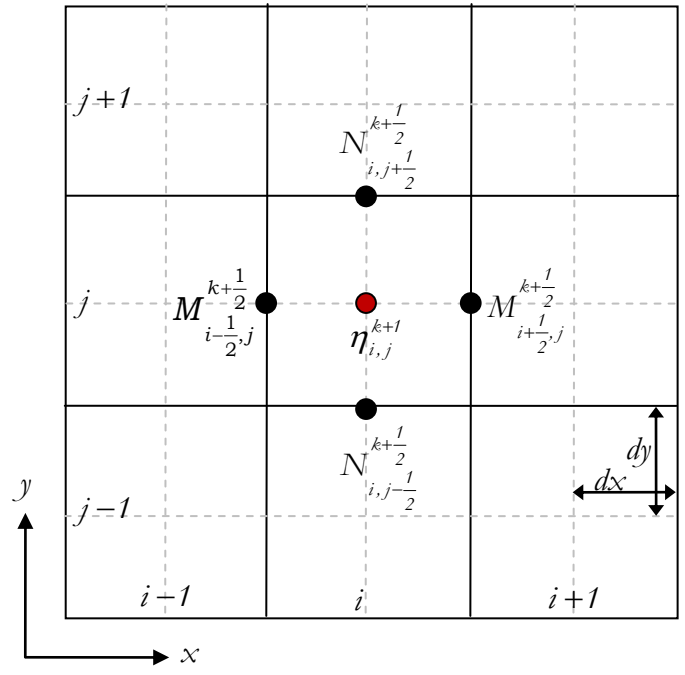


Figure 3.5: The schematic view of staggered-leap frog scheme in time and space

The numerical scheme for the flow depth D is as follows:

$$D_i^k = \eta_i^k + h_i^k \quad [3.28]$$

### 3.3.2. Initial Conditions in Numerical Scheme

The initial conditions should be defined in the numerical code for the initiation of iterations in numerical scheme. The first assumption is the motion in the time k-1. NAMI DANCE assumes no motion in the time k-1 as the water elevation and fluxes in the sea are described by the following equation:

$$\eta_{i,j}^{k-1} = M_{i+\frac{1}{2},j}^{k-\frac{1}{2}} = N_{i,j+\frac{1}{2}}^{k-\frac{1}{2}} = 0 \quad [3.31]$$

The initial condition for water elevation is changed when the waves are inundated on the land. The initial water elevation on land at time k-1 is assumed to be equal to the ground level h which takes negative sign on the land. The initial condition of water elevation on the land is given below:

$$\eta_{i,j}^{k-1} = -h_{i,j} \quad [3.32]$$

If there is any water elevation and fluxes in the sea initially or in any time, it can also be inputted in NAMIDANCE.

## 3.4. Open Boundary Conditions

During the propagation of waves in the study domain, the actual motion on the offshore boundary is not the same with the regular one. If the motion of waves at the boundary is assumed to be purely sinusoidal, a forced oscillation is defined at the boundary that does not allow the reflected waves to pass through the boundary. Nevertheless, the reflected waves should pass from the boundary for not having additional water elevations during the simulation that would prevent the production

of reliable solutions. The open boundary conditions are used in order to avoid this problem.

It is more convenient to explain the boundary condition according to the total derivative of water surface elevation with time.

The total derivative of water surface elevation is constant and given as in the following equation:

$$\underbrace{\frac{D\eta}{Dt}}_{\text{Total Derivative}} = \underbrace{\frac{\partial\eta}{\partial t}}_{\text{Local Derivative}} + \underbrace{u\frac{\partial\eta}{\partial x} + v\frac{\partial\eta}{\partial y}}_{\text{Convective Derivative}} = \text{Constant} \quad [3.33]$$

It should be noted that if the constant in Eqn. [3.33] is zero, the boundary is open boundary (outgoing boundary), and if it is 1, the boundary is reflective boundary.

As seen from Eqn. [3.33], the partial derivative component includes the current velocities in x and y direction. Since it does not represent the exact values, the u and v can be taken as equal to  $\sqrt{gb}$  at the open boundaries for simplicity. Hence, the numerical scheme for the open boundaries can be derived considering Eqn [3.33]:

$$\frac{\eta_{i,j}^{k+1} - \eta_{i,j}^k}{dt} + \sqrt{gb_{i,j}^k} \frac{\eta_{i+1,j}^k - \eta_{i,j}^k}{dx} + \sqrt{gb_{i,j}^k} \frac{\eta_{i,j+1}^k - \eta_{i,j}^k}{dy} = 0 \quad [3.34]$$

In another term, the numerical scheme of the water elevation at the open boundaries can be defined as follows:

$$\eta_{i,j}^{k+1} = \eta_{i,j}^k - \sqrt{gb_{i,j}^k} (\eta_{i+1,j}^k - \eta_{i,j}^k) \frac{dt}{dx} - \sqrt{gb_{i,j}^k} (\eta_{i,j+1}^k - \eta_{i,j}^k) \frac{dt}{dy} \quad [3.35]$$

It should be stated that the second and third terms at the right side of the Eqn. [3.35] are omitted depending on the direction of the boundary. For the bottom and top

boundaries of the study basin, the velocity in x direction is omitted and therefore the numerical scheme of water elevation can be reduced to

$$\eta_{i,j=l}^{k+1} = \eta_{i,j=ff}^{k+1} = \eta_{i,j}^k - \sqrt{gh_{i,j}^k} (\eta_{i,j+1}^k - \eta_{i,j}^k) \frac{dt}{dy} \quad [3.36]$$

where  $ff$  is the number of grids in y direction.

In the same manner, the velocity  $v$  in y direction is omitted and numerical scheme at the left and right boundaries can be given by

$$\eta_{i=1,j}^{k+1} = \eta_{i=if,j}^{k+1} = \eta_{i,j}^k - \sqrt{gh_{i,j}^k} (\eta_{i+1,j}^k - \eta_{i,j}^k) \frac{dt}{dx} \quad [3.37]$$

where  $if$  is the number of grids in x direction.

### 3.5. Boundary Conditions in Runup Calculations

When the waves reach the land, the wave front condition should be controlled in order to have the wave runup. This control is performed by defining each cell whether submerged or dry in every time step. It should be stated that since the linearity is not allowed in shallow zone, the runup calculation is carried out only in non-linear calculations. The submerged and dry cell decision is made according to the evaluation of flow depth at an arbitrary cell as in the following representation:

$$\text{If } D = b + \eta > 0 \text{ , the cell is wet;} \quad [3.38]$$

$$\text{If } D = b + \eta \leq 0 \text{ , the cell is dry.}$$

NAMI DANCE inserts the wave front between the dry and wet cells. In the staggered leap-frog scheme of the model, control of the dry and submerged cell is done at the half-grids, i.e. at  $j+1/2$ . It is difficult to define moving boundary conditions on land. In inundation calculations, NAMI DANCE calculates discharge fluxes if the ground height at the dry cell is lower than the water level in the wet cell.

Otherwise, the discharge is estimated as zero. In other words, if the water level of a cell is higher than the subsequent one, the water will move into the next cell.

### 3.6. Static Source Inputs

NAMI DANCE can calculate tsunami motion by inputting static source in two ways. One way is to introduce an initial wave to the model by defining the coordinates of its center, its length and width, and the initial wave height. This is called “user defined” tsunami source in NAMI DANCE. The second way is to input a tsunami source generated by earthquakes. NAMI DANCE uses Okada (1985) formulas to analyze the sea bottom deformation and to calculate the initial water surface state with the requested grid size that is incompatible with the grid size of bathymetry. At this point, the seismic parameters should be defined properly in order to obtain more reliable simulation results. The clear definition of fault parameters is provided in this section. Table 3.3 lists the necessary fault parameters to compute the tsunami source by applying the Okada formula.

**Table 3.3:** The List of Seismic Rupture Parameters

Parameter	Notation	Unit
Location of earthquake Epicenter (latitude, longitude)	X and Y	degree
Fault length	L	km
Fault width	W	km
Fault displacement	d	m
Focal depth	H	km
Strike angle	$\theta$	degree
Dip angle	$\lambda$	degree
Rake angle	$\sigma$	degree

Figure 3.6 shows the rupture parameters of the earthquake in a three-dimensional projection. It is particularly essential to estimate the realistic value of rupture angles in order to predict the direction and shape of the wave fronts no matter if it acts as an advancing or receding wave.

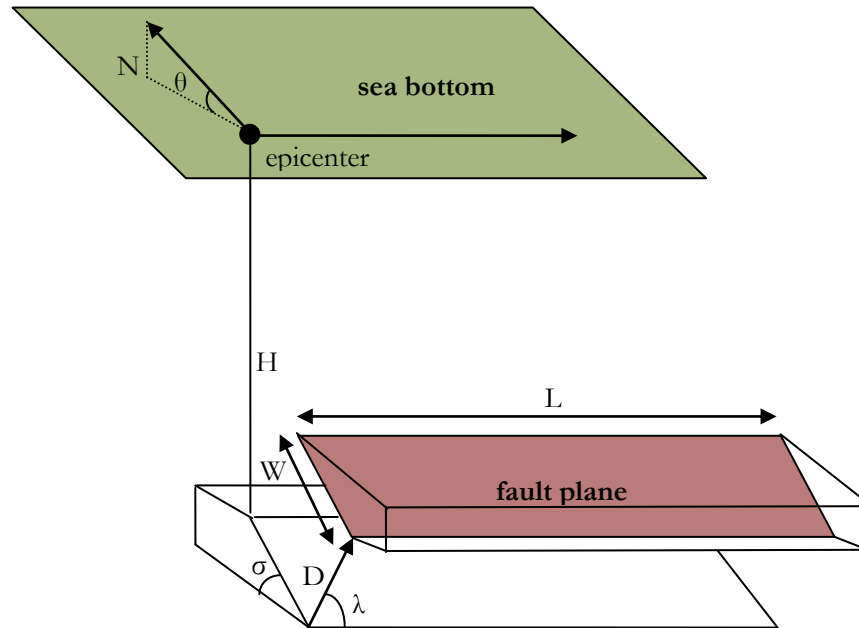


**Figure 3.6:** Seismic rupture parameters in three-dimensional projection

### 3.7. Stability of the Model

The stability of calculations with NAMI DANCE is achieved by using leap-frog scheme in finite difference technique and by following Courant-Friedrichs-Lewy (CFL) condition in simulations which defines that the numerical speed ( $\frac{\Delta x}{\Delta t}$ ) must be faster than the maximum speed of the tsunami ( $c_{\max}$ ) the calculations. In other words, during one time step, the waves in the simulation should pass one grid in x or y direction faster than the maximum speed of the real wave passing through that grid.

This condition is given by the relation

$$\frac{\Delta x}{\Delta t} > c_{max} \quad , \quad \frac{\Delta y}{\Delta t} > c_{max} \quad [3.39]$$

where  $c_{max} = \sqrt{gD_{max}}$  and  $D_{max} = (h + \eta)_{max}$ .

After inputting the bathymetry file of the study domain, NAMI DANCE automatically calculates the stability condition given in Eqn. [3.43] and suggests the time step satisfying the stability. The user can secure the stability in the calculations by selecting the time step of the simulation smaller than the suggested value.

### **3.8. Conditions for Residential Areas in Inundation Zone**

This thesis basically investigates the effects of tsunami hydrodynamic parameters in inundation zone with the buildings. It is recommended to apply some specific conditions in case of having buildings on land in a tsunami simulation. The first one is to use proper Manning's coefficient  $n$  in residential areas. It is feasible to define a specific Manning's coefficient scheme for the whole bathymetry with the same size. For instance, it is appropriate to use the values of Manning's coefficient as 0.035 in the sea, 0.060 on the land and 0.2 to 1.0 for the area of buildings in the whole bathymetry. It is possible to state any predefined value of  $n$  in every single grid node.

The second way of obtaining more reliable results is using finer grid sizes. If the grid size of bathymetry is less than 5m, most of the large buildings can be defined as impermeable boundaries. This condition will increase the number of grid nodes, which means longer computation time. However, the values of hydrodynamic parameters in inundation zones are more likely to be reliable.

### **3.9. Derivation of Hydrodynamic Demand and the Role of Froude Number**

The 2011 Great East Japan Tsunami once again revealed that the main cause of damage on land in the inundation zone is the strong currents occurring with the

corresponding high flow depths. When tsunamis approach the shallower zone and inundate on land, the behavior of water changes from normal wave motion to the open channel flow. This flow occurring with extremely strong current velocities and corresponding high flow depths has the power of dragging all the objects in front even in huge dimensions.

A new parameter derived and studied qualitatively in Ozer (2007) is investigated at length in this study both qualitatively and quantitatively. The hydrodynamic demand is actually the representation of drag force normalized with the hydrostatic force. The relation of hydrostatic force is given in the following equation

$$F_b = \frac{1}{2} \rho_w g b^2 w = \frac{1}{2} \rho_w g b A \quad [3.40]$$

where  $\rho_w$  is the density of sea water,  $b$  is the depth of water and  $A$  is the cross-sectional area exposed to the hydrostatic force in the wave direction. Figure 3.7 shows the hydrostatic force exerted onto the cross-sectional area of a structure.

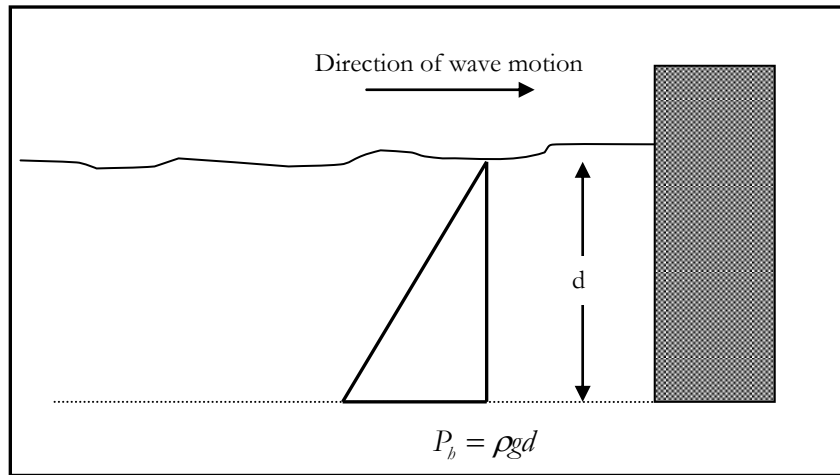


**Figure 3.7:** Sectional View of Hydrostatic Pressure on a Coastal Structure

The drag force is used to calculate the force of flowing water onto an object. The relation for the drag force on the other side is given by

$$F_D = \frac{1}{2} C_D \rho_w A u^2 \quad [3.41]$$

where  $C_D$  is the drag coefficient that depends on the shape of dragged object and  $u$  is the current velocity.

Hydrodynamic demand is introduced as a dimensionless parameter obtained by the normalization of the drag force. Hydrostatic force can be used as the reference force to obtain a relative and comparative dimensionless value representing the dragging force. The normalization of drag force with the hydrostatic one results in the following relation:

$$\begin{aligned}
 HD &= \frac{F_D}{F_b} = \frac{\frac{1}{2} C_D \rho_w A u^2}{\frac{1}{2} \rho_w g d A} \\
 &= C_D \frac{u^2}{g d}
 \end{aligned}
 \tag{3.42}$$

Here,  $u^2/(gd)$  is directly equal to the square of Froude number  $Fr^2$ . Hence, hydrodynamic demand is related with the drag coefficient and  $Fr^2$  and can be expressed as follows:

$$HD = C_D * F_R^2
 \tag{3.43}$$

The drag coefficient  $C_D$  mainly depends on structure shape and secondarily the flow conditions. It describes a characteristic amount of drag caused by water flow. Two objects having the same frontal area exposed to the same flow velocity will experience a drag force proportional to their  $C_D$  values. Therefore, the drag coefficient for identically shaped structures can change with the Reynolds number (a useful dimensionless number that is the ratio of the inertial force of the medium over its viscous force) and also with the roughness of the surfaces (Ozer, 2007; Sumer and Fredsøe, 1997).

The suggested values for drag coefficient  $C_D$  vary between 1.0 and 2.0 depending on the structure type and the wave conditions. Table 3.4 summarizes the suggestions for  $C_D$  values in literature.

This study considers the tsunami effect on the same type of structures in inundation zone under the same wave conditions. On account of this, the drag coefficient is presumed to be same in all of the analyses. As a result, hydrodynamic demand parameter is directly related to the  $Fr^2$ . The simulations in this study will focus on the investigation of changes in maximum and average values of  $Fr^2$  values inundation zone especially in residential areas. The maximum values of  $Fr^2$  are the governing parameters referred for the interpretation of damage level in coastal settlements. The details of these analyses are described in Chapter 5.

**Table 3.4:** Suggestions for the Value of Drag Coefficient  $C_D$  (Ozer, 2007)

Reference	Structure Type	$C_D$ value
CCM in Synolakis (2003)	Piles	1.2 for non-breaking waves
		1.75 for breaking waves
CCM in Synolakis (2003)	All Type of Coastal structures	1.25 for $b^*/d_s^* < 12$
		2.0 for $b^*/d_s^* > 12$
Arnason (2004) in Yeh (2006)	All Type of Coastal structures	1.0 – 2.0
Yalçiner and Synolakis in Sumer et al. (2007)	All Type of Coastal structures	less than 2

\*b: horizontal length of the structure perpendicular to the wave direction,  $d_s$ = water depth at the location of the structure

## CHAPTER 4

### VERIFICATION AND VALIDATION OF NUMERICAL CODE: NAMI DANCE

Numerical modeling is the most frequently used tool for making short-term or long-term tsunami forecasts. The short-term forecasts predict tsunami hydrodynamics produced faster than the real time of the event for operational purposes. As part of long-term forecasting, the numerical modeling produces inundation maps for hazard assessment and mitigation planning. All numerical models should be validated and verified in order to ensure the reliability and accuracy of their results. Validation is described as the process of ensuring that the model accurately solves the relevant equations of motion. Verification, on the other hand, is the process of ensuring that the model clearly represents the geophysical reality (Synolakis et al, 2008).

Since the numerical codes are widely used in short-term tsunami forecasts in early warning systems having no tolerance for unrealistic predictions that could endanger human lives, their validation and verification should be attributed to internationally agreed and accredited procedures. The first significant attempt was the organization of the 2<sup>nd</sup> Workshop on Long-Wave Runup Models in Friday Harbor, Washington, USA in 1995, which introduced a series of benchmark problems to validate the tsunami calculations in the sea and on land (Yeh et al, 1996). Tsunami scientists having reached a consensus on the use of benchmark problems for the validation of numerical codes, the 3<sup>rd</sup> workshop of the series was held in Catalina, California in 2004, and four benchmark problems were selected (Liu et al, 2008). In the following years, a few benchmark series were added to the list in order to reinforce the validation of reliability.

Benchmarking of numerical models can be classified into three categories: (i) analytical, (ii) laboratory, and (iii) field benchmarking. The numerical code NAMI DANCE used in this study is validated and verified by applying laboratory and field benchmarking. The code is also tested by simulating the propagation and runup of Solitary wave and by comparing the results with the runup law and the results given in the well-known benchmark study on solitary wave runup (Synolakis, 1987). Furthermore, the evaluation of the scientific and operational quality of the code is mentioned in this section.

#### **4.1 Laboratory Benchmarking - Verification of NAMI DANCE Comparing with the Experimental Results**

The simulation results of NAMI DANCE are compared with the results of laboratory experiment of a real event in order to confirm and validate its reliability. The name of this benchmark problem is “the calculation of tsunami runup onto a complex three-dimensional beach” that was assigned as Benchmark Problem #2 in Catalina Workshop 2005 (Liu et al, 2008). This problem is based on the laboratory experiment of the 1993 Hokkaido-Nansei-Oki (named shortly as Okushiri) tsunami, causing 30m runup and around 10-18 m/s currents near the village of Monai in Okushiri Island (Hokkaido Tsunami Survey Group, 1993). The experiment was performed on a 1/400 scale with a large-scale tank (205 m long, 6 m deep, 3.5 m wide) at Central Research Institute for Electric Power Industry (CRIEPI) in Abiko, Japan. Figure 4.1 shows the bathymetry and topography of the study area in the laboratory tank. The tide gauges shown with red stars in the figure are selected for the measurement and recording of the water level fluctuations during the experiment (Takahashi, 1996).

The initial wave is a single Leading Elevation wave having -5m leading-depression and a 6m crest, as shown in Figure 4.2. It should be noted that the values of this input wave are the real values of the wave calculated using the prototype scale. The wave paddle is placed on the left side of the tank facing directly the Monai coast. The

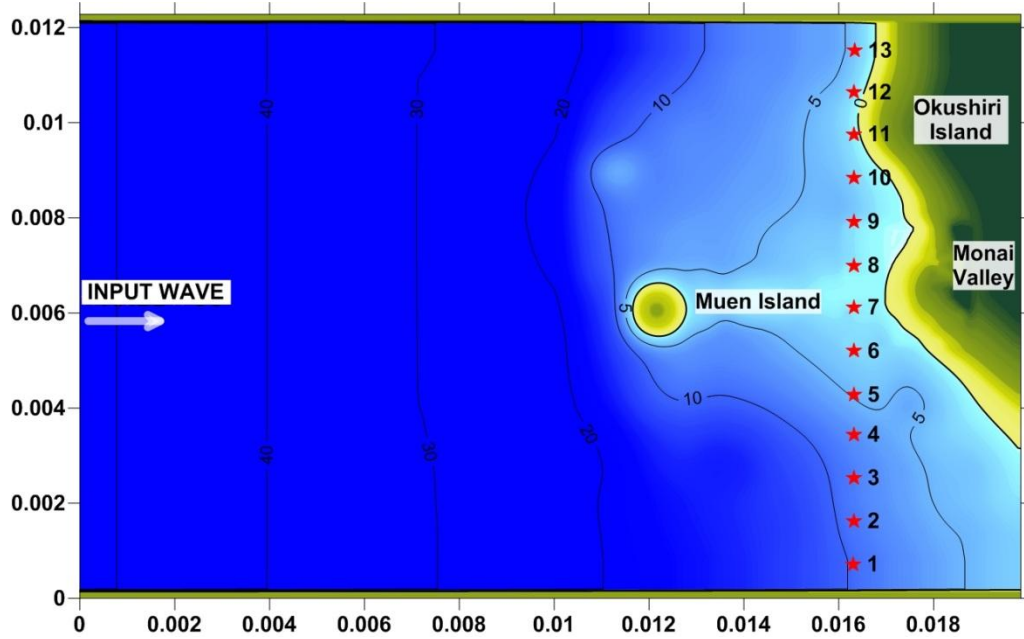


Figure 4.1: The bathymetry and topography of the study area in the laboratory tank (red stars show the location of tide gauges)

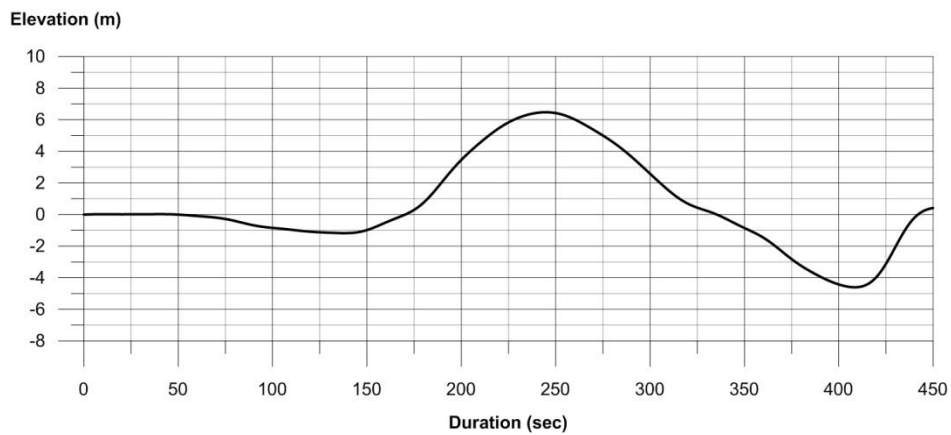


Figure 4.2: The profile of input wave

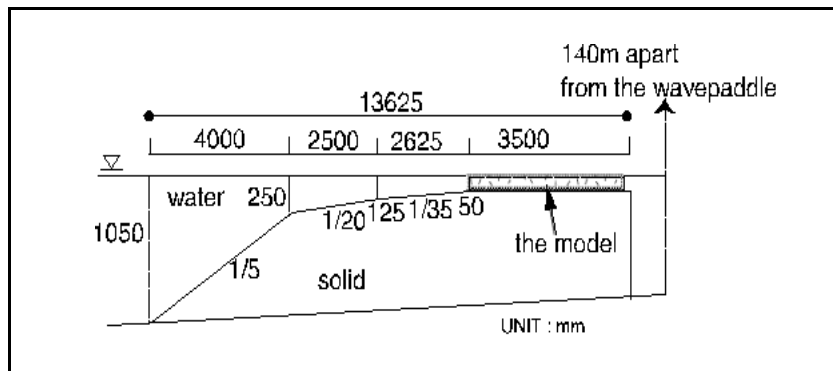


Figure 4.3: The offshore profile of laboratory tank (Takahashi, 1996)

profile of the laboratory tank is given in Figure 4.3 with the dimensions (Takahashi, 1996) in GPS coordinates (degree decimal).

The simulations are performed with NAMI DANCE based on the input wave in the given study domain. The analyses were done both in Cartesian and spherical coordinates. Figure 4.4 shows the comparison of the numerical results calculated both in Cartesian and spherical coordinates with the experimental measurements at the tide gauges of #5, #7 and #9.

As seen from Figure 4.4, computed results agreed well with the experimental results. Since the scale of physical model is 1/400, which may cause some deviations in the measurement of water level in the experiments, a discrepancy in acceptable limits can be expected as obtained in the applications of other codes (LeVeque and George, 2008, Liu et al., 2008) The results of NAMI DANCE can be said to be compatible with the experimental results in this benchmark problem. The results also show how well it performs in a rapid sequence of runup and withdrawal.

Table 4.1 gives the measured and computed results at each channel during the time when the first wave reaches to the gauges, that is between 5.1<sup>st</sup> and 7.4<sup>th</sup> minutes. The relative absolute percent error is calculated at each time step and given in the table according to the error equation given below

$$\%E = \frac{|measured - computed|}{|measured|} * 100 \quad [\text{Eqn. 4.1}]$$

where %E is the percent relative absolute error. One must pay attention to that the time step given in Table 4.1 is not the time step of simulation. The time interval 0.05min is selected in order to compare the measured and computed data at the same time steps because it was the only time step where the time of measured and computed data coincide.

**Table 4.1:** Relative Absolute Mean Percent Error for the Laboratory Benchmarking

Time (min)	CHANNEL 5			CHANNEL 7			CHANNEL 9		
	Measured	Computed	% Absolute Error	Measured	Computed	% Absolute Error	Measured	Computed	% Absolute Error
5.1	3.5	3.9	11.42	5.1	4.27	16.19	4.1	3.2	21.88
5.15	3.86	4.31	11.87	5.38	5	7.13	4.34	4.16	4.04
5.2	4.38	4.88	11.5	5.7	5.47	4.11	4.98	4.83	3
5.25	4.86	5.29	9.02	6.26	5.87	6.23	5.62	5.61	0.23
5.3	4.94	5.5	11.51	6.82	6.21	8.96	6.1	6.44	5.54
5.35	4.98	5.68	14.16	7.06	6.42	9.11	6.74	7.23	7.23
5.4	5.02	5.83	16.25	7.22	7.36	1.98	7.74	9.52	23.01
5.45	5.06	5.97	18.05	7.22	9.72	34.57	9.42	10.31	9.45
5.5	5.14	6.07	18.15	7.26	9.25	27.4	10.74	12.23	13.86
5.55	5.22	6.14	17.75	7.34	9.14	24.53	10.7	14	30.86
5.6	5.22	6.17	18.24	7.86	9.28	18.11	16.74	16.56	1.05
5.65	5.22	6.15	17.87	14.62	14.09	3.65	14.78	15.04	1.76
5.7	5.22	6.08	16.62	14.5	14.06	3	13.22	14.67	10.96
5.75	5.26	6.02	14.52	14.06	13.4	4.67	16.58	15.32	7.61
5.8	7.86	6.84	12.87	13.3	13.12	1.37	14.34	14.35	0.09
5.85	13.7	10.97	19.91	12.66	12.84	1.39	14.98	14.01	6.47
5.9	11.14	10.98	1.44	13.14	13.22	0.64	14.18	13.13	7.43
5.95	10.86	12.42	14.39	12.06	13.15	9	12.54	12.4	1.09
6	10.78	11.8	9.49	11.02	12.35	12.09	12.14	11.98	1.34
6.05	11.74	11.83	0.8	10.18	11.58	13.73	10.9	11.43	4.89
6.1	14.22	12.57	11.55	9.66	10.9	12.85	10.06	10.56	4.98
6.15	12.7	11.9	6.28	9.58	10.48	9.43	9.9	10.82	9.26
6.2	11.54	11.38	1.39	9.06	9.91	9.4	8.42	9.78	16.13
6.25	13.46	11.83	12.06	8.86	9.5	7.19	7.98	9.7	21.5
6.3	11.98	11.06	7.63	9.34	9.32	0.21	7.46	9.01	20.74
6.35	12.34	10.88	11.78	13.58	10.33	23.93	7.22	8.38	16.02
6.4	12.02	10.42	13.29	10.1	8.93	11.58	6.54	8.35	27.73
6.45	10.86	9.68	10.81	8.26	7.95	3.78	6.06	7.72	27.35
6.5	13.58	10.26	24.45	8.66	7.78	10.21	5.82	7.31	25.58
6.55	10.94	8.92	18.4	9.42	7.79	17.32	5.62	7.13	26.95
6.6	11.7	8.76	25.1	7.98	8.47	6.19	5.66	6.65	17.57
6.65	9.46	7.59	19.7	6.74	7.68	13.98	7.02	6.77	3.61
6.7	8.34	6.82	18.14	7.18	7.7	7.24	5.7	6.16	8.1
6.75	8.5	6.53	23.15	7.58	7.48	1.37	4.78	5.53	15.77
6.8	9.34	6.52	30.12	6.3	6.79	7.84	4.22	5.26	24.64
6.85	8.06	5.76	28.45	8.78	7.38	15.99	4.38	5.19	18.4
6.9	7.5	5.3	29.36	5.86	6.04	3.11	4.42	4.87	10.15
6.95	7.7	5.11	33.67	4.9	5.38	9.82	4.1	4.57	11.41
7	7.1	4.66	34.31	5.58	5.37	3.73	4.02	4.4	9.54
7.05	6.86	4.7	31.44	6.38	5.48	14.06	4.22	4.73	12.17
7.1	7.02	5.51	21.46	5.98	5.23	12.5	4.38	4.63	5.64
7.15	4.58	4.62	0.91	4.7	4.76	1.38	4.22	4.39	4
7.2	4.02	4.34	8	4.5	4.66	3.47	3.9	4.1	5.17
7.25	3.5	4.01	14.58	4.14	4.41	6.44	3.62	3.78	4.49
7.3	2.62	3.51	34.14	3.3	4.01	21.67	3.66	3.65	0.36
7.35	2.74	3.32	21.24	3.74	4.06	8.52	3.38	3.46	2.5
7.4	2.1	2.87	36.72	3.22	3.72	15.54	2.58	2.9	12.6
<b>% Error</b>	<b>16.9</b>			<b>9.9</b>			<b>11.2</b>		

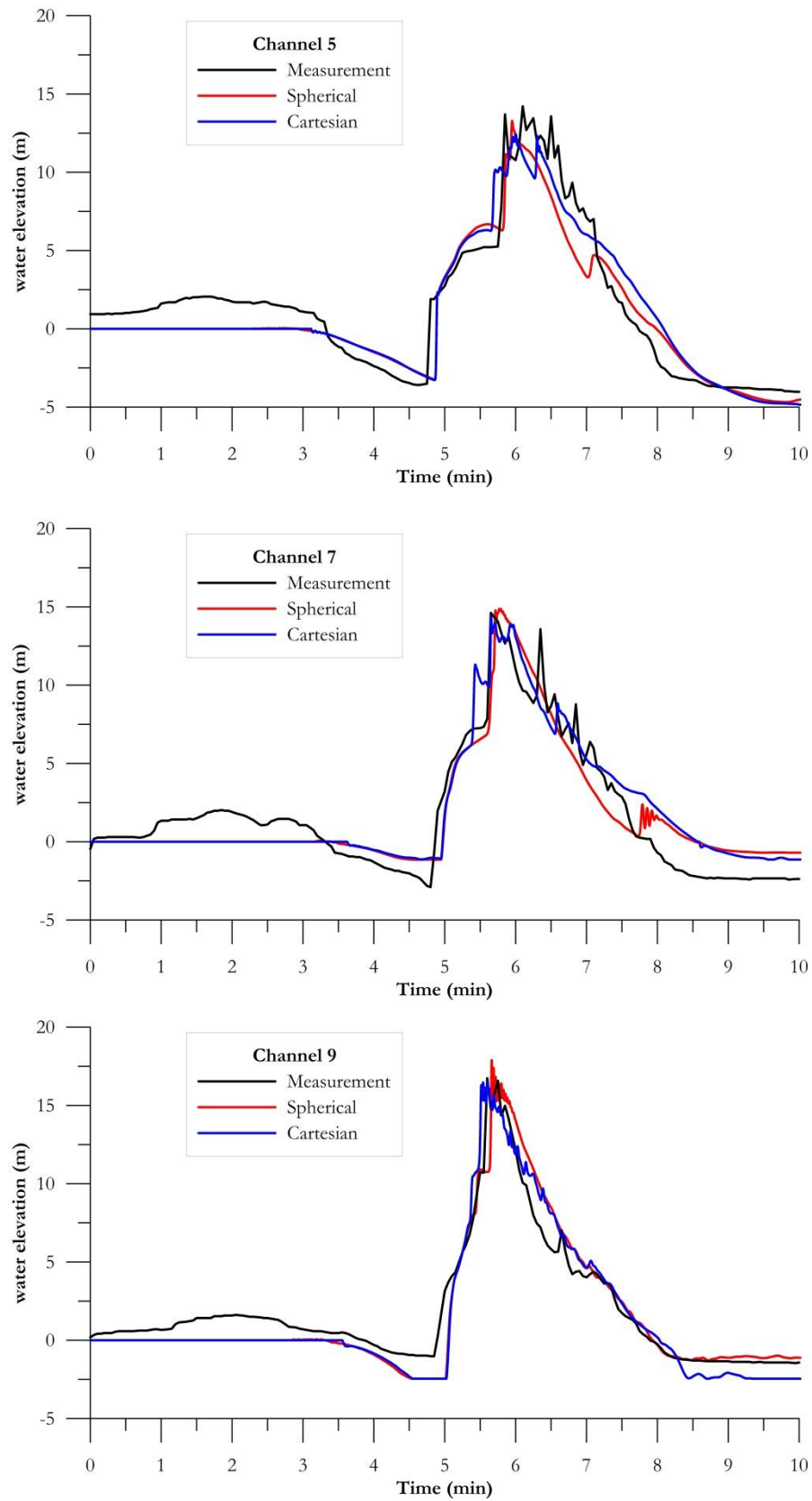


**Figure 4.4:** The comparison of experimental and numerical results at the gauge points #5, #7 and #9

After the calculation of %E at each time step, the mean relative absolute percent error is found at every channel, as shown in Table 4.1. It is obtained that the mean value of the percent deviation is 16.9% for Channel #5, 9.9% for Channel #5 and 11.2% for Channel #9. The error is around 10% around the peak where the sudden rise and fall of the water surface were recorded. These fluctuations at the peak may be related to either accuracy of the measurements, or small scale of the model or both.

## **4.2 Field Benchmarking- Verification of NAMI DANCE with Real Measurements of March 11, 2011 Great East Japan Tsunami**

It is essential to verify numerical models with the real-world measurement data in order to ensure geophysical reality, especially for the models used for operational purposes. There are some uncertainties in the definition of tsunami source in benchmark problems both in analytical and laboratory cases (Synolakis et al., 2008). Therefore, it is necessary to compare the results of the numerical model with the real measurements taken during a tsunami event. For this purpose, the wave record obtained from the GPS buoy of Independent Administrative Institute Port and Airport Research Institute (PARI) located at 24 km off Kamaishi city during 2011 Great East Japan (GEJE) tsunami event is used to compare to the numerical results of NAMI DANCE for verification.

The 2011 Great East Japan Earthquake with a magnitude of 9.0 is ranked as the 5<sup>th</sup> largest earthquake ever recorded in the last 2000 years. The ground accelerations of this enormous earthquake were calculated as up to 3g that triggered a huge tsunami affecting all the east coasts of Japan. The tsunami also had far-field effects along the coasts of Hawaii and North-west of America. The maximum tsunami runup height was measured as 40.5 m (Coastal Engineering Committee, 2011). The inundated area was estimated to be as large as 507 km<sup>2</sup> (Suppasri et al, 2011a, b; Iwate-Miyagi-Fukushima Prefecture, 2011; Geospatial Information Authority, 2011; JMA, 2011; Koizumi, 2011; Yalciner et. al, 2012) overwhelming mostly the area from Taro to Kesenuma towns along the coasts of east Japan.

The ground deformation models developed by Imamura et al (2011) and Koketsu et al (2011) are used as the tsunami sources for the simulations of 2011 Japan event (Figure 4.5). Both of the models used tsunami waveform inversion method while Imamura model used tsunami height, inundation area and land uplift/subsidence.

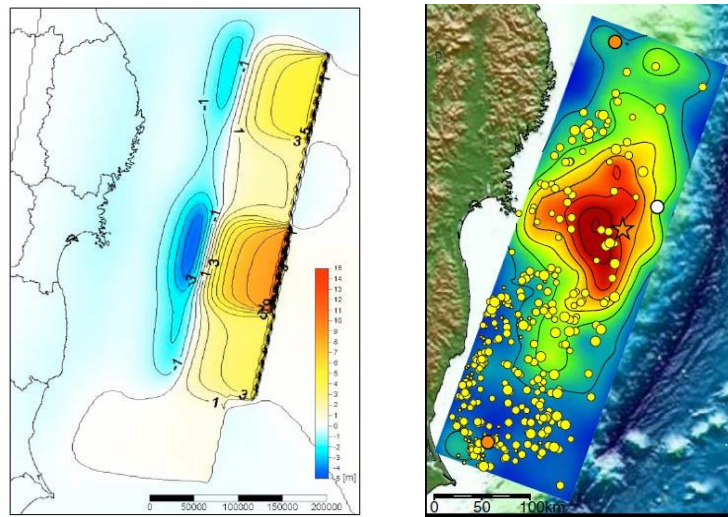


**Figure 4.5:** Source models for the 2011 Great East Japan Earthquake. (Left, the Tohoku University-Imamura Source (Imamura et al, 2011); Right, the Fujii-Satake Source (Koketsu et al, 2011))

The ground deformation models are digitized and converted to tsunami sources as in several segments. The segments are then combined to form one single tsunami source. After this procedure, the initial water surfaces of 2011 GEJE tsunami wave computed by NAMI DANCE for both models are given in Figure 4.6. Even if there are discrepancies between the tsunami sources, they have been determined by using the ground motion data due to seismic event and by comparing the observed and computed peak coastal tsunami amplitudes.

The tsunami wave records of a GPS buoy operated by PARI located 24 km off Kamaishi are provided by Japanese colleagues from PARI and shown in Figure 4.7. As seen from the record, the first peak occurred at about 15:10 local time, which was

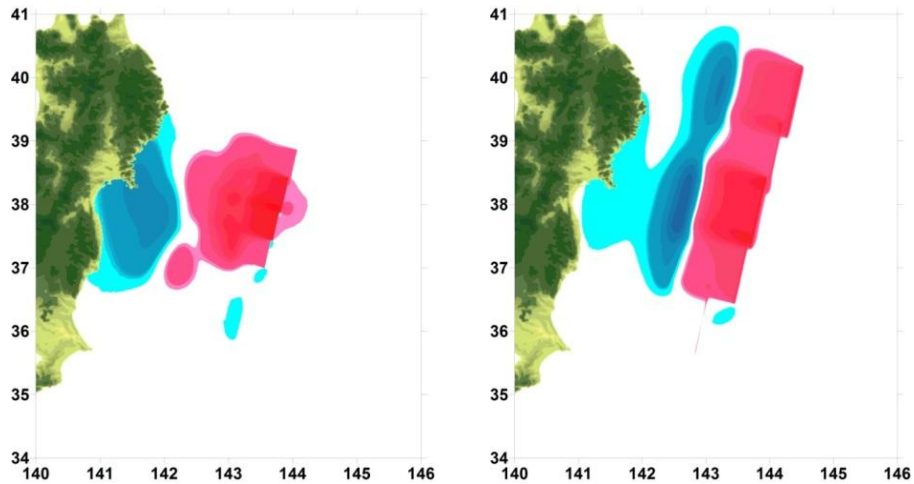


**Figure 4.6:** The computed initial water surfaces for the Great East Japan Tsunami using the tsunami sources in Figure 4.5

about 25 minutes after the earthquake time 14:46 (Japan Standard Time). The first peak of water surface elevation, which was very steep and high, was recorded as about 6.7m. The wave periods are not regular for the first and the third waves. Then, the wave period was observed as 55 min in a regular pattern (PARI, 2011). The average sea level rise in the record is about 55 cm.

The bathymetry of the study area that is close to the east coast of Japan is obtained by using GEBCO 30 sec. The best possible finer grid size of bathymetry is selected in order to achieve a better match of numerical results with the recorded data. Two different simulations with two different tsunami source models (i.e. Imamura source model and Fujii-Satake source model) given in Figure 4.6 are performed to compute water surface elevations at the GPS buoy 24 km off Kamaishi at 400m water depth. The comparison of numerical results of two simulations with the wave record (Figure 4.7) is shown in Figure 4.8. The results show that the computed water surface elevations of both source models fit quite well with the wave record off Kamaishi. This result enables us to conclude that either of these models can satisfy the coastal tsunami amplitudes in Japan.

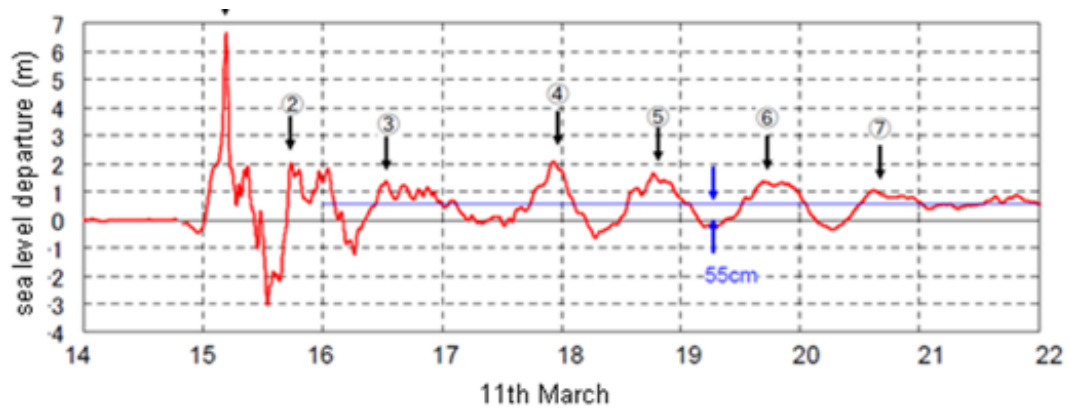


**Figure 4.7:** The wave record after the earthquake at 24 km off Kamaishi by PARI Japan

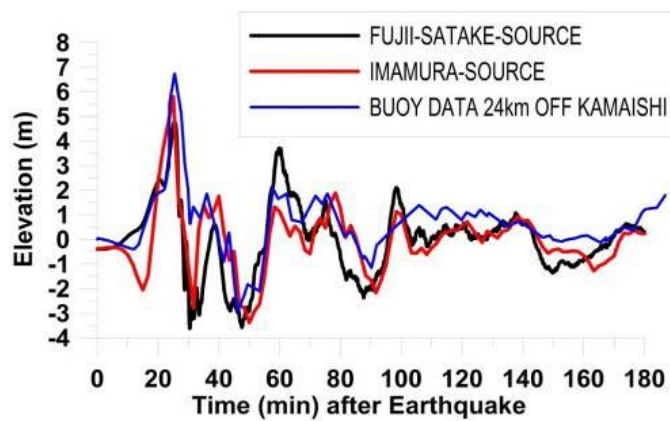


**Figure 4.8:** The comparison of the measured data and the computed data using both the Fujii-Satake and Imamura sources of Figures 4.1 and 4.2

After comparing the computed results with the wave record, 2011 GEJE tsunami is simulated with a large study domain covering all of the Pacific Ocean with the Chilean, Australian, New Zealand and North America coasts. The snapshots at the selected times during the transpacific propagation of the waves are shown in Figure 4.9.

In order to check and validate the performance of the code and check the reliability of the tsunami sources in long distance propagation of 2011 GEJE tsunami, another simulation is performed in large domain bounded by the coordinates  $65^{\circ}\text{N}$   $135^{\circ}\text{E}$  and  $15^{\circ}\text{N}$   $150^{\circ}\text{W}$ . The numerical results of this simulation are compared with the real data measured by DART buoys. Four DART buoys are selected for the

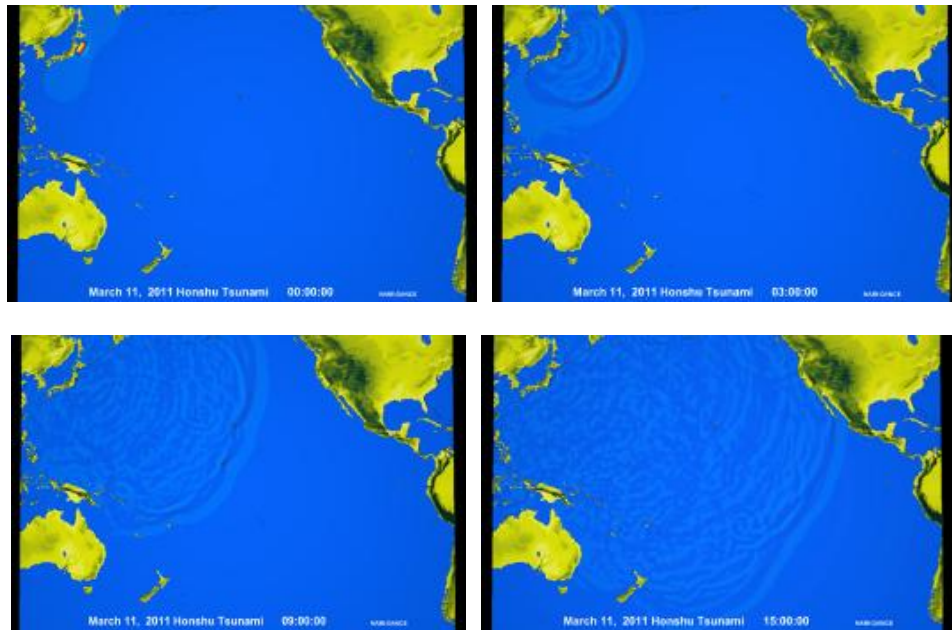


**Figure 4.9:** Propagation modeling of Great East Japan Tsunami across the Pacific

comparison. Three of them are near the tsunami source, and one of them is at the far-field region (Figure 4.10).

The DART data measured on March 11, 2011 GEJE tsunami as shown in Figure 4.10 is obtained from NOAA website (NOAA, 2012). The data provides the water level fluctuations within 24 or 48 hours including tsunami event. This data also includes the tidal changes during that period. Therefore, it is necessary to filter the mean tide level from the plots. For that reason, the plots were digitized in the duration of simulation at as small as possible time intervals by following the mean water level. The data is, then, interpolated in accordance with the time step of buoy measurement provided in every minute. The computed data is also sorted out to obtain water elevations at every 1 minute, and the results are compared. Figures 4.11, 4.12, 4.13 and 4.14 show the comparison of measured and computed data both with Imamura and Satake sources. The water surface elevations computed by NAMIDANCE at that four DART buoys are listed and given in Appendix A.

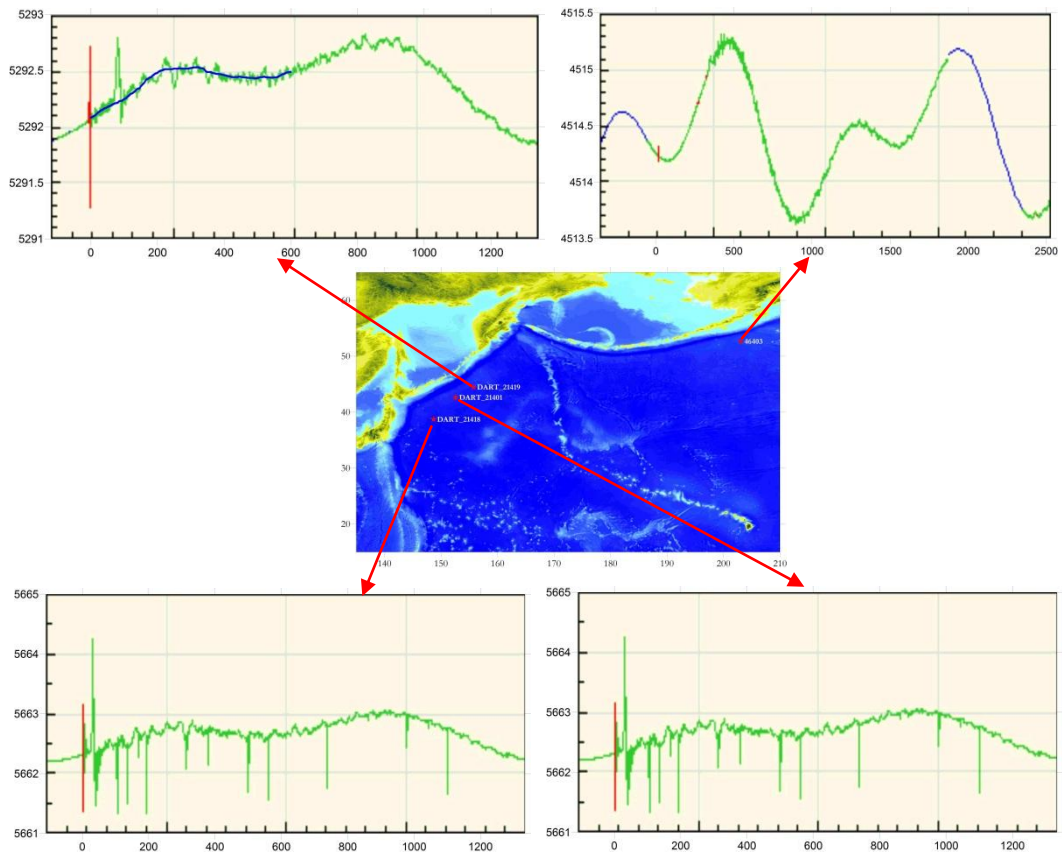


**Figure 4.10:** The location of the selected DART buoys and the water level fluctuations measured during March 11, 2011 Japan Tsunami

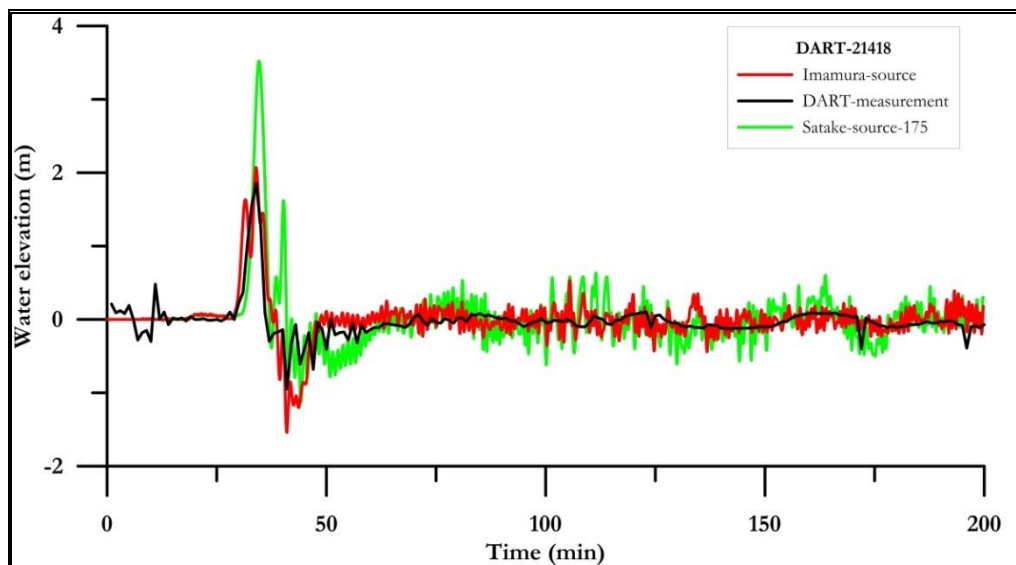


**Figure 4.11:** The comparison of computed results with the data measured by DART-21418 during March 11, 2011 Great East Japan Tsunami

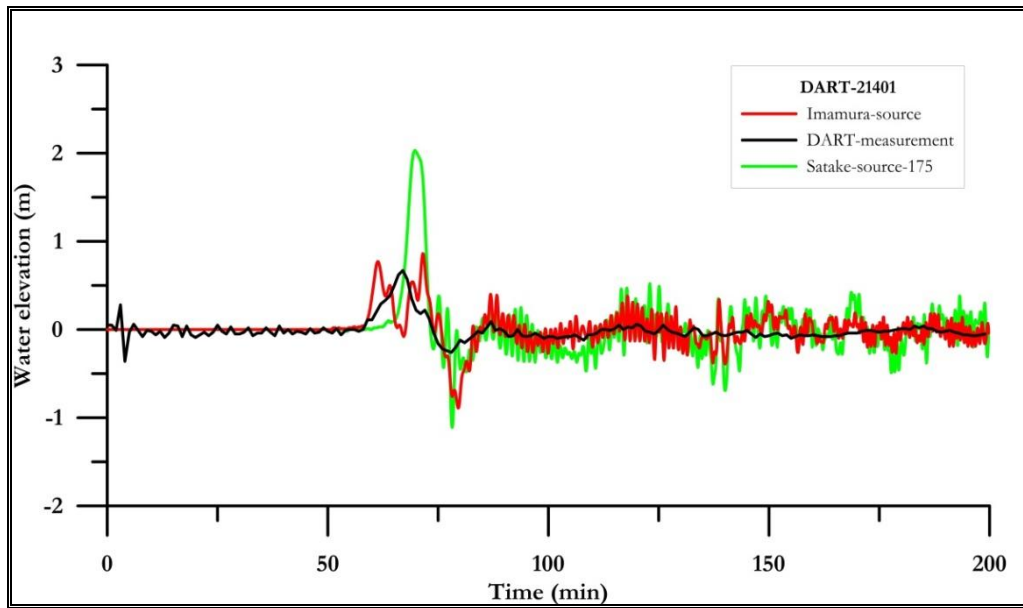


**Figure 4.12:** The comparison of computed results with the data measured by DART-21401 during March 11, 2011 Great East Japan Tsunami

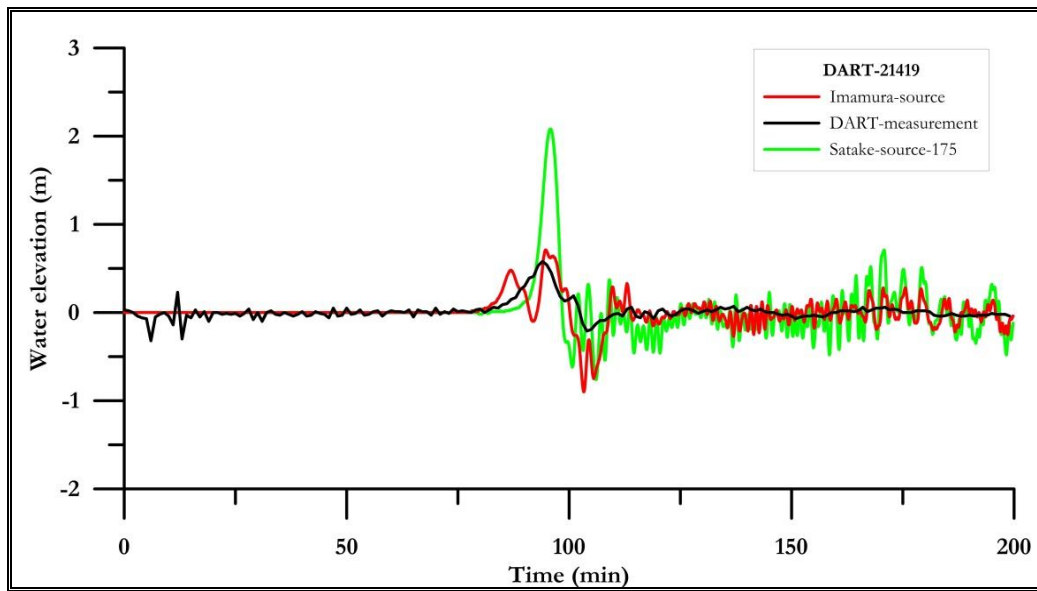


**Figure 4.13:** The comparison of computed results with the data measured by DART-21419 during March 11, 2011 Great East Japan Tsunami

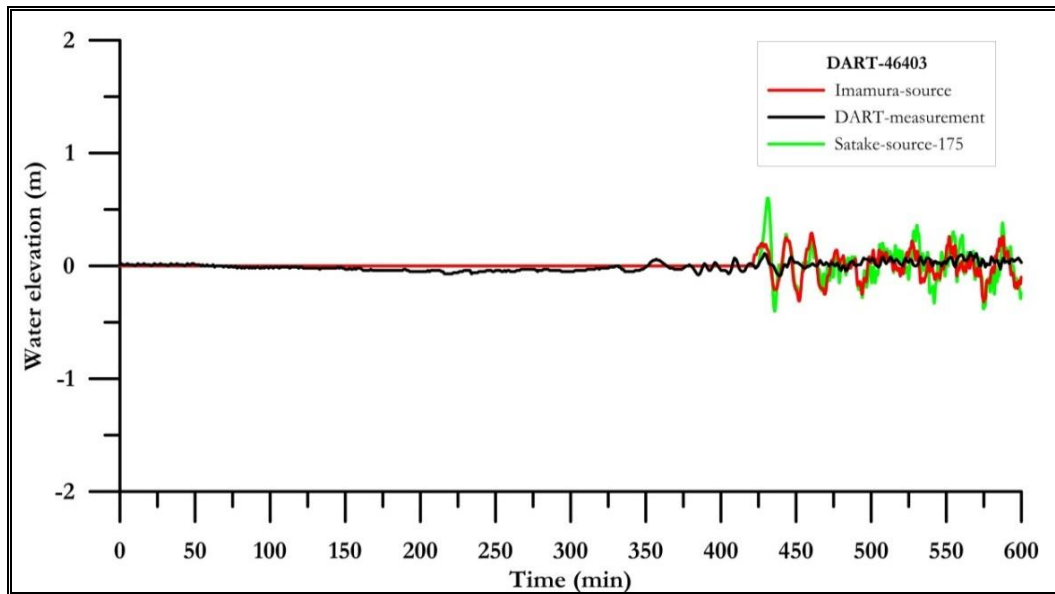


**Figure 4.14:** The comparison of computed results with the data measured by DART-46403 during March 11, 2011 Great East Japan Tsunami

Good fit of arrival time at the DART's locations at near and far distances verify the model performance. The comparison of the time histories of water level fluctuations show that the numerical results computed by using Imamura source fit fairly well with the DART measurements. The computed double peaks of simulation by Imamura source shown in Figures 4.13 and 4.14 may indicate that small adjustments in the north part of the source given by Imamura may be necessary. It has also been mentioned by Imamura that better fit of the peak coastal tsunami amplitudes near Hokkaido (North of Japan) needs some adjustment in the proposed source. However, Satake source provides overestimated values especially as regards the first peak. It is also observed that the computed results show better concurrence with the measured data at Kamaishi buoy. Since this buoy is closer to the tsunami source, it is obvious that the numerical results tend to fit better to the measured data. This deviation is more explicitly observed in the comparison with DART-46403, which is almost 5000km away from the tsunami source.

### 4.3. Verification of the Model with the Problem of Solitary Wave Runup on a Sloping Beach

Verification of NAMIDANCE with the computation of the runup of solitary waves on a plane beach is performed by using the experimental data and Runup Law given in Synolakis (1986). Actually, long wave runup on sloping beaches is modelled by using TUNAMI-N2 and the Runup Law is satisfied in Demirtas (2002). The Runup Law is an asymptotic result of the maximum runup of solitary waves derived in Synolakis (1986) by performing a complete (analytical, numerical and experimental) study of breaking and nonbreaking solitary waves on a beach of 1 on 20 slope. The test basin used in this study is 3400m long and 400m wide and is discretized in 2m grid size. There is a constant depth of 50m till the toe and a constant slope till the shoreline. The analyses are performed by using a static form of solitary wave at the toe of the slope as used in the analytical approaches for the solutions of this kind of problems (Aydin and Kanoglu, 2007; Kanoglu 2004). Different bottom slopes (1/10, 1/15, 1/20 and 1/25) and solitary wave amplitudes (0.5m, 1m, 1.5m., 2m, 2.5m and 3m) are used in the computations in order to make a better comparison with the relationships provided by Synolakis (1986).

The well known runup law is represented by the relation

$$\frac{R_u}{d} = 2.831\sqrt{\cot \beta} \left(\frac{H}{d}\right)^{5/4} \quad [4.2]$$

where  $R_u$  is the Runup,  $d$  is the depth at the toe of the slope,  $H$  is the wave height,  $\beta$  is the sea bottom slope angle and  $R_u/d$  is the normalized (dimensionless) Runup.

The computed normalized Runup values for the selected slope, solitary wave amplitude and slope conditions are given in Table 4.2, together with the calculated (corresponding) dimensionless runup values according to Runup Law of Synolakis (1986). The third column in Table 4.2 shows the maximum horizontal distance of

the inundation limit from the original shoreline computed by NAMIDANCE. Different from the other slopes, the solitary waves with the amplitudes of 4m, 5m and 6m are inputted on 1/20 bottom slope in order to observe the breaking wave condition and compare the computed runup values with the corresponding laboratory data in Synolakis (1986).

**Table 4.2:** The computed and calculated runup values of solitary waves with different wave amplitudes on different bottom slopes

Cot $\beta$	H (m)	Inundation distance	Runup (Ru) computed by NAMIDANCE	Ru/d	$2.831\sqrt{\cot\beta}\left(\frac{H}{d}\right)^{5/4}$
10	0.5	14	1.54	0.031	0.028
10	1	36	3.53	0.071	0.067
10	1.5	54	5.66	0.113	0.112
10	2	76	7.68	0.156	0.160
10	2.5	98	9.60	0.192	0.194
10	3	114	12.50	0.250	0.266
15	0.5	26	1.81	0.036	0.035
15	1	60	4.06	0.081	0.082
15	1.5	92	6.25	0.125	0.137
15	2	122	8.13	0.165	0.196
15	2.5	225	10.00	0.20	0.201
15	3	174	11.60	0.232	0.326
20	0.5	40	2.00	0.04	0.040
20	1	86	4.40	0.088	0.095
20	1.5	130	6.60	0.13	0.158
20	2	168	8.50	0.17	0.226
20	2.5	200	9.50	0.19	0.221
20	3	226	10.50	0.21	0.376
20	4	162	13.50	0.27	0.277
20	5	143	15.50	0.31	0.315
20	6	131	17.50	0.35	0.339
25	0.5	54	2.21	0.044	0.045
25	1	114	4.62	0.092	0.106
25	1.5	166	6.69	0.134	0.177
25	2	206	8.38	0.168	0.253
25	2.5	178	9.76	0.195	0.197
25	3	276	11.04	0.221	0.420

Figure 4.15 displays the comparison of the computed and laboratory results according to the normalized maximum runup of solitary waves on a 1/20 beach with respect to the normalized wave height. It is observed that the computed results (colored data) are in high concordance with the laboratory data and runup law on

1/20 slope. In addition, the wave breaking starts with the wave height of 2.5m. The asymptotic solution in the figure represents the runup law, and the black symbols as cross and triangle are laboratory data for breaking and nonbreaking waves.

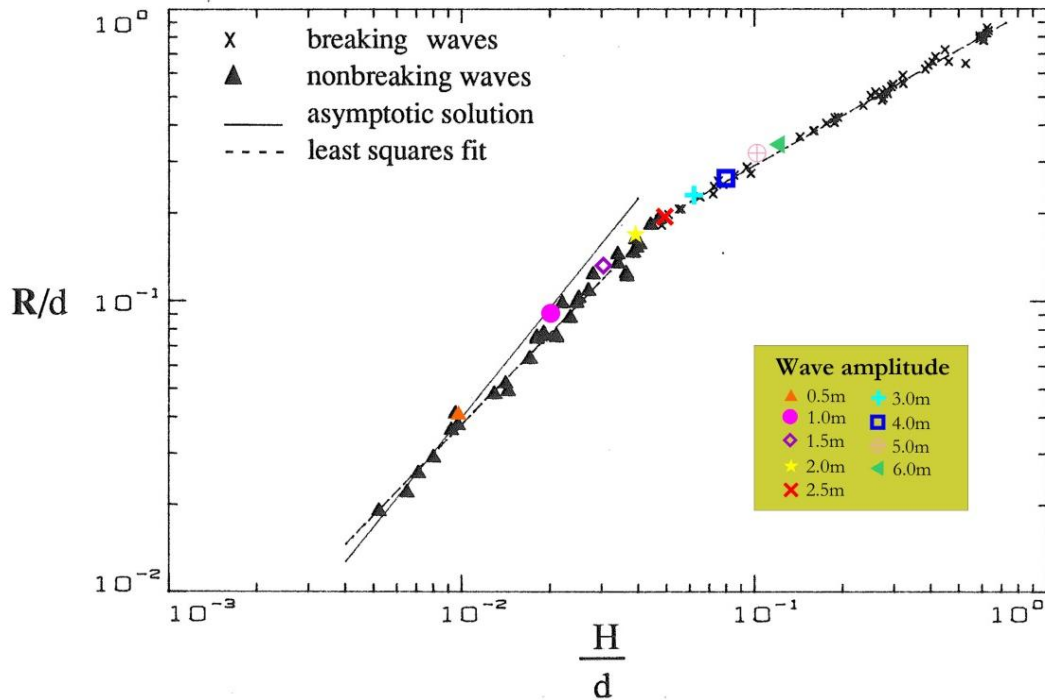


**Figure 4.15:** The comparison of laboratory data given in Synolakis (1986) with the computed results of NAMI DANCE according to the normalized maximum runup of solitary waves on a 1/20 slope with respect to the normalized wave height.

After registering the wave height for breaking condition, the computed runup values for different beach slopes are compared with the laboratory data (Figure 4.16). Synolakis (1986) provides a figure for normalized maximum runup of nonbreaking solitary waves climbing up different beaches with respect to the normalized wave height. Figure 4.16 includes the results of different laboratory experiments and the provided relation of runup law accordingly. The comparison of numerical results with the laboratory data in Synolakis (1986) indicates that the computed runup values fit well with the laboratory data.

Figures 4.17 and 4.18 show the comparison of numerical results of water surface profile computed by NAMIDANCE with the non-linear theory and laboratory data

given in Synolakis (1986) during the climb of a solitary wave with  $H/d = 0.019$  ( $H \approx 1\text{m}$ ) onto a  $1/20$  slope at dimensionless time steps from  $t=25$  to  $t=70$ . The non-dimensional form of the time is obtained by using the factor  $\sqrt{\frac{g}{d}}$ .

In Figures 4.17 and 4.18, the vertical axis is the normalized surface profiles ( $\eta/d$ ) as functions of the normalized distance ( $x/d$ ) where the shoreline is located at  $x/d = 0$ . The symbols in black color indicate different realizations of the same initial conditions in the laboratory, and the black straight line shows the non-linear theory (Synolakis, 1986).

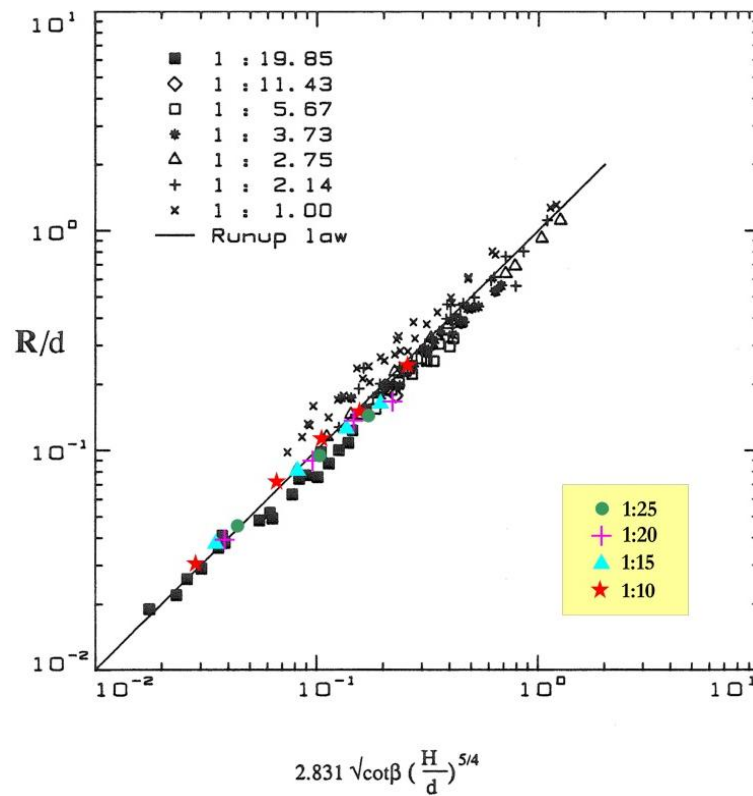


**Figure 4.16:** The comparison of different laboratory data in Synolakis (1986) with the computed results of NAMIDANCE according to the normalized maximum runup of nonbreaking solitary waves climbing up different beaches with respect to the normalized wave height.

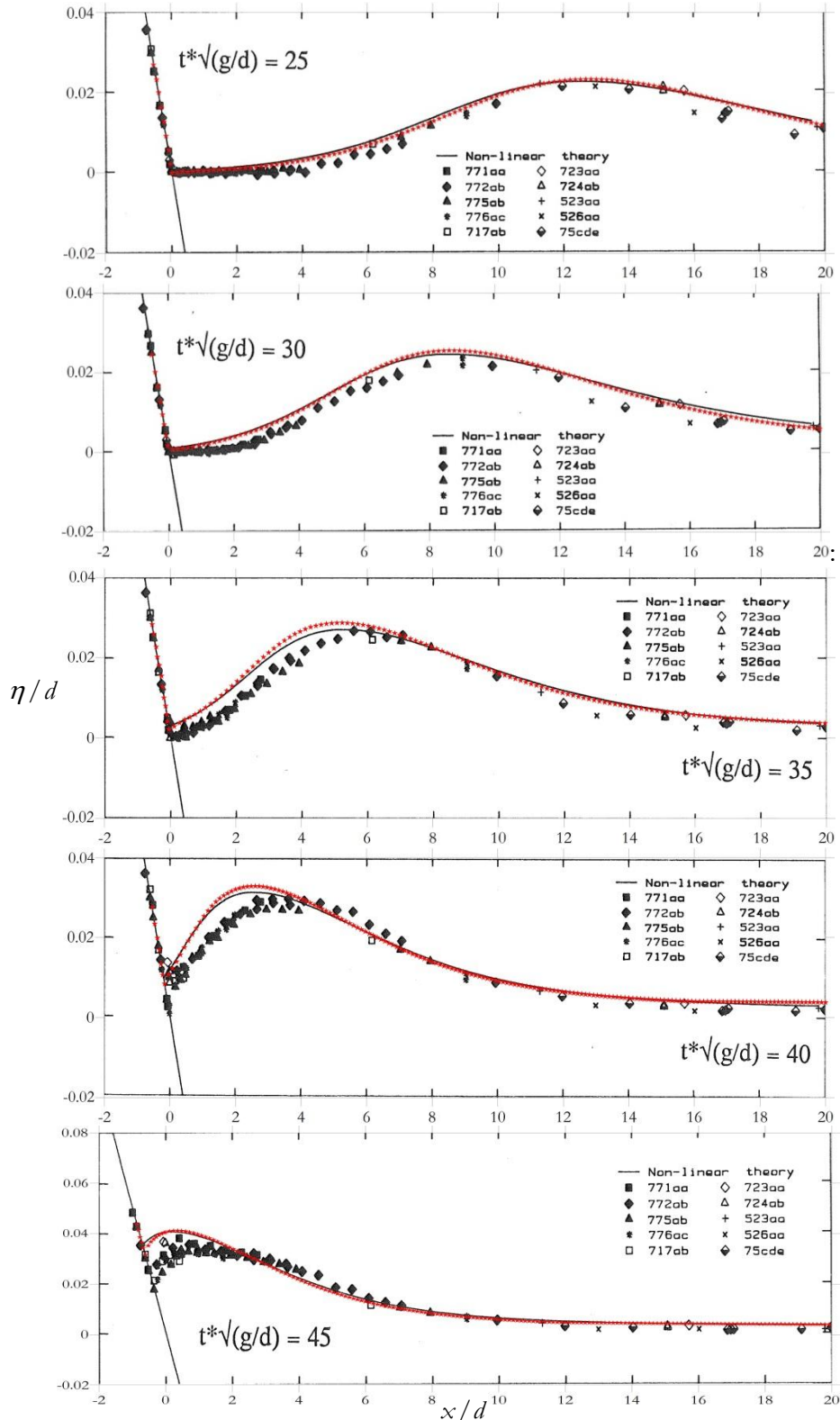


**Figure 4.17:** The comparison of numerical results computed by NAMIDANCE (red dots) with non-linear theory and laboratory data in Synolakis (1986) according to the climb of a solitary wave with  $H/d= 0.019$  ( $H \approx 1\text{m}$ ) up a  $1/20$  beach for dimensionless times  $t=25$ ,  $t=30$ ,  $t=35$ ,  $t=40$  and  $t=45$ .

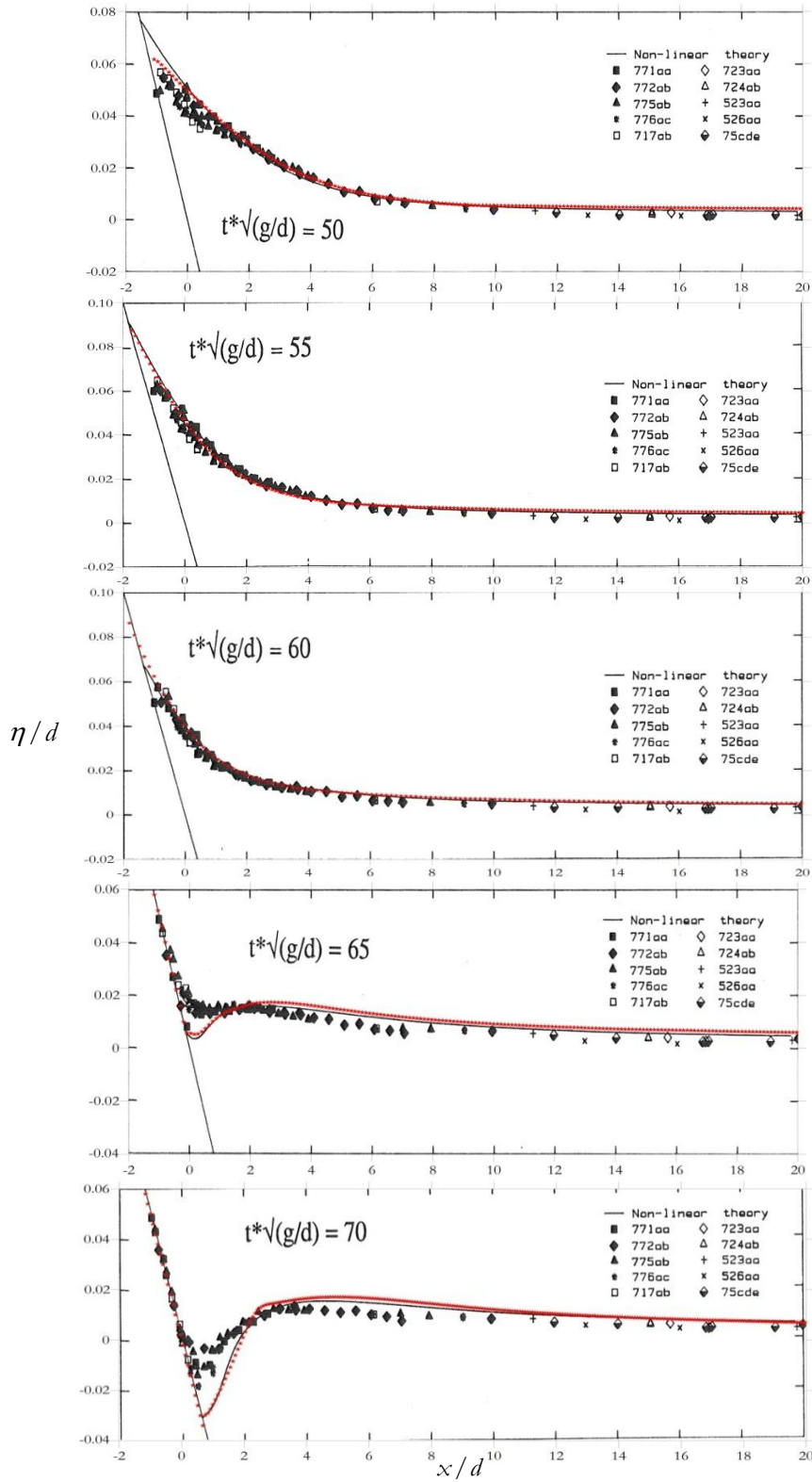


**Figure 4.18:** The comparison of numerical results computed by NAMIDANCE (red dots) with non-linear theory and laboratory data in Synolakis (1986) according to the climb of a solitary wave with  $H/d=0.019$  ( $H \approx 1\text{m}$ ) up a  $1/20$  beach for dimensionless times  $t=50$ ,  $t=55$ ,  $t=60$ ,  $t=65$  and  $t=70$ .

The comparisons manifest that the climb of solitary wave on a sloing surface computed by NAMIDANCE fits almost exactly with the non-linear theory and are compatible with the laboratory data (Figures 4.17 and 4.18). As a result, it can be stated that NAMIDANCE provides valid and verified results for the runup of solitary waves on plane beaches and satisfies the runup law.

#### **4.4. Scientific and Operational Evaluation**

After applying the benchmark procedures, it is also essential for any model to be published in peer-reviewed scientific journals. These publications can contain the validation and verification of the model by benchmark problems or any other application of the model with real tsunami events. NAMI DANCE is used in many international and national projects for tsunami analyses in the sea and on the land. The model is also used for the simulations of 2011 Great East Japan Tsunami and the results are published in a peer-reviewed scientific journal (Yalciner et al, 2012).

The numerical models should also be used for operational forecasts in order to be consistent in validation and verification processes. A model should meet the following five requirements in order to succeed in operational evaluation: operational forecasting and inundation mapping, modular development, test bed and model, operational testing and implementation (Synolakis et al., 2008). NAMI DANCE was used as the operational tsunami forecasting model in Malaysian Tsunami Early Warning Center in the early times. The model was installed to the center and made operational by the developers and researchers of NAMIDANCE in 2005. NAMI DANCE is also established at the Regional and International Tsunami Early Warning Center in Kandilli Observatory and Earthquake Research Institute, Istanbul, which will start operating at the end of 2012 and produce tsunami forecasts and warnings in Eastern Mediterranean and North Atlantic. This project is performed by the steering of International Oceanographic Commission (IOC) of UNESCO and the participation of neighbor countries. NAMI DANCE is accepted and will be used in the Turkish Tsunami Early Warning Center for operational tsunami forecasting.

These operational utilizations of NAMI DANCE are further evidence to its reliability and functionality, validating and verifying the model.

## CHAPTER 5

### MODEL APPLICATION

This section describes the investigation of tsunami hydrodynamic parameters in inundation zone by applying the modified version of numerical code NAMI DANCE to the regular shaped test basins. The analyses are performed in two parts (i) the determination of wave behavior with different wave characteristics on plain beaches with different slopes, (ii) the investigation of hydrodynamic parameters in inundation zone on various types of test basins with or without structures in different layout. As explained in Chapter 3, the governing hydrodynamic parameter of this study is the square of maximum Froude number ( $Fr_{\max}^2$ ) in inundation zone as it is a representing value of wave energy and an index of the damage level on residential areas.

The tests are performed by inputting a single sinusoidal wave in two different shapes as leading elevation wave (LEW) and leading depression wave (LDW) near the left boundary of the basin along the duration of wave period. The analyses of hydrodynamic parameters on different types of basins are worked out by inputting waves with different periods on beaches with the same slope. The details of inputted waves and the types of test basins are described in detail in the following section.

#### 5.1. Model Parameters

The tests in the first part of the thesis are performed by using different types of study basins by inputting waves with different characteristics on the beaches with various sea bottom slopes. In the second part, the test basins have different structural layout

but having the same bottom slope of 1/20. The explanation of model parameters in part two is twofold: the types of test basins and the characteristics of inputted wave.

### **5.1.1. The Properties of Test Basins**

The main objective of this study is to investigate the distribution of hydrodynamic parameters on land with the residential areas and the capability of shore protected structures to avoid or reduce the tsunami damage by diminishing the high values of flow depths and strong current velocities.

In the first part of the analyses, different bottom slopes of the test basins are used as 1/10, 1/15, 1/15 and 1/20. The details of basins and inputted waves are described in Section 5.3.

In the second part of the analyses, a total of 22 different test basins are used in the simulations with varying layout of buildings, seawall (SW) and offshore breakwater (BW) and with varying heights and damage levels. These analyses may enable the researchers to utilize the capability of tsunami seawalls and breakwaters damaged by the earthquake that triggered the incoming tsunami or by the effect of first waves produced by strong currents.

Table 5.1 gives the properties of each test basin including such criteria as the layout of buildings, the existence of seawall and/or offshore breakwater, the height of seawalls and breakwaters, the extent to which they are damaged. The test basins are formed according to the variations of these criteria. Each basin is named, and henceforward referred to by, a number given in Table 5.1.

Each test basin has a rectangular shape with the dimensions of 2000m length and 1000m width. The water has a constant depth of 50m till the toe of basin. After the toe, the sea bottom has a constant 1/20 slope. The distance from the left boundary of the basin to the toe is 800m and the sloped sea bottom up to the shoreline is 1000m. The remaining 200 m distance is determined as the land area. The 1/20 slope of the land is the same with the sea bottom. The highest elevation on the land is - 10m with respect to undisturbed sea surface. The buildings considered as impermeable boundaries, the grid size of each cell is taken as 2m to have more

**Table 5.1:** The List of Test Basins with Their Properties

No. of Basin	Property	Building Layout	Seawall (SW)		Offshore Breakwater (BW)	
			Height (m) above GL*	Status of damage	Height (m) from sea bottom	Status of damage
01	Plain beach	—	—	—	—	—
02	With buildings	Frequent	—	—	—	—
03	With buildings	Apart	—	—	—	—
04	Buildings and seawall	Frequent	4	NO	—	—
05	Buildings and breakwater	Frequent	—	—	14	NO
06	Buildings, seawall and breakwater	Frequent	4	NO	14	NO
07	Buildings and breakwater	Frequent	—	—	3	YES
08	Buildings and seawall	Apart	4	NO	—	—
09	Buildings and breakwater	Apart	—	—	14	NO
10	Buildings, seawall and breakwater	Apart	4	NO	14	NO
11	Buildings and breakwater	Apart	—	—	3	YES
12	Buildings, seawall and breakwater	Frequent	2	YES	3	YES
13	Buildings, seawall and breakwater	Apart	2	YES	3	YES
14	Buildings, seawall and breakwater	Frequent	4	NO	3	YES
15	Buildings, seawall and breakwater	Apart	4	NO	3	YES
16	Buildings and breakwater	Frequent	—	—	16	NO
17	Buildings, seawall and breakwater	Frequent	4	NO	16	NO
18	Buildings and breakwater	Apart	—	—	16	NO
19	Buildings, seawall and breakwater	Apart	4	NO	16	NO
20	Buildings and seawall	Frequent	6	NO	—	—
21	Buildings, seawall and breakwater	Frequent	6	NO	16	NO
22	Buildings, seawall and breakwater	Frequent	6	NO	14	NO

\* GL: Ground level

reliable results in inundation zone as described in Section 3.9. Therefore, the test basins are meshed into the cells with 1001 x 501 nodes in x and y directions, respectively. The numerical gauge points are placed at every 20m along x direction passing through the middle of the basin. Figure 5.1 shows the top view of a sample test basin with its dimensions, the location of structures, the gauge points, the number of grid nodes in x and y and the wave direction.

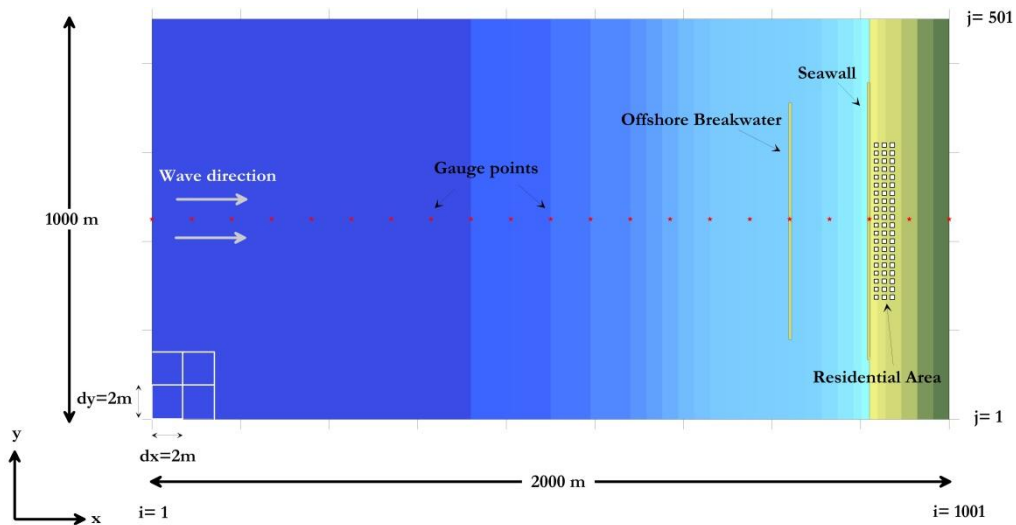


**Figure 5.1:** The top view of a sample basin with the location of structures

The stereotypical three-storey concrete buildings on the residential area are modeled in sizes of 10m width, length and height. The model of the residential areas had three rows of 20 buildings, each starting from 10m behind the shoreline. There are 10m wide corridors between each buildings both in x and y direction representing the pedestrian roads or motorways.

The buildings are laid down wide apart in some test basins with 30m intervals in y direction in order to increase the width of the corridor through which tsunami passes and to determine the effect of residential layout to the hydrodynamic parameters.

The breakwater having 6m berm width is placed 200m offshore at the water depth of 10m. The seawall is 6m wide and 690m long, lying 10m ahead of the first row of buildings along the shoreline. The height of breakwater with respect to undisturbed water surface is taken as 4m or 6m considering the height of offshore breakwaters

constructed particularly for the protection against tsunamis in Japan (Shuto, 1991). Similarly, the height of seawall is decided as 4m according to the general design of tsunami walls constructed along the shoreline in front of the residential areas in many towns located at the end of long narrow bays in Japan (Yalciner et al, 2012). Although the seawalls are generally designed with the heights not more than 4m, the height of seawall is designated as 6m in some basins for testing the prevention capacity of the walls by increasing its height. It should be indicated that, in this study, the buildings or other coastal protection structures are assumed to be fixed, rigid and stable against the wave attack.

The sample test basins are given in Figure 5.2 in order to visualize the orientation of both undamaged and damaged buildings, seawall and offshore breakwaters. The plot of Basin-01 shows the whole basin with the constant depth, toe, slope, shoreline and the land. The other plots are focusing on the structural area. The basins between 08 and 22 are formed by the variations of these main basins with different orientation of buildings, height of seawall and breakwater.

### **5.1.2. Characteristics of Inputted Wave for the Tests**

The numerical code NAMI DANCE is modified in order to make simulations with an inputted tsunami source during a constant time. This inputted data is in the form of a “dat” file in four columns including time in second (*sec*), water elevation in meter (*m*) and discharge fluxes M and N in metersquare/second ( $m^2/s$ ). NAMI DANCE reads this water elevation data at every corresponding time and specifies the water surface elevation as that inputted data.

The test analyses in this thesis are performed by inputting single sinusoidal leading elevation and depression wave at a certain location that is in between the nodes of 20 and 30 in x direction as shown in Figure 5.2, during the period of one wave.

The first part of the analyses, the investigation of wave behavior on a plain beach, is performed by using different wave heights and periods. Various sea bottom slopes are also used in order to observe the change of hydrodynamic parameters according to the bathymetric and topographic changes.

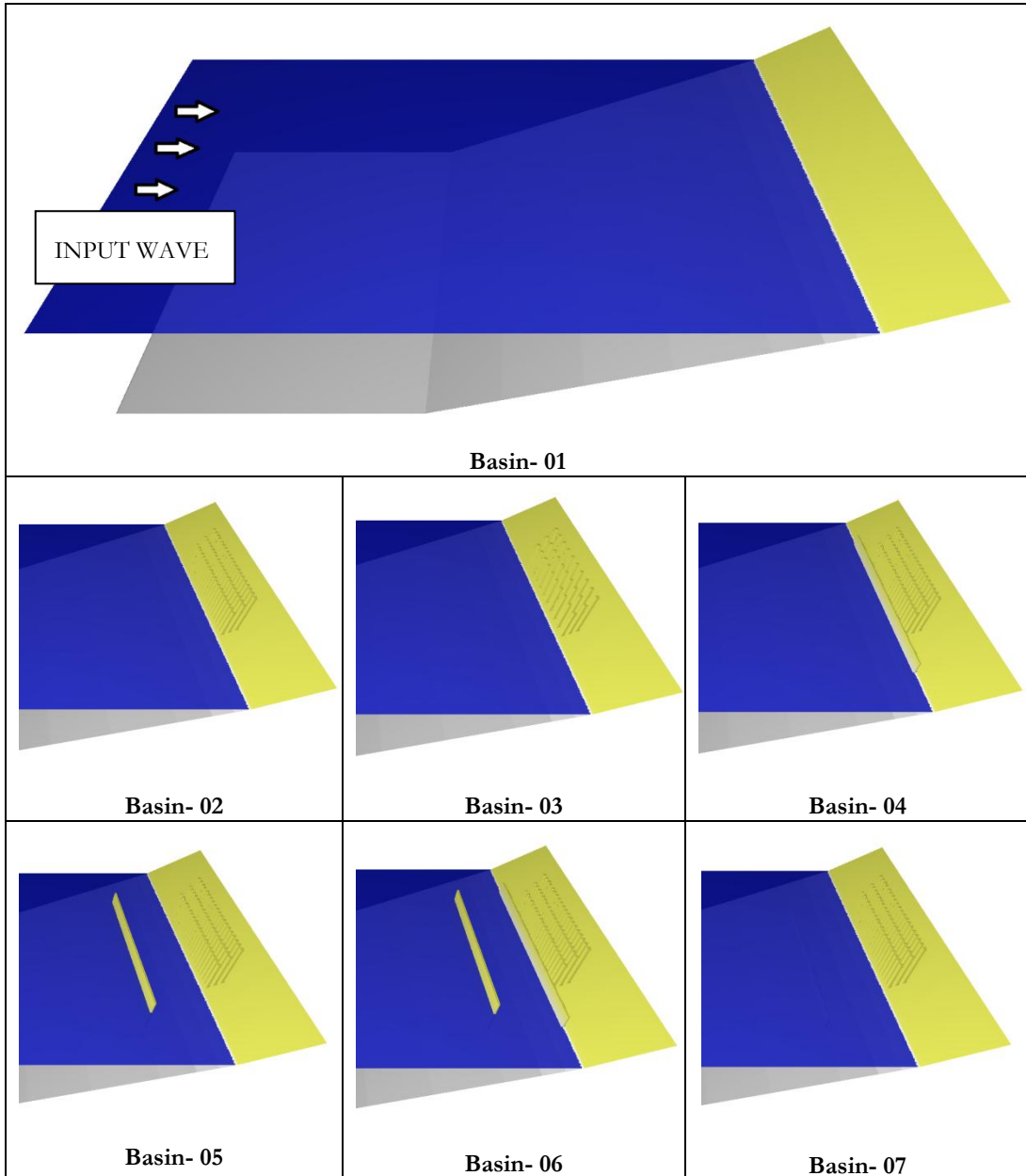


**Figure 5.2:** The 3D visualization of Representative Test Basins

In the simulations, four different initial wave heights are inputted as a single sinusoidal wave with ascending front as  $a = 4\text{m}$ ,  $5\text{m}$ ,  $6\text{m}$  and  $8\text{m}$ . Each wave is inputted having five different wave periods as  $T = 3\text{min}$ ,  $6\text{min}$ ,  $12\text{min}$ ,  $24\text{min}$  and  $48\text{min}$ . The sea bottom is also changed in the analyses with four different slopes:  $1/10$ ,  $1/15$ ,  $1/20$  and  $1/25$ . A sample figure of the inputted wave with  $4\text{m}$  amplitude and  $48\text{min}$  period is shown in three dimensional form in Figure 5.3.

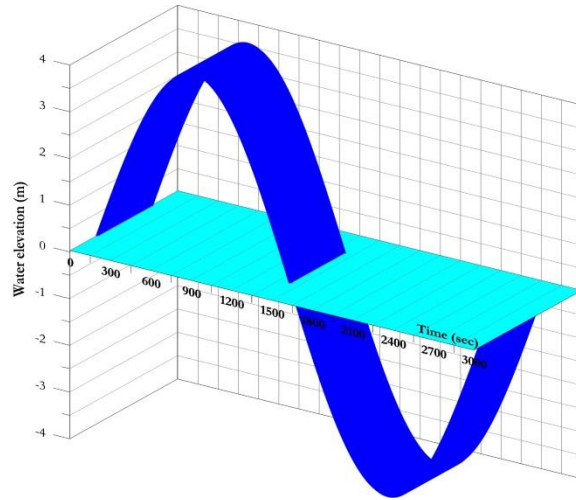


**Figure 5.3:** The 3D view of inputted sinusoidal wave with 4m height and 48min period

The combination of simulations using four different wave heights, five different wave periods and two different wave shapes propagating on four different bottom slopes leads to 160 different test simulations. These tests will shed light onto the change of tsunami hydrodynamic parameters in inundation zone depending on the wave characteristics and bathymetric variations.

The main reason for tsunami damage in inundation zone is the hydrodynamic parameters, which are the main cause of tsunami effect in inundation zone. These are (i) maximum positive amplitude, (ii) maximum current velocity, (iii) maximum flow depth, (iv) hydrodynamic demand, and (v) maximum negative amplitude.

As explained in Chapter 3, the hydrodynamic demand parameter includes the effect of currents and corresponding flow depth at a certain location. It is an instantaneous dimensionless value called Froude Number square ( $Fr^2$ ) calculated during tsunami inundation depending on the current velocity at a single point and the corresponding flow depth at every instant. Hence, the maximum value of the square of Froude number ( $Fr_{max}^2$ ) is the governing parameter for the examination of damage level in inundation zone. The evaluation of tsunami damage in residential areas is based on the distribution of this parameter in the inundation zone.

It is essential to include the backward motion of the waves in simulations since the maximum current velocities and accelerations are observed during the run-down of

the wave (Kanoglu, 2004). Taking into account of this property, the duration of simulations is taken as sufficiently long to fully cover the forward and backward motion in inundation zone.

In the second part of the analyses, the simulations on different types of basins are performed with the initial wave amplitude of 4m on 1/20 sloped beach. Since the inputted wave is a single sinusoidal wave, the initial wave amplitude is 8m, which is a representative value of a strong tsunami. The four different wave periods are selected as  $T= 3\text{min}$ ,  $12\text{min}$ ,  $24\text{min}$  and  $48\text{min}$ . Among these, the representative wave period for the tsunamis is chosen as 48min considering the real seismic tsunami events.

As part of the two stages of the analyses in this study and the test simulations performed during the modification stage of numerical code NAMI DANCE, more than 900 simulations were performed in order to include the effects of various characteristics during the investigation of changes in hydrodynamic parameters particularly in inundation zone. The following sections describe the observations in two parts and give the test results.

## **5.2 Symmetry Test of the NAMI DANCE computations in Circular Bathymetry with Forced Disturbance**

The code is tested in a circular bathymetry with a forced sudden water surface disturbance in terms of its symmetric and reasonable propagation in the sea and amplification on land.

This analysis is performed in order to test NAMI DANCE with respect to the performance of hydrodynamic parameter calculations both in backward and forward direction. The results of this test enable the users to measure the reliability of iterative calculations between the grids. The best way to test the performance and reliability of NAMI DANCE calculations in every direction is using a circular bathymetry as the test basin. Figure 4.11 shows the test basin with the bathymetry contour lines. The size of test basin is 1000m by 1000m with the grid size of 2m and the maximum depth is 50m.

The source is defined in the middle of the basin having 200m length both in major and minor axis. The amplitude of the initial wave is defines as 10m. The simulation results as to the wave generation from the middle of the bathymetry and propagation in all direction towards the zero line in time are given in Figure 5.4.

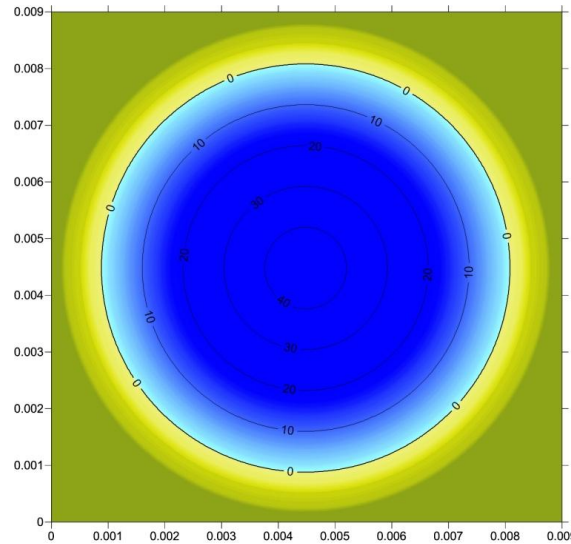


**Figure 5.4:** The bathymetry and topography of circular test basin for the verification of NAMI DANCE calculations in every direction

It is observed from the results in Figure 5.5 that the motion of the wave has a symmetric pattern towards the shoreline during the simulation time. This situation proves that the iteration pattern of the model between each cell is reliable in every direction both in forward and backward motion.

### **5.3. Investigation of Tsunami Behavior with Different Wave Characteristics on a Plain Beach**

#### **5.3.1. Calculation of Hydrodynamic Parameters on a Plain Beach**

This part of the study aims to obtain a correlation for the variation of average of  $Fr_{max}^2$  according to the change of wave period or wave height. The analyses were performed by inputting single sinusoidal waves with four different initial wave

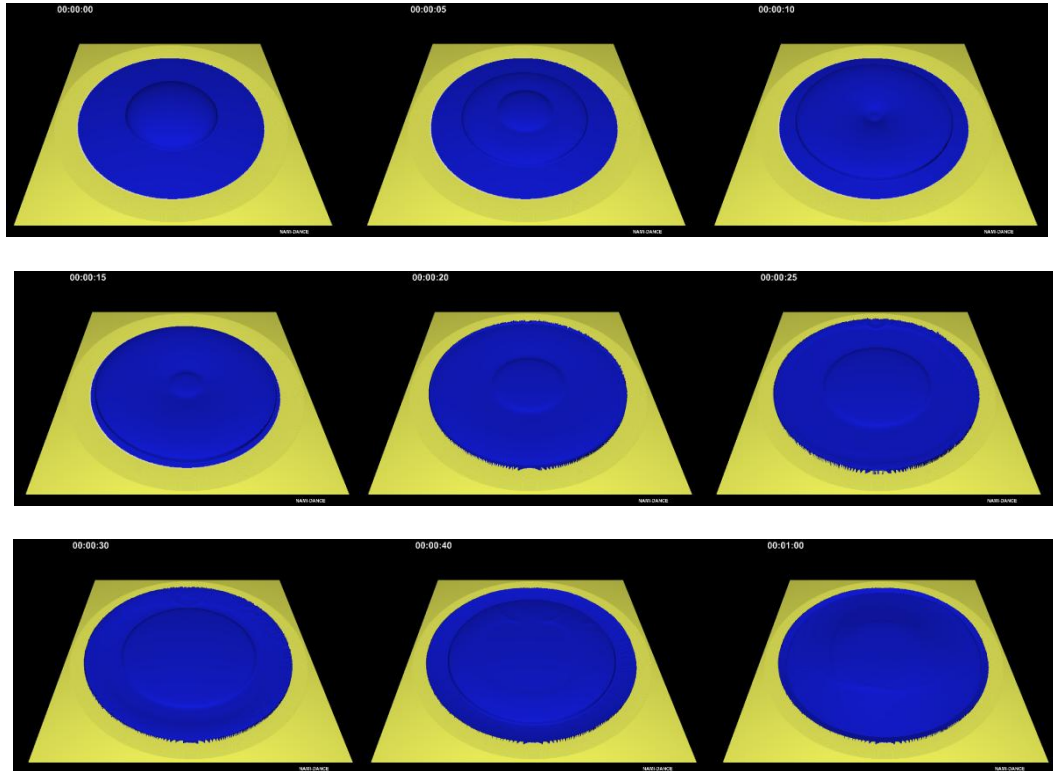


**Figure 5.5:** The snapshots of generation and propagation of the wave in circular test basin (the plot at  $t=0$  shows the initial user defined source at the middle of the basin)

amplitudes ( $a= 2\text{m}, 3\text{m}, 4\text{m}, 5\text{m}$  and  $6\text{m}$ ) both in leading elevation and leading depression shapes. The period of waves are altered in each test as follows:  $T= 3\text{min}, 6\text{ min}, 12\text{min}, 24\text{min}$  and  $48\text{min}$ . The waves are simulated on the plain beaches having four different sea bottom slopes:  $1/10, 1/15, 1/20$  and  $1/25$ . According to the simulation matrix depending on these input parameters, 160 simulations are carried out.

The analyses provide the maximum values of hydrodynamic parameters that occurred during the simulation time. As described in Chapter 3, the main subject of this study is the maximum value of  $Fr^2$  occurring in inundation zone. However, some instantaneous extreme values of  $Fr^2$  may occur when waves first inundate the land with strong currents but relatively low flow depths. There is also the boundary effect that may cause instant high values of  $Fr^2$ . In order to discard this situation, the average of maximum  $Fr^2$  values ( $\overline{Fr_{max}^2}$ ) occurred while the simulation time is calculated on land with extracting the area 100m close to the upper and lower

boundaries. In other words, calculation area is restricted to the ranges  $i=901$  to  $1001$  and  $j= 51$  to  $451$ .

The flow of water is called *supercritical* when the flow velocity is greater than wave velocity. The other way around is called *subcritical*. The supercritical flow occurs when the flow velocity rises and the flow depth becomes less than critical depth (Munson et al, 2002). One of the dimensionless parameters representing supercritical and subcritical flow is Froude number. When Froude number is higher than 1, the flow is said to be supercritical. In the light of this phenomenon, this study considers the maximum values of  $Fr^2$  greater than 1. For this purpose, the maximum  $Fr^2$  values greater than 1 are selected in the extracted study area together with the number of these values. Then, the averages of these maximum values are calculated for every wave height and period propagating on each wave slope. Considering the wave height as the reference parameter, the  $\overline{Fr_{max}^2}$  values calculated for each wave period are plotted with respect to the bottom slope  $\cot\beta$ . The plots are given in Figures 5.6 - 5.10 for  $H=2m, 3m, 4m, 5m$  and  $6m$ , respectively.

The figures firstly reveal that  $\overline{Fr_{max}^2}$  values increase when the waves with larger wave heights inundate the land. Second, lower averages of maximum  $Fr^2$  are obtained for the waves with longer wave periods because the motion gets longer and wave energy comes to the shoreline in longer duration with longer wave periods. The reason for this is that when the wave periods increase, or when the duration of wave inundation gets longer, the waves come to the land with less concentrated energy. This result is consistent since  $Fr^2$  values are presumed as representative indexes for energy and hydrodynamic forces on land.

The Figures 5.6 to 5.10 also indicated that, for a single wave, the change of  $\overline{Fr_{max}^2}$  that occurred as a result of propagation on different bottom slopes show a linear variation. It is possible to search a correlation between  $\overline{Fr_{max}^2}$  values and the wave characteristics as wave height and period including the bottom slope.  $\overline{Fr_{max}^2}$  is the function of wave height, wave period and bottom slope that is expressed as follows:

$$\overline{Fr_{max}^2} = f(H, T, \cot \beta) \quad [5.1]$$

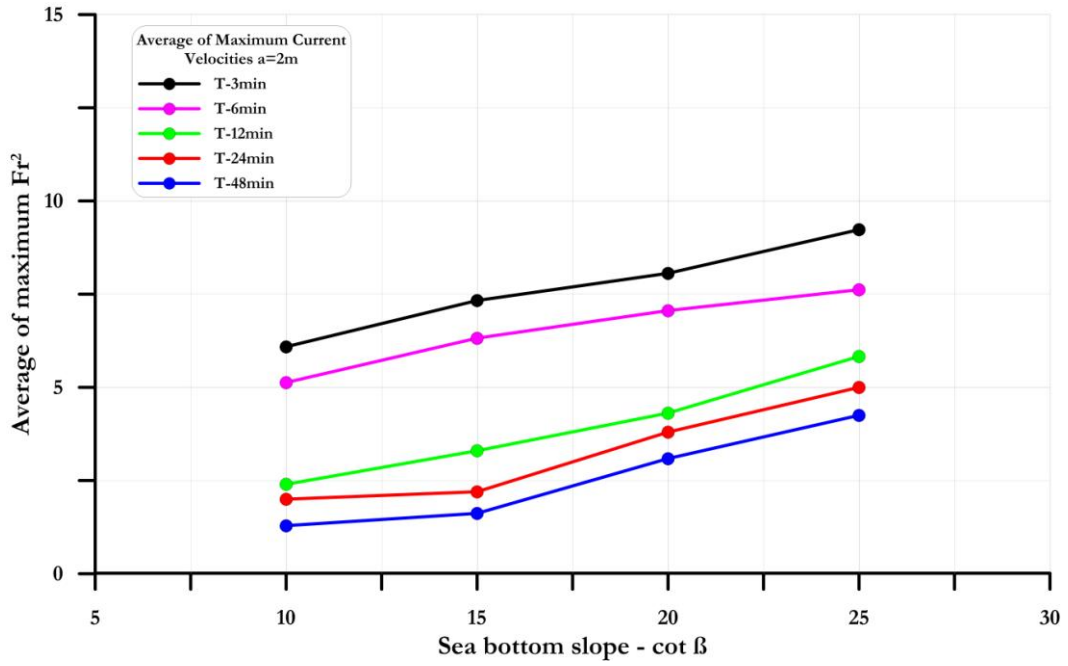


Figure 5.6: The plot of  $\overline{Fr_{max}^2}$  values calculated for the waves with initial wave amplitude  $a=2m$

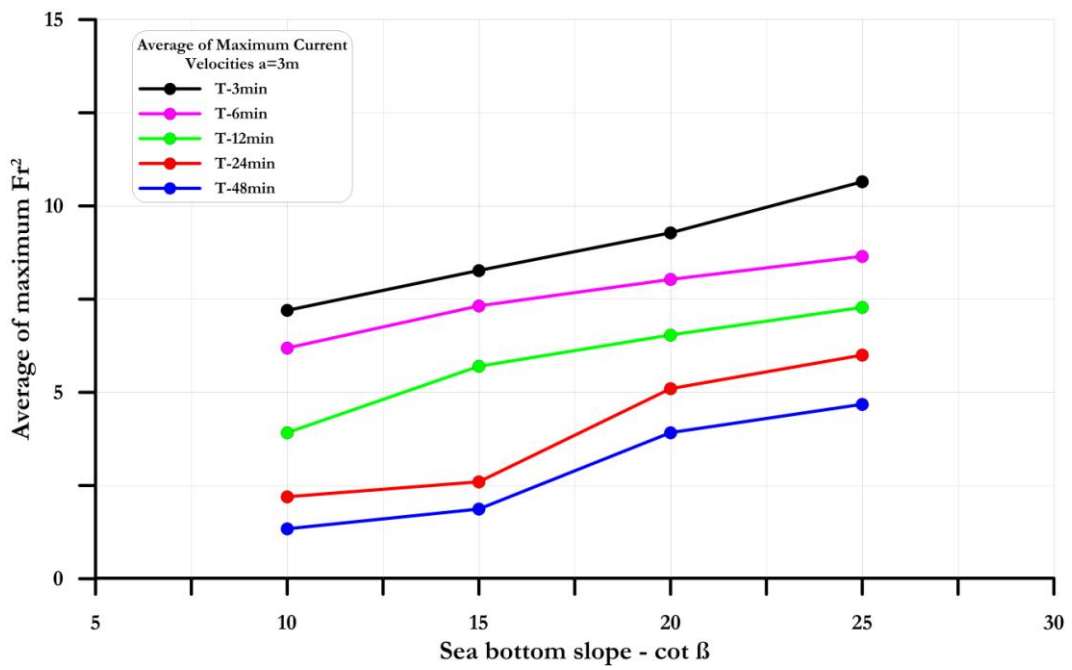


Figure 5.7: The plot of  $\overline{Fr_{max}^2}$  values calculated for the waves with initial wave amplitude  $a=3m$

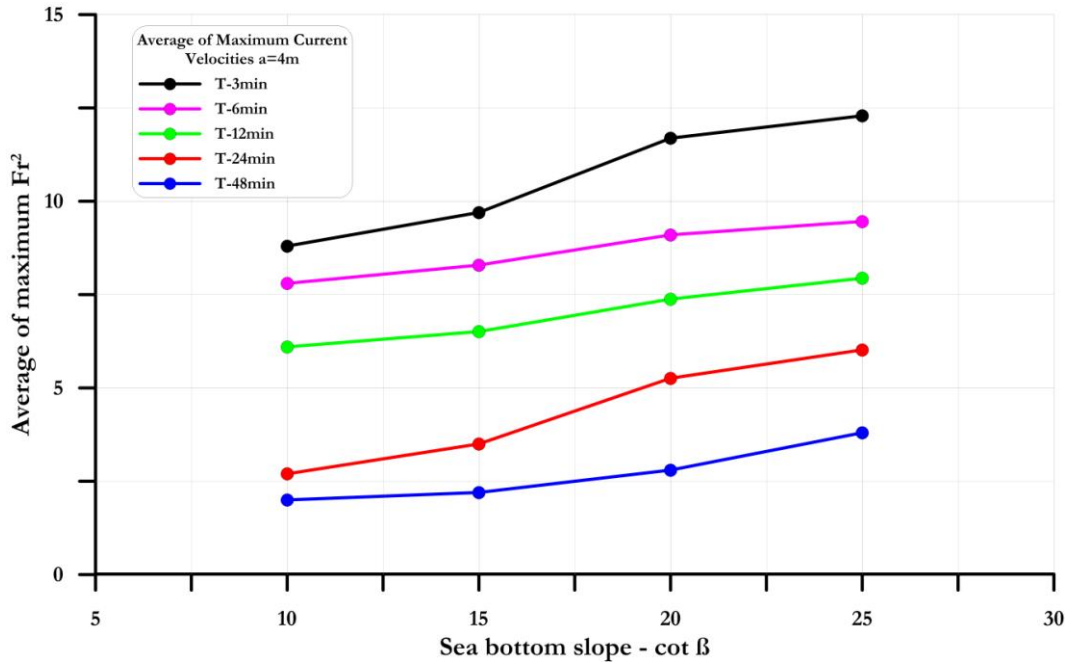


Figure 5.8: The plot of  $\overline{Fr_{max}^2}$  values calculated for the waves with initial wave amplitude  $a=4m$

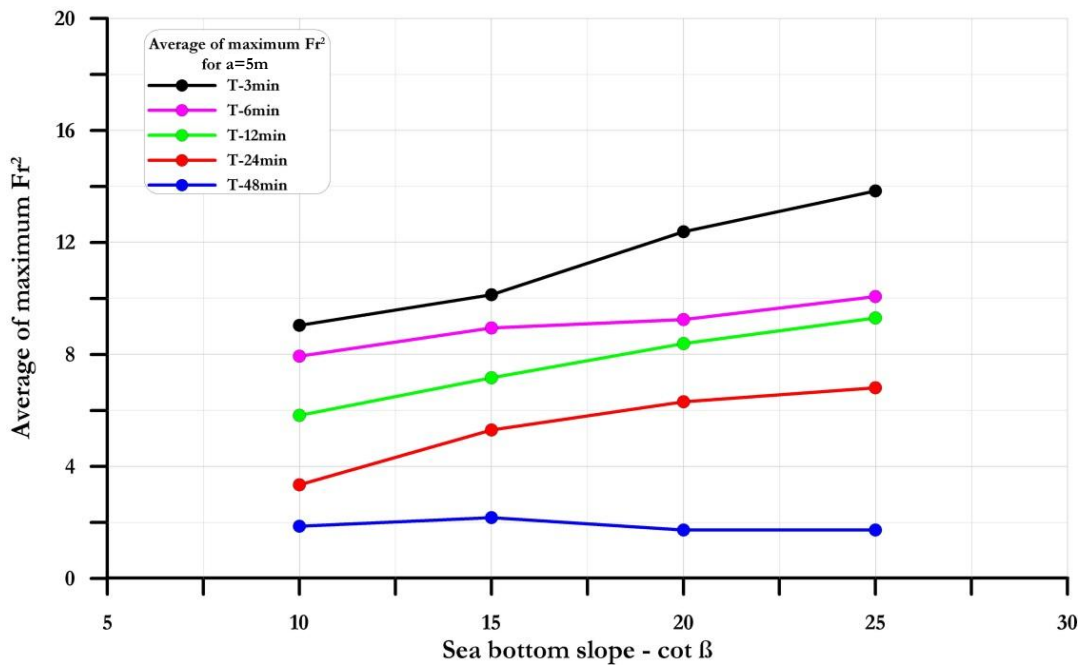
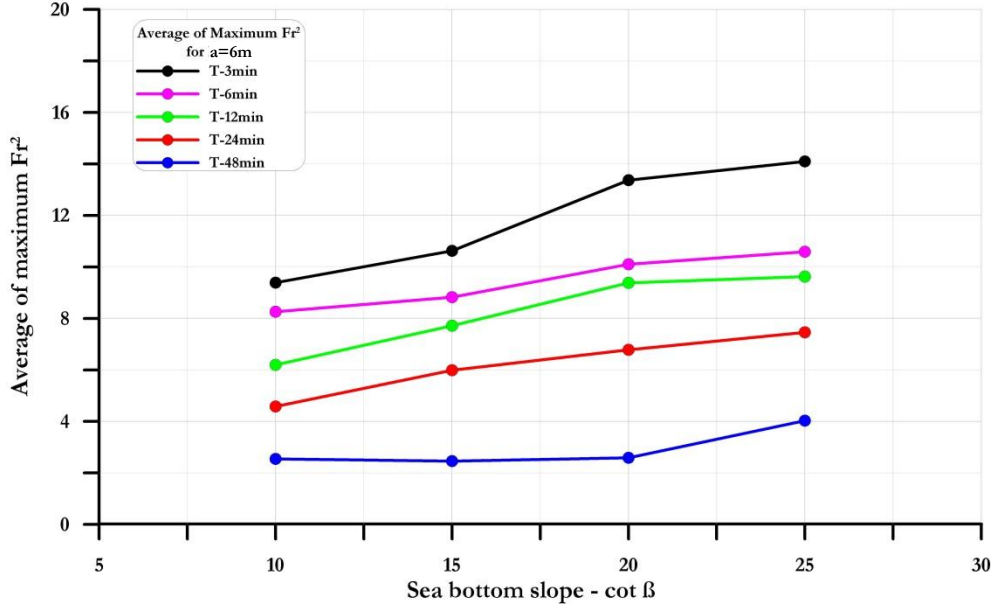


Figure 5.9: The Plot of  $\overline{Fr_{max}^2}$  values calculated for the waves with initial wave amplitude  $a=5m$



**Figure 5.10:** The Plot of  $\overline{Fr_{max}^2}$  values calculated for the waves with initial wave height  $a=6m$

Buckingham Pi Theorem is applied here in order to obtain a dimensionless correlation between  $H$ ,  $T$  and  $\cot\beta$ . Two possible relations are derived for  $\overline{Fr_{max}^2}$  calculation:

$$\overline{Fr_{max}^2} = C_{n1} \frac{H\sqrt{\cot \beta}}{2T\sqrt{gd_c}} \quad [5.2]$$

$$\overline{Fr_{max}^2} = C_{n2} \frac{H^2\sqrt{\cot \beta}}{4T\sqrt{gd_c^3}} \quad [5.3]$$

where  $d_c$  is the typical (maximum) water depth and  $C_{n1}$  and  $C_{n2}$  are empirical coefficients representing the correlation between  $\overline{Fr_{max}^2}$ , the wave height, wave period and sea bottom slope.

The relations provided in Eqns. [5.2] and [5.3] represent similar approaches. However, Eqn [5.3] is chosen for correlation since the parameter  $H^2$  reflects wave energy in the equation. Using the data obtained from the test results both for leading

elevation wave (LEW) and leading depression wave (LDW) shapes, the values for  $C_{n1}$  and  $C_{n2}$  are calculated from Eqns. [5.2] and [5.3]. The calculated  $C_n$  values are plotted for each relation both for LEW and LDW.

Figures 5.11 and 5.12 give the distribution of  $C_{n1}$  versus  $\overline{Fr_{max}^2}$  values obtained from Eqn. [5.2] for LEW depending on wave period and wave height, respectively. The data is plotted separately for each wave period in Figure 5.11 in order to see the change of  $\overline{Fr_{max}^2}$  with respect to wave period. It is seen from the figure that, the shorter the wave period, the higher the values of  $\overline{Fr_{max}^2}$ .

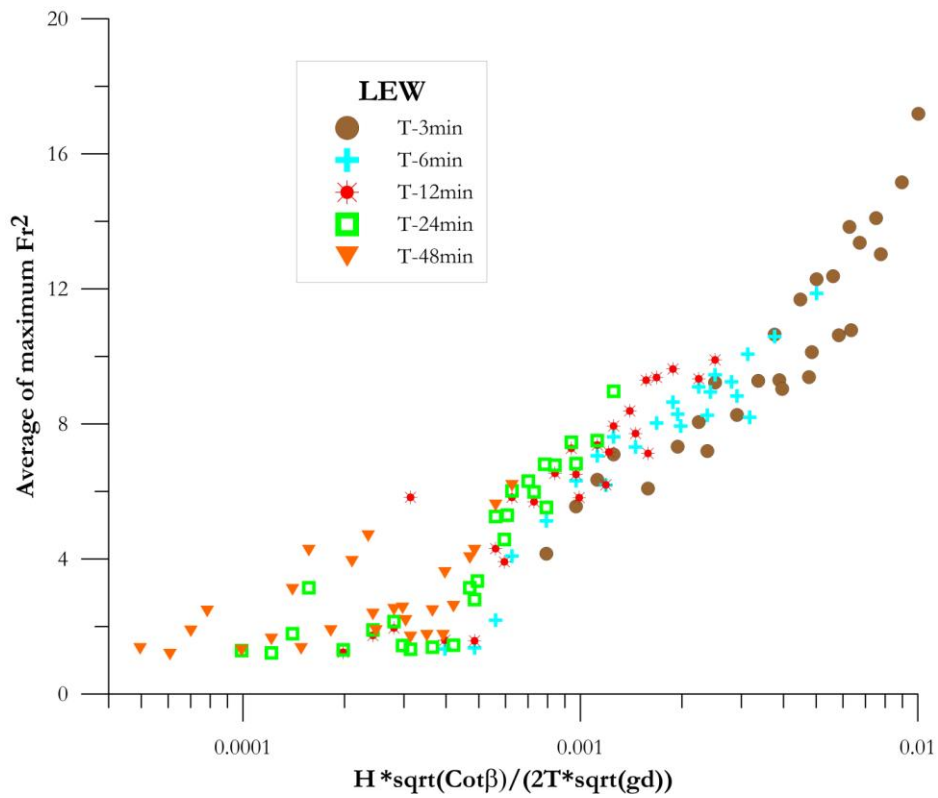


**Figure 5.11:** The distribution of empirical relationship in Eqn. [5.2] between  $\overline{Fr_{max}^2}$  and wave characteristics-bottom slope with respect to wave period for LEW

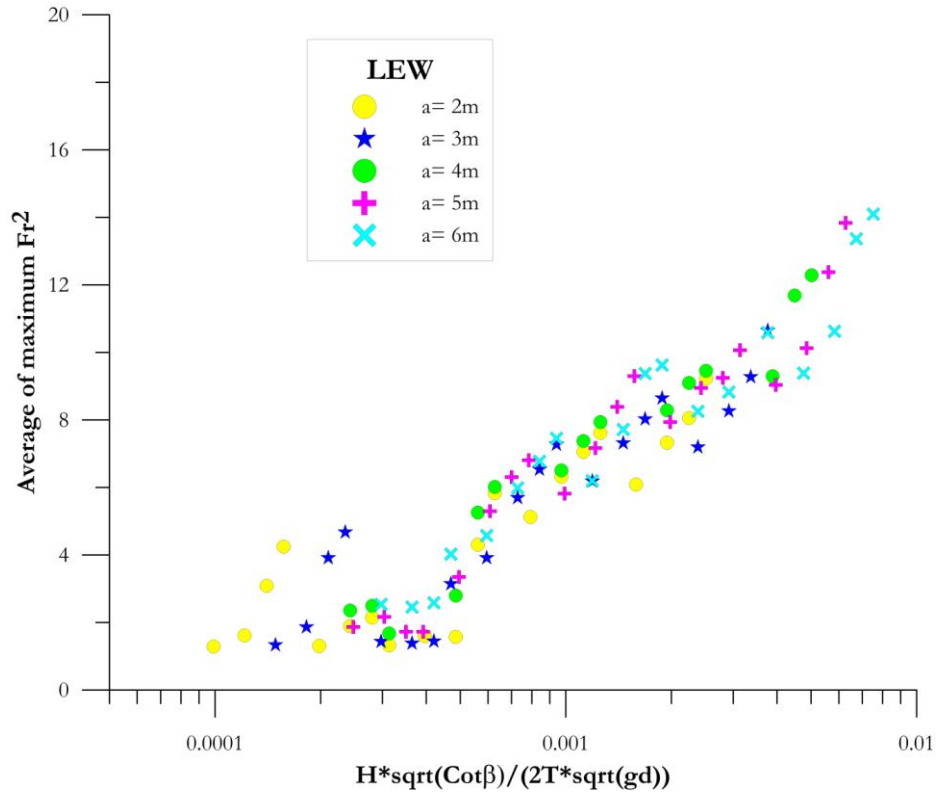


**Figure 5.12:** The distribution of empirical relationship in Eqn. [5.2] between  $\overline{Fr_{max}^2}$  and wave characteristics-bottom slope with respect to wave amplitude for LEW

Figures 5.13 and 5.14 give the distribution of  $C_{n1}$  versus  $\overline{Fr_{max}^2}$  values obtained from Eqn. [5.2] for LDW depending on wave period and wave height, respectively. Similar with the LEW case, the data is plotted separately for each wave period in Figure 5.13 in order to see the change of  $\overline{Fr_{max}^2}$  with respect to wave period. The same phenomenon is observed for LDW case that the shorter-period waves cause higher values of  $\overline{Fr_{max}^2}$ .

As seen from the figures, the x-axis is used in a logarithmic form since there is a curvilinear correlation between  $C_n$  and  $\overline{Fr_{max}^2}$ . The data calculated both for LEW and LDW is combined and then plotted together in Figure 5.15.

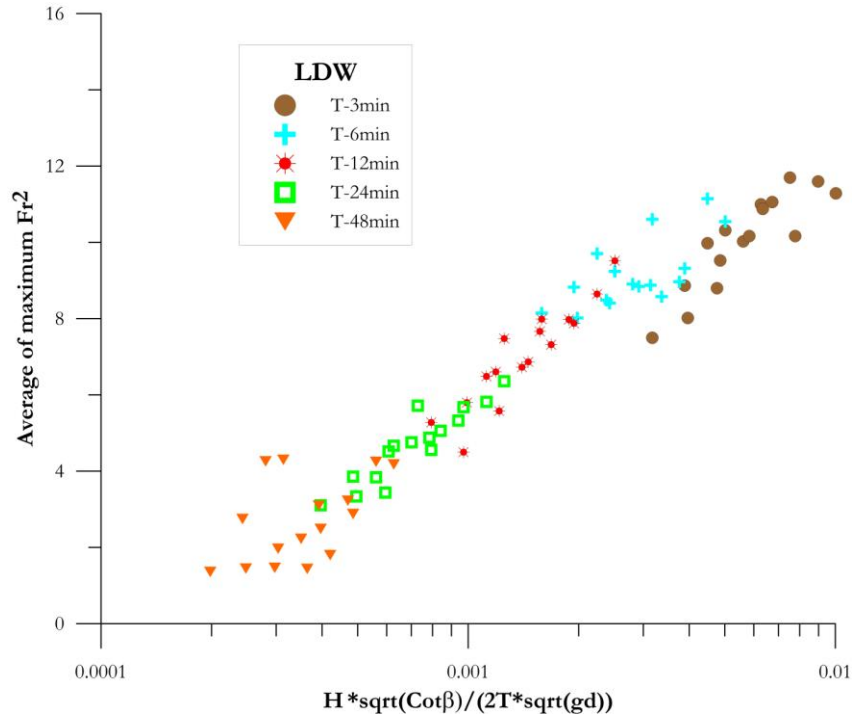


**Figure 5.13:** The distribution of empirical relationship in Eqn. [5.2] between  $\overline{Fr_{max}^2}$  and wave characteristics-bottom slope with respect to wave period for LDW

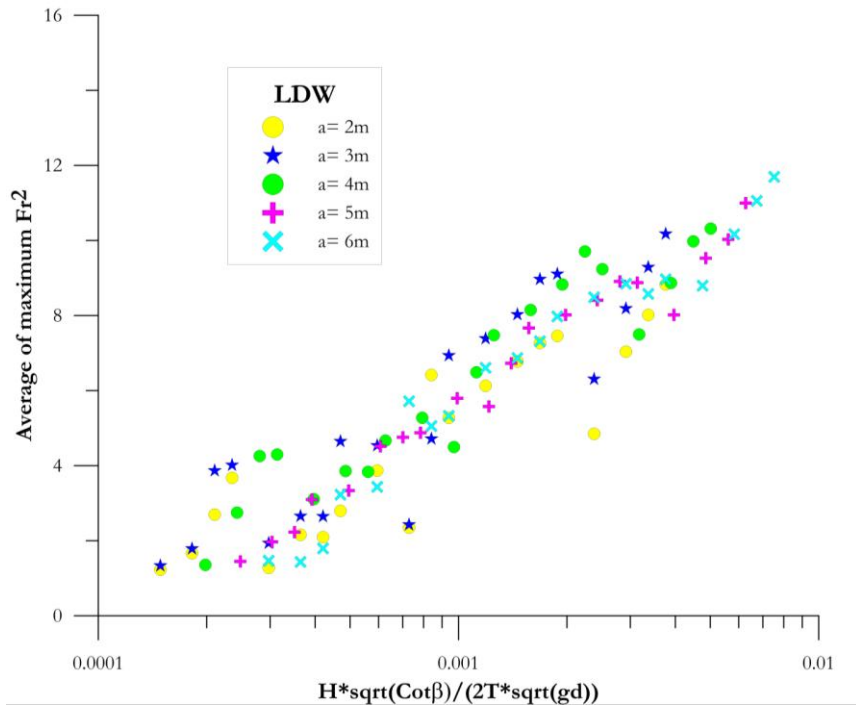


**Figure 5.14:** The distribution of empirical relationship in Eqn. [5.2] between  $\overline{Fr_{max}^2}$  and wave characteristics-bottom slope with respect to wave amplitude for LDW

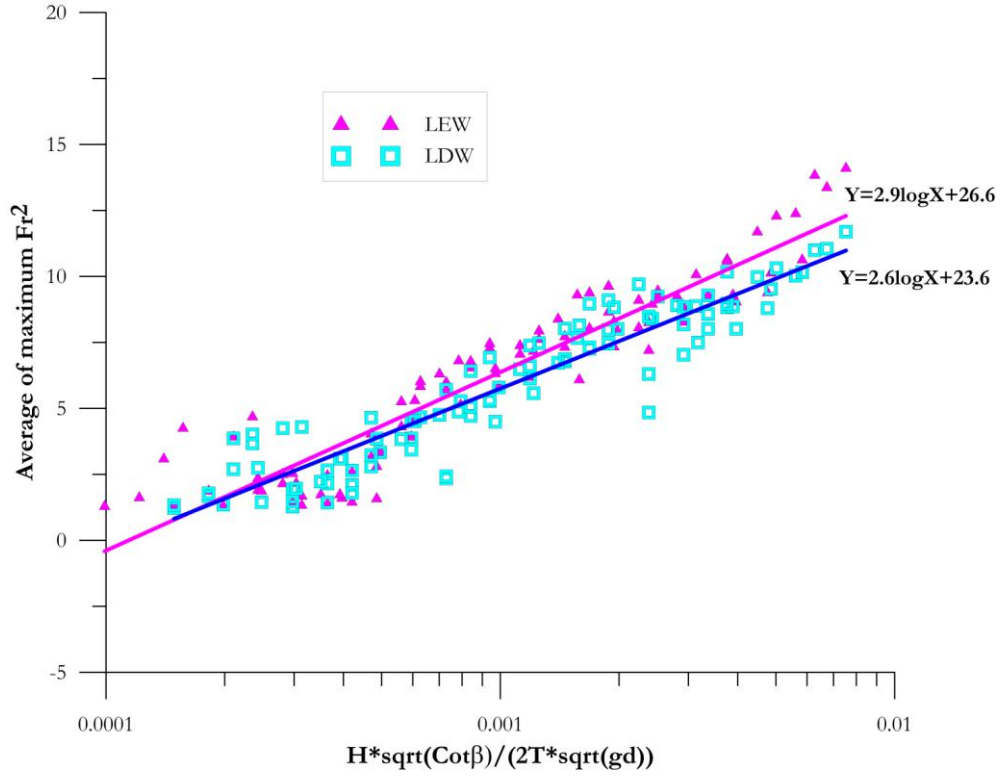


**Figure 5.15:** The distribution of empirical relationship in Eqn. [5.2] between  $\overline{Fr_{max}^2}$  and wave characteristics-bottom slope for LEW and LDW

Figure 5.15 shows that LDW causes slightly lower values of  $\overline{Fr_{max}^2}$  than LEW in inundation zone. The best fit is plotted, and then an empirical relation is obtained according to the test results.

Therefore, for single sinusoidal waves on a plane beach, the average of square of Froude Number  $\overline{Fr_{max}^2}$  in inundation zone can be calculated by using the following relations for LEW and LDW separately:

$$\overline{Fr_{max}^2} = 2.9 \log \left( \frac{H \sqrt{\cot \beta}}{2T \sqrt{gd_c}} \right) + 26.6 \quad \text{for LEW} \quad [5.4]$$

$$\overline{Fr_{max}^2} = 2.6 \log \left( \frac{H \sqrt{\cot \beta}}{2T \sqrt{gd_c}} \right) + 23.6 \quad \text{for LDW} \quad [5.5]$$

Likewise, the distributions of  $C_{n2}$  versus  $\overline{Fr_{max}^2}$  values obtained from Eqn. [5.3] for LEW are given in Figures 5.16 and 5.17 depending on wave period and wave height, respectively. The data is plotted separately for each wave period in order to see the change of  $\overline{Fr_{max}^2}$  with respect to wave period in Figure 5.16. It is seen from both of the two figures that when the wave period gets shorter, higher values of  $\overline{Fr_{max}^2}$  are observed.

In Figures 5.18 and 5.19, the distributions of  $C_{n2}$  versus  $\overline{Fr_{max}^2}$  values obtained from Eqn. [5.3] for LDW are given depending on wave period and wave height, respectively.

The data obtained from Eqn. [5.3] both for LEW and LDW is combined and plotted together in Figure 5.20. The best fit provides a logarithmic relation with respect to the test results.

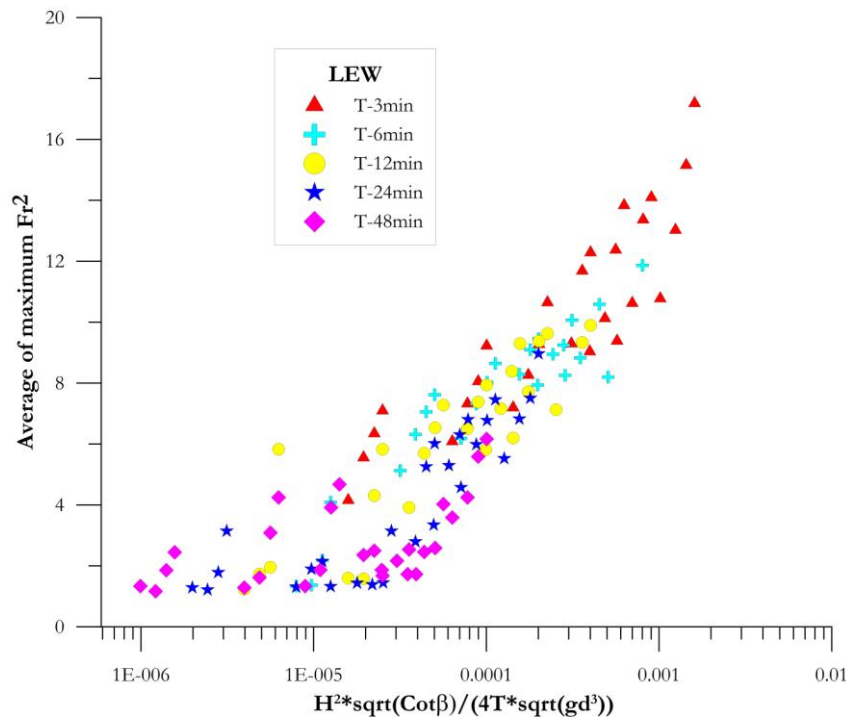


**Figure 5.16:** The distribution of empirical relationship in Eqn. [5.3] between  $\overline{Fr_{max}^2}$  and wave characteristics-bottom slope with respect to wave period for LEW

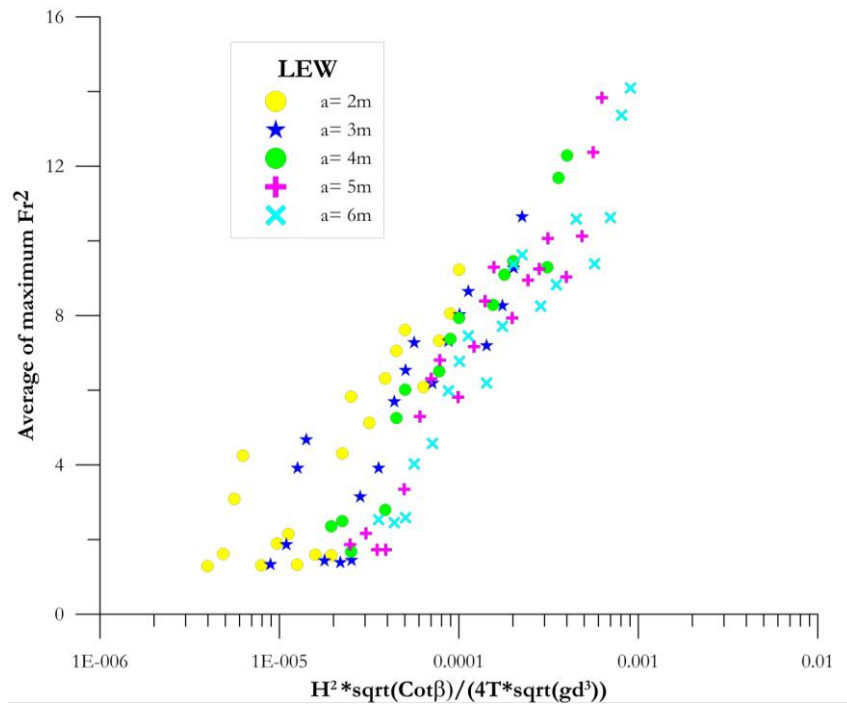


**Figure 5.17:** The distribution of empirical relationship in Eqn. [5.3] between  $\overline{Fr_{max}^2}$  and wave characteristics-bottom slope with respect to wave amplitude for LEW

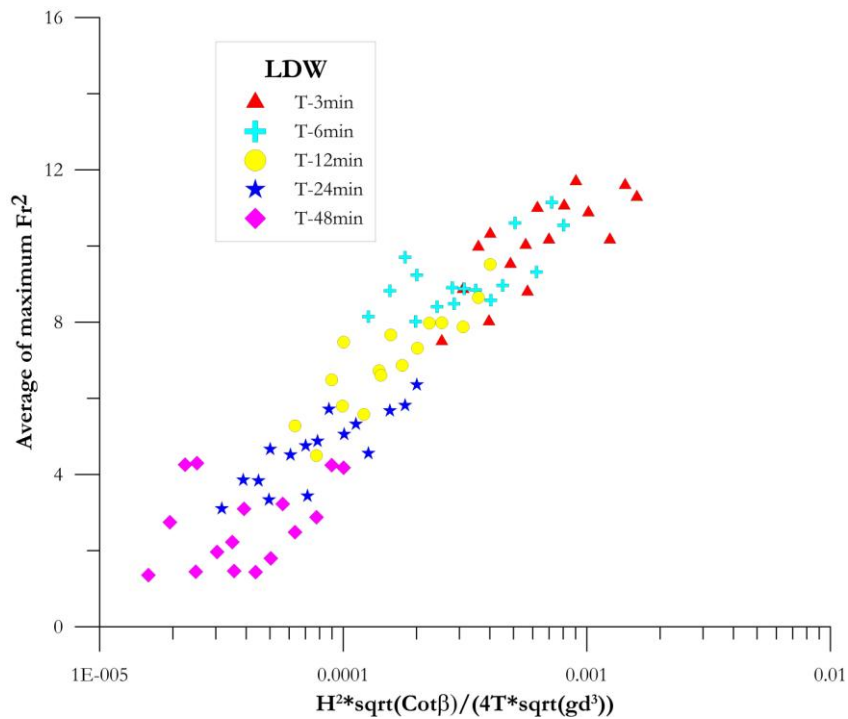


**Figure 5.18:** The distribution of empirical relationship in Eqn. [5.3] between  $\overline{Fr_{max}^2}$  and wave characteristics-bottom slope with respect to wave period for LDW

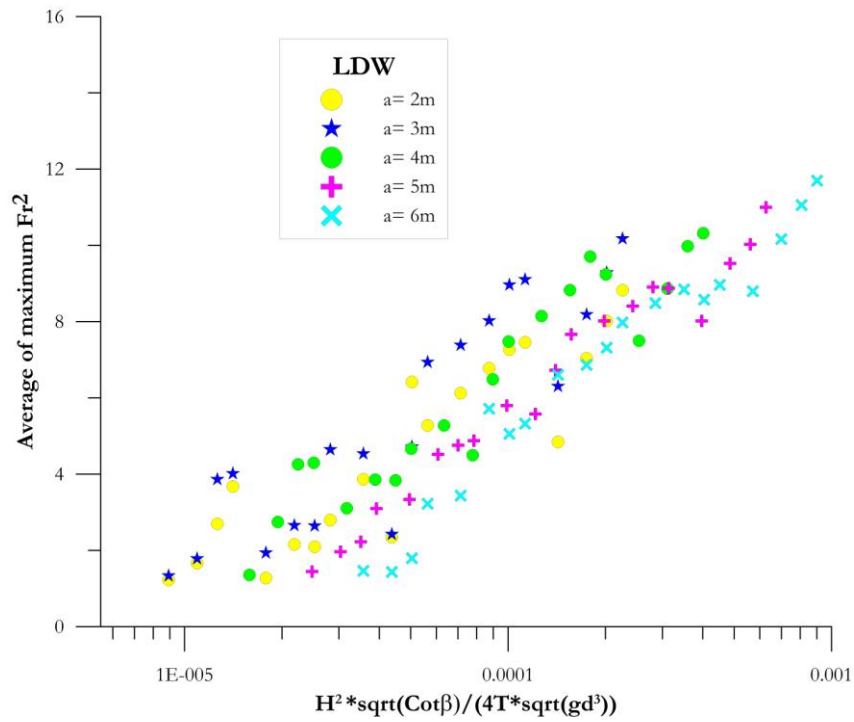


**Figure 5.19:** The distribution of empirical relationship in Eqn. [5.3] between  $\overline{Fr_{max}^2}$  and wave characteristics-bottom slope with respect to wave amplitude for LDW

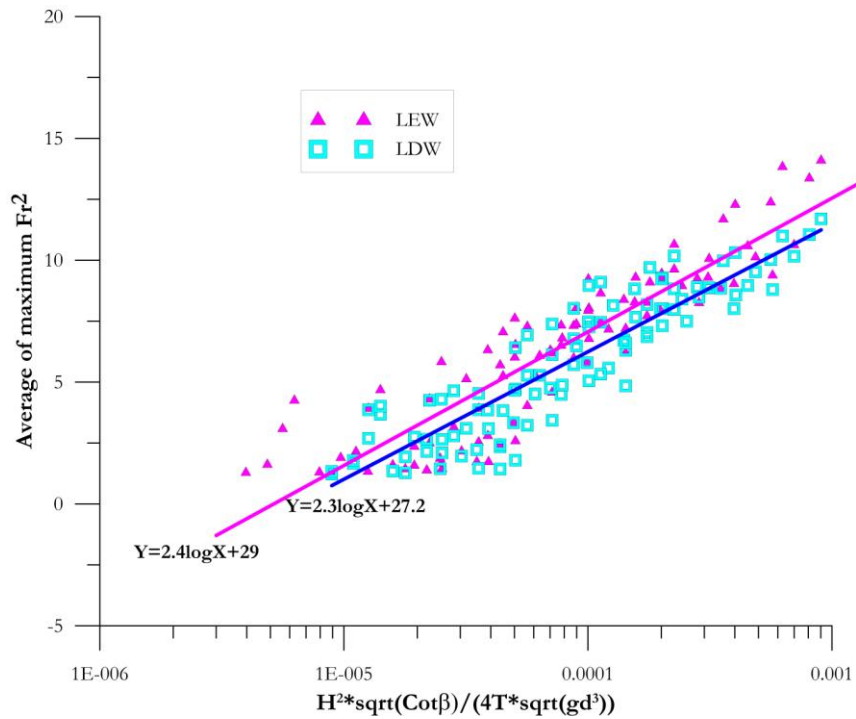


**Figure 5.20:** The distribution of empirical relationship in Eqn. [5.3] between  $\overline{Fr_{max}^2}$  and wave characteristics-bottom slope for LEW and LDW

The equations of the best fits for LEW and LDW cases in Figure 5.20 provide the average maximum of square of Froude Number in inundation zone that can be calculated for single sinusoidal waves for leading elevation and leading depression wave shapes by using the following relationships:

$$\overline{Fr_{\max}^2} = 2.4 \log \left( \frac{H^2 \sqrt{\cot \beta}}{4T \sqrt{gd_c^3}} \right) + 29 \quad \text{for LEW} \quad [5.6]$$

$$\overline{Fr_{\max}^2} = 2.3 \log \left( \frac{H^2 \sqrt{\cot \beta}}{4T \sqrt{gd_c^3}} \right) + 27 \quad \text{for LDW} \quad [5.7]$$

Since the square of wave height represents wave energy, the relations for  $\overline{Fr_{\max}^2}$  in Eqns. [5.6] and [5.7] are said to be preferable.

The average of maximum Froude number (Fr) is also calculated in the corresponding extracted inundation area. The square root of maximum  $Fr^2$  values is calculated at every grid nodes where maximum  $Fr^2$  values exceed 1. Then, the averages of maximum Fr are calculated for each wave height and period as in the previous procedure.

The average of maximum Froude number as well as maximum values of other hydrodynamic values, current velocity, flow depth and water surface elevation, are calculated with the same principal in inundation zone. The  $\overline{Fr_{\max}^2}$  values are plotted with respect to bottom slope for each wave height by changing the wave period. Besides the average values, the maximum inundation distance is calculated for each test and plotted versus bottom slope. The graphs of average hydrodynamic parameters and maximum inundation distance are given in Appendix C.

### 5.3.2. Runup Calculation for Single Sinusoidal Wave climbing on a Plain Beach

Synolakis (1986) computes the runup of solitary waves on a plane beach. He provides Runup Law that is an asymptotic result of the maximum runup of solitary waves by performing a complete (analytical, numerical and experimental) study of breaking and nonbreaking solitary waves on a beach of 1 on 20 slope. There are some analytical approaches for the solutions of static form of solitary wave at the toe of the slope (Aydin and Kanoglu, 2007; Kanoglu 2004). However, there is no relation provided for the calculation of sinusoidal wave runup climbing on a plain beach. The runup values are obtained from the analyses of LEW and LDW cases for five different wave amplitudes (2m, 3m, 4m, 5m, 6m) with five different wave periods (3min, 6min, 12min, 24min, 48min) on four different wave slopes (1/10, 1/15, 1/20, 1/25). A correlation is provided for the normalized maximum runup of sinusoidal waves climbing up different sloped beaches and given in the following:

$$\frac{Ru}{d_c} = C_n \left( \frac{H}{d_c} \right)^2 \frac{\sqrt{\cot \beta}}{4T \sqrt{(g/d_c)}} \quad [5.8]$$

Actually, the relation in Eqn [5.8] is directly the same with the one in Eqn [5.3]. However, the notation including the power of (H/d) is selected to be relevant with the Runup Law for solitary waves. The normalized maximum runup of sinusoidal waves climbing up different sloped beaches with respect to the wave amplitude are plotted for LEW and LDW in Figures 5.21 and 5.22, respectively.

Different from the Runup Law for solitary waves, the relation for the runup of sinusoidal waves on a plain beach includes the wave period. Figures 5.23 and 5.24 show the normalized maximum runup of sinusoidal waves climbing up different sloped beaches with respect to different wave periods for LEW and LDW, respectively. The effect of wave period on the runup height is observed clearly that when the wave period gets shorter the runup height increases for both LEW and LDW cases.

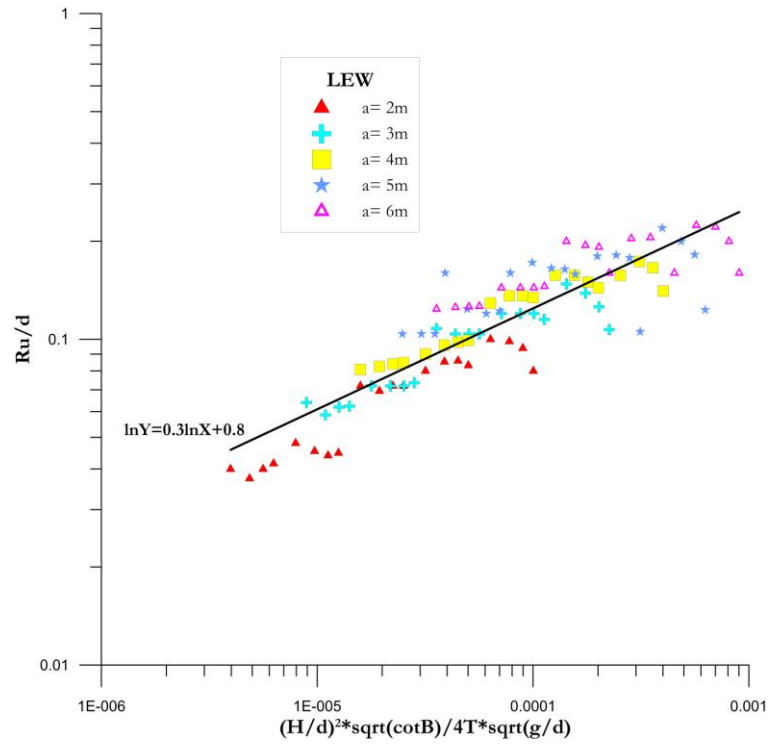


**Figure 5.21:** Normalized maximum runup of sinusoidal waves climbing up different sloped beaches with respect to the wave amplitude for LEW

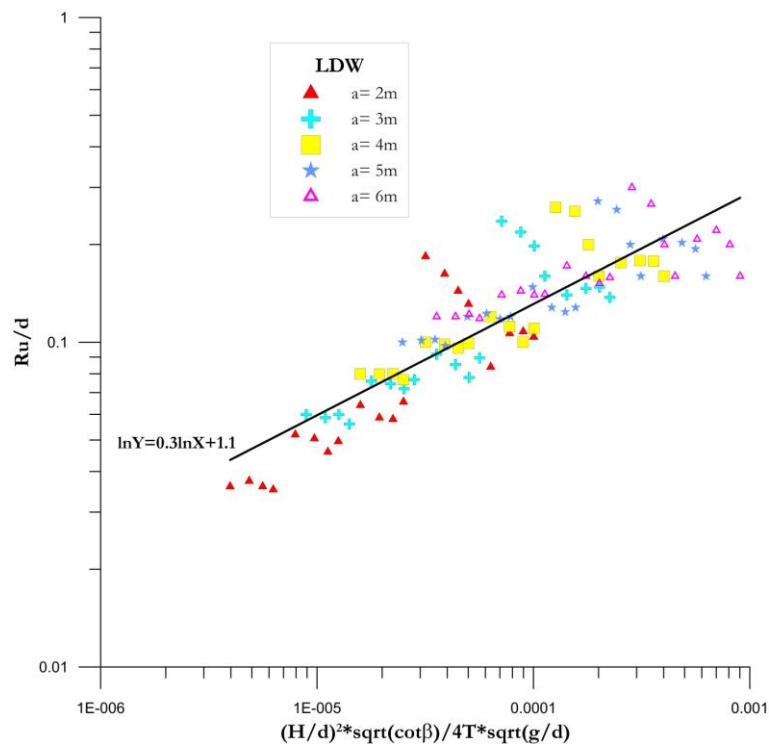


**Figure 5.22:** Normalized maximum runup of sinusoidal waves climbing up different sloped beaches with respect to the wave amplitude for LDW

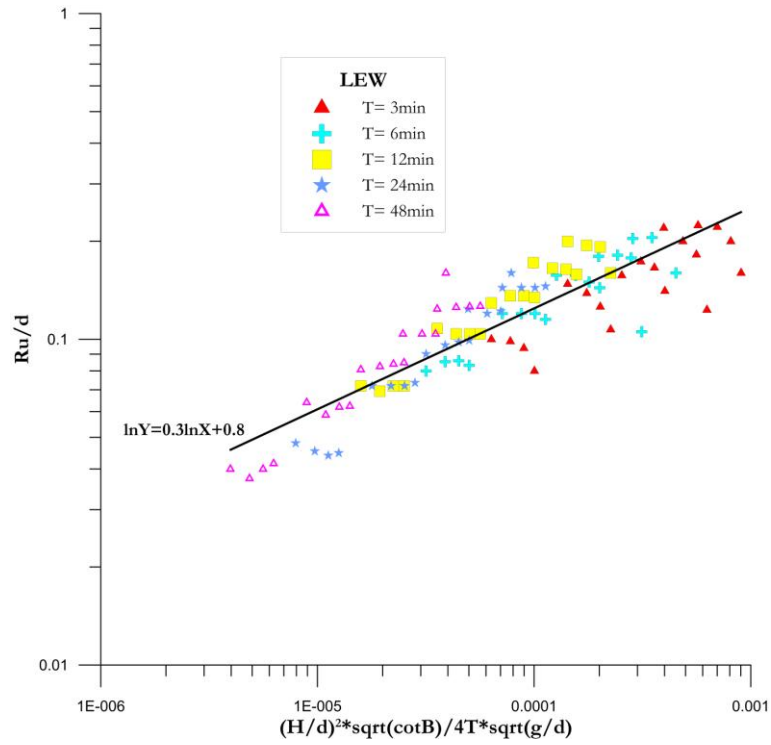


**Figure 5.23:** Normalized maximum runup of sinusoidal waves climbing up different sloped beaches with respect to the wave period for LEW

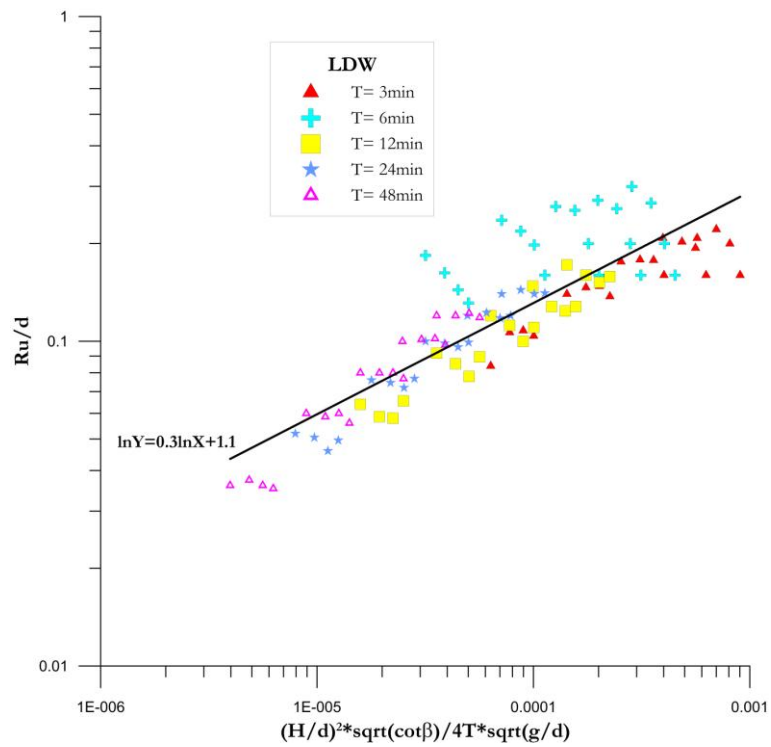


**Figure 5.24:** Normalized maximum runup of sinusoidal waves climbing up different sloped beaches with respect to the wave period for LDW

According to the results of analyses, the relations for the calculation of maximum runup of sinusoidal waves climbing on a plain beach are provided as in the following for LEW and LDW, respectively:

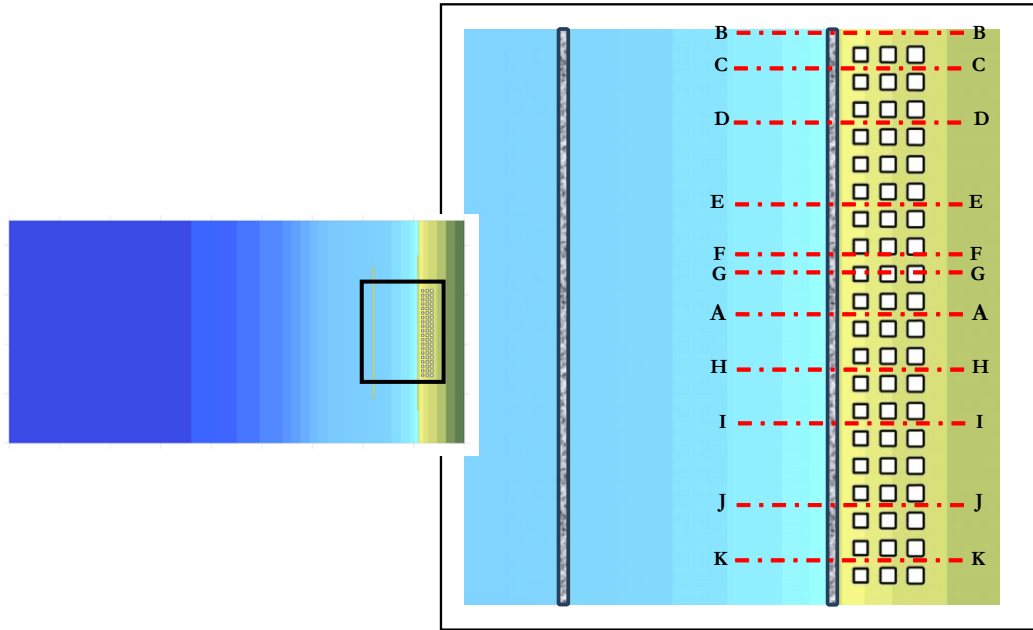
$$\ln \frac{R_H}{d_c} = 0.3 * \ln \left[ \left( \frac{H}{d_c} \right)^2 \frac{\sqrt{\cot \beta}}{4T \sqrt{(g/d_c)}} \right] + 0.8 \quad \text{for LEW} \quad [5.9]$$

$$\ln \frac{R_H}{d_c} = 0.3 * \ln \left[ \left( \frac{H}{d_c} \right)^2 \frac{\sqrt{\cot \beta}}{4T \sqrt{(g/d_c)}} \right] + 1.1 \quad \text{for LDW} \quad [5.10]$$

As seen from Figures [5.21] to [5.24] and Eqns. [5.9] and [5.10] that the maximum normalized runup height for LEW and LDW are quite similar. Different from the Runup Law for solitary waves, the effect of wave period is included in the relation for maximum normalized runup for sinusoidal waves.

#### **5.4. Investigation of Hydrodynamic Parameters for Different Basin Layout**

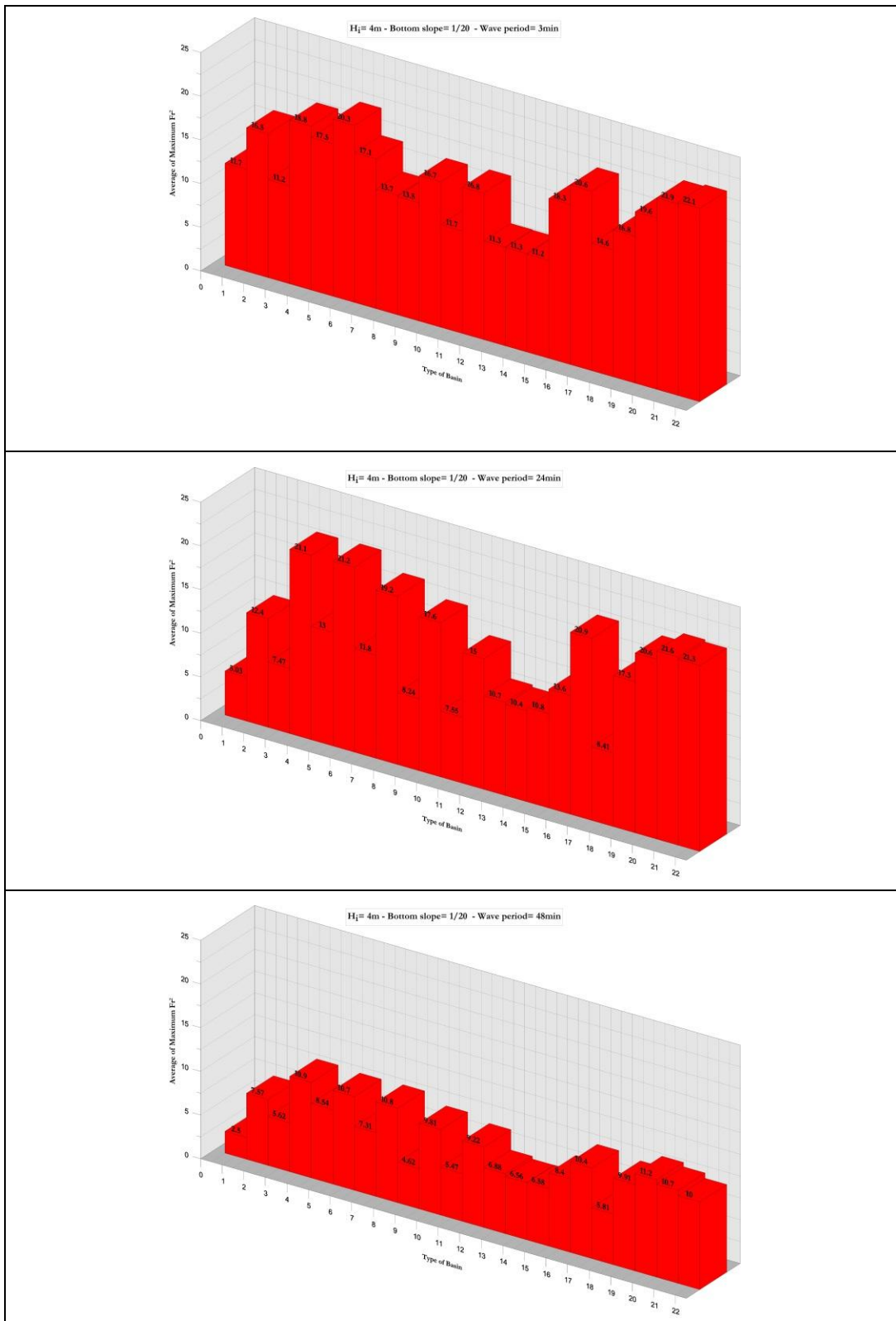
This section gives the results of analyses for the determination of hydrodynamic parameters in inundation zone on different layout of basins as listed in Table 5.2 and shown in Figure 5.2. The change of hydrodynamic parameters is investigated both qualitatively and quantitatively. The distribution of parameters in inundation zone reflects the *qualitative* determination while the values of parameters along selected cross-sections give the *quantitative* investigation. The variations of hydrodynamic parameters in inundation zone are found by investigating their values along the cross-sections as shown in the residential area extracted from the whole bathymetry in Figure 5.25. The sections are selected mostly at the corridors between the buildings. One section is taken at the outside of residential area to observe the values occurring due to the waves in lateral direction. In addition, one section that is to pass through one column of the buildings is determined to compare the values of parameters in close or far allocation layouts.



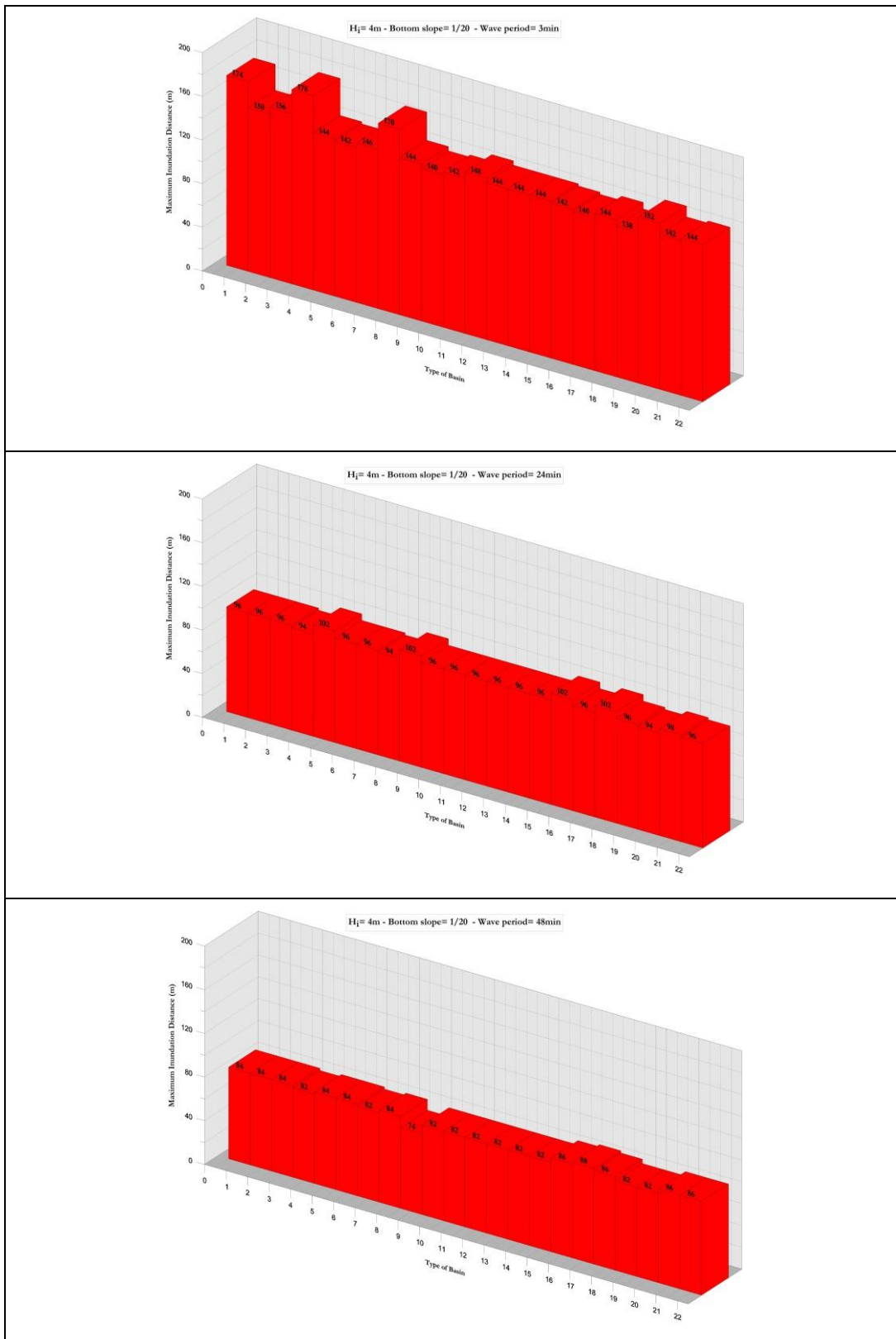
**Figure 5.25:** The cross-sections passing through the openings between the buildings on the top view of extracted bathymetry

The analyses in each basin are performed by inputting single sinusoidal wave of 4m wave height with the wave periods of 3min, 24min and 48min propagating on the bottom slope of 1/20. The maximum and average maximum values of hydrodynamic parameters are calculated in each case. The comparison of average maximum  $Fr^2$  values calculated for three different wave periods in each test basin are shown in Figure 5.26. The comparison of  $\overline{Fr_{max}^2}$  values reveal that the wave motion shows uniformity when the wave period gets longer and the wave behavior does not show a significant variance according the protection status of the residential area.

Figure 5.27 demonstrates the comparison of maximum inundation distances observed in each test basin with the wave periods of 3min, 24min and 48min. The values indicate that the maximum inundated point does not vary significantly for longer periods. In addition, when the waves can pass over any coastal protection structures, they can climb up the land and flow through the same distances inland.



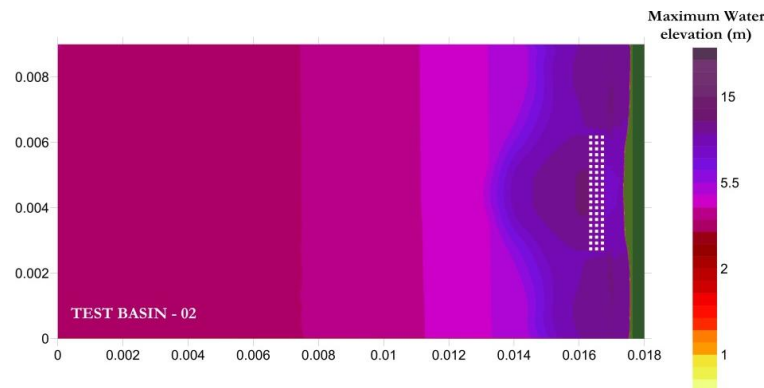
**Figure 5.26:** The values of average maximum  $Fr^2$  observed in each type of basins for the wave period of 3min, 24min and 48min



**Figure 5.27:** The values of maximum inundation distance observed in each type of basins for the wave period of 3min, 24min and 48min

#### 5.4.1. Spatial Distribution of Hydrodynamic Parameters

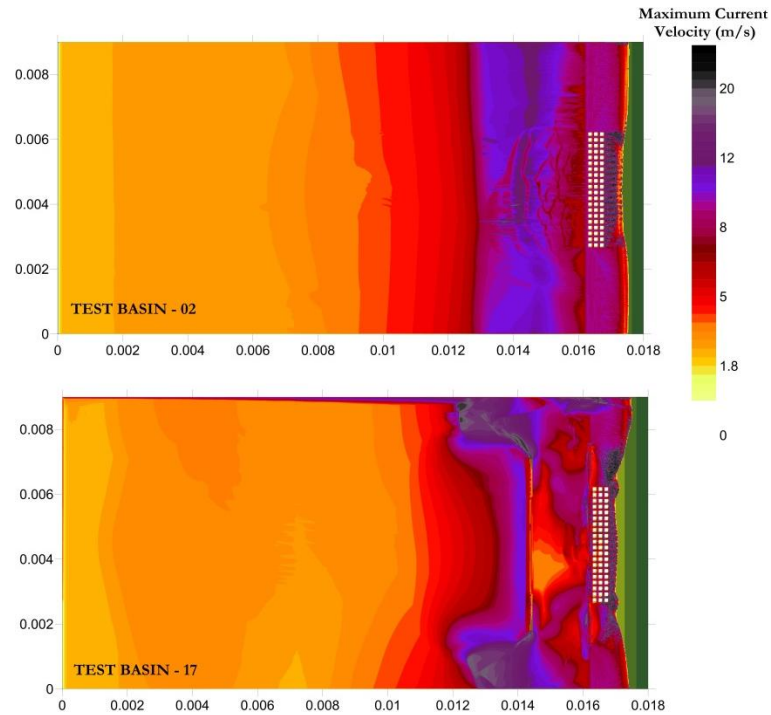
Regarding the results of simulations and the general wave characteristics of tsunamis, the changes of hydrodynamic parameters are discussed for the inundation of waves within a 48minute period. The distribution of parameters is first investigated for the protected and unprotected beaches with residential areas. Basin-02 is the model of a coastal residential area without protection and Basin-17 reflects a fully-protected beach including seawall and offshore breakwater. Figure 5.28 displays the distribution of maximum water elevations within 3min wave periods in each basin. The distributions show that, except for small irregularities at the edges, there is a uniform wave propagation and inundation for both basins. The water surface elevations show a symmetric pattern with the reflections from the buildings and coastal protection structures.



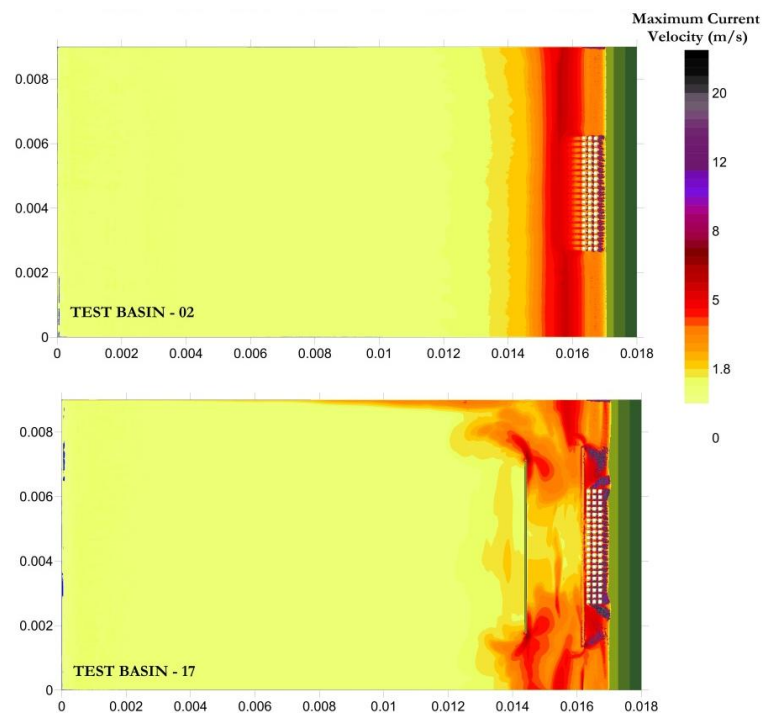
**Figure 5.28:** The distribution of maximum water elevations for the waves propagating on the 1/20 slope with the wave amplitude of 4m and wave period of 3min

The distribution of water surface elevations for the wave periods of 24min and 48 min are also investigated. The results show that the elevations reduce when the wave period gets longer. The uniformity of wave motion is more significant when longer period waves inundate the land.

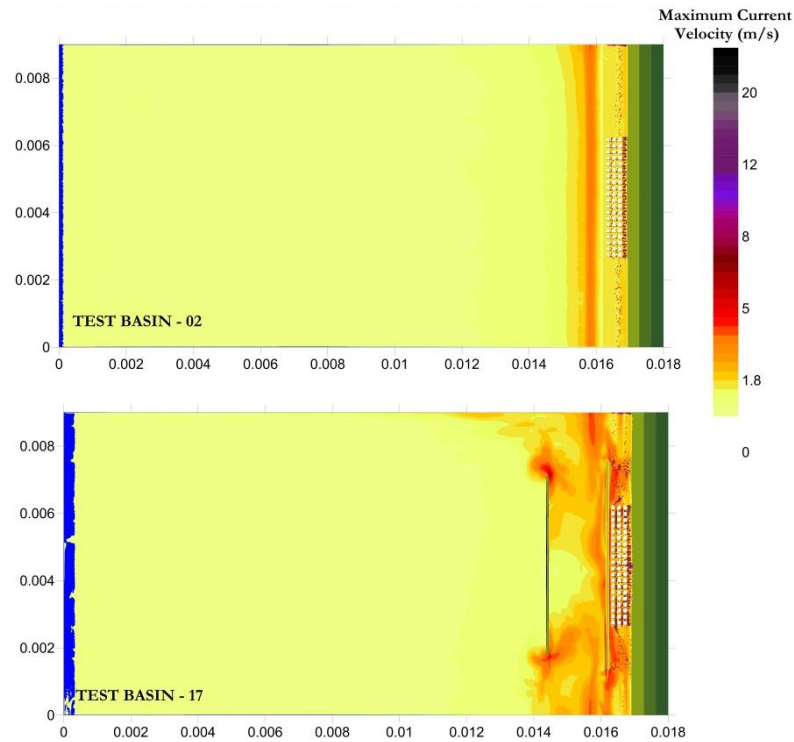
The distribution of maximum current velocities observed during the inundation of waves with wave periods of 3min, 24min and 48min are given in Figures 5.29, 5.30 and 5.31, respectively. The current velocities show a descending attribute when the wave period gets longer. The results for Basin-17 indicate that relatively high values



**Figure 5.29:** The distribution of maximum current velocities for the waves propagating on the 1/20 slope with the wave amplitude of 4m and wave period of 3min



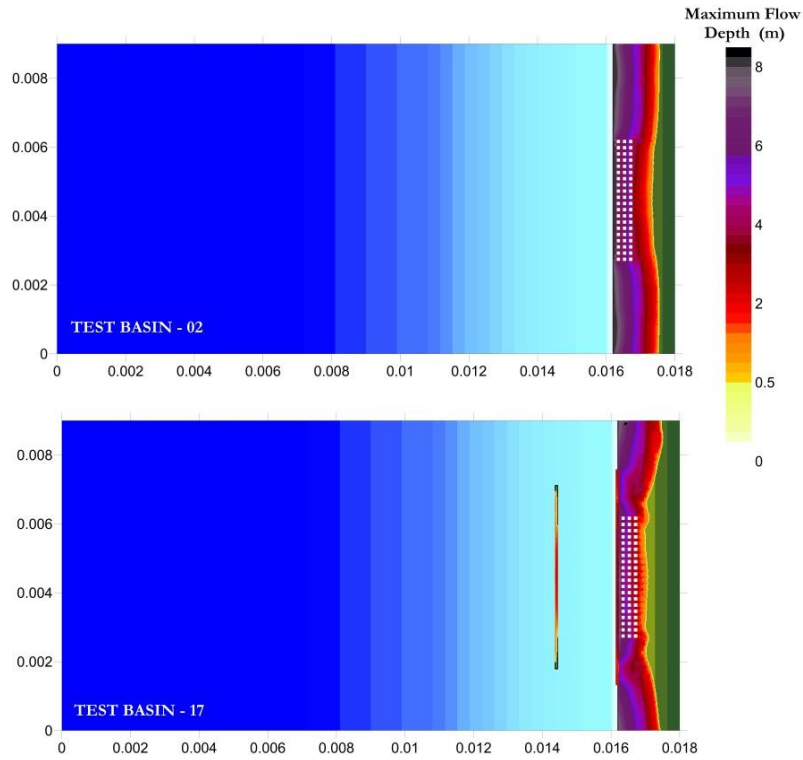
**Figure 5.30:** The distribution of maximum current velocities for the waves propagating on the 1/20 slope with the wave amplitude of 4m and wave period of 24min



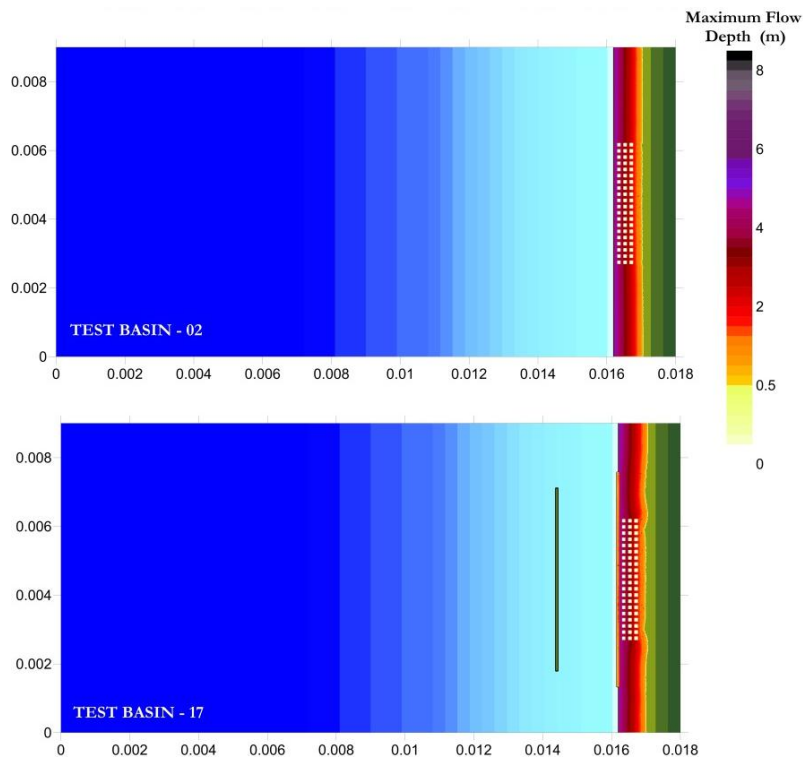
**Figure 5.31:** The distribution of maximum current velocities for the waves propagating on the 1/20 slope with the wave amplitude of 4m and wave period of 48min

of currents occur at the edges of offshore breakwater and seawall due to the reflection of waves and the instantaneous rapid motion in forward and backward directions. The distributions also reveal that higher current velocities are observed at the backside of residential areas due to the wave motion escaping around the edges of seawall and inundating in lateral direction.

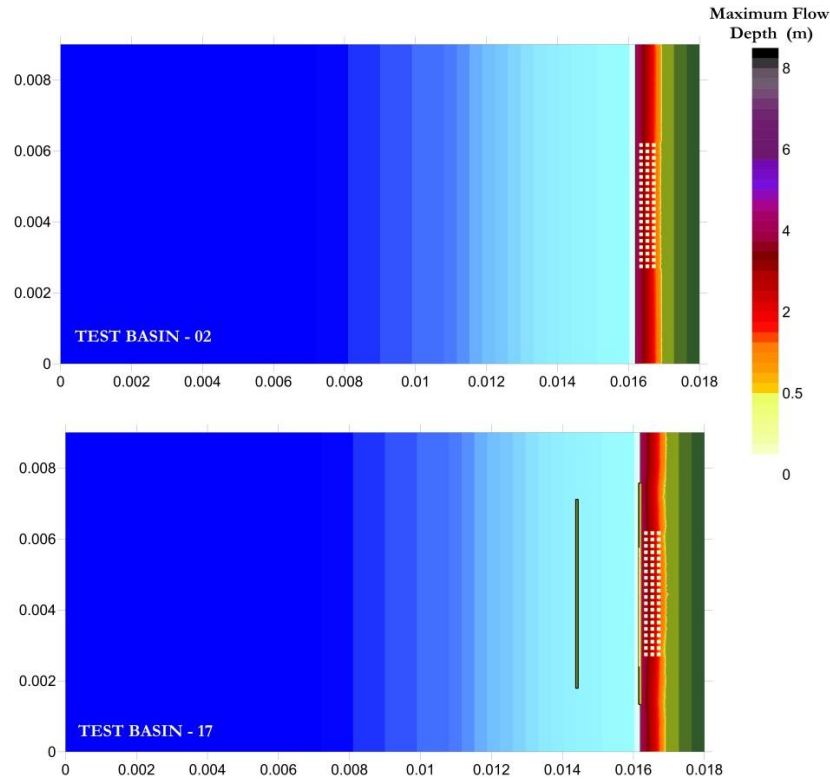
The distribution of maximum flow depths observed during the inundation of waves with wave periods of 3min, 24min and 48min are given in Figures 5.32, 5.33 and 5.34, respectively. The flow depth reduces when the wave period gets longer. Significant uniformity of maximum inundation distances is observed through the flow depth distributions. The figures state that when the tsunami inundation occurs with longer periods, the coastal structures cannot show the required performance for protection of residential areas. If the waves can exceed the height of the structure and overflow, they can inundate up to the maximum point without any obstruction.



**Figure 5.32:** The distribution of maximum flow depths for the waves propagating on the 1/20 slope with the wave amplitude of 4m and wave period of 3min

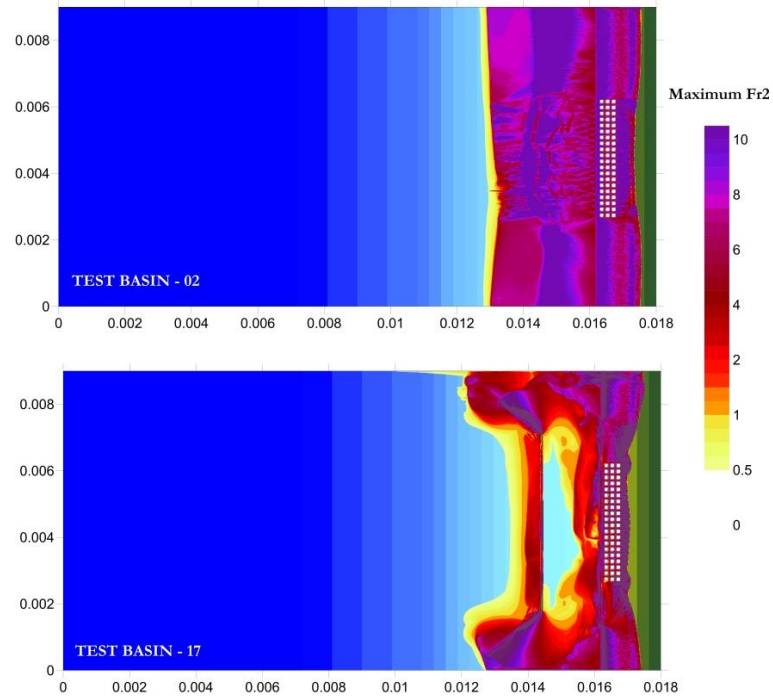


**Figure 5.33:** The distribution of maximum flow depths for the waves propagating on the 1/20 slope with the wave amplitude of 4m and wave period of 24min

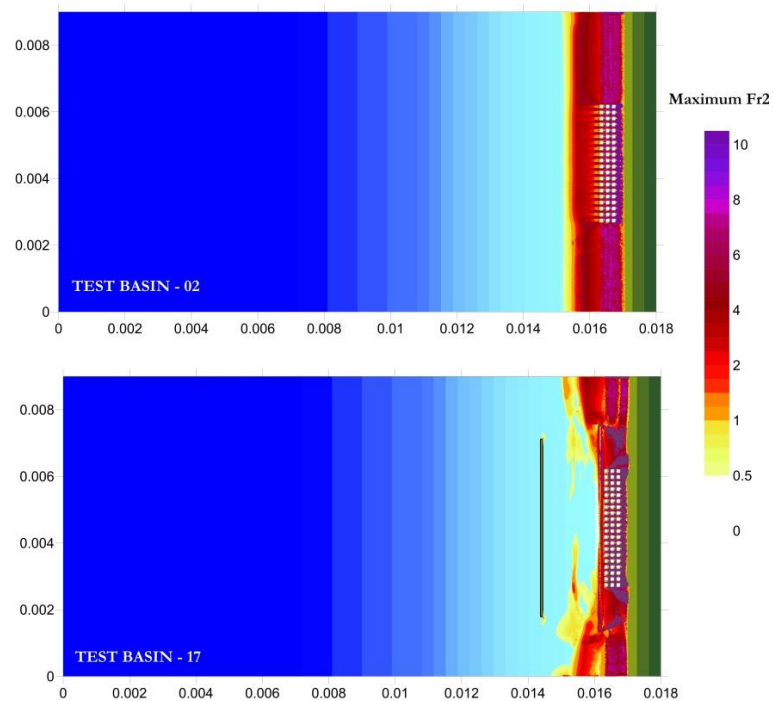


**Figure 5.34:** The distribution of maximum flow depths for the waves propagating on the 1/20 slope with the wave amplitude of 4m and wave period of 48min

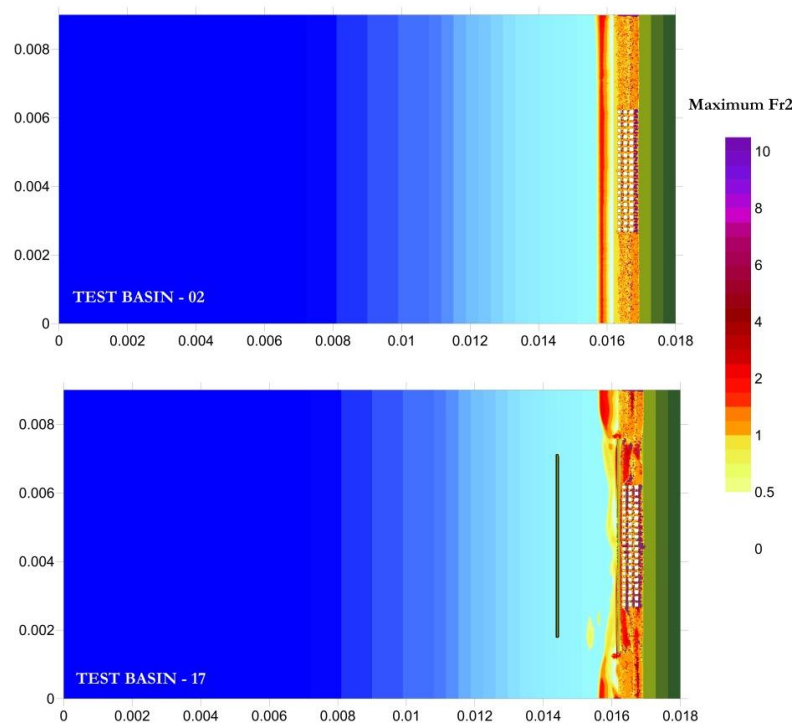
The distribution of maximum  $Fr^2$  observed during the inundation of waves with wave periods of 3min, 24min and 48min are given in Figures 5.35, 5.36 and 5.37, respectively. Since the governing parameter of this study is the square of Froude number in inundation zone, the distribution of this parameter in inundation zone yield essential information about the performance of coastal protection structures and effect of basin layout on the level of tsunami damage. The distributive results reveal that the level of tsunami damage shows uniformity when the wave period gets longer. The comparison of wave forces for protected and unprotected beaches for 48min wave period in Figure 5.35 states that the existence of seawall cannot prevent the tsunami inundation and cannot reduce wave forces. On the contrary, high values of  $Fr_{max}^2$  are observed at the locations of residential area close to the edges of seawall. Furthermore, the backside of buildings is exposed to high values of  $Fr_{max}^2$  due to the wave motion in lateral direction due to the blocking effect of seawall.



**Figure 5.35:** The distribution of maximum Froude Number square ( $Fr_{max}^2$ ) for the waves propagating on the 1/20 slope with the wave amplitude of 4m and wave period of 3min



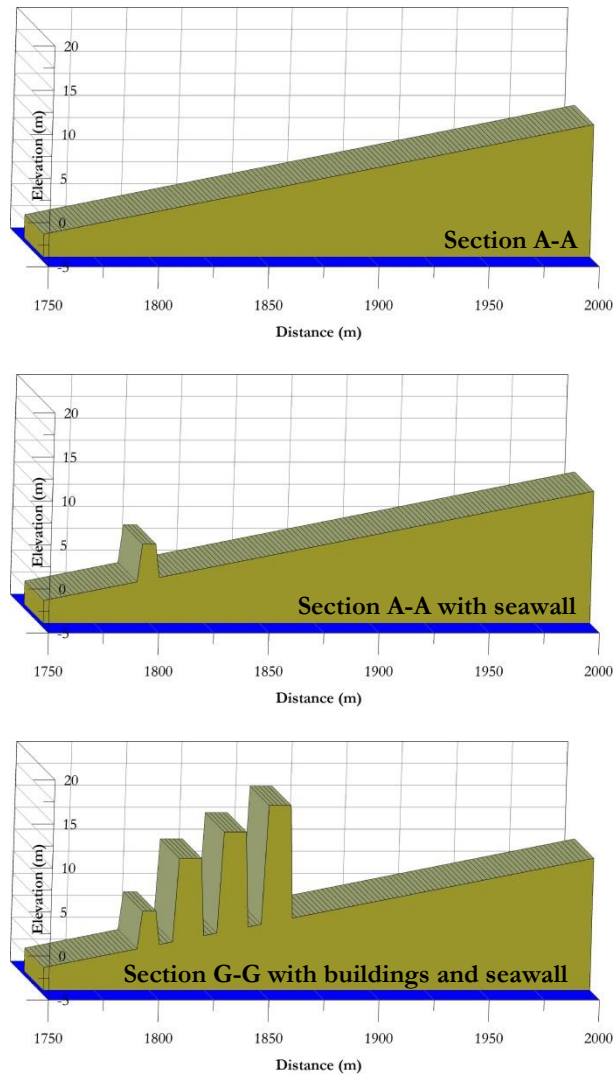
**Figure 5.36:** The distribution of maximum Froude Number square ( $Fr_{max}^2$ ) for the waves propagating on the 1/20 slope with the wave amplitude of 4m and wave period of 24min



**Figure 5.37:** The distribution of maximum Froude Number square ( $Fr_{max}^2$ ) for the waves propagating on the 1/20 slope with the wave amplitude of 4m and wave period of 48min

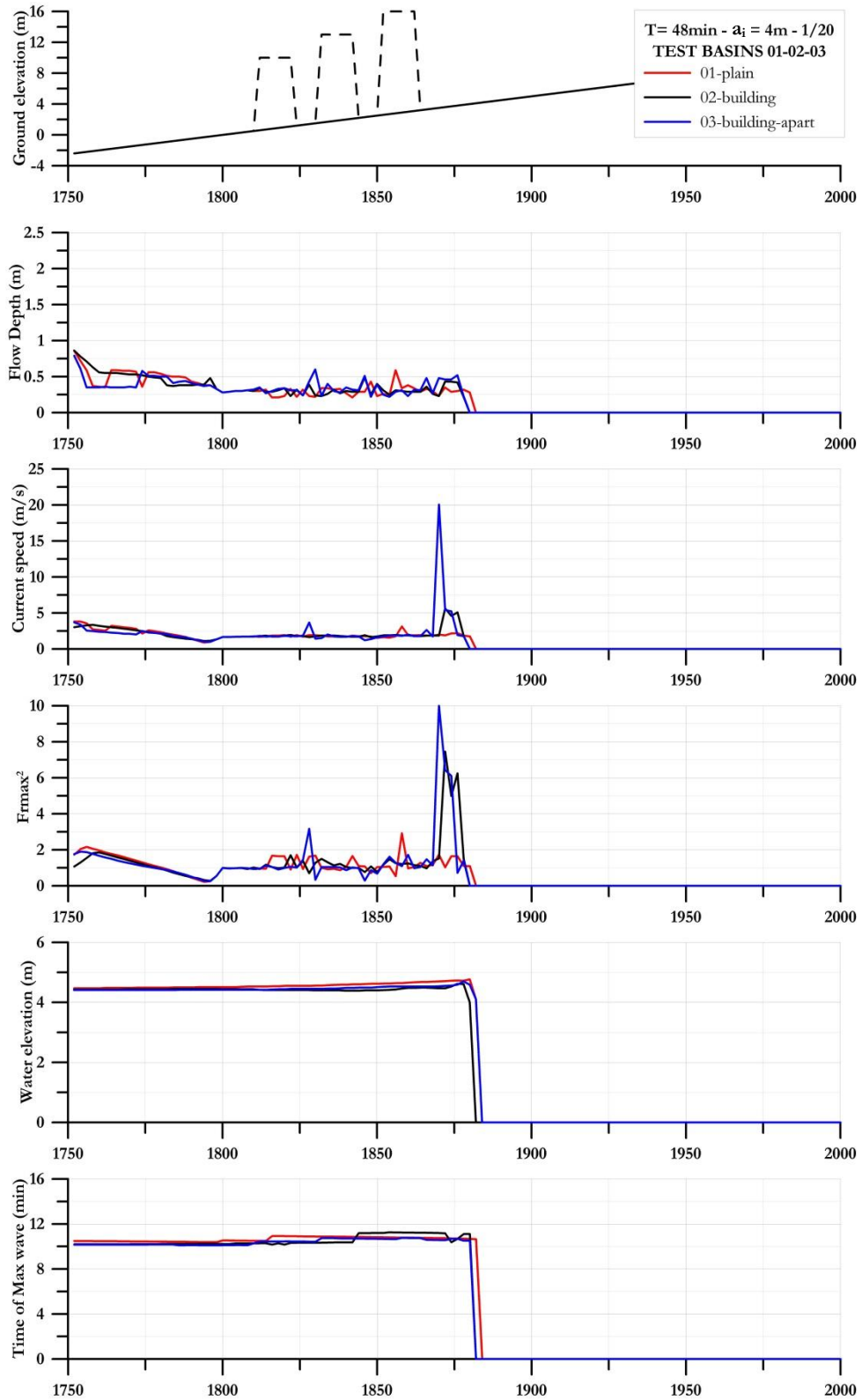
#### 5.4.2. Change of Hydrodynamic Parameters along the Cross-sections

This section covers the variations of hydrodynamic parameters in inundation zone on different test basins in order to observe the effect of layout on wave behavior and to discuss the performance of coastal protection structure under the selected wave conditions. The variations are plotted through Section A-A in the middle of basin that may be more protected or more vulnerable depending on the existence of coastal protection structures. The effects on hydrodynamic parameters are classified and the test basins are selected accordingly. Figure 5.38 shows the 3D view of cross-section A-A with and without seawall. This section represents all other sections except Section G-G since they are all passing through the corridors between the buildings. The figure also shows Section G-G including the buildings and seawall.



**Figure 5.38:** The three-dimensional view of Sections A-A and G-G

Figure 5.39 shows the sectional variation of parameters on three different states of the beach: plain without any buildings, residential area with close layout and with distant layout. This figure depicts the effect of distance between the locations of buildings. The maximum flow depths, water elevations and the time of maximum wave are similar. However,  $Fr_{max}^2$  increases at the backside of the buildings when the tsunami flows along a wider channel between the buildings. The reason is that wider openings allow the water to penetrate more and cause motion in lateral direction at the inundation limit.



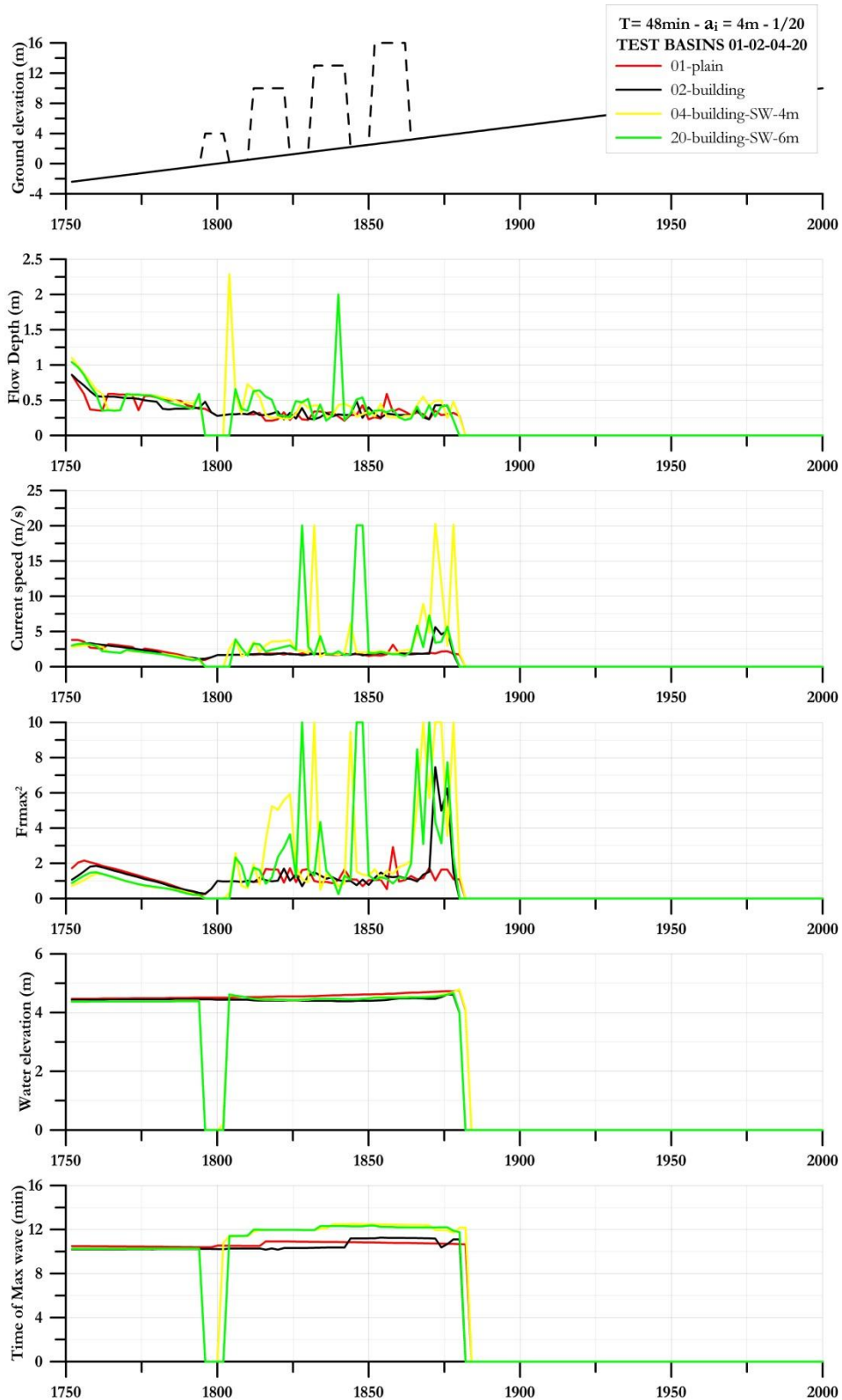
**Figure 5.39:** The variation of hydrodynamic parameters in inundation zone through the Section A-A for the test basins 01, 02 and 03 with the simulation of waves in 4m wave amplitude with 48min period on 1/20 slope

Figure 5.40 shows the effect of seawall on hydrodynamic parameters. As seen from the values of parameters at the location of seawall, the waves cannot overflow the structure. However, high values of current velocities and  $Fr_{max}^2$  occur near the building fronts instantaneously in case of seawall. These values are not observed when there is no protection along the coastline. The reason is that the water flow is blocked by the seawall and directed to its edges. Therefore, the inundation occurs with a concentrated energy of waves and current velocity increases in lateral direction. The benefit of having seawall along the coastline is that the maximum water amplitudes occur 2 to 3 minutes away.

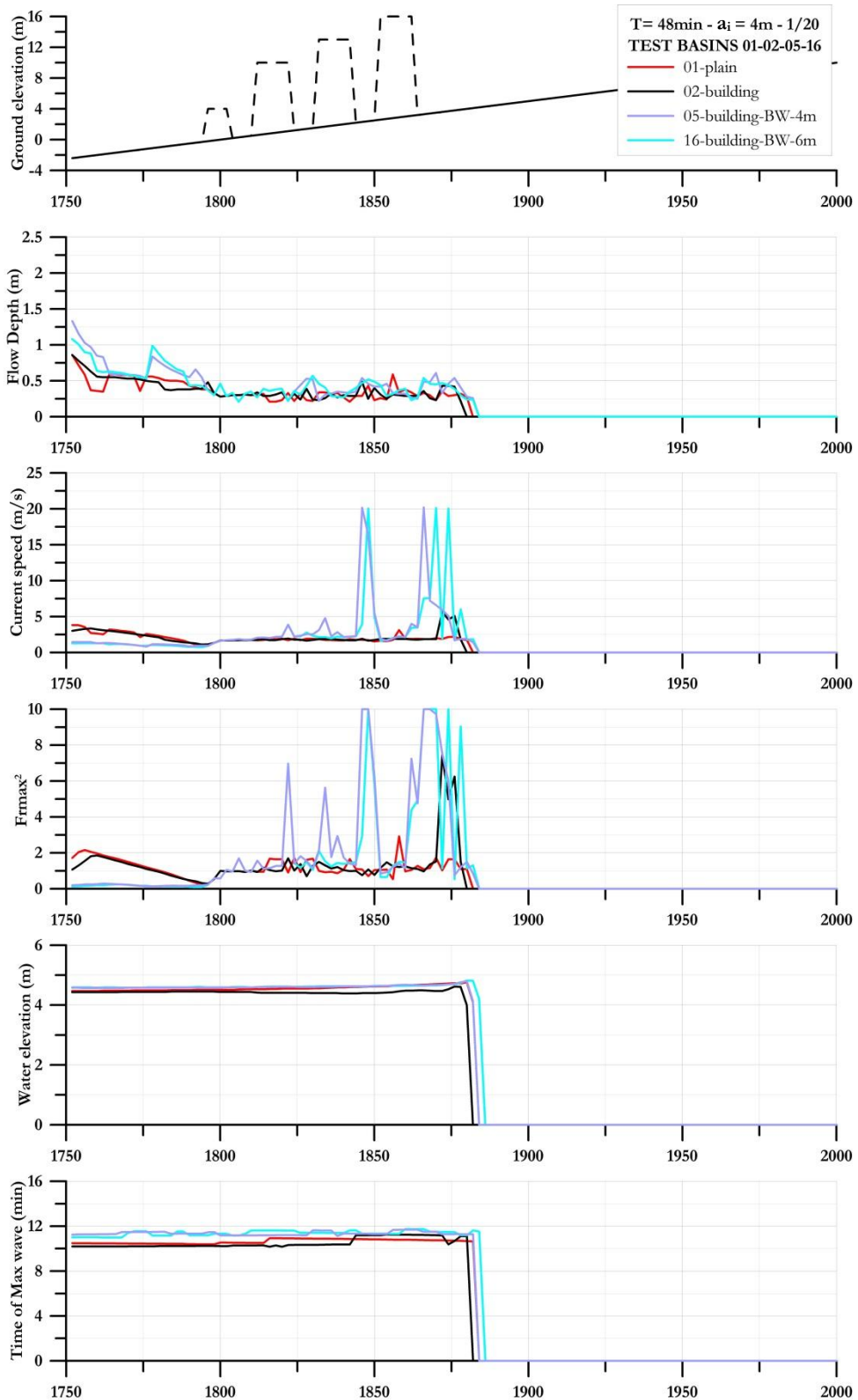
Like in the seawall case, the similar wave behavior is observed in residential area for the coastal protection with offshore breakwater. Figure 5.41 shows the variation of parameters for plain beach, for unprotected residential areas and for protected areas with offshore breakwaters in 4m and 6m crest height. The sectional values reveal that the existence of offshore breakwater does not prevent tsunami inundation even with high crest elevations. Flow depths are quite similar; however, the wave motion in lateral direction is observed as in seawall case. The animation of tsunami inundation during the simulation time explicitly shows this phenomenon. The higher current velocities instantaneously result in high values of  $Fr_{max}^2$  in some locations.

Figure 5.42 shows the effect of crest elevation on the performance of coastal protection. High values of currents and  $Fr_{max}^2$  occurs in some locations, instantaneously. However, the sectional values and the animations of whole wave motion through the simulation time reveal that the crest elevation of offshore breakwater and seawall has no effect on decreasing the  $Fr_{max}^2$  values since the waves blocked by the structure are directed to its edges and climb up to the land in lateral direction with instantaneous high current velocities. The only way to avoid this situation is to completely prevent the structures from the overflow of tsunami. The results of analyses with lengthwise seawall protection will be given in further sections.

Figure 5.43 shows the performance of coastal protection structures if the buildings are placed in distant layout. The results show that there is no significant difference between the cases of distant and close layouts for protected areas since the current velocities in lateral direction are effective and increase the values of  $Fr_{max}^2$ .



**Figure 5.40:** The variation of hydrodynamic parameters in inundation zone through the Section A-A for the test basins 01, 02, 04 and 20 with the simulation of waves in 4m wave amplitude with 48min period on 1/20 slope



**Figure 5.41:** The variation of hydrodynamic parameters in inundation zone through the Section A-A for the test basins 01, 02, 05 and 16 with the simulation of waves in 4m wave amplitude with 48min period on 1/20 slope

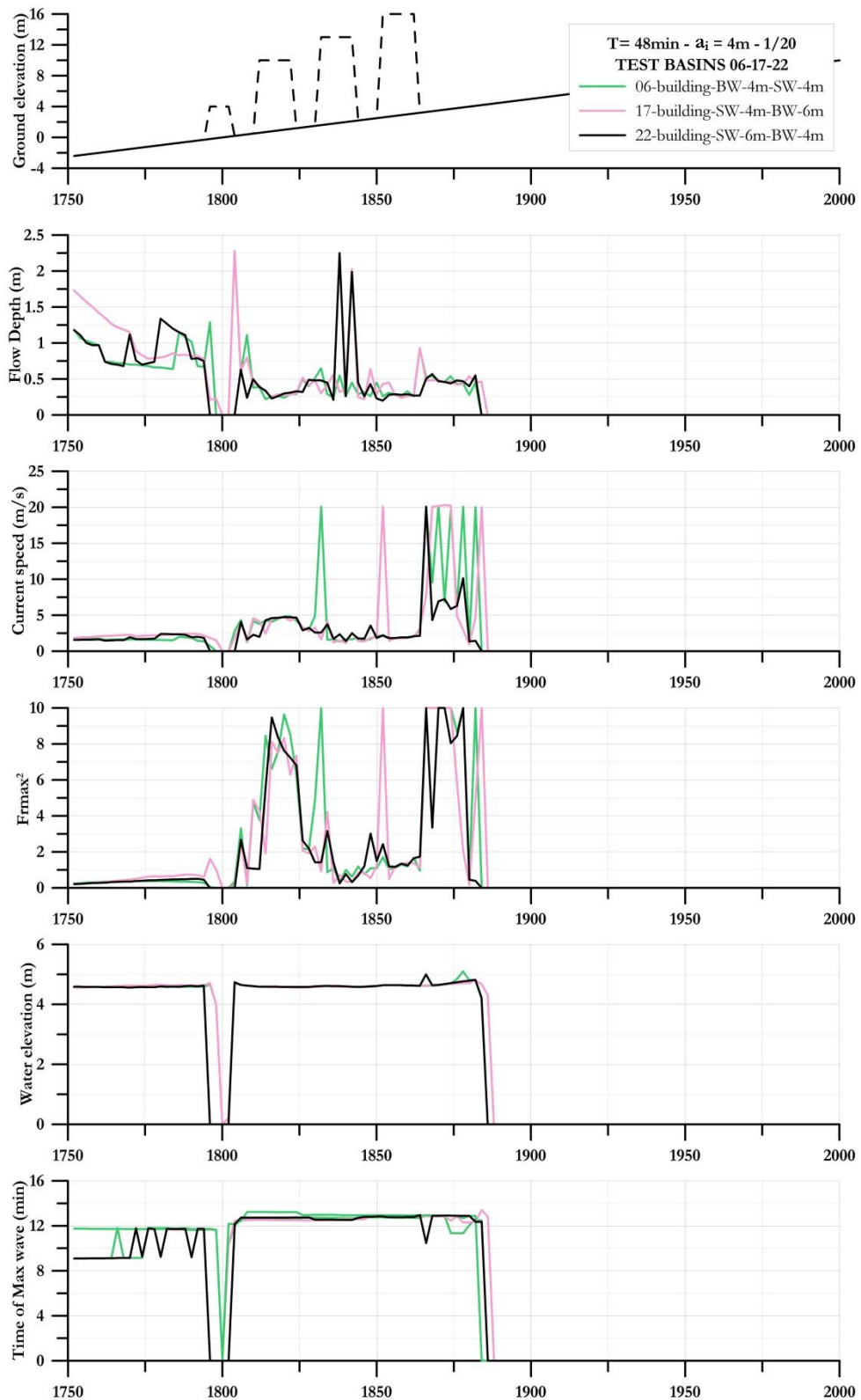


**Figure 5.42:** The variation of hydrodynamic parameters in inundation zone through the Section A-A for the test basins 06, 17 and 22 with the simulation of waves in 4m wave amplitude with 48min period on 1/20 slope

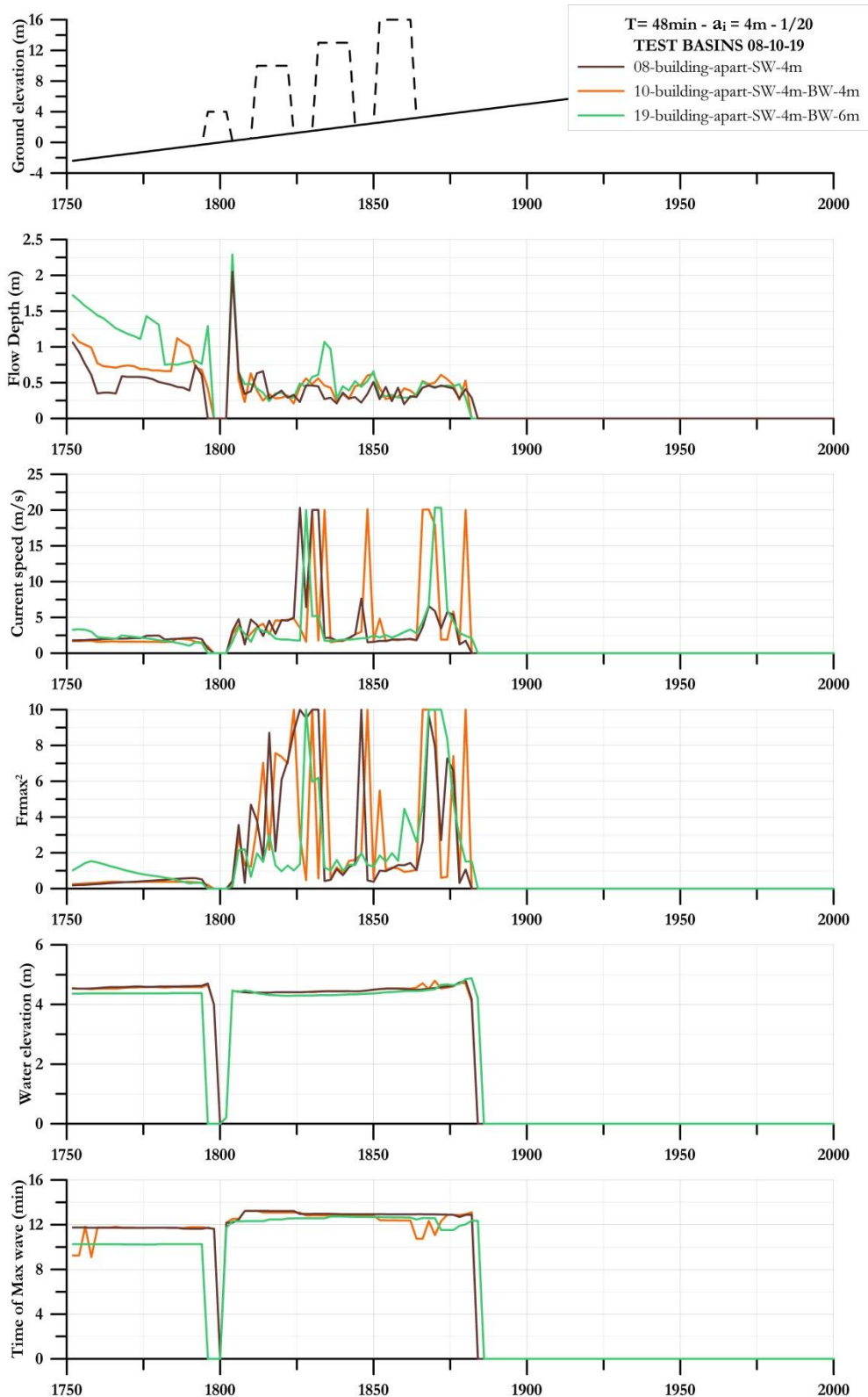


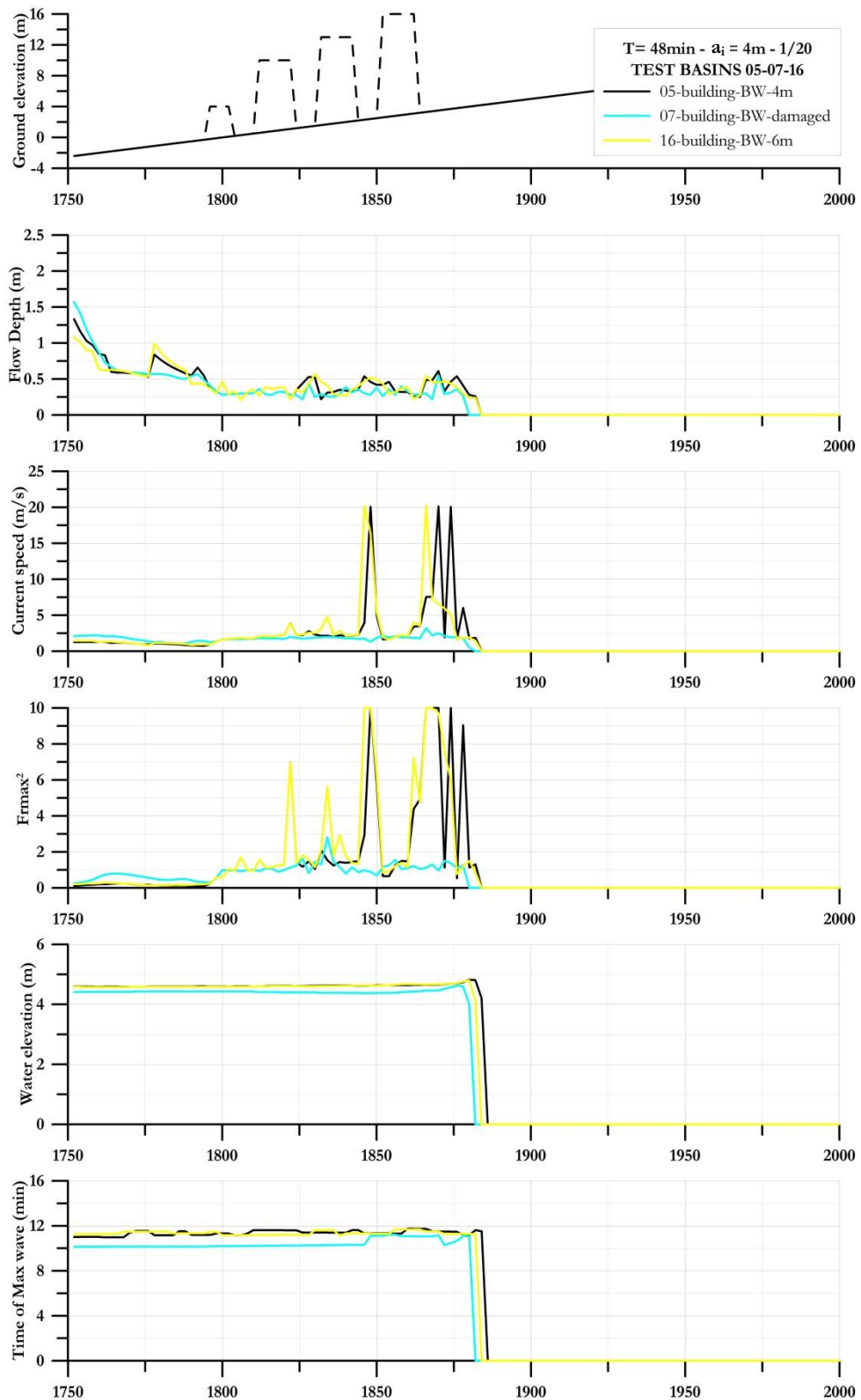
**Figure 5.43:** The variation of hydrodynamic parameters in inundation zone through the Section A-A for the test basins 08, 10 and 19 with the simulation of waves in 4m wave amplitude with 48min period on 1/20 slope

Figures 5.44 and 5.45 show the comparative results of the performance of coastal protection in case an offshore breakwater or a seawall exists but have been damaged during the tsunami attack. The results reveal that higher  $Fr_{max}^2$  values are observed when the beach is protected both with seawall and offshore breakwater. The results of this comparison again support the statement that the existence of coastal protection structures causes rapidly increasing values of currents if the tsunami inundation cannot be fully blocked by the structures.

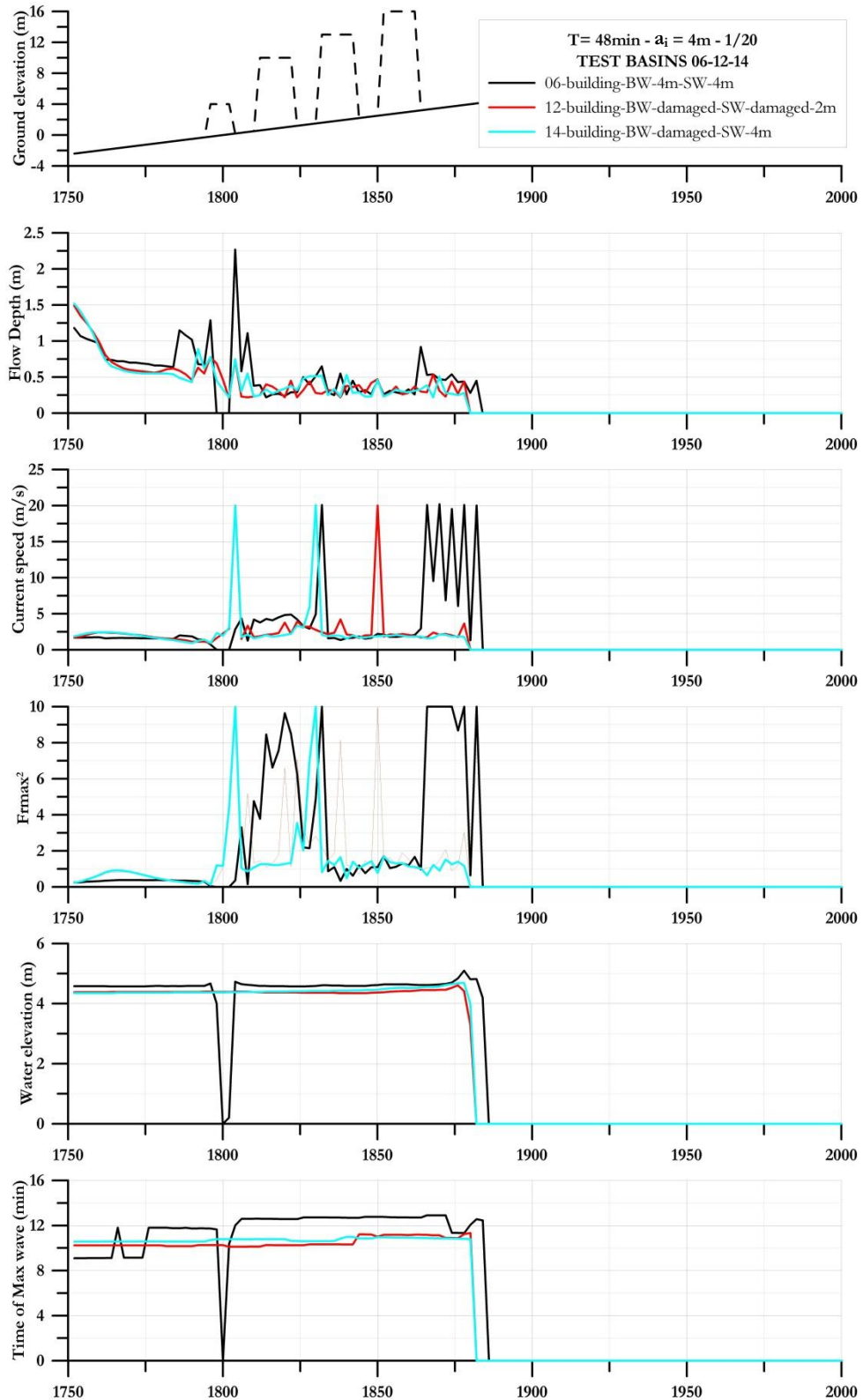
In case of coastal protection with seawall and offshore breakwater, the current velocities evolving in lateral direction become significant. Therefore, the sectional variations of hydrodynamic parameters are investigated through another cross-section. Section D-D is selected as another cross-section to observe the effect wave motion in lateral direction. As mentioned in Section 5.4.1 and shown in Figures 5.28 to 5.37, the distribution of hydrodynamic parameters is symmetric in wave direction. Therefore, the values through Section D-D will represent the parameters through Section J-J.

Figure 5.46 gives the variation of hydrodynamic parameters along Section D-D. As seen from the yellow and blue lines representing coastal protection with seawall only and with seawall and breakwater together, the values of maximum currents and  $Fr_{max}^2$  increase in case of blocking the waves and directing the flow through the edges of structures. These results support the inference introduced for the performance of coastal protection structures.

The variations of hydrodynamic parameters are observed and discussed along all cross-sections given in Figure 5.16. Among those, the variations of governing parameter  $Fr_{max}^2$  are plotted along sections in various types of test basins. Figure 5.47 shows the variation of  $Fr_{max}^2$  along Sections A-A, B-B and E-E for the test basins 01, 02, 03 and 04 in order to observe and discuss the level of exposing wave force depending on the location with respect to the middle of basin. The results in Figure 5.47 show that there is uniformity in tsunami inundation on plain beach since the distribution of  $Fr_{max}^2$  for selected sections are similar. The plot along Section B-B for test basin 04 supports the increase of hydrodynamic parameters at the locations close to the edges of seawall due to the increase of current velocities in lateral direction.



**Figure 5.44:** The variation of hydrodynamic parameters in inundation zone through the Section A-A for the test basins 05, 07 and 16 with the simulation of waves in 4m wave amplitude with 48min period on 1/20 slope



**Figure 5.45:** The variation of hydrodynamic parameters in inundation zone through the Section A-A for the test basins 06, 12 and 14 with the simulation of waves in 4m wave amplitude with 48min period on 1/20 slope

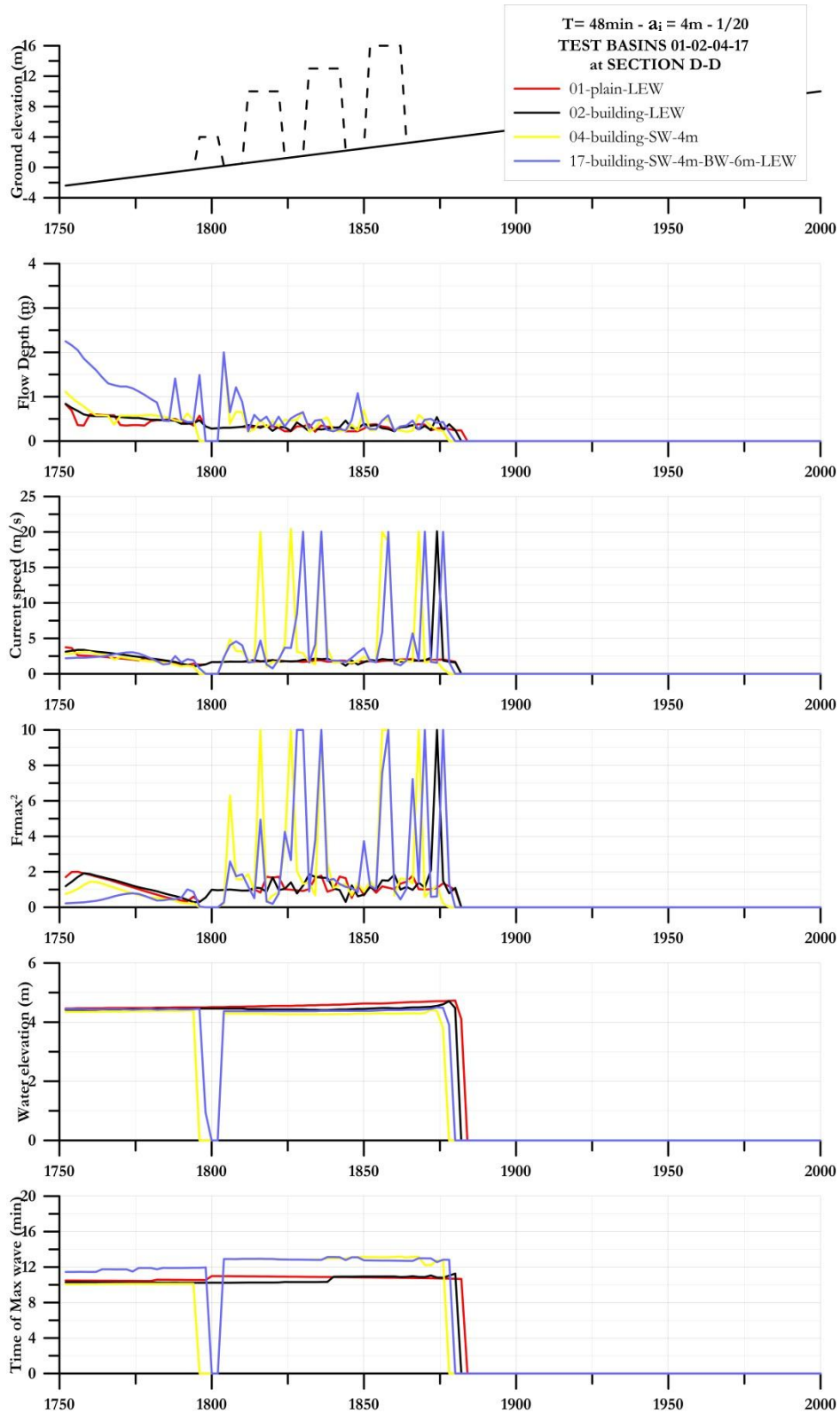


**Figure 5.46:** The variation of hydrodynamic parameters in inundation zone through the Section D-D for the test basins 06, 12 and 14 with the simulation of waves in 4m wave amplitude with 48min period on 1/20 slope

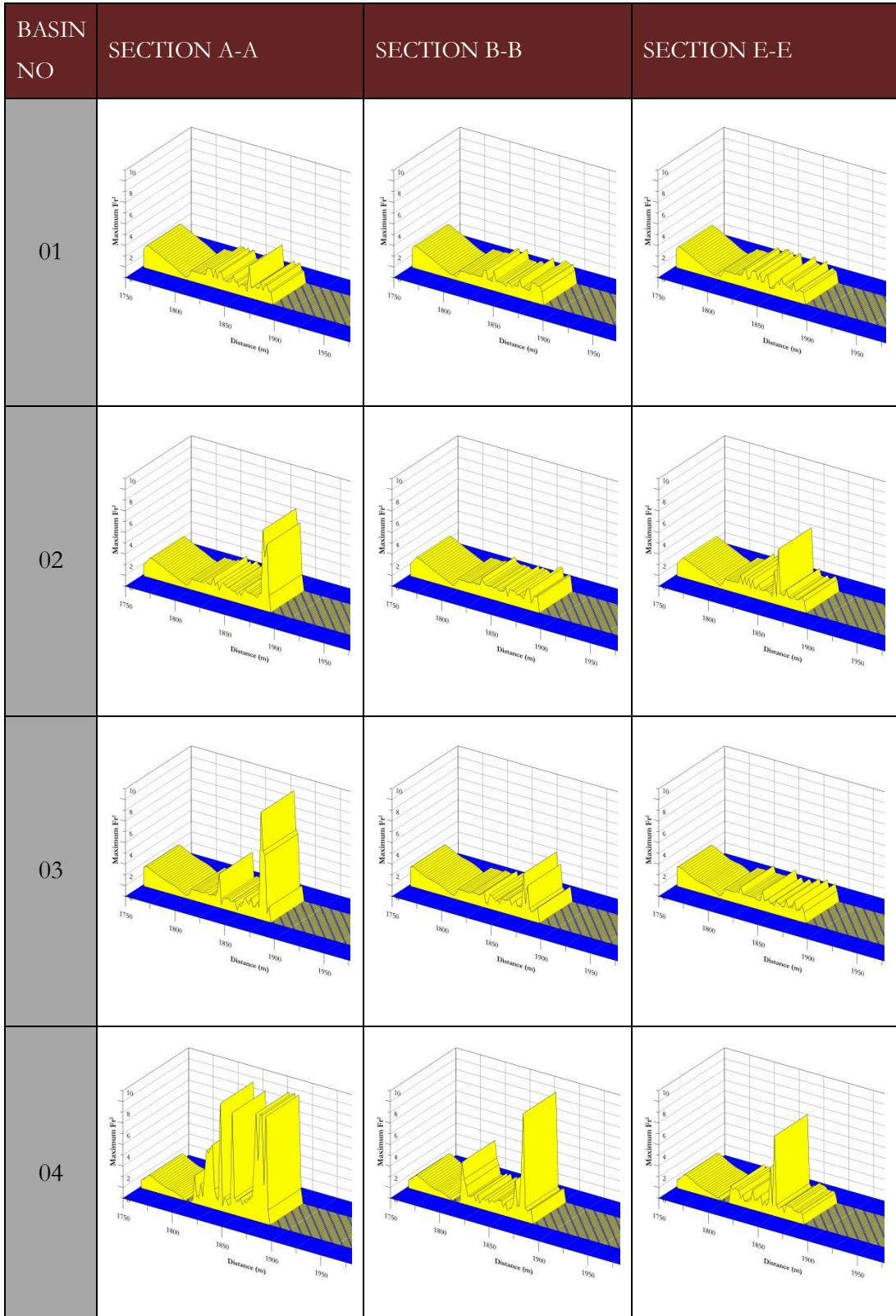


Figure 5.47: The variation of  $Fr_{max}^2$  along Sections A-A, B-B and E-E for the test basins 01, 02, 03 and 04

#### **5.4.3. The Wave Shape Effect on the Hydrodynamic Parameters Along the Cross-sections**

The wave shape effect is investigated by inputting a single sinusoidal wave with leading depression front. The analyses are performed on the plain beach, on unprotected beach with residential area in close layout and on the fully protected beach including seawall and offshore breakwater.

The results of analyses on plain beach are given in Figure 5.48. It is observed that the sectional variation of hydrodynamic parameters are similar for LEW and LDW shapes. However, high values of  $Fr_{max}^2$  is calculated for LDW in some locations. The reason is the difference of forward-backward motion due to the initial receding of the waves. Moreover, the initial receding of waves allow victims time to evacuate from the inundation area since the time of observation of maximum water elevations is twice longer than the case for LEW.

The wave shape effect on the tsunami inundation in residential areas is given in Figure 5.49. LDW shape results in higher values of hydrodynamic parameters in some locations due to the difference in momentum pattern. The accumulation of waves at the backside of the buildings is also observed for LDW shape.

The effect of wave shape on the performance of coastal protection structures is tested and the results are given in Figure 5.50. According to the sectional values, the residential area is better protected for the LDW case as lower values of  $Fr_{max}^2$  are observed.

#### **5.4.4. The Wave Period Effect on the Hydrodynamic Parameters Along the Cross-sections**

The effects of wave period on the hydrodynamic parameters in inundation zone were discussed in Section 5.3.1 according to the wave propagation on plain beach. This section provides the sectional variation of hydrodynamic parameters on different layouts as on the plain beach, unprotected coastal residential area, protected residential area with the seawall and fully protected residential area both with seawall and offshore breakwater. The inputted wave is single sinusoidal LEW with 3min wave period and 4m wave amplitude.

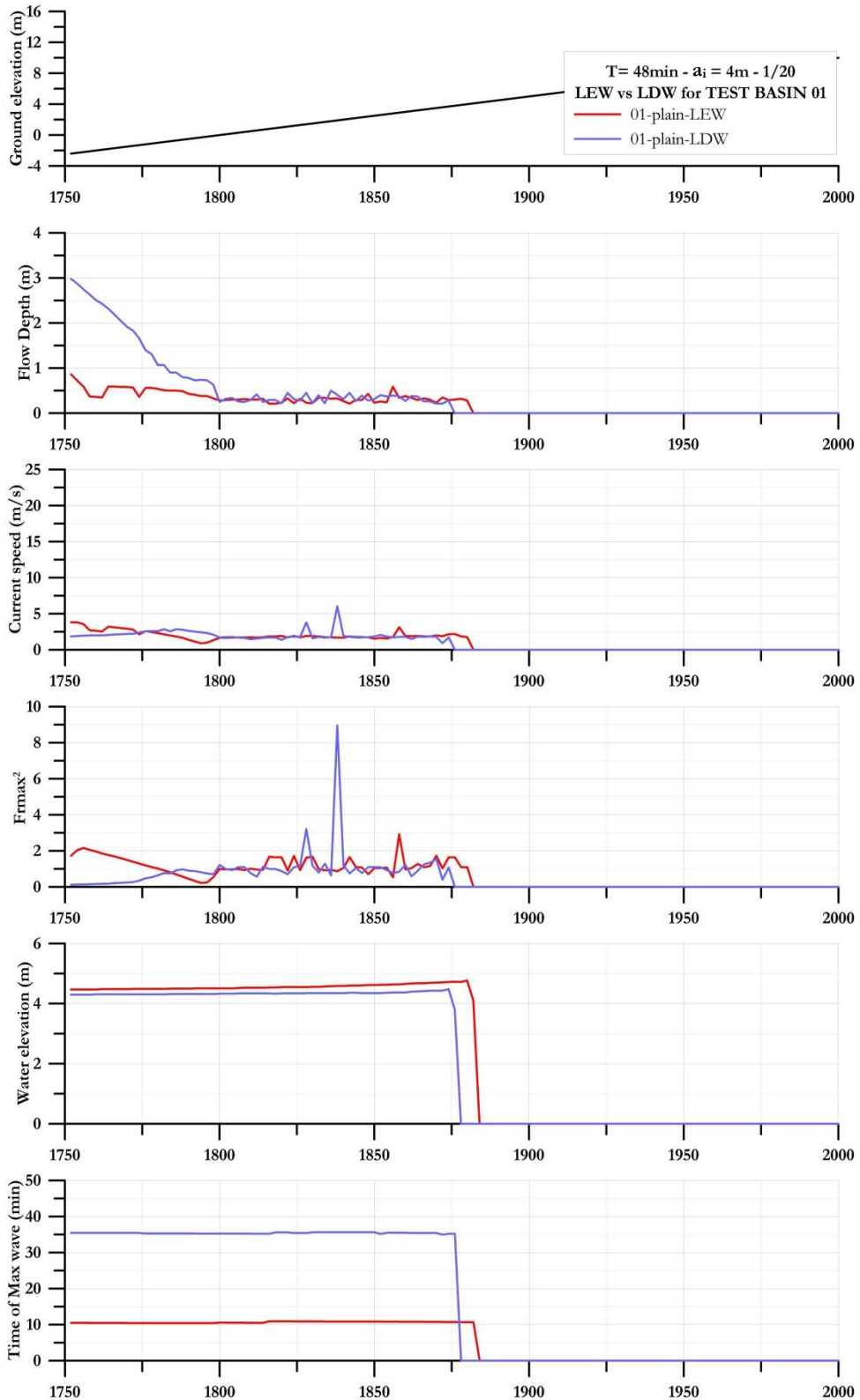


**Figure 5.48:** The comparison of hydrodynamic parameters in inundation zone through the Section A-A with the simulation of waves in 4m wave amplitude with 48min period on plain beach with 1/20 slope for LEW and LDW

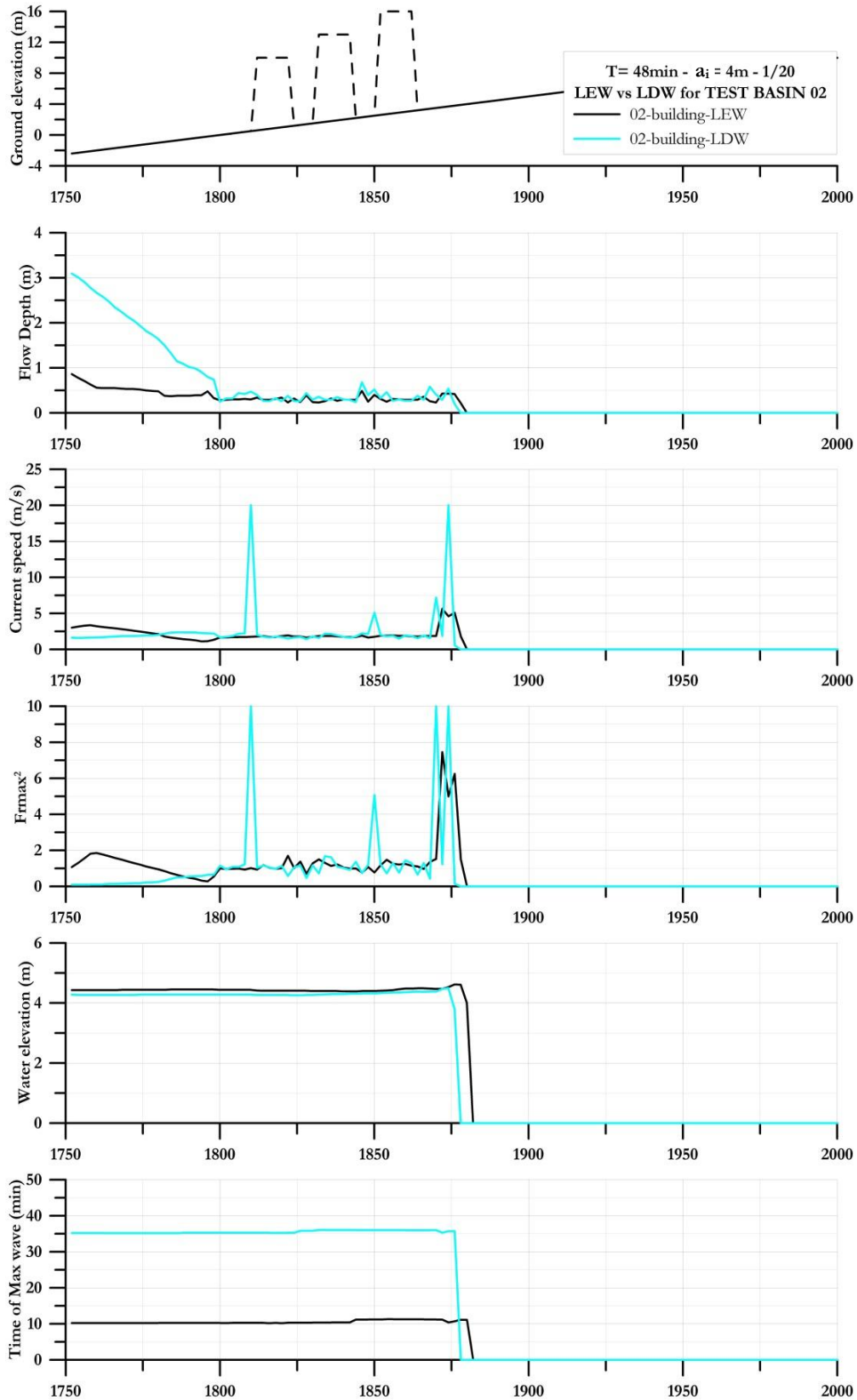


**Figure 5.49:** The comparison of hydrodynamic parameters in inundation zone through the Section A-A with the simulation of waves in 4m wave amplitude with 48min period on residential areas in test basin-02 with 1/20 slope for LEW and LDW

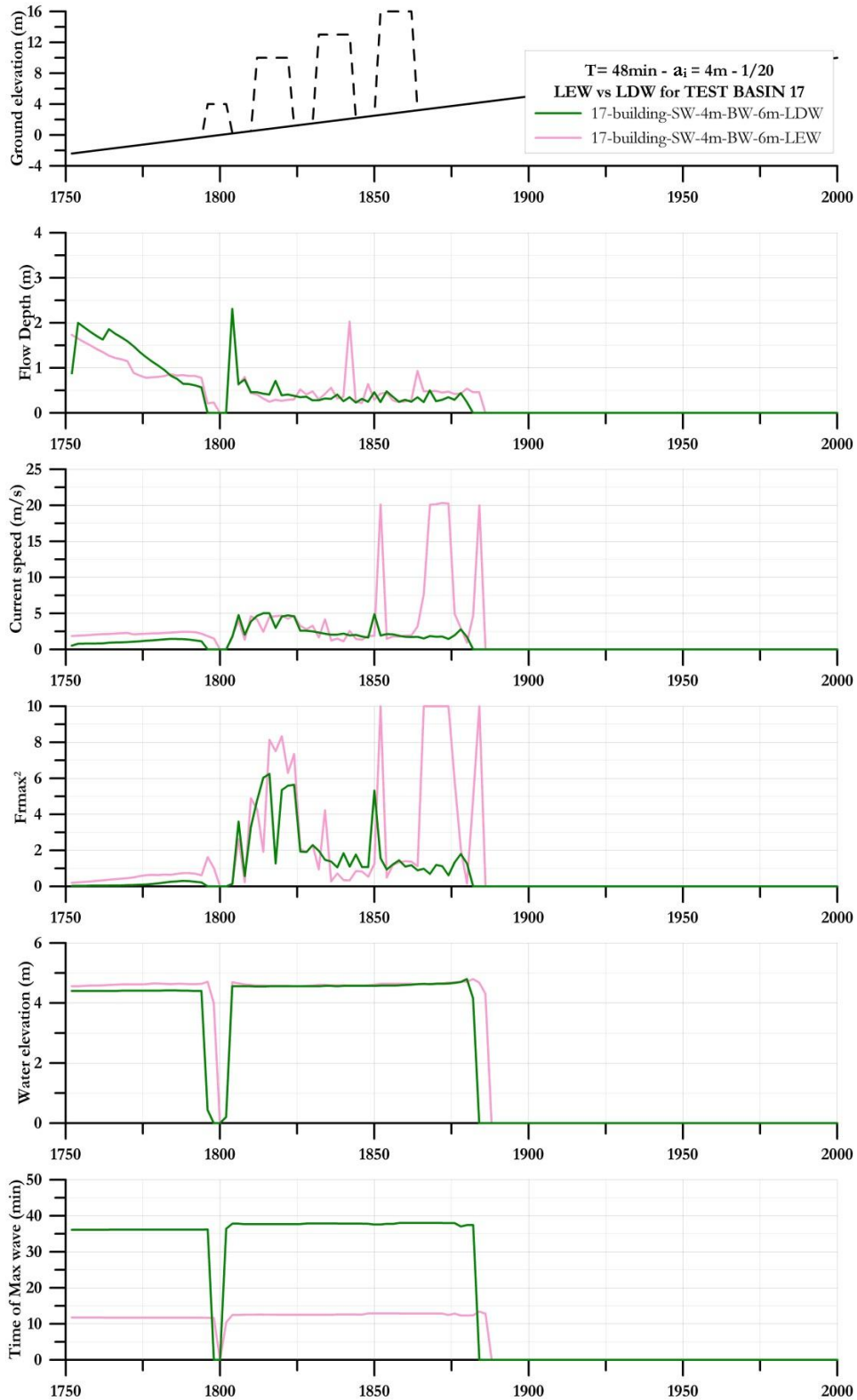


**Figure 5.50:** The comparison of hydrodynamic parameters in inundation zone through the Section A-A with the simulation of waves in 4m wave amplitude with 48min period on fully protected residential areas in test basin-02 with 1/20 slope for LEW and LDW

The results of analyses given in Figure 5.50 show that the wave motion in uniform pattern observed for longer period waves disappears in shorter period waves. The performance of coastal protection including both seawall and offshore breakwater is remarkable for 3min wave period. The protection structures are able to shorten the inundation distance. However, the reason for this is that the wave can complete its inundation motion in shorter time and the waves directing to the edges of structures and reaching to the land cannot flow long enough to build higher current velocities in lateral direction.

The variation of hydrodynamic parameters for the 3min wave period can be interpreted as an indication of the wave motion and flow in inundation zone occurred as a result of submarine/subaerial landslides.

## **5.5. The Performance of Coastal Protection with Lengthwise**

### **Seawall**

The outcomes of the analyses in this thesis reveal that if the waves are blocked by seawall and forced to flow inland through its edges, high current velocities instantaneously occur during the motion in lateral direction and cause tsunami prone areas at the locations near the edge of seawall inland. In order to prove this motion, a new test basin, named as Test Basin-23, is formed including a residential area that is protected by a seawall along the coastline from one end to the other. The seawall height is designated as 4m.

The first test is done by inputting single sinusoidal leading elevation wave with the wave period of 48min and wave amplitude of 4m. According to the simulation results, the inundation of tsunamis with 4m wave amplitude and 48min wave period is successfully prevented by seawall with the height of 4m. Then, the test is continued by inputting single sinusoidal wave with 6m wave amplitude. It is observed that the waves can overflow the structure and inundate the residential area.

The wave having the same characteristics with the one inputted in Test Basin 23 is simulated in Test Basin 04, which represents the residential area protected by seawall

but not covers the coastline lengthwise. The results of two simulations are compared and the values of  $Fr^2_{max}$  are plotted for both test basin (Figure 5.51).

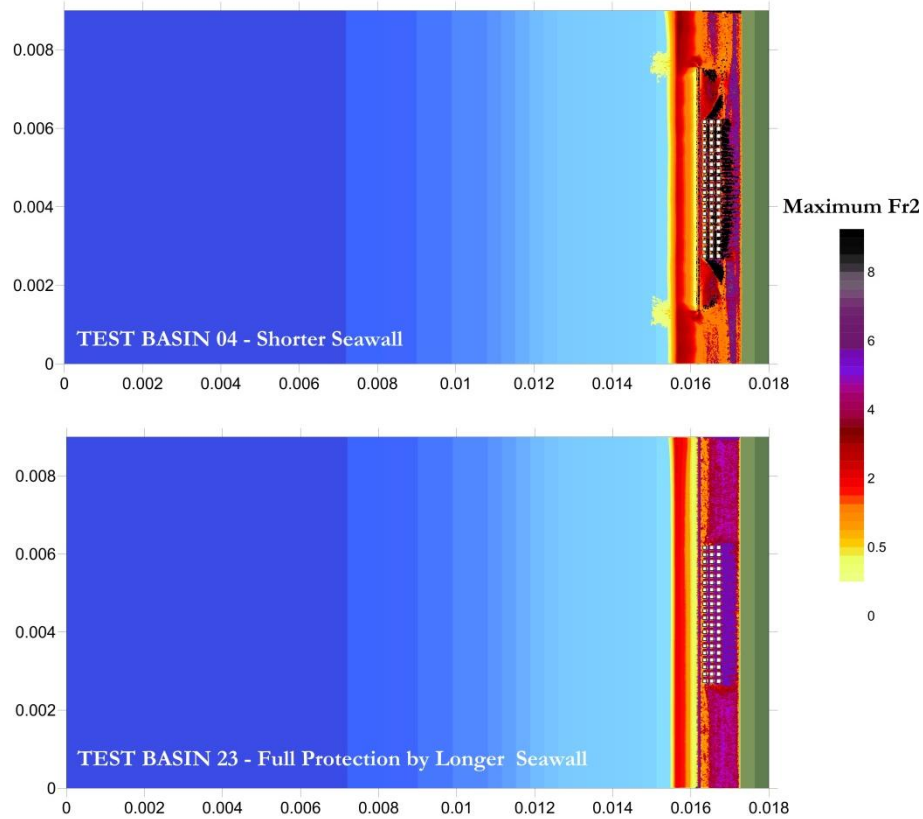


**Figure 5.51:** The distribution of maximum  $Fr^2$  values calculated for Test Basins 04 and 23

Figure 5.51 strongly supports the thesis suggesting the reason for instantaneous high current velocities. As seen from the distribution of maximum  $Fr^2$  for the protected beach with shorter seawall (the plot for Test Basin 04), high values are obtained near the two sides and at the backside of residential area shown with the black color.

However, the distribution is uniform in Test Basin 23 where the beach is fully protected with the seawall lengthwise. The values of  $Fr^2_{max}$  are much lesser than in Test Basin 04 at the two sides and at the backside of the buildings. The reason for this is that there is rigid protection in Test Basin 23 and the waves overflow the structure in the same direction with the flow. It means that there is no gap or any

entrance where waves can change direction while inundating the land. This is a proof for explaining high  $Fr_{max}^2$  values observed instantaneously due to the lateral wave motion.

## 5.6. Investigation of Tsunami Behavior on a Plain Beach for the N-waves

In this thesis, the investigation of tsunami hydrodynamic parameters in inundation zone is performed by modeling the propagation of single sinusoidal wave. The correlations for  $\overline{Fr_{max}^2}$  and for the maximum runup height  $R_H$  are derived in accordance with the wave characteristics and sea bottom slope. For comparison and evaluation, another wave shape is selected as N-wave and the same analyses are performed in order to compare the results. This study is performed into two stages. One of them is comparing the NAMI DANCE results for the runup values of a single N-wave and sinusoidal wave that are both inputted from the toe of the slope and are propagated on the same bottom slope. The other one is comparing the NAMI DANCE runup results for N-waves with some theoretical approaches in literature.

### 5.6.1. Comparison of Runup Values for an N-wave and Sinusoidal Wave computed by NAMI DANCE

A class of N-shaped waves is found by Tadepalli and Synolakis (1994) with very interesting behaviour that is supported as a possible new approach for the studies of tsunami runup. A first-order theory is used for the analyses and asymptotic results are derived for the maximum runup of different types of N-waves. They proposed a different type of N-wave, named as *isosceles N-wave*, and its surface profile is given by

$$\eta(x,0) = \frac{3}{2} \sqrt{3} H_N \sec b^2 [\gamma(x - X_1)] \tanh[\gamma(x - X_1)] \quad [5.11]$$

where  $\gamma = \frac{3}{2} \sqrt{\frac{3}{4} H_N}$ . This profile is for a leading depression N-wave and  $H_N$  is the maximum wave amplitude.

The profiles of N-waves are obtained by using Eqn. [5.11] for the wave amplitudes of 1m, 2m, 3m, 4m and 5m. The wave profiles of sinusoidal and N-wave with the wave amplitude of 1m are given in Figure 5.52. As seen from the figure, they coincide each other quite well. Both waves are inputted from the toe of the slope.

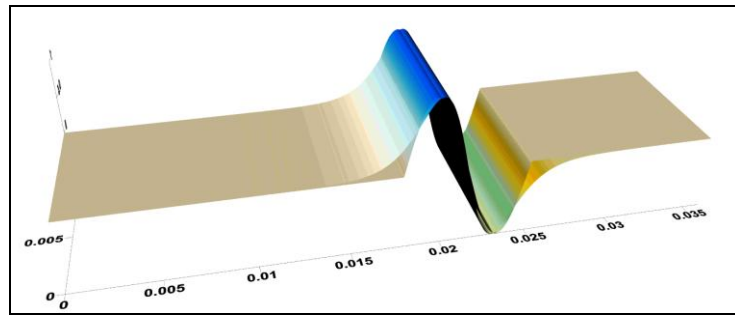


**Figure 5.52:** The wave profiles of sinusoidal and N-wave with the wave amplitude of 1m

The runup heights, average maximum of  $Fr^2$  and  $Fr$  values are obtained for the two wave shapes for five different wave amplitudes and the results are given in Table 5.2.

The data in the table shows that the runup heights and  $\overline{Fr_{\max}^2}$  values fit quite well.

**Table 5.2:** The comparison of runup,  $\overline{Fr_{\max}^2}$  and  $\overline{Fr_{\max}}$  values for sinusoidal wave and N-wave

amp (m)	Wave type	Runup (m)	$\overline{Fr_{\max}^2}$	$\overline{Fr_{\max}}$
1m	Sinusoidal	1,75	7,13	2,64
	N-wave	2,00	6,89	2,58
2m	Sinusoidal	2,50	10,35	3,15
	N-wave	2,50	10,20	3,13
3m	Sinusoidal	2,75	11,76	3,37
	N-wave	3,00	11,83	3,37
4m	Sinusoidal	3,00	11,88	3,37
	N-wave	3,50	13,04	3,48
5m	Sinusoidal	3,25	12,77	3,50
	N-wave	3,50	12,97	3,51

### 5.6.2. Comparison of NAMI DANCE Runup results for N-waves with Analytical Approaches

In this part, the runup of N-wave on a sloping beach computed by NAMI DANCE is compared with some analytical approaches in literature. Tadepalli and Synolakis (1994) proposed a relation for the maximum runup of a leading elevation isosceles N-wave as in the following:

$$\frac{Ru}{d_c} = 3.86(\cot \beta_0)^{1/2} H_N^{5/4} \quad [5.12]$$

where  $d_c$  is the critical water depth that is 50m in this test basin,  $\beta_0$  is the bottom slope and  $H_N$  in the maximum amplitude of N-wave.

The analyses are performed with isosceles N-waves with different wave amplitudes and the runup values are computed by NAMI DANCE. Then, the theoretical approach in Eqn [5.12] is used and the runup values are calculated for the same wave amplitudes. The selected wave amplitudes and corresponding numerical and analytical results are given in Table 5.3. Wave profiles are formed by using the relation in Eqn [5.11] same as in the previous section.

**Table 5.3:** The numerical and analytical runup values of N-wave on a sloping beach

H (m) (Amplitude)	Runup (m) computed by NAMI DANCE	H/d	$3.86 * \sqrt{\cot \beta} \left(\frac{H}{d}\right)^{5/4}$	Ru/d computed by NAMI DANCE
0.175	0.75	0.0035	0.015	0.015
0.2	1.00	0.0040	0.017	0.020
0.225	1.00	0.0045	0.020	0.020
0.25	1.25	0.0050	0.023	0.025
0.3	1.50	0.0060	0.029	0.030
0.35	1.75	0.0070	0.035	0.035
0.375	1.75	0.0075	0.038	0.040
0.4	1.75	0.0080	0.041	0.040
0.425	2.00	0.0085	0.045	0.045
0.45	2.00	0.0090	0.048	0.045
0.475	2.25	0.0095	0.051	0.050
0.5	2.25	0.0100	0.055	0.050

The numerical and analytical results of runup heights for N-wave in Table 5.3 are plotted given in Figure 5.53. In the figure, the solid line indicates the runup relation for isosceles N-waves provided by Tadepalli and Synolakis (1994) and given in Eqn [5.12]. As seen from the figure, the numerical results of NAMI DANCE for the runup of N-wave on a sloping beach are very consistent with the analytical approach.

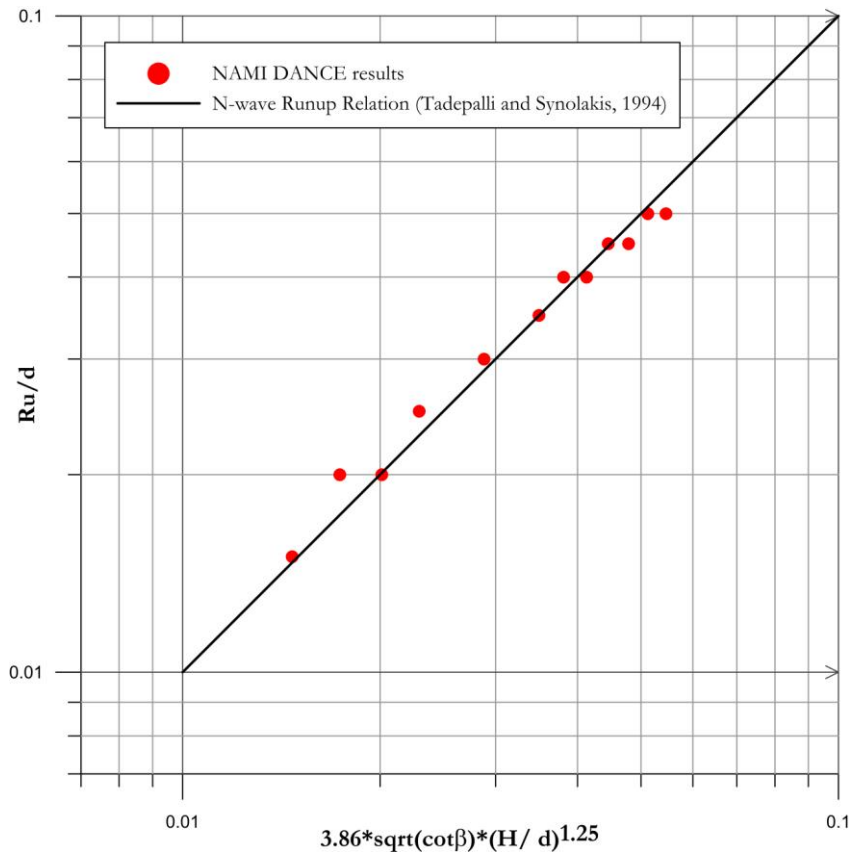


**Figure 5.53:** The normalized maximum runup of isosceles N-wave against the asymptotic expression in Eqn [5.12] on a 1/20 sloped beach

Another analytical study about runup of N-waves is performed by Zhao et al. (2010) that calculates the propagation and runup height by Boussinesq Equations and compare the results with the analytical relation in Eqn [5.12]. Figure 5.54 shows the comparison of maximum runup of leading elevation N-waves computed in three ways; as computed by NAMI DANCE, calculated by Tadepalli and Synolakis (1994)

and by Zhao et al. (2010) analytically. The figure indicates that there is well consistency between the NAMI DANCE results and analytical solutions.

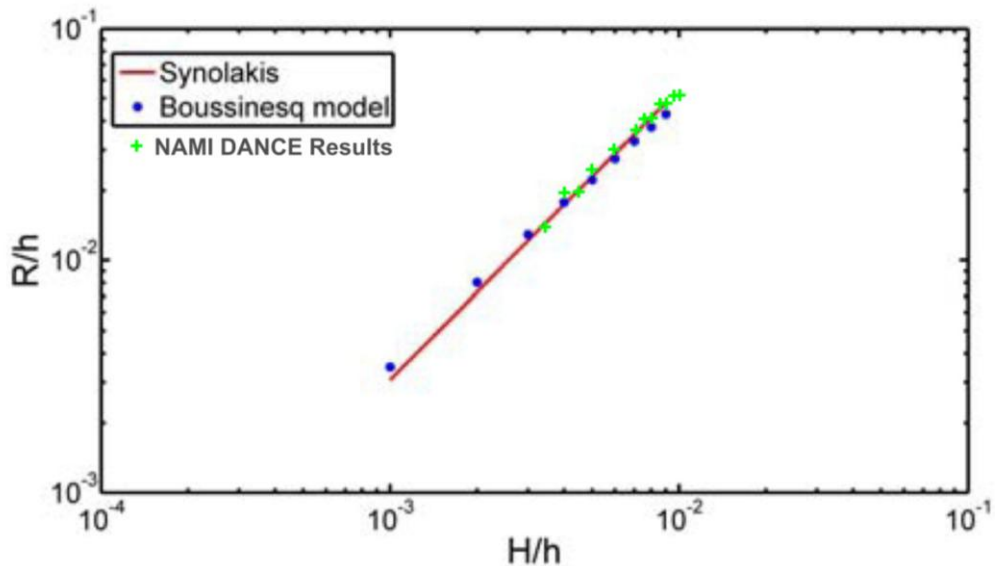


**Figure 5.54:** Comparison of maximum runup of leading elevation N-wave computed by NAMI DANCE and calculated by analytical relations in Tadepalli and Synolakis (1994) and Zhao et al. (2010)

## 5.7. The Effect of Manning Coefficient on Hydrodynamic Parameters in Inundation Zone

As explained in Chapter 3, NAMI DANCE is capable of making calculations either by assuming the Manning's coefficient as uniform everywhere or by inputting different values of Manning's coefficient at each node of the study domain.

In order to test the effect of Manning's coefficient on the change of hydrodynamic parameters in inundation zone, the spatial variety of Manning's coefficient is used by defining a scheme for the whole study domain. This scheme defines different values of Manning's coefficient: 0.035 for the sea, 0.060 for the land and 0.8 for the buildings.

The simulations are done by inputting different values of Manning's coefficient in each grid. The analyses are performed for the propagation of wave with 4m wave amplitude and 48min wave period on three different basins as plain beach (Test Basin 01), unprotected residential area (Test Basin 02) and residential area protected by seawall and offshore breakwater (Test Basin 17). The 1/20 bottom slope is identical in each test.

The distribution of difference in maximum current velocities and  $Fr^2$  are given in Figures 5.54, 5.55 and 5.56 for test basins 01, 02 and 17, respectively. It is seen from the figures that lower values of hydrodynamic parameters are calculated in inundation zone when the spatial variety of Manning's coefficient is inputted. It is expected since higher coefficients are used on the land.

It is obvious that these results are more realistic since the bottom friction on land is higher than that in the sea in real case. According to these results, it can be suggested that using spatial distribution of Manning's coefficient may be preferable if more realistic results are expected in inundation area i.e. for academic purposes. However, the analyses with spatial distribution increases runtime since different values of Manning's coefficient are used at every grid nodes and inputted in the program at every time step. Therefore if faster outcomes are required i.e. the modeling results are used for operational purposes by decision makers in Tsunami Early Warning Systems, it is more feasible to use a constant value for Manning's coefficient in tsunami modeling for shortening runtime.

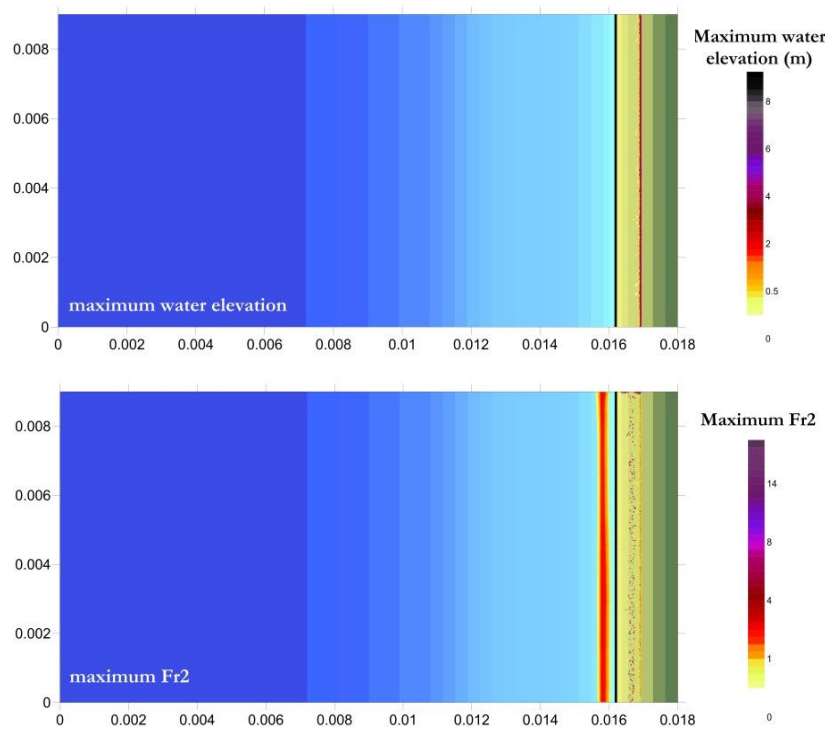


**Figure 5.55:** The difference of maximum current velocity and  $Fr^2$  on plain beach (Test Basin-01) for the spatial variety of Manning's coefficient

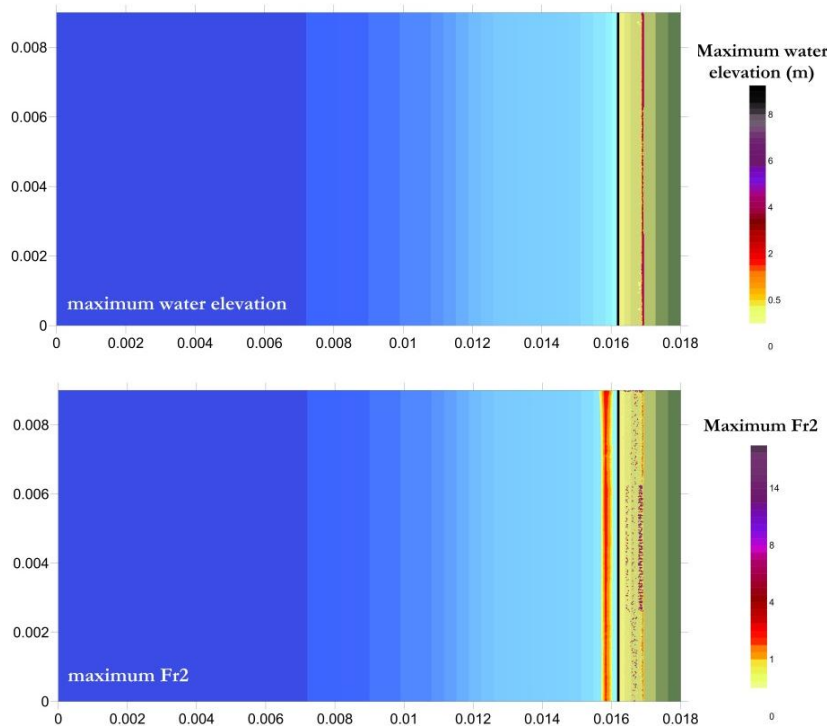


**Figure 5.56:** The difference of maximum current velocity and  $Fr^2$  on unprotected residential area (Test Basin-02) for the spatial variety of Manning's coefficient

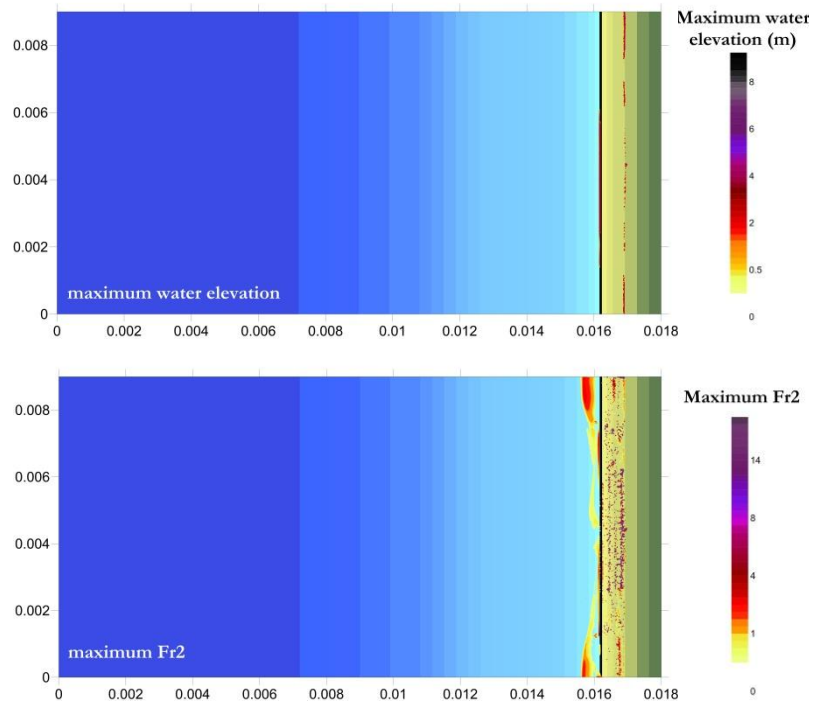


**Figure 5.57:** The difference of maximum current velocity and  $Fr^2$  on fully protected residential area (Test Basin-17) for the spatial variety of Manning's coefficient

## CHAPTER 6

### CASE STUDY – INVESTIGATION OF HYDRODYNAMIC PARAMETERS DURING THE 2011 GREAT EAST JAPAN TSUNAMI IN KAMAISHI BAY

The 2011 Japan Event caused extreme damages along the east coasts of Japan. Kamaishi is one of the coastal cities subjected to extreme tsunami inundation with strong currents and high flow depths. The maximum values of  $Fr^2$  and other hydrodynamic parameters are investigated in Kamaishi Bay occurred during the 2011 Japan event.

Kamaishi is a coastal city located at the North-east coast of Japan, Honshu and protected from sea by a natural harbor (Figure 6.1). It is the birthplace of the modern iron manufacture in Japan, and because of iron and steel industry, it has population of nearly 40,000. According to the historical records, the 1896 Meiji Sanriku tsunami was so devastating for Kamaishi that the city lost more than 75% of the population.

For the mitigation of tsunami disasters, a tsunami breakwater was constructed at the Kamaishi Bay entrance in 1978-2008. The city was protected by two breakwaters with 670m and 990m lengths at the entrance of the bay with 6m crest elevation and 300 m gap distance (Figure 6.1). These breakwaters were built at a water depth of 63m, which is the deepest point in the world where a breakwater has been constructed and thus made it into the Guinness World Records in 2010.

The tsunami amplitudes, as measured by a GPS buoy installed and operated by PARI, Japan, reached to 6.7m at 20 km offshore Kamaishi at a water depth of 300m. It is reported that at least four out of 69 designated evacuation sites of the city were inundated by the tsunami (Kamaishi Port Office, 2011). As seen from the photos in Figure 6.2, most of the timber-framed buildings were dragged; a huge tanker was

carried onto the quay, and the foundations of buildings on the waterfront were highly scoured (Yalciner et al, 2012).

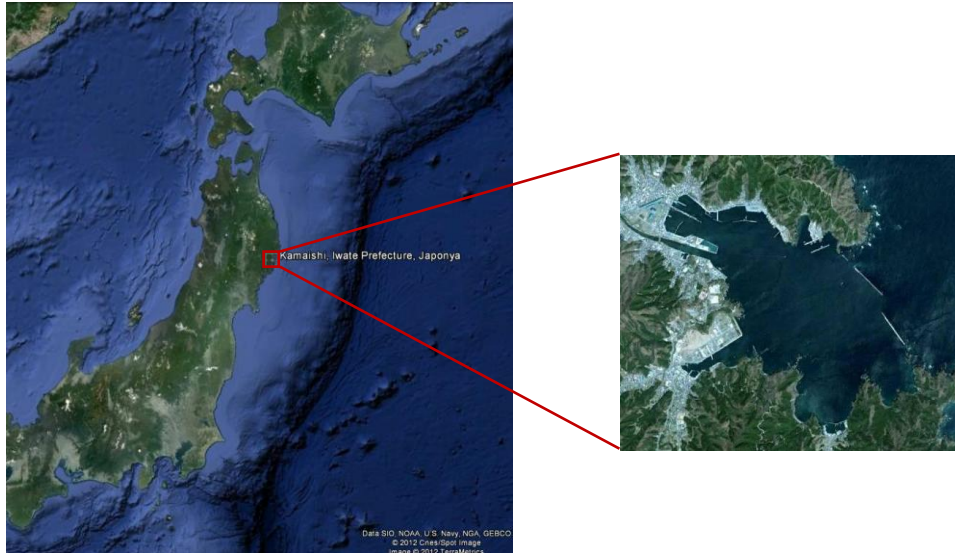


**Figure 6.1:** The Location of Kamaishi city and satellite image of Kamaishi Bay



**Figure 6.2:** Tsunami damage in the Kamaishi City after the event (Yalciner et al., 2012)

In order to compute and compare the distribution of tsunami hydrodynamics as flow depth, current velocities and Froude number in Kamaishi, tsunami simulation is performed for Kamaishi Bay and for the city with a finer grid bathymetry and topography. A well-known footage taken from the roof of a three-storey building at the north of the bay reveals the extent of the devastating effect of tsunami inundation and the resulting damage in Japan event. Therefore, the topography of Kamaishi City was digitized from the satellite image, and the digital data of study domain is generated with 3m spatial grid resolution in order to achieve more realistic

results (Figure 6.3). The tsunami breakwaters of Kamaishi are also inputted by assuming its crest elevation as 6m.

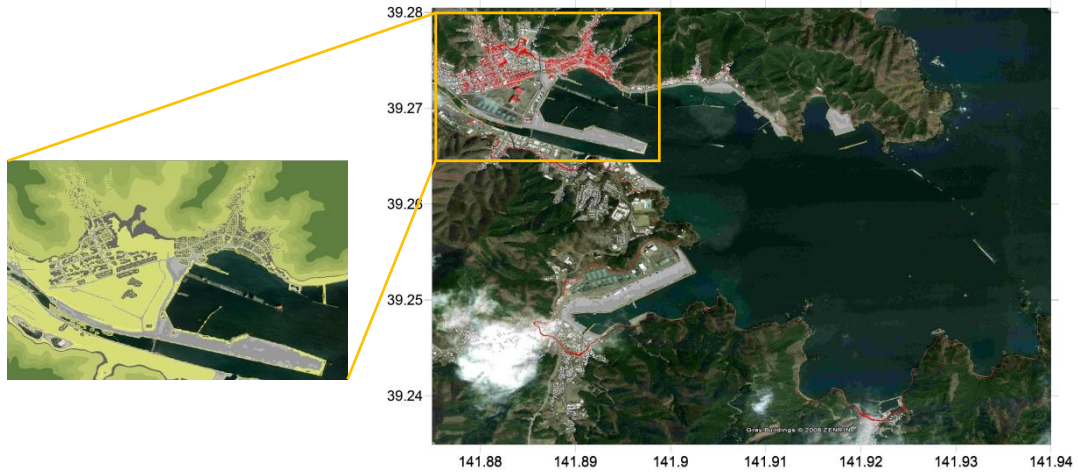


**Figure 6.3:** The digitized bathymetry and topography of Kamaishi Bay and City

The source, mentioned earlier in Chapter 4, proposed by Imamura et al. (2011) is used as input of the near field modeling from source to Kamaishi area. The time histories of water level fluctuations at the entrance of Kamaishi Bay, as obtained from near field modeling, is inputted as forcing function to the fine grid modeling of Kamaishi bay for the computation of inundation and nearshore tsunami parameters.

During the Japan tsunami, the Kamaishi breakwater was heavily damaged by the attack of the first 9-meter-wave, which left Kamaishi defenseless (Onishi, 2011). The waves deflected from the breakwater are also thought to have contributed to the high amplitudes on the northern part of the city (see the digitized topography in Figure 6.3 in the left). In order to analyze the effects of Kamaishi breakwater on tsunami inundation and damage, the analyses of tsunami inundation are focused on three conditions depending on the presence and state of the breakwater: with breakwater, without breakwater and with damaged breakwater which reflect the real case and compare the performance of breakwater.

Analyses done are twofold: (i) investigation of the effect of breakwater on tsunami hydrodynamic parameters and its performance on protecting the bay and (ii) investigation of the behavior of hydrodynamic parameters around the buildings at the North of the bay. Figure 6.4 shows the distribution of numerical gauge points in these two focused areas. The sections are determined along the direction of incoming waves in order to investigate the change of hydrodynamic parameters at the seaside and the protected harbor side. On the other hand, the numerical gauge points at the residential area are selected from among those at the front of the buildings and along the roads.

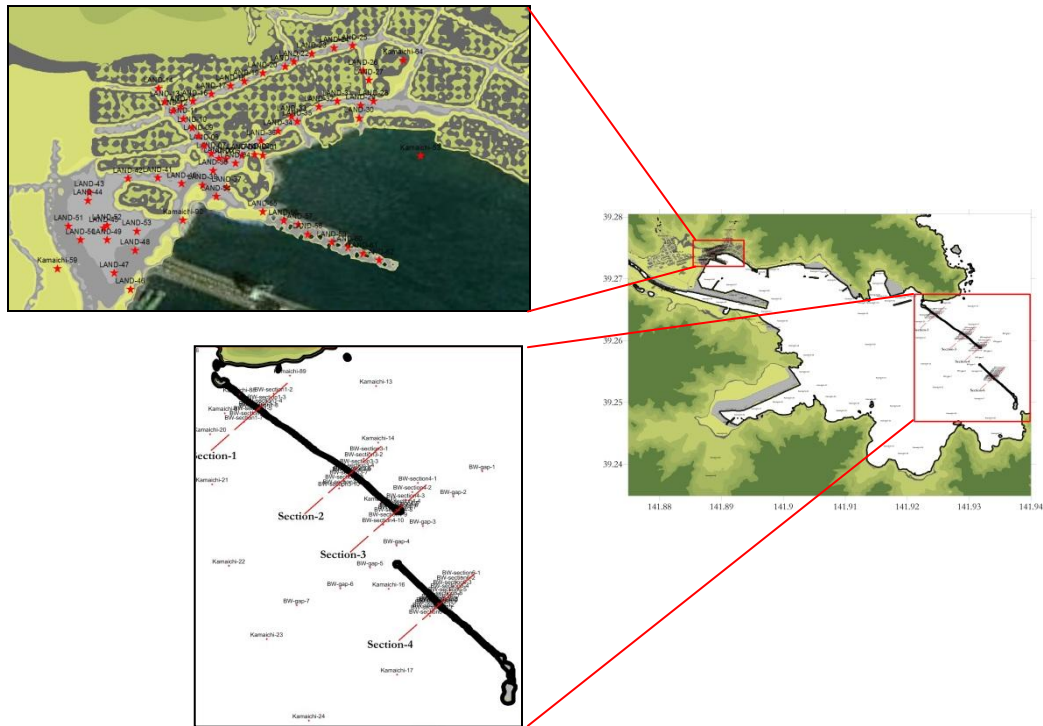


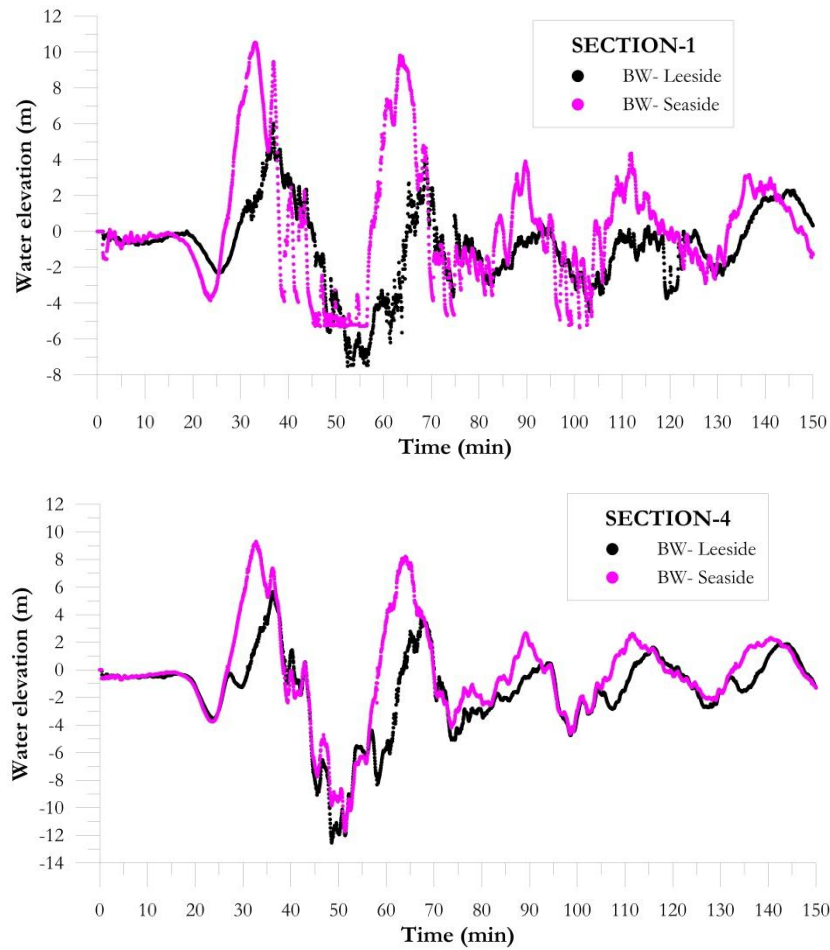
**Figure 6.4:** The gauge points around the buildings at the North of Kamaishi Bay and the sections crossing the two breakwaters

## **6.1. The Investigation of Hydrodynamic Parameters around the Kamaishi Breakwaters**

The Kamaishi Breakwater is recognized by the Guinness World Records as the world's deepest breakwater with the construction depth of 63m. It consists of two breakwaters with the total length of 1690m and with a 300m entrance gap. The breakwater was heavily damaged during the tsunami attack, and the residential area in the bay became defenseless. As this failure had grave consequences, the results of analyses are evaluated, the reasons for the breakwater collapse according to the difference of hydrodynamic parameters at the seaside and leese side of the breakwater are discussed. Section 1 and Section 4, shown in Figure 6.4, are selected for these comparisons.

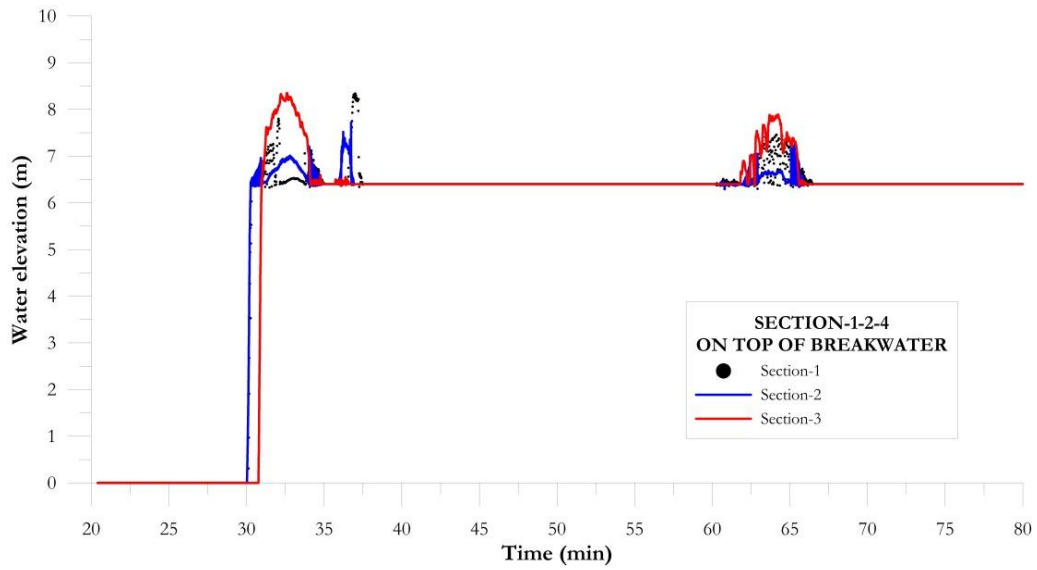
Figure 6.5 shows the comparison of the water surface elevations computed in the simulation duration that occurred at the seaside and leese side of the breakwater. The plots show that water surface elevation at the seaside is considerably higher than that at the leese side. Especially for Section 1, when the first wave hits the breakwater, water elevation at the seaside is almost four times of that at the leese side about 10 minutes. This situation tends to cause significant differences in the hydrostatic pressures between the two sides of the breakwater. Therefore, the resisting forces at the leese side become inadequate against the sliding and overturning forces, and hence the collapse due to the sliding and overturning becomes inevitable.

Figure 6.5 also indicates that the difference of water elevation at the two sides of the breakwater decreases at the toe. This result corresponds well with the expectations since the waves pass from the gap and therefore cannot raise the water elevation at the seaside of Section 4. However, the seaside of the breakwater at Section 1 is directly exposed to the tsunami attack without the passage of waves through any gap.



**Figure 6.5:** The comparison of water surface elevation at the seaside and leeside of the breakwater during the simulation time

The wave overtopping during the tsunami attack is investigated by plotting the water surface elevation at the gauge points located at the breakwater crest. Figure 6.6 shows the water surface fluctuation on the crest of breakwater at Sections 1, 2 and 4 during the simulation time. The results show that the first wave hits the breakwater at around 30<sup>th</sup> minute of the simulation at Sections 1 and 2, and 1 minute later at Sections 4. The water elevation reaches around 8.5m during in about the 5<sup>th</sup> minute of overtopping, and the water passage continues with 0.5m flow depth at the top of breakwater. The second wave hits at around 62<sup>nd</sup> minute again with the 8m water elevation.



**Figure 6.6:** The water surface fluctuation at the top of breakwater in Section 1, 2 and 4 during simulation time

Another investigation on Kamaishi breakwater was geared toward understanding the role of breakwater gap on the change of tsunami hydrodynamic parameters. Figure 6.7 shows the ratio of maximum current velocity between with and without breakwater cases. As seen from the figure, the current velocity is concentrated through the gap of breakwater that may instantaneously cause high values of currents in inundation area. It should be noted here that the occurrence times of maximum current velocity in these two cases may not coincide.

Similar to this, Figure 6.8 shows the ratio of maximum  $Fr^2$  between with and without breakwater cases. The figure indicates that high values of  $Fr^2$  are observed at some locations on land when Kamaishi breakwater exists. This means that in case of protection with breakwater, higher damage may be expected at some locations in inundation area due to high current velocities that may occur instantaneously and be directed by the existence of breakwater. This phenomenon is discussed in Section 6.2.

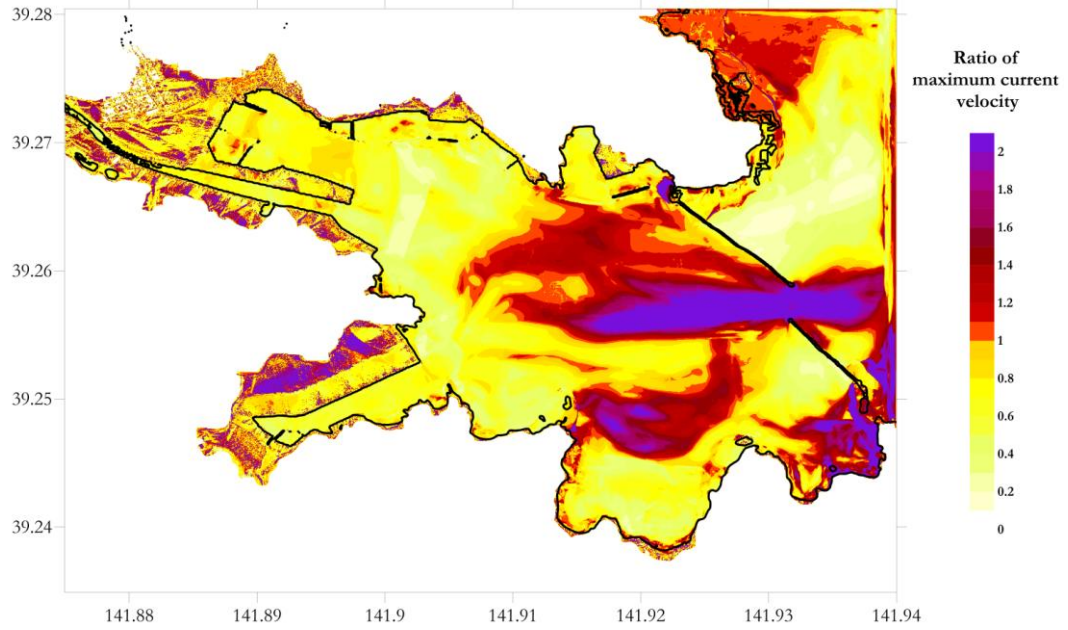


**Figure 6.7:** The ratio of maximum current velocity between with and without breakwater cases

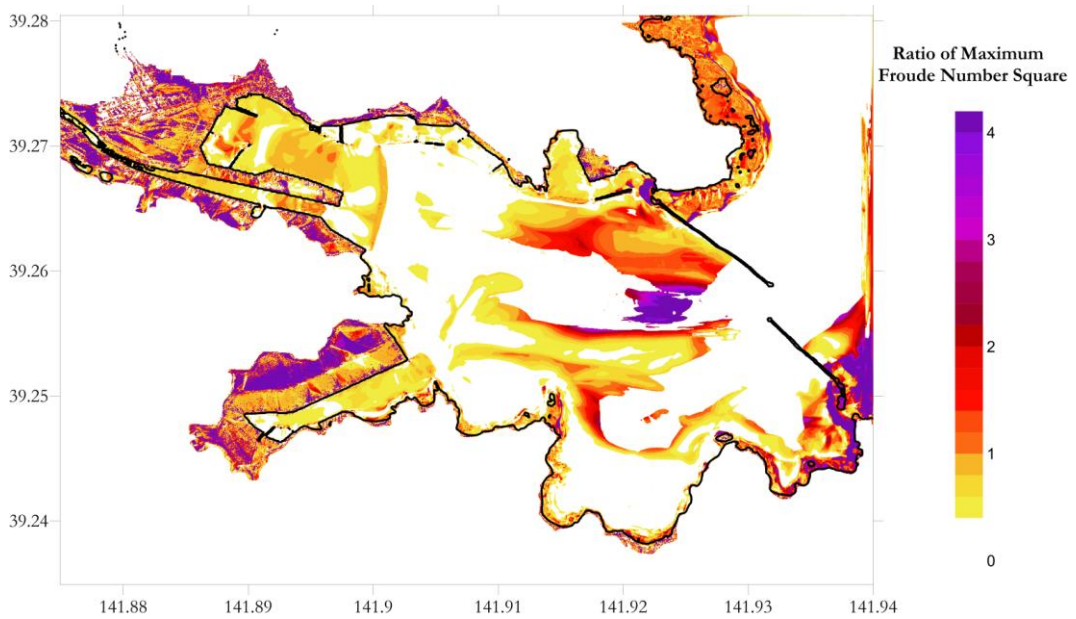


**Figure 6.8:** The ratio of maximum  $Fr^2$  between with and without breakwater cases

Figure 6.9 highlights the change of current velocity at numerical gauge points along the gap for the cases of with- and without-breakwater conditions. The results demonstrated in Figure 6.7 also support the presence of concentrated distribution of

current velocity through the gap. The plots in Figure 6.9 reveal that the current velocities at the numerical gauge points Gap\_3 and Gap\_4 are fairly higher when breakwater exists. This is due to the intrusion of water through the gap in a concentrated manner even if waves overtop. The difference of current velocities between with- and without-breakwater cases decreases at the gauge point Gap\_5 since this point is farther from the gap entrance.

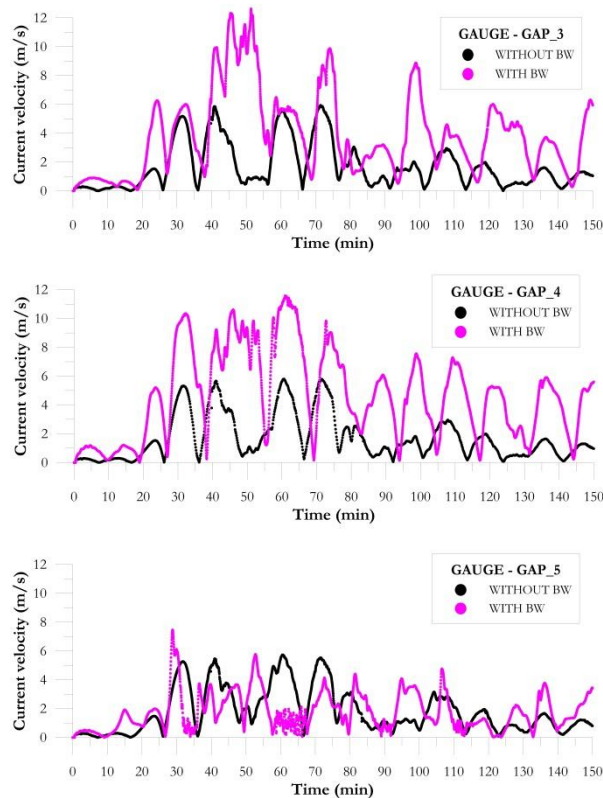


**Figure 6.9:** The change of current velocity during simulation time at the gauge points located through the breakwater gap for with and without breakwater cases

## 6.2. The Effect of Kamaishi Breakwater on Hydrodynamic Parameters in Residential Area

In the light of results summarized in Section 6.1, the changes of hydrodynamic parameters are evaluated in inundation area compared to the performance of three

conditions: with breakwater, without breakwater and with breakwater damaged during the tsunami attack.

Figure 6.10 shows the water level fluctuations in the residential area at three selected gauge points, Land\_04, Land\_08 and Land\_20, Land\_04 being at entrance of a road that is parallel to the incoming wave direction near the shoreline, Land\_08 being along that road and Land\_20 being on another road that is parallel to the shoreline. The well-known footage mentioned at the beginning of this Chapter was taken near the gauge point Land\_04.

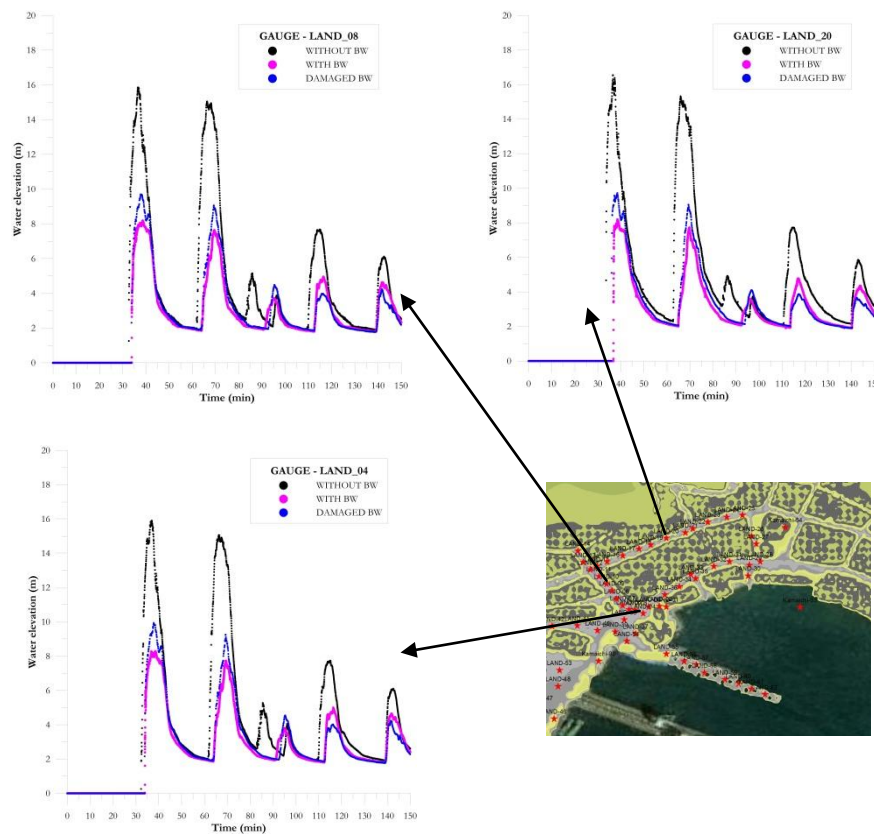
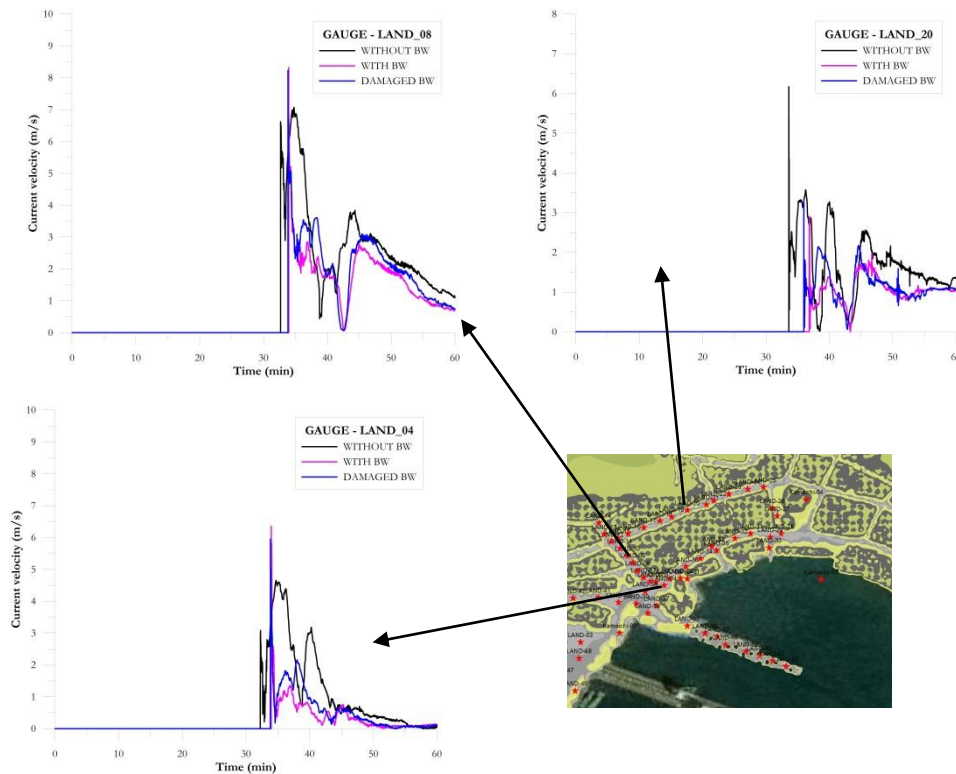


**Figure 6.10:** The water level fluctuations during the simulation time at three selected gauges for with, without and damaged breakwater cases

Figure 6.10 also shows that higher water elevations are observed. On the other hand, lowest values occur when the bay is protected by the breakwater. The results also

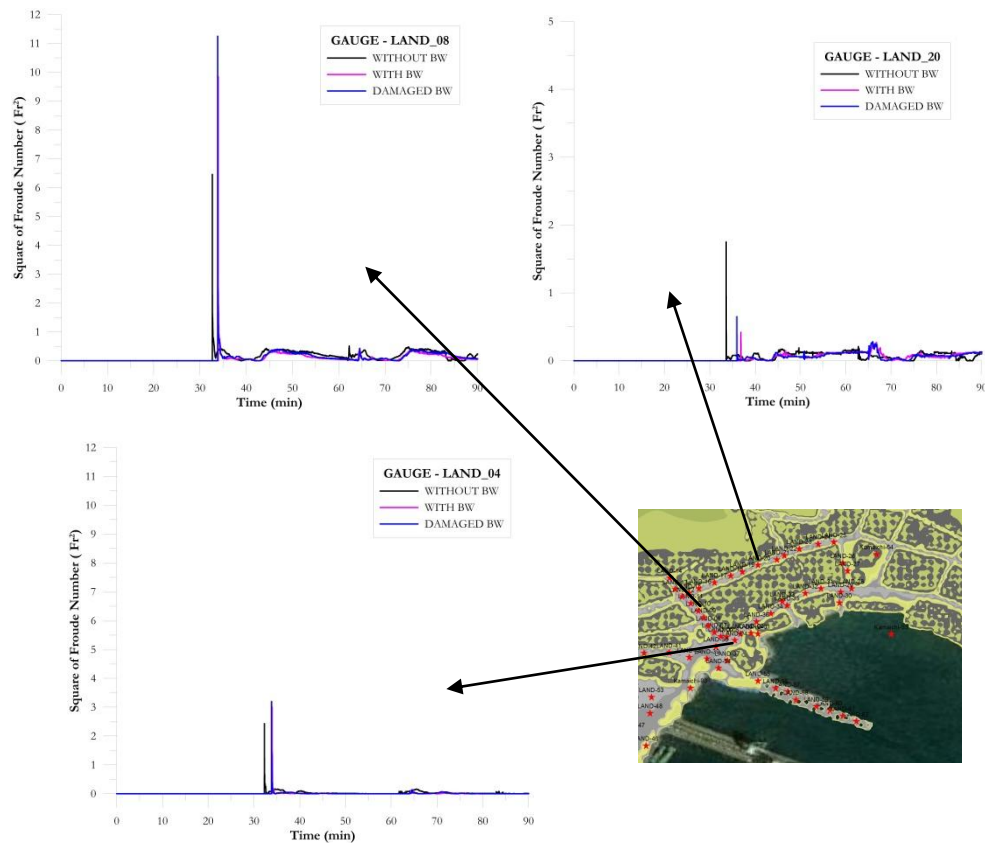
show that, although it is not as much effective as in a non-damaged breakwater case, the damaged breakwater can partly decrease the water elevations and prevent tsunami damage even if the top part of the breakwater has collapsed.

Figure 6.11 shows the current velocities at the same gauge points for the three breakwater cases. The results indicate that when the waves first inundate, the existence of breakwater causes instantaneous high current velocities at the locations in the direction of the incoming wave. For the locations along the road parallel to the shoreline, no significant change of current velocities are observed.



**Figure 6.11:** The change of current velocities during simulation time at three selected gauge points for with, without and damaged breakwater cases

Figure 6.12 shows the change of  $Fr^2$  at these gauge points for the same breakwater conditions. Similar to the change of current velocities, higher values of  $Fr^2$  are observed at the locations along the incoming wave direction in residential areas if the breakwater exists. These results are directly consistent with the outcomes for current velocities as expected.



**Figure 6.12:** The change of square of Froude Number during simulation time at three selected gauge points for with, without and damaged breakwater cases

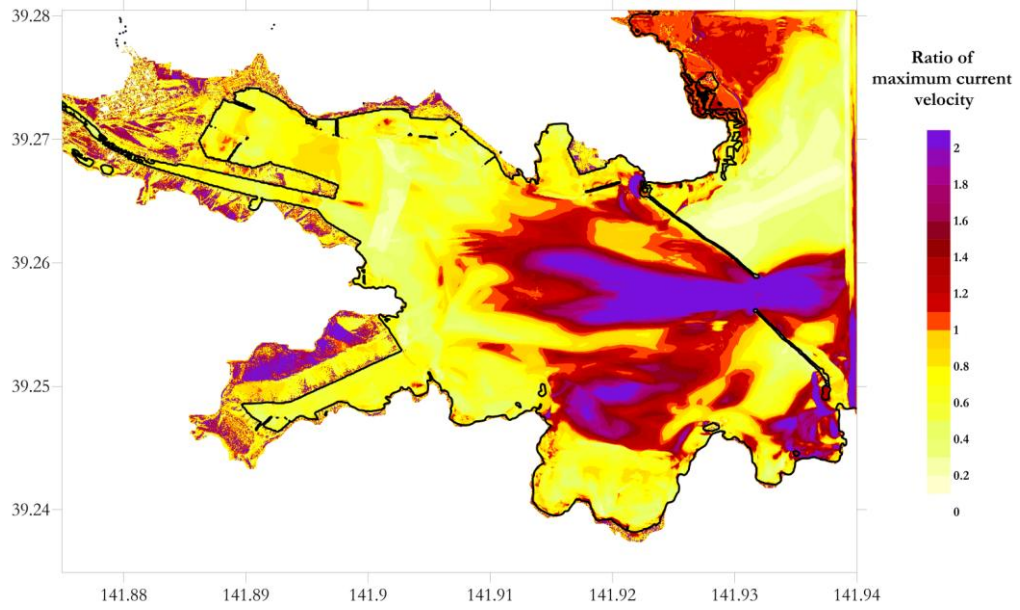
A similar study for assessment of the Kamaishi breakwater performance during this tsunami was performed by PARI (Takahashi, et al., 2011). It is also indicated that the breakwaters maintained their function until the peak and could delay tsunami arrival by about 4 minutes and reduce tsunami runup about 50% (Yalciner et al, 2012). This case study also supports that maximum wave amplitude, current velocity; square of Froude Number and flow depth are major parameters for tsunami inundation.

### **6.3. The Investigation of Hydrodynamic Parameters in case of Full Protection of Breakwater without Overtopping**

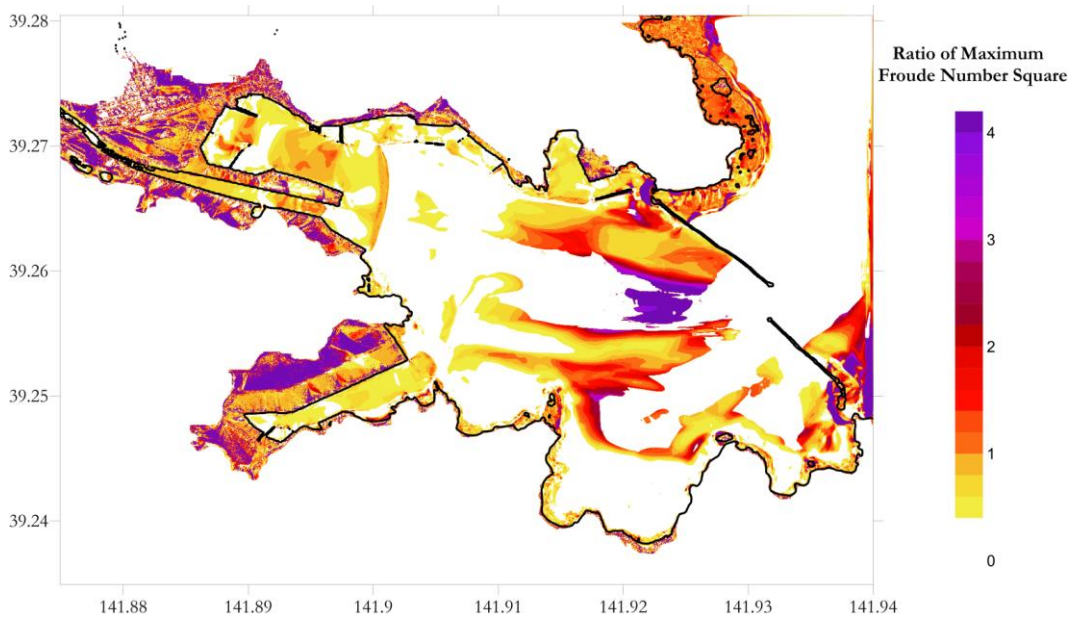
The previous section investigates the change of hydrodynamic parameters in relation with whether the bay is protected by breakwater or not. However, the wave overtopping is allowed, and the differences of current velocities and  $Fr^2$  between with and without breakwater cases can not reflect the actual effect of breakwaters resulting in the concentrated energy penetrating into the bay through the breakwater gap. For this reason, the hydrodynamic parameters are investigated in case of high crested breakwaters that do not allow overtopping. The crest height of breakwater is assigned 20m though it is not realistic.

Figure 6.13 shows the ratio of current velocity between the two cases of the existence of breakwater with 20m crest height that does not allow overtopping and the existence of none. The distribution of current velocity in the figure indicates that the fully concentrated energy due to the breakwater results in higher currents in some locations on the land. This means that, some parts of the residential area become vulnerable to tsunami attacks due to the effect of breakwaters and the gap between them at the entrance of the bay.

Similarly, Figure 6.14 shows the ratio of maximum  $Fr^2$  between the cases of fully protection of breakwater with no overtopping and no breakwater protection. The figure indicates that when the breakwater does not allow overtopping, the concentration of wave energy through the breakwater gap is more significant and results much higher values of  $Fr^2$  at some locations in residential area instantaneously.



**Figure 6.13:** The ratio of maximum current velocity between the cases of with breakwater of 20m crest height (no overtopping) and without breakwater



**Figure 6.14:** The ratio of maximum  $Fr^2$  between the cases of with breakwater of 20m crest height (no overtopping) and without breakwater

## CHAPTER 7

### GENERAL EVALUATION, DISCUSSION AND CONCLUSION

#### 7.1 General Discussion and Evaluation of the Results

The main objective of this study is to investigate the change of hydrodynamic parameters during tsunami inundation as a result of numerical modeling. The tsunami disasters of the last decade, 2004 Sumatra and 2011 Great East Japan events, taught us that the main cause of tsunami damage is the extremely strong currents occurring with corresponding high flow depths. When the waves climb up the land, the wave motion shows a different attribute that turns from its normal pattern into the open channel flow.

The numerical modeling method is used to simulate the wave propagation and inundation and to determine tsunami hydrodynamic parameters in inundation zone. The numerical code NAMI DANCE is modified and adapted to calculate hydrodynamic parameters for finer grid sizes accurately.

A governing parameter is introduced in this thesis representing flow behavior of tsunamis in inundation zone. The strong dragging forces are the major cause of damage tsunamis as they climb up to the land. Therefore, the drag force is normalized by hydrostatic force and a representing relation called *Hydrodynamic Demand* is obtained depending on the current velocity and flow depth. This term

simply equals to the square of Froude Number ( $Fr^2$ ) multiplied by the drag coefficient. Considering the same shape of the structures exposed to dragging force, the governing parameter was determined as Froude number ( $Fr$ ), the square of which has direct relationship with the tsunami energy, a major determinant of the level of damage on coastal areas.

The flow is called supercritical when the flow velocity is greater than the velocity of wave. The Froude Number is greater than 1 when supercritical flow occurs. Therefore, the values of square of Froude Number greater than 1 are more significant in this thesis to enable the determination of tsunami prone areas in residential areas. The claim of this thesis is to associate the tsunami damage with the maximum of square of Froude number ( $Fr_{max}^2$ ).

Based on the governing parameter  $Fr_{max}^2$  and other tsunami hydrodynamic parameters in inundation zone, the outcomes of this study are evaluated in two aspects. The first one is the effect of wave characteristics on the variation of hydrodynamic parameters. A series of numerical simulations were performed on the plain beach in order to obtain a correlation between the wave characteristics and average of  $Fr_{max}^2$  ( $\overline{Fr_{max}^2}$ ). The other aspect of evaluation is the performance of coastal protection structures against tsunami damage and the effect of building layout in residential areas on hydrodynamic parameters.

Such effects of wave characteristics as wave amplitude, wave period, wave shape and the effect of sea bottom were investigated quantitatively in Özer (2007). This thesis searched the correlation between the average values of hydrodynamic parameters and wave characteristics in inundation zone qualitatively.

The combined effect of wave characteristics was studied through the correlation analyses for the calculation of  $\overline{Fr_{max}^2}$  inland. The simulations of wave motion were performed with different wave heights and periods on different bottom slopes. The

analyses provide the maximum values of hydrodynamic parameters that occurred during the simulation time. However, some extreme values of current velocities and corresponding  $Fr^2$  may occur instantaneously when waves first inundate the land with strong currents but relatively low flow depths. There is also the boundary effect that may cause instant high values of  $Fr^2$ . In order to discard this situation, the  $\overline{Fr_{max}^2}$  observed during the simulation time is calculated on land by discarding an amount of area close to the upper and lower boundaries.

The outcomes of this study are compatible with the qualitative results in Özer (2007). As for the propagation of wave on plain beach, the simulations in this thesis reveal that average maximum of the water elevation, current velocity, flow depth and the square of Froude Number increase when the wave amplitude increases and the bottom slope gets milder. However, the hydrodynamic parameters show a descending trend when longer-period incoming wave is inputted.

A single sinusoidal wave is inputted both with leading elevation and leading depression front on the constant-sloped plain beach. The results show that wave period is the governing wave characteristics that affect the change of average  $Fr_{max}^2$  values. Five different wave heights with five different wave periods are inputted on four different bottom slopes. The maximum and average maximum of each hydrodynamic parameters are calculated. A correlation study is performed defining the average maximum of  $Fr^2$  as a function of wave height, wave period and bottom slope. The following relations are introduced (Eqns. [5.6] and [5.7]) in this thesis for leading elevation and leading depression single sinusoidal waves separately depending on various wave periods:

$$\overline{Fr_{max}^2} = 2.4 \log \left( \frac{H^2 \sqrt{\cot \beta}}{4T \sqrt{gd_c^3}} \right) + 29 \quad \text{for LEW} \quad [7.1]$$

$$\overline{Fr_{\max}^2} = 2.3 \log \left( \frac{H^2 \sqrt{\cot \beta}}{4T \sqrt{g d_c^3}} \right) + 27 \quad \text{for LDW} \quad [7.2]$$

It is stated that this relation is governed for the calculation of average  $Fr_{\max}^2$  valid for the runup of a single sinusoidal wave on a plain beach for leading elevation and depression wave forms, separately. Since the square of wave height represents wave energy, the relations for  $\overline{Fr_{\max}^2}$  in Eqns. [7.1] and [7.2] are said to be preferable among other correlations.

The runup of sinusoidal waves on a plain beach is investigated for both LEW and LDW cases and a correlation is derived between the normalized runup height and wave characteristics together with the beach slope. According to the results of analyses, the relations for the calculation of maximum runup of sinusoidal waves climbing on a plain beach are provided as in the following for LEW and LDW (as in Eqns. [5.9] and [5.10], respectively:

$$\ln \frac{Ru}{d_c} = 0.3 * \ln \left[ \left( \frac{H}{d_c} \right)^2 \frac{\sqrt{\cot \beta}}{4T \sqrt{(g/d_c)}} \right] + 0.8 \quad \text{for LEW} \quad [7.3]$$

$$\ln \frac{Ru}{d_c} = 0.3 * \ln \left[ \left( \frac{H}{d_c} \right)^2 \frac{\sqrt{\cot \beta}}{4T \sqrt{(g/d_c)}} \right] + 1.1 \quad \text{for LDW} \quad [7.4]$$

The other objective of this study is to determine the tsunami prone areas in residential areas exposed to tsunami attack. For this purpose, 22 different regular shaped test basins were prepared to simulate the tsunami inundation and calculate the maximum hydrodynamic parameters. The tsunami attack was modeled by inputting a single sinusoidal wave with three different wave periods on 1/20 bottom slope with the wave amplitude of 4m.

The test basins were prepared according to the measurement of the performance of coastal protection structures along the coasts with high possibility of exposure to tsunami attack. For this purpose, a residential area was formed including 3 rows of buildings, with 10 units in each. A seawall is placed along the coastline 10m ahead the first row of buildings and a breakwater is located 200m offshore. The buildings or other coastal protection structures are assumed to be fixed, rigid and stable against the wave attack. The maximum values of square of Froude Number are used to discuss the performance of coastal protection structures in different layouts.

The results of simulations prove that the performance of coastal protection structures is not significant if the waves can overtop the structures. This phenomenon is valid for the performance of both seawall and tsunami breakwaters. The protection structures may retard the tsunami flow through their incoming direction. The currents perpendicular to the structures may be reduced by the banking of structures. However, the waves take round the edges of the structures, grow in height and speed and climb up the land with current velocities in lateral direction. Those currents may cause high values of  $Fr_{\max}^2$  in some locations. Thus, it can be stated that the coastal protection structures may cause higher regional tsunami damage in inundation zone compared with unprotected beaches having the same slope. The wave energy that is interrupted by the seawall may penetrate to the land from the edge of the structure in a concentrated way and may cause damage at the backside of the residential areas that are far from the shoreline and supposed to be safer than other locations. The reason for this unpredicted damage is the high current velocities occurring in lateral direction.

In order to measure the effect of wave motion in lateral direction, the tests were performed by placing seawall along the shoreline from one end to the other. By that way, the water is not allowed to penetrate from the gaps at the two sides of the seawall. The results show that the waves overflow the seawall and inundate the land in a uniform pattern. The lateral motion is not significant.

According to the test results, this thesis provides evidence for the statement that the only way to assure a full protection against tsunami inundation is to prevent the wave overflow. If the wave amplitudes are higher than the structure height and thus can overflow the structure, the inundation of wave continues till its energy ends. Considering the high values of wave amplitudes in large scale tsunami events, we can say that it is required to construct seawalls with height crest elevations in order to prevent the overflow. It is not feasible to construct such a high concrete wall along the shoreline of a coastal town. This protection strategy directly blocks the relation between the sea and the residents, which is not a logical engineering solution. Hence, the most reasonable suggestion for coastal protection is to construct at-least-three-storey rigid structures along the coastal areas exposed to risk of tsunami attack.

The test results on different type of basins also show that the wave motion reaches a uniform pattern when the wave period gets larger. In other words, the layout of residential area or the existence of coastal protection structures are not important if the waves can overflow the structures and inundate the land. The water flows through every gap in its way till the wave energy runs out.

The wave shape effect is also tested by inputting leading depression sinusoidal wave on the following three different test basins: plain beach, unprotected residential area and the residential area fully protected with the seawall and offshore breakwater. It is observed that the sectional variation of hydrodynamic parameters are similar for LEW and LDW shapes. However, high values of  $Fr_{\max}^2$  is calculated for LDW in some locations. The reason is the difference of forward-backward motion due to the initial receding of the waves. Moreover, the initial receding of waves allows people time to evacuate from the inundation area since the time of observation of maximum water elevations is twice longer than the case for LEW.

LDW shape results in higher values of hydrodynamic parameters in some locations due to the difference in the momentum pattern. The accumulation of waves at the backside of the buildings is also observed for LDW shape.

The runup of N-wave on a sloping beach computed by NAMI DANCE is compared with some analytical approaches in literature. The results show that the calculations of NAMI DANCE for the runup of N-wave on a sloping beach are very consistent with the analytical approaches.

The effect of Manning's coefficient is tested in this thesis. For this purpose, the Manning's coefficient is inputted as it varies spatially in the study domain. The different values of friction are considered for the sea, the land and the residential area and are inputted at every grid node of the basin.

A case study is performed in Kamaishi Bay by simulating March 11, 2011 Great East Japan Tsunami. According to the results of the study, the similarity between then pattern of square of Froude Number and current velocity obtained in this study can also indicate that these parameters must be included in tsunami hazard assessment studies together with the water elevations.

Depending on the outcomes of case study, it can be stated that when a breakwater is constructed for the protection of a bay or a semi-enclosed area against tsunami attacks, an assessment of the changes in flow pattern by tsunami should be assessed by mathematical modeling at the design stage.

## 7.2 Summary of the Results and Conclusion

What follows is the summary of the results:

1. The main tsunami parameters at shallow region and inundation zone are the maximum values of wave amplitude, flow depth, current velocities, square of Froude Number and inundation distance.
2. The dimensionless parameter, square of Froude Number ( $Fr^2$ ), takes an important role governing the level of impact forces on the structures and the determination of tsunami prone areas in residential areas.
3. There is a correlation between the bottom slope and square of Froude Number. Lower square of Froude Number values occur on steeper slopes comparing to milder slope.
4. A more uniform distribution of square of Froude Number occurs during the inundation of longer-period tsunami waves.
5. The runup of sinusoidal waves climbing on plain beaches increases for the shorter-period waves.
6. The wave motion during tsunami propagation in the deep sea turns into an open flow at shallower regions and land when the period gets longer.
7. The higher amplitude of incoming tsunami causes a stronger tsunami attack according to the higher values of square of Froude Number.
8. The impacts of leading depression wave (LDW) are higher than the impacts of leading elevation wave (LEW).
9. The time of occurrence of highest impact by LDW is later comparing to the time of occurrence of highest impact in case of LEW

10. More scarcely distributed buildings or roads provide more inland penetration of wave and higher effects
11. The motion of wave in lateral direction between the buildings may be important if the buildings are rigid and stable.
12. The crest elevation (height) of coastal protection structures, e.g. seawall or offshore breakwater, is important for the reduction of tsunami damage. When tsunami overtops on these structures, the tsunami effect cannot be reduced significantly.
13. Due to the diffraction of tsunami wave at the tips of the shore-parallel structures (either offshore breakwater or seawall), higher tsunami impact occur at the backside of the structure tips. Therefore, the length of these shore-parallel coastal protection structures must be determined properly in order to avoid an additional diffraction effect in protected coastal areas.
14. The spatial distribution of bottom friction may be included in the modeling. There are minor changes of maximum  $Fr^2$  values when spatial distribution of bottom friction is considered.
15. The changes in the tsunami flow pattern should be assessed by numerical modeling at the design stage when a breakwater is constructed for the protection of a bay against tsunami attack.

The results of analyses in this thesis point to the fact that, when the longer-period waves inundate the residential areas, uniformity is observed in the behavior of waves for all configurations of layout in inundation zone. Tsunami damage occurs in any way even when the buildings are located near each other or distant from each other. The same inference is repeated here that the most feasible strategy to protect the coastal areas against tsunami damage is to build rigid buildings with at least three storeys. It is also essential to plan the tsunami evacuation roads in the coastal areas properly to mitigate the severity of a disaster.

## CHAPTER 8

### SUGGESTIONS FOR FURTHER STUDIES

In this study, the distributions and sectional changes of hydrodynamic parameters, i.e. maximum water elevation, maximum current velocities and maximum hydrodynamic demands, were investigated in inundation zone on bottom slopes of 1/10, 1/15, 1/20 and 1/25, with different wave heights, with the wave shapes of LEW and LDW, for the wave periods of 3min, 6min, 12min, 24min and 48min. The tsunami hydrodynamic parameters are investigated on both plain beaches and test basins with different layout of structures. A single sinusoidal wave was propagated in inundation zone to identify a correlation between average maximum square of Froude Number and wave characteristics together with the beach slope.

It is suggested that further studies should be performed by using different wave shapes to be able to generalize the numerical results to more diverse situations. The analyses can be performed by increasing the number of incoming waves.

Various orientations and greater amount of coastal and land structures can also be used in simulations to investigate the distribution of hydrodynamic parameters and make a broader generalization for the tsunami prone areas in residential areas.

The wave propagation can be simulated with different incoming directions. By that way, the effect of wave characteristics can be interpreted by multidirectional evaluations. The structural vulnerability can also be included in the modeling to determine the level of damage.

This study indicates that there is proportionality with experimental and numerical results of wave front velocity. However, only one experiment is not sufficient for comparison. Therefore, it is necessary to make additional experiments to determine wave front velocity and current velocity for further comparisons. These experiments will also enable us to discover hydrodynamic demands by using both current velocities and wave front velocities and discuss the distribution of this ratio to see which velocity is more effective at which location of the inundation zone. An experimental study is necessary to verify, and carry out more reliable comparisons and discussions.

## REFERENCES

- Arikawa, T. (2009). *Structural Behavior under Impulsive Tsunami Loading*, Journal of Disaster Research, Vol.4 No.6, Dec. 2009, pp. 377-381.
- Aydin, B. and Kânoğlu, U. (2007). *Wind set-down relaxation*, Computer Modeling in Engineering and Sciences (CMES), 21(2), pp. 149-155.
- Borrero J.C., Yalciner, A.C., Kanoğlu, U., Titov, V., McCathy, D., Synolakis, C.E. (2003). *Producing tsunami inundation maps in California, Submarine Landslides and Tsunamis*, Kluwer Academic Publishers, Dordrecht, pp. 315-329.
- Cabinet Office of Japanese National Government (2004). *Tsunami Simulation Methodology*, Homepage of CAO (in Japanese)
- Carstensen, S., Sumer, B.M., Fredsøe, J. (2010). *Coherent Structures in Wave Boundary Layers. Part 1. Oscillatory Motion*, J. Fluid Mech., Vol. 646, pp. 169-206.
- Choi, B.H., Hong, S.J., Hwang, D., Hidayat, R., Kaistrenko, V., Korolev, Yu., Kurkin, A., Pelinovsky, E., Polukhin, N., Prasetya, G., Razzhigaeva, N., Subandono, D., Yalciner, A.C., Yoon, S.B., and Zaitsev, A. (2005). *Catastrophic Tsunami in the Indian Ocean (December 26, 2004): Data of Two Field Surveys and Numerical Simulation*, Sumatra Tsunami on 26<sup>th</sup> December, 2004, Proceedings of the Special Asia Tsunami Session at APAC 2005, editors: Choi, B.H., Imamura, F., ISBN: 89-5708-082-1 98530, pp. 159-187
- Coastal Engineering Committee, Japan (2011). *Tsunami height distribution*, <http://www.coastal.jp/tjit/index.php?%E7%8F%BE%E5%9C%B0%E8%AA%BF%E6%9F%BB%E7%B5%90%E6%9E%9C>

Dao, M.H. and Tkalich, P. (2007). Tsunami Propagation Modeling- A Sensitivity Study, Nat. Hazards Earth Syst. Sci., Vol. 7, pp. 741-754

Demirbas, E. (2002). *Comparison of Analytical and Numerical Approaches for Long Wave Runup*, M.Sc. Thesis, Middle East Technical University, 72 pages.

Ergin, A. and Balas, C. E. (2006). "Damage Risk Assessment of Breakwaters under Tsunami Attack", Nat Hazards (2006), Vol. 39, pp. 231–243, DOI 10.1007/s11069-006-0025-7

Franchello, G. and Krausmann, E. (2008). *HyFlux2: A Numerical Model for the Impact Assessment of Severe Inundation Scenario to Chemical Facilities and Downstream Environment*, Scientific and Technical Research Series, European Commission, JRC 36005, EUR 23354 EN, ISBN 1018-5593, 15 pages

Fujima, K. (2009). *Necessity of advanced Tsunami Damage Index*, Proceedings of the 6th International Workshop on Coastal Disaster Prevention, Bangkok, Thailand, December 1-2, 2009, pp. 61-70.

Geospatial Information Authority, Japan (2011). *Tsunami inundation map*, Retrieved from <http://www.gsi.go.jp/kikaku/kikaku60003.html>

Goto C., Ogawa, Y., Shuto, N., Imamura, F. (1997). *IUGG/IOC TIME Project: Numerical Method of Tsunami Simulation with the Leap-Frog Scheme*, Intergovernmental Oceanographic Commission of UNESCO, Manuals and Guides # 35, Paris, 4 Parts

IMAMURA, F. (1989). *Tsunami Numerical Simulation with the Staggered Leap-Frog Scheme (Numerical Code of TUNAMI-N1)*, School of Civil Engineering, Asian Inst. Tech. and Disaster Control Research Center, Tohoku University

Imamura, F. (1995). *Numerical Method of Tsunami Simulation with the Leap-Frog Scheme, Part 2: Propagation in the Ocean in the Spherical Coordinates, TUNAMI-F1 and its Program List*, Sendai-Japan

Imamura, F. (1996). *Review of Tsunami Simulation with a Finite Difference Method*, Long-Wave Runup Models, Proceedings of the International Workshop, Friday Harbour,

USA, 12-17 September 1995 by World Scientific Publishing Co Pte Ltd., Eds. Yeh, H., Liu, P. and Synolakis, C., pp. 25-42

Imamura, F., Koshimura, S., Murashima, Y., Akita, Y., Shintani, Y. (2011). *The 2011 East Japan off the Pacific coast Earthquake and Tsunami, Tohoku University Source Model version 1.1*, Sendai, Miyagi, Japan: Disaster Control Research Center

Iwate-Miyagi-Fukushima Province, Japan, (2011), *Observed Tsunami around Iwate-Miyagi-Fukushima Province*, Retrieved from [http://www.jma.go.jp/jma/en/2011\\_Earthquake/2011\\_Earthquake\\_Tsunami.pdf](http://www.jma.go.jp/jma/en/2011_Earthquake/2011_Earthquake_Tsunami.pdf)

JMA (2011), Japan Meteorological Agency, Retrieved from [http://www.jma.go.jp/jma/en/2011\\_Earthquake.html](http://www.jma.go.jp/jma/en/2011_Earthquake.html)

Kamaishi Port Office, (2011), Retrieved from <http://www.pa.thr.mlit.go.jp/kamaishi/bousai/index.html>

Kanoglu, U. (2004). *Nonlinear Evolution and Runup-Rundown of Long Waves over a Sloping Beach*, J. Fluid Mech., Vol. 513, pp. 363-372

Kanoglu, U., and Synolakis, C.E., (1998). *Long Wave Runup on Piecewise Linear Topographies*, J. Fluid Mech., Vol. 374, pp. 1-28

Koizumi T., (2011) “*The Tohoku Tsunami of 11th March: the Response of Tsunami Early Warning Systems and the Tsunami Analysis*” – Takeshi Koizumi (JMA); UNESCO/IOC Tsunami and Civil Protection Workshop: “Tsunami hazard in the North-eastern Atlantic, the Mediterranean and connected seas (NEAM region) – A challenge for Science and Civil protection”; 15-16 June, JRC-Ispra, Italy

Koketsu, K., Yokota, Y., Nishimura, N., Yagi, Y., Miyazaki, S., Satake, K., Fujii, Y., Miyake, H., Sakai, S., Yamanaka, Y. and Okada, T., (2011). “*A Unified Source Model for the 2011 Tohoku Earthquake*”, Earth and Planetary Science Letters, doi: 10.1016/j.epsl.2011.09.009, Vol. 310 (2011), pp. 480-487.

Koshimura, S., Namegaya, Y. and Yanagisawa, H., (2009). “*Tsunami fragility – A new measure to identify tsunami damage*”, Journal of Disaster Research, Vol.4 No.6, 2009, pp. 404-409

Kotani, M, F. Imamura and N. Shuto (1999) Tsunami run-up simulation and damage estimation method using GIS. Coastal Engineering, Vol. 45, pp.356-360 (in Japanese)

Kurkin A.A., Kozelkov A.c., Zaitsev A.I., Zahibo N., and Yalciner A.C., (2003). *Tsunami risk for the Caribbean Sea Coast*, Izvestiya, Russian Academy of Engineering Sciences, vol. 4, pp. 126 – 149 (in Russian)

LeVeque and George, D. L. (2008). *High Resolution Finite Volume Methods For The Shallow Water Equations with Bathymetry and Dry States*, in Advanced Numerical Models for Simulating Tsunami Waves and Runup (Eds. Liu, Yeh and Synolakis), World Scientific Publishing Co. Pte. Ltd., Singapore, Chapter 2, pp. 43-74

Liu, P. L.-F., Cho, Y.-S. Yoon, S.B., Seo. S.N. (1994). *Numerical Simulations of the 1960 Chilean Tsunami Propagation and Inundation at Hilo, Hawaii*, Recent Development in Tsunami Research, pages 99–115, Kluwer Academic Publishers, 1994.

Liu, P.L.-F., Cho, Y.-S., Briggs, M.J., Kanoglu, U., and Synolakis, C.E. (1995). *Run-up of Solitary Waves on a Circular Island*, J. Fluid Mech., Vol. 320, pp. 259-285

Liu, P. L.-F., Woo, S-B., Cho, Y.-S. (1998). *Computer Programs for Tsunami Propagation and Inundation*, Technical report, Cornell University, 1998

Munson, B., Young, D., Okiishi, T., (2002). *Fundamentals of Fluid Mechanics*, 4<sup>th</sup> Ed., Wiley 2002

NAMI DANCE (2011). *Manual of Numerical Code NAMI DANCE*, Published in <http://namidance.cc.metu.edu.tr>

NOAA (2012), National Data Buoy Center of NOAA, last visited: March 18, 2012, Retrieved from <http://www.ndbc.noaa.gov/dart.shtml>

- Okada, Y. (1985). *Surface Deformation Due to Shear and Tensile Faults in a Half-Space*, Bull. Seis. Soc. Am., Vol. 75, No.4, pp. 1135-1154, August 1985
- Onishi, N. (2011). *Japan Revives a Sea Barrier That Failed to Hold*, an article in The New York Times, [http://www.nytimes.com/2011/11/03/world/asia/japan-revives-a-sea-barrier-that-failed-to-hold.html?\\_r=1&emc=eta1](http://www.nytimes.com/2011/11/03/world/asia/japan-revives-a-sea-barrier-that-failed-to-hold.html?_r=1&emc=eta1), Nov. 2, 2011
- OYO, (2007). *Simulation and Vulnerability Analysis of Tsunamis Affecting the Istanbul Coasts*, Project report performed for Istanbul Metropolitan Municipality by Oyo Int. Co, Japan.
- Ozer, C. (2007). *Investigation of Hydrodynamic Demands of Tsunamis in Inundation Zone*, M.Sc. Thesis, Middle East Technical University, Ankara, Turkey, 2007, 124 pages.
- Ozer, C., Karakus, H., Yalciner, A.C. (2008). *Investigation of Hydrodynamic Demands of Tsunamis in Inundation Zone*, Proceedings of 7<sup>th</sup> International Conference on Coastal and Port Engineering in Developing Countries, Dubai, UAE, February 24-28, 2008
- Ozer, C. and Yalciner, A.C. (2011). *Sensitivity Study of Hydrodynamic Parameters during Numerical Simulations of Tsunami Inundation*, Pure Appl. Geophys., Springer Basel AG, DOI 10.1007/s00024-011-0290-6
- PARI (The Port and Airport Research Institute, Japan) (2011). *Executive Summary of Urgent Field Survey of Earthquake and Tsunami Disasters by the 2011 off the Pacific coast of Tohoku Earthquake*, March 25, 2011
- Peregrine, D.H. (1972). *Equations for water waves and the approximation behind them*, in: Waves on Beaches and Resulting Sediment Transport, Proceedings of an Advanced Seminar Conducted by the Mathematics Research Center, New York, Academic Press, New York, 1972, pp. 95-121
- Sato, S., (1996). "Numerical Simulation of 1993 Southwest Hokkaido Earthquake Tsunami Around Okushiri Island", Journal of Waterway, Port, Coastal, and Ocean Engineering, September/October 1996, pp. 209-215

- Shuto, N., Goto C., Imamura, F., (1990). *Numerical Simulation as a Means of Warning for Near-field Tsunamis*, Coastal Engineering in Japan, Vol. 33(2), pp. 173-193
- Shuto, N. (1991). *Numerical Simulation of Tsunamis- Its Present and Near Future*, Natural Hazards, Vol. 4, pp. 171-191
- Shuto, N. (2009). *Damage to Coastal Structures by Tsunami-Induced Currents in the Past*, Journal of Disaster Research, Vol.4, No.6, 2009, pp. 462-468
- Sumer, B.M., Jensen, P.M., Sørensen, L.B., Fredsøe, J., Liu, P. L.-F., Carstensen, S., (2010). *Coherent Structures in Wave Boundary Layers. Part 2. Solitary Motion*, J. Fluid Mech., Vol. 646, pp. 207-231.
- Sumer, B.M., Ansal, A., Cetin, K.O., Damgaard, J., Gunbak, A.R., Ottesen Hansen, N-E., Sawicki, A., Synolakis, C.E., Yalciner, A.C., Yuksel, Y., Zen, K. (2007). *Earthquake-Induced Liquefaction around Marine Structures*, J. of Waterway Port, Coastal and Ocean Engineering, ASCE, doi: 10.1061/ (ASCE)0733-950X(2007), 133:1(55)
- Sumer, M. and Fredsøe, J. (1997). *Hydrodynamic Around Cylindrical Structures*, World Scientific, 530 pages.
- Suppasri, A., Imamura, F. and Koshimura, S. (2011a). *The 2011 East Japan Earthquake and Tsunami Damage*, in: Proceedings of the 4th National Convention on Water Resource Engineering, Thailand (WRECON2011), Invited paper, 18 August 2011.
- Suppasri, A., Muhari, A. and Imamura, F. (2011b). *JST-JICA and RISTEK Indonesia: Guide Book of the 2011 Tsunami Field Trip in Sendai*, 12 pages.
- Suzuki, T. and Arikawa, T. (2010). *Numerical Analysis of Bulk Drag Coefficient in Dense Vegetation by Immersed Boundary Method*, Proceedings of 32<sup>nd</sup> International Conference on Coastal Engineering (ICCE 2010), Shanghai, China, June 30 – July 5, 2010
- Synolakis, C.E. (1986). *The Run-up of Long Waves*, Ph. D. Thesis, California Institute of Technology, Pasadena, California, 91125, 228 pages
- Synolakis, C.E. (1987). *Run-up of Solitary Waves*, J. Fluid Mech., Vol. 185, pp. 523-545.

Synolakis, C.E. (2003). *Tsunami and Seiche*, in *Earthquake Engineering Handbook*, W.F. Chen and C. Scawthorn (eds), CRC Press, New York, 9-1 to 9-99.

Synolakis, C. and Bernard, E. (2006). *Tsunami Science before and beyond Boxing Day 2004*, Phil. Trans. R. Soc. A 2006, Vol. 364, pp. 2231-2265, doi: 10.1098/rsta.2006.1824

Synolakis, C., Bernard, E.N., Titov, V.V., Kanoglu, U. and Gonzalez, F.I. (2008). *Validation and Verification of Tsunami Numerical Models*, Pure Appl. Geophys., Vol. 165, pp. 2197-2228

Tadepalli, S. and Synolakis, C.E. (1994). *The Run-up of N-Waves on Sloping Beaches*, Proc. R. Soc. Lond. A, Vol. 445, pp. 99-112

Takahashi, T. (1996). *Benchmark Problem 4: The 1993 Okushiri Tsunami- Data, Conditions and Phenomena*, Long-Wave Runup Models, Proceedings of the International Workshop, Friday Harbour, USA, 12-17 September 1995 by World Scientific Publishing Co Pte Ltd., Eds. Yeh, H., Liu, P. and Synolakis, C., pp. 383-403

Takahashi, S., Kuriyama, Y., Takashi, T., Kawai, Y., Arikawa, T., Tatsumi, D., Negi, T. (2011). *Urgent Survey for 2011 Great East Japan Earthquake and Tsunami Disaster in Ports and Coasts – Part I (Tsunami)*, An English Abstract of Technical Note of Port and Airport Research Institute, No: 1231, April 28, 2011

Thaker, W.C. (1981). *Some Exact Solutions to the Nonlinear Shallow-water Wave Equations*, J. Fluid Mech., Vol. 107, pp. 499-508.

The Overseas Coastal Area Development Institute of Japan (OCDI) (2002). *Technical Standards and Commentaries for Port and Harbor Facilities in Japan*, editors for translation version: Goda, Y., Tabata, T., Yamamoto, S., printed by Daikousha Printing Co., Ltd.

Titov, V.V. and Synolakis, C.E. (1998). *Numerical modeling of tidal wave run-up*, Journal of Waterway, Port, Coastal and Ocean Engineering, Vol. 124 (4), pp. 157-171.

TUNAMI-N2 (2001). *“Tsunami Modelling Manual (Tunami Model)”* by Imamura, F., Yalciner, A. C. and Ozyurt, G.

Vreugdenhil, C.B. (1994). *Numerical Methods for Shallow-Water Flow*, Water Science and Technology Library, Vol. 13, Kluwer Academic Publishers, 1994, ISBN 0-7923-3164-8

Yalciner, A.C., Synolakis, C.E., Alpar, B., Borrero, J., Altinok, Y., Imamura, F., Tinti, S., Ersoy, Ş., Kuran, U., Pamukcu, S., Kanoglu, U. (2001). *Field Surveys and Modeling 1999 Izmit Tsunami*, International Tsunami Symposium ITS 2001, Paper 4-6, Seattle, Washington, pp. 557-563

Yalciner, A.C., Alpar, B., Altinok, Y., Ozbay, I., Imamura, F. (2002). *Tsunamis in the Sea of Marmara: Historical Documents for the Past, Models for Future*, Marine Geology, 2002, 190, pp. 445-463

Yalciner, A.C., Pelinovsky, E., Synolakis, C., Okal, E. (2003). *NATO SCIENCE SERIES, Submarine Landslides and Tsunamis*, Publisher: Kluwer Academic Publishers, Netherlands, (Editors; Yalciner, A.C., Pelinovsky, E., Synolakis, C., Okal, E.), 329 Pages, ISBN: 1-4020-1348-5 (HB), ISBN: 1-4020-1349-3 (PB)

Yalciner, A., Pelinovsky, E., Talipova, T., Kurkin, A., Kozelkov, A. and Zaitsev, A. (2004). *Tsunamis in the Black Sea: Comparison of the Historical, Instrumental, and Numerical Data*, J. Geophys. Res., AGU, V 109, C12023, doi:10.1029/2003JC002113

Yalciner, A.C., Perincek, D., Ersoy, S., Prasetya, G., Rahman, H., McAdoo, B. (2005). *Report on January 21-31, 2005 North Sumatra Survey on December 26, 2004 Indian Ocean Tsunami*, by ITST of UNESCO IOC. Publ. in <http://ioc.unesco.org/iosurveys/Indonesia/yalciner/yalciner.htm>

Yalciner, A.C. and Pelinovsky, E. (2007). *A Short Cut Numerical Method for Determination of Resonance Periods of Free Oscillations in Irregular Shaped Basins*, Ocean Engineering, Vol. 34, Issues 5–6, April 2007, pp. 747-757

Yalciner, A.C., Ozer, C., Karakus, H., Zaytsev, A., Guler, I. (2010). *Evaluation of Coastal Risk at Selected Sites against Eastern Mediterranean Tsunamis*, Proceedings of 32<sup>nd</sup> International Conference on Coastal Engineering (ICCE 2010), Shanghai, China, June 30 – July 5, 2010

Yalciner, A.C., Suppasri, A., Mas, E., Kalligeris, N., Necmioglu, O., Imamura, F., Ozer, C., Zaitsev, A., Ozel, N.M., Synolakis, C. (2012). *Field Survey on the Coastal Impacts of March 11, 2011 Great East Japan Tsunami*, Pure Appl. Geophys., 2012 (in review)

Yeh, H., (2006). *Tsunami Forces in the Runup Zone*, NSF Caribbean Tsunami Workshop, World Scientific, Editors: Mercado-Irizarry, A., Liu, P., pp. 275-287

Yeh, H., Liu, P-L.F., Synolakis, C.E. (1996). *Long Wave Runup Models*, World Scientific, London.

Zahibo, N., Pelinovsky, E., Yalciner, A.C., Kurkin, A., Kozelkov, A., Zaitsev, A. (2003). *Modeling the 1867 Virgin Island Tsunami*, Journal of Natural Hazards and Earth System Sciences, European Geosciences Union, 3, June-2003, pp. 367-376

Zaitsev, A.I., Kozelkov, A.C., Kurkin, A.A., Pelinovsky, E.N., Talipova, T.G., Yalciner, A.C. (in Russian order of alphabet) (2002). *Tsunami Modeling in Black Sea*, published in Izvestiya of Russian Academy of Engineering Sciences, Series: Applied Mathematics and Mechanics, 2002, Vol. 3, pp. 27-45

Zaitsev, A., Yalciner, A.C., Pelinovsky, E., Kurkin, A., Ozer, C., Insel, I., Karakus, H., Ozyurt, G. (2008). *Tsunamis in Eastern Mediterranean, Histories, Possibilities and Realities*, Proceedings of 7<sup>th</sup> International Conference on Coastal and Port Engineering in Developing Countries, Dubai, UAE, February 24-28, 2008

Zhao, X., Wang, B., Liu, H. (2010). *Propagation and Runup of Tsunami Waves with Boussinesq Model*, Proceedings of 32nd International Conference on Coastal Engineering (ICCE 2010), Shanghai, China, June 30 – July 5, 2010

## APPENDIX A

By omitting the non-linear terms in the previous equations, the Linear Shallow Water Equations are obtained. NAMI DANCE can use these equations in deep sea propagation up to the water depth of 50m, when the simulation area is so large i.e. in an entire ocean basin. These LSWE are therefore expressed as in the following:

$$\frac{\partial \eta}{\partial t} + \frac{\partial M}{\partial x} + \frac{\partial N}{\partial y} = 0 \quad [\text{A.1}]$$

$$\frac{\partial M}{\partial t} + gD \frac{\partial \eta}{\partial x} = 0 \quad [\text{A.2}]$$

$$\frac{\partial N}{\partial t} + gD \frac{\partial \eta}{\partial y} = 0 \quad [\text{A.3}]$$

It should be noted that both Linear and Non-Linear SWE are non-dispersive. If we include the dispersion terms in Eqns. [3.20] and [3.21] in Chapter 3, Non-Linear Dispersive Shallow Water Equations known as the Boussinesq Model are obtained (Peregrine, 1972).

The NSW E including dispersive terms are given in the following:

$$\frac{\partial \eta}{\partial t} + \frac{\partial M}{\partial x} + \frac{\partial N}{\partial y} = 0 \quad [\text{A.4}]$$

$$\frac{\partial M}{\partial t} + \frac{\partial}{\partial x} \left( \frac{M^2}{D} \right) + \frac{\partial}{\partial y} \left( \frac{MN}{D} \right) + gD \frac{\partial \eta}{\partial x} + \frac{\tau_x}{\rho} = \frac{\partial \psi}{\partial x} \quad [\text{A.5}]$$

$$\frac{\partial N}{\partial t} + \frac{\partial}{\partial x} \left( \frac{MN}{D} \right) + \frac{\partial}{\partial y} \left( \frac{N^2}{D} \right) + gD \frac{\partial \eta}{\partial y} + \frac{\tau_y}{\rho} = \frac{\partial \psi}{\partial y} \quad [\text{A.6}]$$

Where

$$\psi = \frac{h^2}{3} \left( \frac{\partial^2 u}{\partial x \partial t} + \frac{\partial^2 v}{\partial y \partial t} \right) \quad [\text{A.7}]$$

The dispersion term may be important when the wave amplifies near the shore and also when the waves propagate very long distances in the ocean.

The previous given NSWE are derived in Cartesian coordinate system. For far-field tsunamis, it is more reliable to formulate the governing equations in spherical coordinates. When the propagation distance gets longer, Coriolis force which triggers the effect caused by the rotation of the Earth and the inertia of the mass experiencing the effect may be important and affect the values of wave amplitudes and arrival time of first wave. Therefore, the NSWE are governed in spherical coordinate system expressed as:

$$\frac{\partial \eta}{\partial t} + \frac{1}{R \cos \phi} \left[ \frac{\partial M}{\partial \lambda} + \frac{\partial (N \cos \phi)}{\partial \phi} \right] = 0 \quad [\text{A.8}]$$

$$\begin{aligned} \frac{\partial M}{\partial t} + \frac{1}{R \cos \phi} \frac{\partial}{\partial \lambda} \left( \frac{M^2}{D} \right) + \frac{1}{R} \frac{\partial}{\partial \phi} \left( \frac{MN}{D} \right) + \frac{gd}{R \cos \phi} \frac{\partial \eta}{\partial \lambda} + \frac{\tau_\lambda}{\rho} = \\ \frac{gd}{R \cos \phi} \frac{\partial h}{\partial \lambda} + (2\omega \sin \phi)N + \frac{1}{R \cos \phi} \frac{\partial d\omega}{\partial \lambda} \end{aligned} \quad [\text{A.9}]$$

$$\begin{aligned} \frac{\partial N}{\partial t} + \frac{1}{R \cos \phi} \frac{\partial}{\partial \lambda} \left( \frac{MN}{D} \right) + \frac{1}{R} \frac{\partial}{\partial \phi} \left( \frac{N^2}{D} \right) + \frac{gd}{R} \frac{\partial \eta}{\partial \phi} + \frac{\tau_\phi}{\rho} = \\ \frac{gd}{R} \frac{\partial h}{\partial \phi} - (2\omega \sin \phi)M + \frac{1}{R} \frac{\partial d\psi}{\partial \phi} \end{aligned} \quad [\text{A.10}]$$

Where R is the radius of earth taken as 6378.137km and  $\omega$  is the angular velocity of the earth taken as  $7.27 \times 10^{-3}$  rad/s

## APPENDIX B

**Table B.1:** Water surface elevations calculated by NAMI DANCE at the selected DART buoys during the simulation of March 11, 2011 Great East Japan tsunami

Time(min)	Water surface Elevation (m)			
	DART_21401	DART_21418	DART_21419	DART_46403
0	0.05	0.20	0.03	0.01
1	0.05	0.21	0.02	0.02
2	-0.01	0.09	0.00	0.01
3	0.28	0.12	-0.04	0.01
4	-0.36	0.08	-0.06	0.01
5	-0.03	0.19	-0.07	0.02
6	0.06	0.00	-0.32	0.01
7	-0.01	-0.28	-0.05	0.01
8	-0.08	-0.18	-0.02	0.01
9	-0.01	-0.15	0.00	0.01
10	-0.02	-0.30	-0.04	0.00
11	-0.06	0.48	-0.14	0.01
12	-0.02	0.00	0.23	0.02
13	-0.09	0.10	-0.30	0.01
14	-0.04	-0.07	-0.03	0.01
15	0.05	0.02	-0.06	0.01
16	0.04	0.00	0.03	0.02
17	-0.08	0.02	-0.05	0.01
18	0.04	-0.02	0.01	0.01
19	-0.06	0.04	-0.10	0.01
20	-0.09	0.00	0.00	0.01
21	-0.06	0.00	0.00	0.00
22	-0.03	0.01	-0.02	0.01
23	-0.07	-0.01	-0.01	0.02
24	-0.03	-0.01	-0.02	0.01
25	0.05	0.00	-0.01	0.01
26	-0.02	-0.02	-0.04	0.01
27	-0.05	0.01	-0.01	0.02
28	0.03	0.10	0.04	0.01
29	-0.05	0.00	-0.08	0.01
30	-0.05	0.22	0.00	0.01
31	-0.03	0.37	-0.10	0.01
32	0.02	1.04	0.00	0.00
33	-0.07	1.56	0.02	0.01
34	-0.04	1.86	-0.02	0.02
35	-0.04	1.29	-0.03	0.01
36	0.02	0.09	0.00	0.01
37	-0.03	-0.30	-0.02	0.01
38	-0.07	-0.19	-0.04	0.02
39	0.04	-0.17	-0.02	0.01
40	-0.04	-0.14	0.01	0.01

41	0.00	-0.95	-0.04	0.01
42	-0.05	-0.33	-0.03	0.01
43	-0.02	-0.07	0.01	0.00
44	-0.03	-0.61	-0.01	0.01
45	-0.05	-0.40	-0.02	0.02
46	0.01	-0.18	-0.06	0.01
47	-0.04	-0.68	0.05	0.01
48	-0.03	-0.04	-0.04	0.02
49	0.02	-0.13	-0.03	0.02
50	-0.02	-0.41	0.05	0.01
51	-0.04	0.00	-0.02	0.01
52	0.01	-0.21	-0.01	0.01
53	-0.06	-0.18	0.03	0.01
54	-0.01	-0.17	-0.03	0.00
55	0.00	-0.28	-0.02	0.01
56	0.00	-0.05	0.01	0.00
57	-0.02	-0.32	0.02	0.00
58	0.00	-0.08	-0.04	0.01
59	0.11	-0.18	0.00	0.00
60	0.11	-0.14	0.02	0.00
61	0.20	-0.11	0.01	0.00
62	0.29	-0.11	0.01	0.01
63	0.33	-0.06	0.00	-0.01
64	0.38	-0.06	0.03	0.00
65	0.49	-0.07	-0.05	0.00
66	0.62	-0.08	0.03	0.00
67	0.67	-0.09	0.01	0.00
68	0.57	-0.11	0.01	0.00
69	0.35	-0.06	-0.03	-0.01
70	0.22	0.03	0.05	0.00
71	0.18	0.07	-0.02	0.00
72	0.22	-0.02	0.01	-0.01
73	0.12	-0.08	-0.01	-0.01
74	-0.04	0.01	0.04	0.00
75	-0.16	-0.04	0.01	-0.01
76	-0.22	-0.05	0.02	-0.01
77	-0.24	0.01	0.01	0.00
78	-0.26	-0.01	0.00	-0.02
79	-0.20	-0.05	0.03	-0.01
80	-0.12	0.02	0.04	-0.01
81	-0.15	0.02	0.00	-0.02
82	-0.11	-0.03	0.03	-0.01
83	-0.07	0.06	0.06	-0.02
84	-0.02	0.06	0.05	-0.01
85	-0.04	0.08	0.09	-0.01
86	0.02	0.05	0.10	-0.02
87	0.09	0.06	0.15	-0.01
88	-0.01	0.04	0.17	-0.02
89	0.01	0.02	0.26	-0.01
90	-0.02	0.01	0.30	-0.02
91	-0.08	0.02	0.39	-0.01
92	-0.07	-0.02	0.41	-0.01
93	0.00	-0.02	0.53	-0.02
94	-0.07	-0.06	0.58	-0.02
95	-0.08	-0.10	0.54	-0.01
96	-0.07	-0.07	0.45	-0.02

97	-0.04	-0.04	0.30	-0.01
98	-0.07	-0.03	0.18	-0.01
99	-0.10	0.01	0.13	-0.02
100	-0.08	-0.04	0.15	-0.01
101	-0.08	-0.04	0.19	-0.01
102	-0.10	-0.01	0.08	-0.02
103	-0.09	-0.02	-0.12	-0.01
104	-0.08	-0.03	-0.21	-0.01
105	-0.08	0.00	-0.19	-0.01
106	-0.06	-0.03	-0.13	-0.02
107	-0.09	-0.09	-0.09	-0.01
108	-0.12	-0.10	-0.09	-0.01
109	-0.06	-0.10	-0.05	-0.01
110	-0.06	-0.04	-0.02	-0.01
111	-0.04	0.05	-0.01	-0.01
112	0.00	0.02	-0.04	-0.01
113	0.00	0.00	0.04	-0.02
114	-0.01	-0.06	0.06	-0.01
115	0.01	-0.07	-0.04	-0.01
116	0.05	-0.01	-0.06	-0.01
117	0.00	-0.01	0.01	-0.01
118	0.03	0.04	-0.01	-0.01
119	0.02	0.06	-0.07	-0.02
120	0.06	0.07	0.02	-0.01
121	0.04	0.08	0.04	-0.01
122	-0.02	0.09	-0.01	-0.02
123	-0.03	0.10	-0.04	-0.02
124	-0.05	-0.11	-0.02	-0.02
125	-0.01	0.05	0.02	-0.02
126	0.05	0.06	0.04	-0.02
127	0.00	0.00	0.04	-0.02
128	-0.03	-0.03	0.02	-0.02
129	-0.04	-0.05	-0.01	-0.02
130	-0.06	-0.05	0.01	-0.02
131	-0.08	-0.09	0.03	-0.02
132	-0.03	-0.10	0.01	-0.02
133	0.02	-0.09	0.03	-0.03
134	0.00	-0.11	0.06	-0.02
135	-0.07	-0.11	0.04	-0.02
136	-0.07	-0.12	0.05	-0.02
137	-0.05	-0.07	0.07	-0.02
138	-0.03	-0.08	0.01	-0.02
139	-0.06	-0.08	0.03	-0.02
140	-0.07	-0.12	0.06	-0.02
141	-0.06	-0.12	0.03	-0.02
142	-0.04	-0.13	0.02	-0.02
143	-0.03	-0.12	0.04	-0.02
144	-0.03	-0.12	0.01	-0.02
145	-0.01	-0.12	0.00	-0.01
146	-0.05	-0.12	0.00	-0.02
147	-0.09	-0.11	-0.02	-0.01
148	-0.05	-0.11	-0.03	-0.02
149	-0.08	-0.10	-0.02	-0.02
150	-0.07	-0.10	-0.04	-0.03
151	-0.05	-0.10	-0.07	-0.03
152	-0.04	-0.09	-0.05	-0.03

153	-0.07	-0.06	-0.04	-0.02
154	-0.06	-0.03	-0.04	-0.03
155	-0.10	-0.03	-0.03	-0.03
156	-0.08	0.02	-0.04	-0.02
157	-0.06	0.04	-0.05	-0.03
158	-0.07	0.06	-0.03	-0.02
159	-0.07	0.07	0.00	-0.02
160	-0.06	0.08	0.00	-0.02
161	-0.07	0.09	0.02	-0.03
162	-0.08	0.08	0.02	-0.04
163	-0.08	0.08	0.02	-0.04
164	-0.08	0.08	0.01	-0.04
165	-0.07	0.08	0.02	-0.04
166	-0.07	0.09	0.06	-0.04
167	-0.05	0.06	0.01	-0.03
168	-0.04	0.06	0.03	-0.04
169	-0.04	0.05	0.05	-0.04
170	-0.04	0.03	0.05	-0.04
171	-0.02	0.04	0.06	-0.04
172	-0.01	-0.40	0.03	-0.04
173	-0.01	0.02	0.04	-0.04
174	-0.02	-0.02	0.03	-0.04
175	-0.03	-0.05	0.00	-0.04
176	-0.02	-0.08	0.00	-0.04
177	-0.02	-0.09	0.00	-0.04
178	-0.01	-0.11	0.02	-0.04
179	0.00	-0.09	0.02	-0.04
180	0.01	-0.11	0.02	-0.04
181	0.01	-0.10	0.01	-0.04
182	0.00	-0.09	-0.03	-0.04
183	0.04	-0.07	-0.04	-0.04
184	0.02	-0.07	-0.04	-0.04
185	0.04	-0.07	-0.03	-0.04
186	0.01	-0.05	-0.01	-0.04
187	0.01	-0.03	-0.03	-0.04
188	-0.02	-0.05	-0.04	-0.04
189	-0.03	-0.05	-0.04	-0.03
190	-0.02	-0.03	-0.03	-0.03
191	-0.01	-0.03	-0.04	-0.04
192	-0.03	-0.02	-0.03	-0.04
193	-0.04	-0.03	-0.03	-0.05
194	-0.06	-0.07	-0.03	-0.05
195	-0.06	-0.08	-0.01	-0.05
196	-0.07	-0.39	-0.02	-0.05
197	-0.07	-0.10	-0.02	-0.05
198	-0.06	-0.09	-0.02	-0.05
199	-0.05	-0.11	-0.04	-0.05
200	-0.06	-0.07	-0.05	-0.05
201	-0.04	-0.07	-0.05	-0.05
202	-0.02	-0.22	-0.06	-0.05
203	-0.02	-0.06	-0.07	-0.05
204	-0.02	-0.05	-0.07	-0.05
205	0.03	-0.02	-0.07	-0.04
206	0.04	0.00	-0.08	-0.05
207	0.05	-0.01	-0.08	-0.04
208	0.07	-0.03	-0.08	-0.04

209	0.05	-0.01	-0.08	-0.04
210	0.04	0.03	-0.10	-0.04
211	0.02	0.07	-0.08	-0.04
212	0.02	0.07	-0.08	-0.04
213	0.03	0.06	-0.06	-0.04
214	0.07	0.07	-0.06	-0.05
215	0.05	0.05	-0.06	-0.05
216	0.03	0.01	-0.03	-0.07
217	0.01	-0.01	-0.03	-0.07
218	0.02	-0.03	-0.04	-0.07
219	0.02	-0.03	-0.04	-0.07
220	0.01	-0.03	-0.03	-0.07
221	-0.02	-0.03	-0.04	-0.07
222	-0.02	-0.05	-0.04	-0.06
223	-0.03	-0.05	-0.02	-0.06
224	-0.03	-0.06	-0.01	-0.06
225	-0.02	-0.08	0.00	-0.06
226	-0.02	-0.08	0.01	-0.05
227	-0.03	-0.08	0.03	-0.05
228	-0.03	-0.09	0.04	-0.05
229	-0.03	-0.08	0.04	-0.04
230	-0.03	-0.07	0.07	-0.04
231	-0.02	-0.08	0.08	-0.04
232	-0.03	-0.09	0.09	-0.04
233	-0.05	-0.09	0.10	-0.04
234	-0.04	-0.08	0.11	-0.07
235	-0.04	-0.09	0.12	-0.06
236	-0.05	-0.11	0.10	-0.06
237	-0.05	-0.14	0.08	-0.06
238	-0.06	-0.14	0.05	-0.06
239	-0.05	-0.13	0.05	-0.05
240	-0.06	-0.12	0.05	-0.05
241	-0.07	-0.12	0.08	-0.05
242	-0.09	-0.12	0.08	-0.05
243	-0.09	-0.10	0.09	-0.05
244	-0.07	-0.08	0.07	-0.04
245	-0.07	-0.07	0.05	-0.04
246	-0.06	-0.07	0.04	-0.04
247	-0.05	-0.07	0.05	-0.04
248	-0.03	-0.07	0.04	-0.05
249	-0.04	-0.06	0.04	-0.05
250	-0.06	-0.05	0.01	-0.04
251	-0.06	-0.05	0.01	-0.04
252	-0.06	-0.02	-0.01	-0.04
253	-0.05	0.00	-0.02	-0.04
254	-0.03	0.03	-0.04	-0.05
255	-0.02	0.06	-0.07	-0.05
256	-0.01	0.04	-0.09	-0.04
257	0.00	0.06	-0.12	-0.05
258	0.03	0.04	-0.14	-0.04
259	0.03	0.03	-0.15	-0.04
260	0.02	0.02	-0.16	-0.05
261	0.06	0.03	-0.16	-0.05
262	0.07	-0.05	-0.16	-0.05
263	0.08	-0.01	-0.15	-0.05
264	0.09	-0.04	-0.13	-0.04

265	0.11	-0.05	-0.12	-0.04
266	0.10	-0.06	-0.11	-0.04
267	0.09	-0.04	-0.10	-0.03
268	0.09	-0.03	-0.08	-0.03
269	0.08	-0.05	-0.06	-0.03
270	0.08	-0.06	-0.05	-0.03
271	0.08	-0.04	-0.03	-0.03
272	0.04	-0.03	-0.03	-0.03
273	0.02	-0.05	0.01	-0.03
274	-0.01	-0.05	0.01	-0.03
275	-0.04	-0.07	0.03	-0.03
276	-0.10	-0.07	0.02	-0.03
277	-0.12	-0.07	0.01	-0.04
278	-0.14	-0.09	0.00	-0.04
279	-0.15	-0.08	0.02	-0.04
280	-0.15	-0.08	0.06	-0.04
281	-0.14	-0.10	0.03	-0.04
282	-0.15	-0.10	0.00	-0.03
283	-0.13	-0.07	0.00	-0.03
284	-0.09	-0.05	0.00	-0.03
285	-0.07	-0.05	-0.01	-0.03
286	-0.06	-0.04	-0.03	-0.04
287	-0.02	-0.06	-0.03	-0.04
288	0.02	-0.05	-0.02	-0.04
289	0.04	-0.02	0.01	-0.04
290	0.08	0.00	0.01	-0.04
291	0.10	0.01	0.02	-0.04
292	0.10	0.01	0.04	-0.04
293	0.09	0.03	0.02	-0.04
294	0.09	0.04	-0.01	-0.05
295	0.10	0.04	0.01	-0.05
296	0.09	0.04	0.04	-0.05
297	0.09	0.05	0.04	-0.05
298	0.09	0.04	0.04	-0.05
299	0.06	0.04	0.05	-0.05
300	0.06	0.03	0.03	-0.05
301	0.07	0.02	0.01	-0.05
302	0.04	0.02	-0.01	-0.05
303	0.03	0.01	-0.01	-0.04
304	0.03	0.00	-0.02	-0.04
305	0.00	-0.03	0.00	-0.04
306	0.00	-0.08	-0.02	-0.04
307	0.02	-0.13	-0.04	-0.04
308	0.01	-0.17	-0.05	-0.04
309	0.01	-0.21	-0.04	-0.04
310	0.04	-0.23	-0.04	-0.04
311	0.05	-0.24	-0.05	-0.03
312	0.05	-0.25	-0.05	-0.03
313	0.05	-0.24	-0.03	-0.03
314	0.05	-0.22	-0.01	-0.03
315	0.05	-0.20	0.01	-0.03
316	0.03	-0.75	0.02	-0.03
317	0.03	-0.18	0.02	-0.02
318	0.06	-0.15	0.03	-0.02
319	0.07	-0.18	0.06	-0.03
320	0.09	-0.14	0.07	-0.02

321	0.10	-0.11	0.07	-0.02
322	0.10	-0.16	0.05	-0.02
323	0.10	-0.08	0.05	-0.02
324	0.09	-0.06	0.08	-0.02
325	0.07	-0.04	0.10	-0.02
326	0.02	-0.02	0.08	-0.01
327	-0.01	-0.03	0.04	-0.01
328	-0.01	-0.02	0.02	-0.01
329	-0.01	0.00	0.03	-0.01
330	-0.01	0.02	0.04	0.00
331	-0.02	0.03	0.00	0.00
332	-0.04	0.05	-0.03	0.00
333	-0.05	0.08	-0.02	-0.01
334	-0.07	0.09	-0.02	-0.03
335	-0.09	0.07	-0.01	-0.03
336	-0.10	0.02	-0.01	-0.05
337	-0.12	-0.01	0.01	-0.05
338	-0.14	-0.02	0.03	-0.05
339	-0.12	-0.02	0.03	-0.05
340	-0.11	-0.01	0.01	-0.05
341	-0.10	0.00	-0.01	-0.05
342	-0.10	-0.04	-0.02	-0.05
343	-0.07	-0.06	-0.02	-0.04
344	-0.04	-0.06	0.00	-0.04
345	-0.03	-0.06	-0.01	-0.04
346	-0.04	-0.07	-0.01	-0.04
347	-0.05	-0.08	0.00	-0.03
348	-0.07	-0.10	0.03	-0.03
349	-0.07	-0.10	0.05	-0.02
350	-0.08	-0.09	0.03	-0.01
351	-0.06	-0.08	0.02	0.00
352	-0.04	-0.08	0.03	0.01
353	-0.03	-0.06	0.02	0.03
354	-0.03	-0.05	0.00	0.04
355	-0.01	-0.03	0.00	0.05
356	0.01	-0.03	-0.02	0.05
357	0.04	-0.04	-0.02	0.06
358	0.07	-0.06	-0.03	0.05
359	0.09	-0.05	-0.06	0.05
360	0.09	-0.02	-0.08	0.04
361	0.08	0.00	-0.08	0.03
362	0.06	-0.03	-0.07	0.02
363	0.06	-0.09	-0.07	0.01
364	0.04	-0.11	-0.09	0.00
365	0.02	-0.10	-0.09	-0.01
366	0.04	-0.07	-0.05	-0.02
367	0.07	-0.06	-0.03	-0.02
368	0.08	-0.08	-0.02	-0.02
369	0.06	-0.11	-0.01	-0.03
370	0.02	-0.11	0.01	-0.03
371	0.00	-0.07	0.02	-0.03
372	-0.02	-0.04	0.00	-0.03
373	-0.01	-0.05	-0.03	-0.03
374	0.03	-0.04	-0.03	-0.03
375	0.03	-0.04	-0.02	-0.02
376	0.01	-0.08	-0.01	-0.01

377	0.00	-0.06	0.03	0.00
378	-0.01	-0.06	0.04	0.00
379	-0.02	-0.05	0.05	0.01
380	0.00	-0.05	0.05	0.00
381	0.02	-0.05	0.06	-0.01
382	0.02	-0.61	0.07	-0.03
383	0.01	0.01	0.06	-0.05
384	-0.03	0.03	0.05	-0.07
385	-0.06	0.02	0.08	-0.08
386	-0.07	0.00	0.11	-0.07
387	-0.06	-0.04	0.10	-0.04
388	-0.06	-0.05	0.08	0.00
389	-0.03	-0.05	0.06	0.02
390	-0.03	-0.05	0.05	0.01
391	-0.04	-0.05	0.07	-0.02
392	-0.04	-0.02	0.07	-0.04
393	-0.05	0.00	0.02	-0.04
394	-0.06	0.01	-0.01	-0.02
395	-0.05	-0.01	0.01	0.01
396	-0.02	-0.03	0.03	0.03
397	0.02	-0.01	0.01	0.02
398	0.03	0.00	0.00	0.00
399	0.01	-0.02	0.00	-0.02
400	-0.02	-0.02	-0.01	-0.04
401	-0.03	0.00	-0.03	-0.04
402	0.02	0.00	-0.04	-0.04
403	0.06	-0.01	-0.03	-0.04
404	0.02	-0.01	0.02	-0.05
405	-0.04	-0.02	0.01	-0.07
406	-0.08	-0.05	-0.02	-0.06
407	-0.06	-0.06	-0.02	-0.03
408	-0.03	-0.04	0.00	0.03
409	-0.01	-0.02	0.02	0.07
410	-0.02	-0.02	0.02	0.06
411	-0.04	-0.02	0.00	0.03
412	-0.01	-0.03	-0.03	-0.02
413	0.02	-0.02	-0.04	-0.04
414	0.01	0.00	-0.02	-0.05
415	0.00	-0.01	0.01	-0.05
416	-0.01	-0.05	0.01	-0.04
417	-0.02	-0.08	-0.02	-0.01
418	-0.03	-0.06	-0.03	0.01
419	-0.02	-0.07	0.00	0.02
420	-0.01	-0.09	0.00	0.02
421	0.00	-0.07	0.00	0.01
422	-0.02	-0.04	0.02	0.00
423	-0.03	-0.03	0.03	-0.02
424	-0.01	-0.03	0.02	-0.01
425	-0.01	-0.06	0.03	0.01
426	-0.03	-0.08	0.01	0.04
427	-0.02	-0.05	-0.01	0.06
428	0.03	-0.02	0.01	0.08
429	0.04	-0.05	0.03	0.11
430	0.03	-0.06	0.03	0.10
431	0.01	-0.03	0.03	0.06
432	0.00	-0.04	0.03	0.02

433	0.03	-0.04	0.03	0.01
434	0.04	-0.03	0.00	0.01
435	0.02	-0.06	-0.01	0.00
436	0.03	-0.09	0.00	-0.03
437	0.05	-0.08	-0.01	-0.06
438	0.02	-0.06	-0.01	-0.08
439	0.00	-0.11	0.00	-0.09
440	0.02	-0.02	0.00	-0.08
441	0.01	-0.04	-0.02	-0.03
442	0.01	-0.03	-0.02	0.01
443	-0.01	0.02	0.02	0.01
444	-0.02	0.00	0.03	-0.01
445	-0.02	-0.04	0.00	0.02
446	-0.02	-0.03	0.01	0.07
447	-0.02	0.00	0.01	0.08
448	-0.02	0.00	-0.01	0.05
449	-0.04	-0.03	0.01	0.03
450	-0.04	-0.05	0.04	0.03
451	-0.02	-0.04	0.02	0.03
452	-0.04	-0.03	0.01	0.02
453	-0.05	-0.02	-0.01	0.01
454	-0.03	-0.01	-0.02	0.00
455	-0.04	-0.01	-0.03	-0.02
456	-0.05	-0.02	-0.04	-0.02
457	-0.03	-0.02	-0.02	-0.01
458	-0.02	-0.03	-0.01	0.00
459	-0.02	-0.03	-0.03	0.00
460	0.01	-0.01	-0.01	0.01
461	0.02	-0.02	0.03	0.02
462	0.00	-0.03	0.02	0.01
463	0.01	-0.04	0.01	0.00
464	0.03	-0.05	0.04	0.00
465	0.03	-0.04	0.06	0.02
466	0.02	-0.04	0.02	0.05
467	0.01	-0.05	0.02	0.03
468	0.00	-0.05	0.04	0.01
469	0.03	-0.04	0.03	0.01
470	0.02	-0.03	0.03	0.03
471	0.00	-0.01	0.04	0.02
472	0.02	0.01	0.02	0.00
473	0.01	0.03	0.01	0.02
474	-0.01	0.02	0.01	0.03
475	-0.01	0.00	-0.01	0.01
476	0.02	-0.02	-0.02	0.00
477	0.02	-0.03	-0.01	0.02
478	-0.02	-0.04	-0.01	0.02
479	0.01	-0.07	-0.03	-0.03
480	0.03	-0.07	-0.03	-0.04
481	0.00	-0.06	-0.04	0.00
482	0.03	-0.07	-0.03	0.00
483	0.03	-0.09	0.02	-0.04
484	0.00	-0.08	0.03	-0.04
485	-0.01	-0.07	0.07	0.00
486	-0.02	-0.07	0.07	0.03
487	-0.01	-0.07	0.02	0.04
488	-0.02	-0.07	0.00	0.04

489	-0.03	-0.07	-0.01	0.01
490	-0.02	-0.08	-0.03	0.00
491	-0.03	-0.08	-0.01	0.01
492	-0.02	-0.08	0.00	0.01
493	-0.01	-0.09	0.00	0.01
494	-0.02	-0.11	0.03	0.04
495	-0.02	-0.12	0.04	0.07
496	-0.01	-0.16	0.02	0.06
497	0.01	-0.11	0.03	0.06
498	0.02	-0.08	0.02	0.06
499	0.04	-0.10	0.00	0.04
500	0.05	-0.06	0.02	0.05
501	0.02	-0.04	0.01	0.07
502	0.01	-1.00	0.01	0.05
503	0.01	-0.05	-0.01	0.01
504	0.00	-0.03	-0.04	0.00
505	0.00	-0.03	-0.02	-0.01
506	-0.01	-0.03	-0.01	0.01
507	0.00	0.02	0.01	0.07
508	-0.02	0.02	0.03	0.08
509	-0.04	-0.02	0.00	0.04
510	-0.03	0.01	-0.01	0.02
511	-0.02	0.00	-0.01	0.04
512	0.00	-0.03	-0.03	0.06
513	0.03	-0.03	-0.01	0.08
514	0.02	-0.02	0.01	0.05
515	0.02	-0.03	0.00	0.03
516	0.03	-0.04	-0.01	0.05
517	0.02	-0.02	-0.03	0.06
518	0.02	-0.02	-0.02	0.04
519	0.04	-0.07	0.02	0.02
520	0.02	-0.08	0.03	0.01
521	0.00	-0.09	0.05	0.00
522	-0.03	-0.08	0.05	0.05
523	-0.04	-0.06	0.02	0.07
524	-0.06	-0.05	0.02	0.04
525	-0.06	-0.05	0.03	0.03
526	-0.04	-0.01	0.06	0.06
527	-0.05	0.01	0.07	0.05
528	-0.04	0.01	0.08	0.01
529	-0.04	0.02	0.09	0.00
530	-0.06	0.01	0.10	0.00
531	-0.04	0.00	0.09	0.01
532	-0.03	0.00	0.07	0.06
533	-0.03	-0.02	0.07	0.08
534	-0.01	-0.04	0.05	0.04
535	-0.01	-0.05	0.03	0.01
536	0.00	-0.06	0.03	0.04
537	0.02	-0.05	0.02	0.07
538	0.02	-0.03	0.02	0.07
539	0.02	0.00	0.00	0.06
540	0.00	0.02	0.00	0.02
541	0.03	0.02	0.02	0.00
542	0.03	0.02	-0.03	0.04
543	0.02	-0.01	-0.07	0.04
544	0.04	-0.05	-0.06	0.02

545	0.01	-0.06	-0.06	0.03
546	-0.02	-0.08	-0.05	0.02
547	-0.02	-0.10	-0.03	0.00
548	-0.04	-0.10	-0.01	0.03
549	-0.04	-0.11	0.01	0.04
550	-0.05	-0.09	0.02	0.02
551	-0.05	-0.05	0.04	0.05
552	-0.03	-0.08	0.04	0.07
553	-0.03	-0.09	0.02	0.08
554	-0.01	-0.05	0.01	0.06
555	0.03	-0.03	0.02	0.01
556	0.00	-0.08	0.02	-0.01
557	-0.01	-0.05	0.00	0.05
558	0.00	-0.04	-0.01	0.08
559	-0.01	-0.04	-0.02	0.09
560	0.01	-0.06	-0.02	0.10
561	0.02	-0.06	-0.01	0.09
562	0.03	-1.09	-0.04	0.05
563	0.02	-0.03	-0.05	0.05
564	0.00	0.01	-0.01	0.05
565	-0.01	0.03	0.01	0.08
566	-0.02	0.02	0.00	0.12
567	-0.01	0.01	0.00	0.09
568	-0.04	-0.02	0.00	0.05
569	-0.04	-0.04	0.01	0.09
570	-0.01	-0.02	0.01	0.11
571	-0.03	0.00	0.01	0.06
572	-0.02	0.00	0.02	0.00
573	-0.03	0.01	0.03	0.00
574	-0.05	0.03	0.05	0.06
575	-0.03	0.03	0.06	0.04
576	-0.03	0.03	0.04	-0.01
577	-0.05	0.04	0.03	0.02
578	-0.05	0.06	0.00	0.01
579	-0.03	0.06	-0.03	0.01
580	-0.03	0.06	0.00	0.08
581	-0.04	0.06	0.00	0.06
582	-0.05	0.04	-0.01	0.03
583	-0.05	0.05	-0.02	0.04
584	-0.05	0.04	-0.04	0.05
585	-0.06	0.03	-0.02	0.01
586	-0.05	0.05	0.00	-0.03
587	-0.03	0.03	0.01	0.04
588	-0.05	-0.01	0.01	0.07
589	-0.05	-0.01	0.04	0.03
590	-0.03	-0.01	0.03	0.04
591	0.02	-0.03	0.03	0.04
592	0.03	-0.05	0.02	0.02
593	0.02	-0.05	0.01	0.06
594	0.03	-0.05	0.03	0.06
595	0.02	-0.03	0.05	0.04
596	0.01	-0.02	0.06	0.05
597	0.02	0.00	0.04	0.06
598	0.03	0.01	0.03	0.07
599	0.03	-0.01	0.04	0.05
600	0.02	-0.02	0.02	0.03

## APPENDIX C

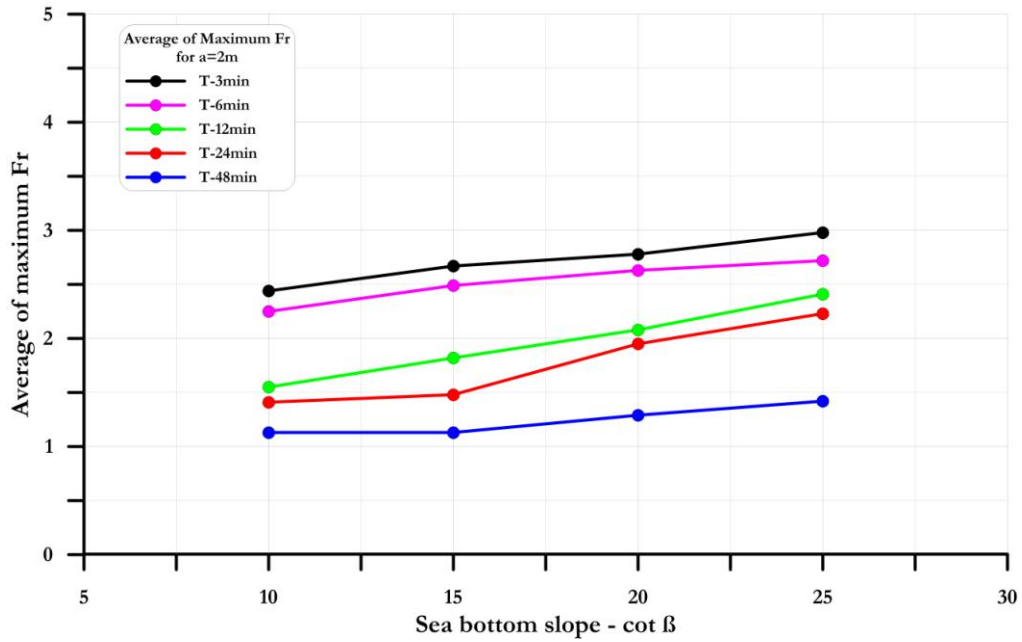


**Figure C.1:** The plot of  $\overline{Fr}_{max}$  values with respect to bottom slope for the LEW of various wave periods with initial wave amplitude  $a=2m$  on plain beach

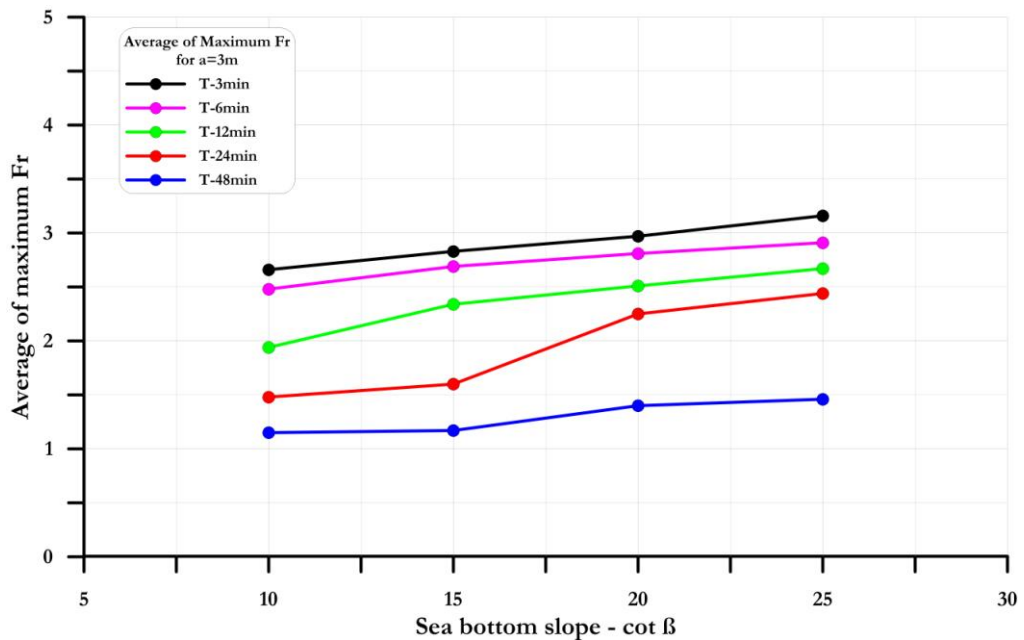


**Figure C.2:** The plot of  $\overline{Fr}_{max}$  values with respect to bottom slope for the LEW of various wave periods with initial wave amplitude  $a=3m$  on plain beach

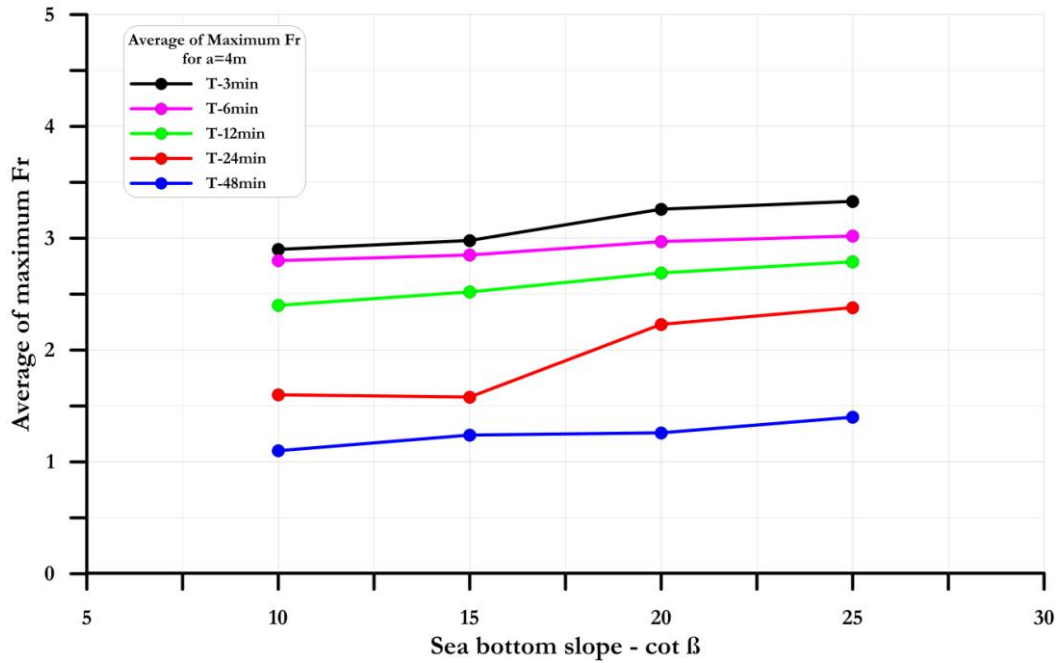


**Figure C.3:** The plot of  $\overline{Fr}_{max}$  values with respect to bottom slope for the LEW of various wave periods with initial wave amplitude  $a=4m$  on plain beach

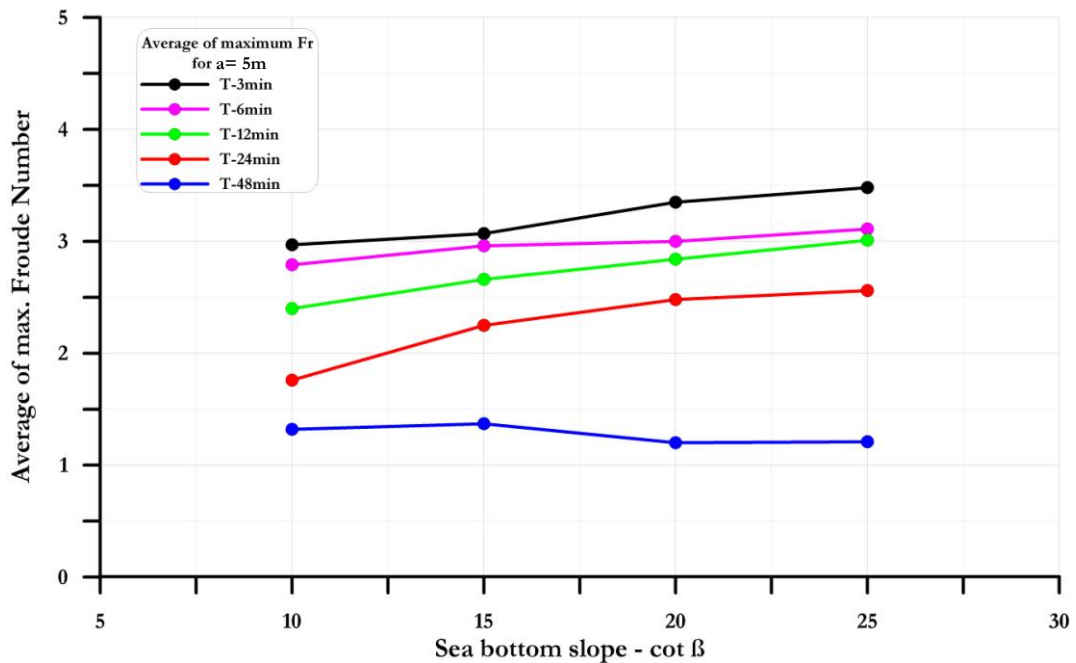


**Figure C.4:** The plot of  $\overline{Fr}_{max}$  values with respect to bottom slope for the LEW of various wave periods with initial wave amplitude  $a=5m$  on plain beach

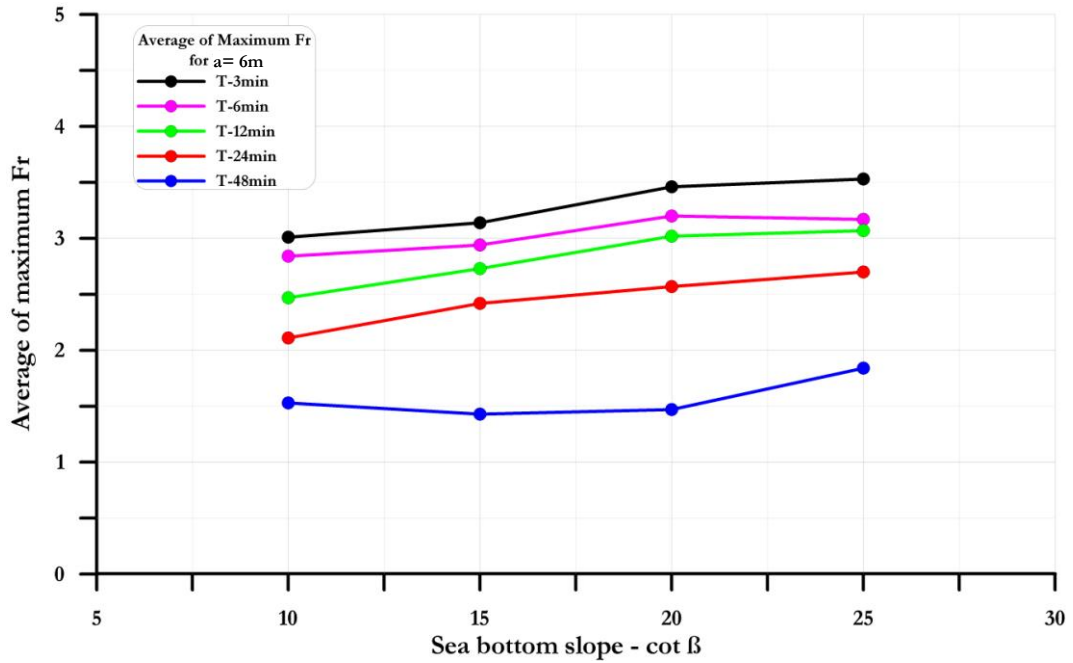


**Figure C.5:** The plot of  $\overline{Fr_{max}}$  values with respect to bottom slope for the waves of various wave periods with initial wave amplitude  $a=6m$  on plain beach

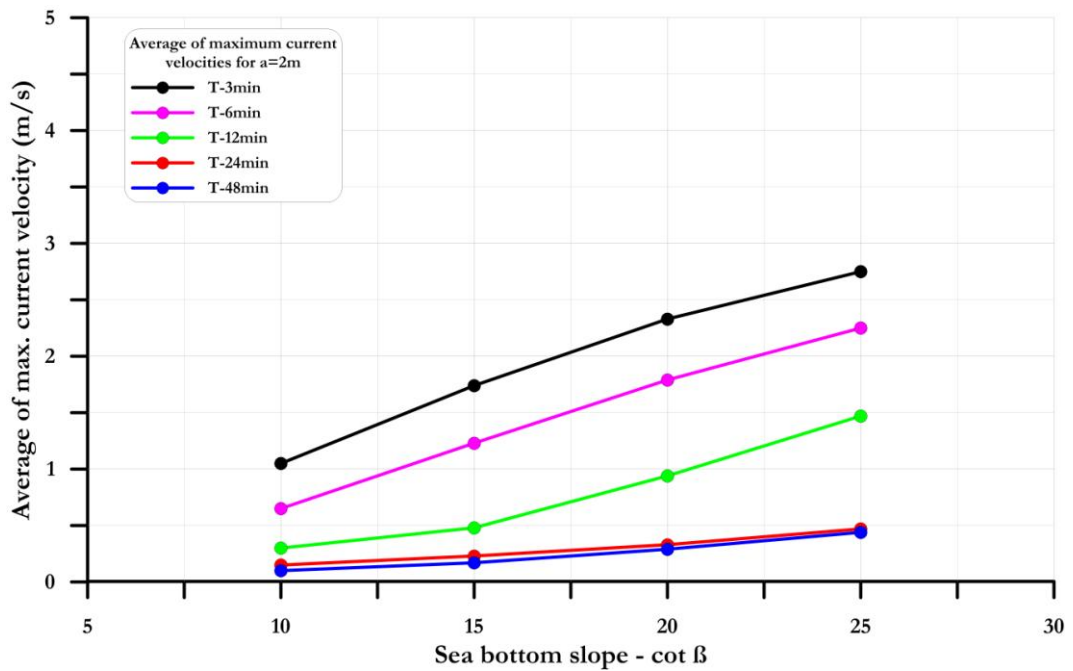


**Figure C.6:** The plot of average maximum current velocities with respect to bottom slope for the LEW of various wave periods with initial wave amplitude  $a=2m$  on plain beach

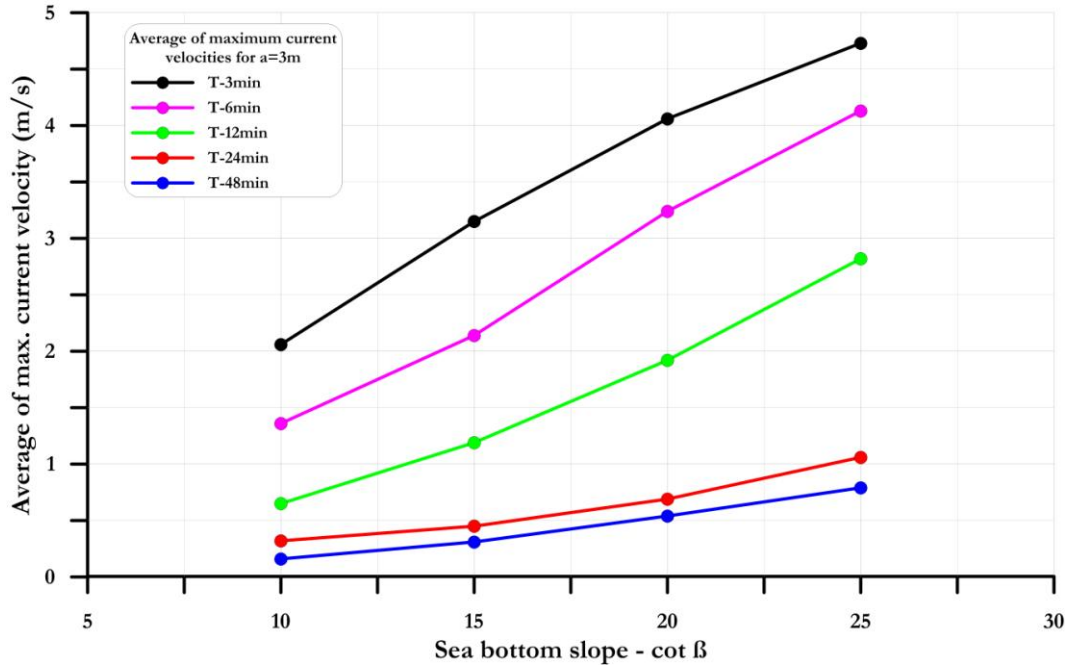


**Figure C.7:** The plot of average maximum current velocities with respect to bottom slope for the LEW of various wave periods with initial wave amplitude  $a= 3\text{m}$  on plain beach

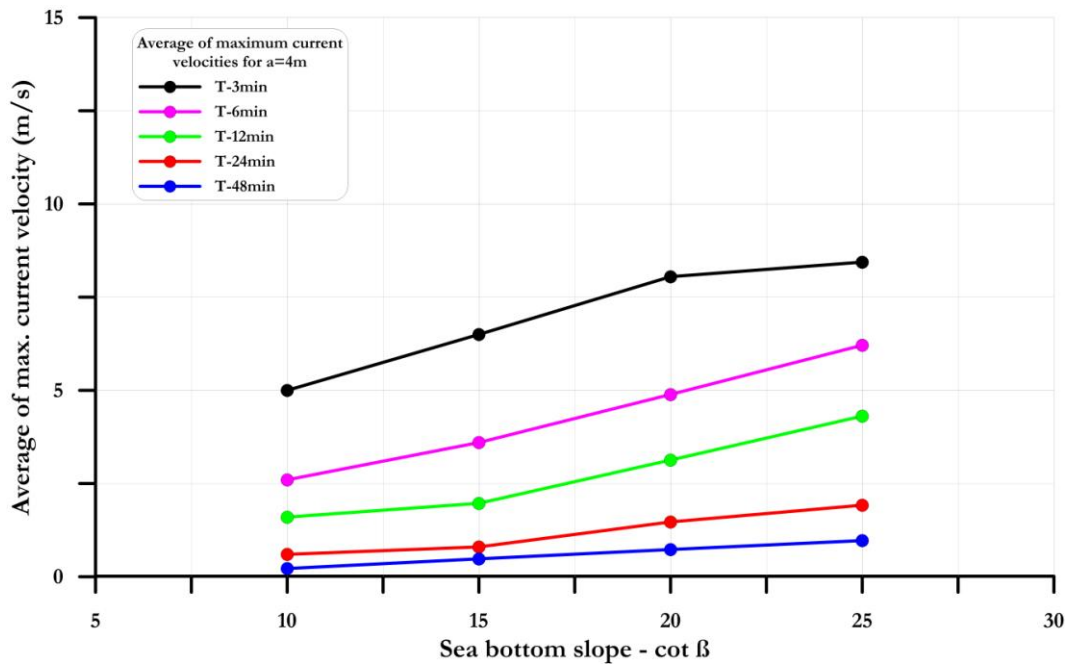


**Figure C.8:** The plot of average maximum current velocities with respect to bottom slope for the LEW of various wave periods with initial wave amplitude  $a= 4\text{m}$  on plain beach

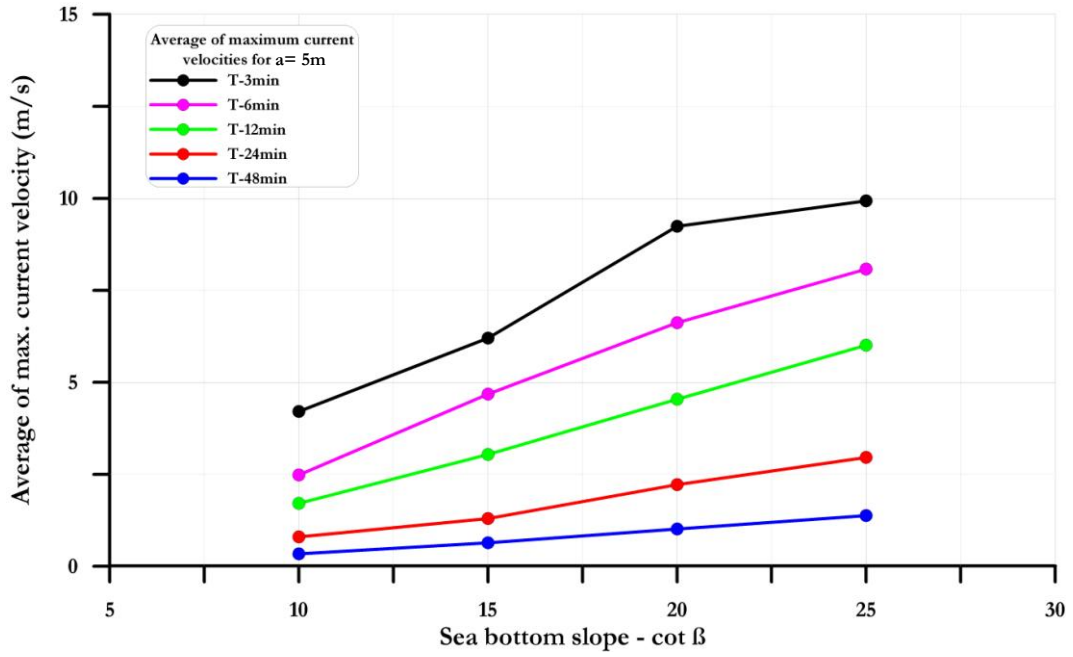


**Figure C.9:** The plot of average maximum current velocities with respect to bottom slope for the LEW of various wave periods with initial wave amplitude  $a= 5\text{m}$  on plain beach

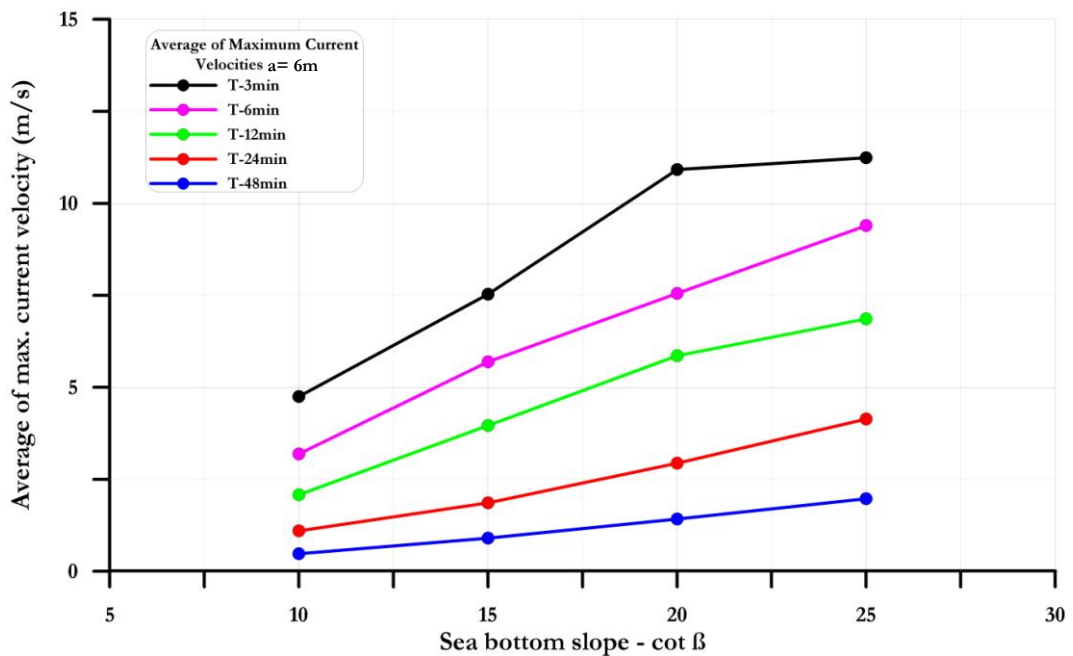


**Figure C.10:** The plot of average maximum current velocities with respect to bottom slope for the LEW of various wave periods with initial wave amplitude  $a= 6\text{m}$  on plain beach

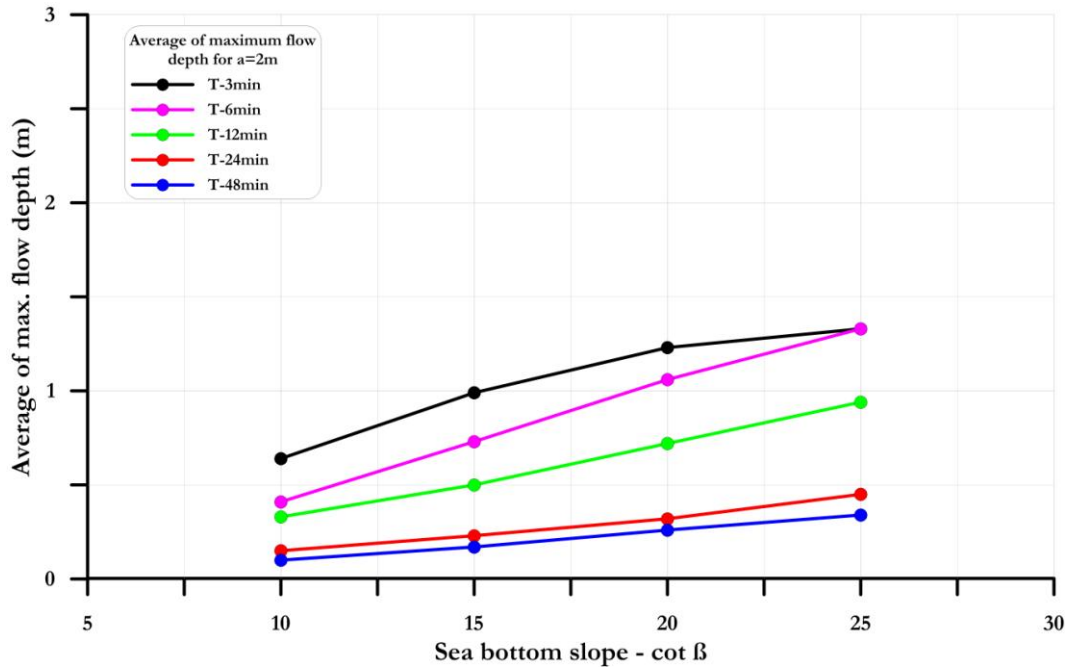


**Figure C.11:** The plot of average maximum flow depths with respect to bottom slope for the LEW of various wave periods with initial wave amplitude  $a= 2\text{m}$  on plain beach

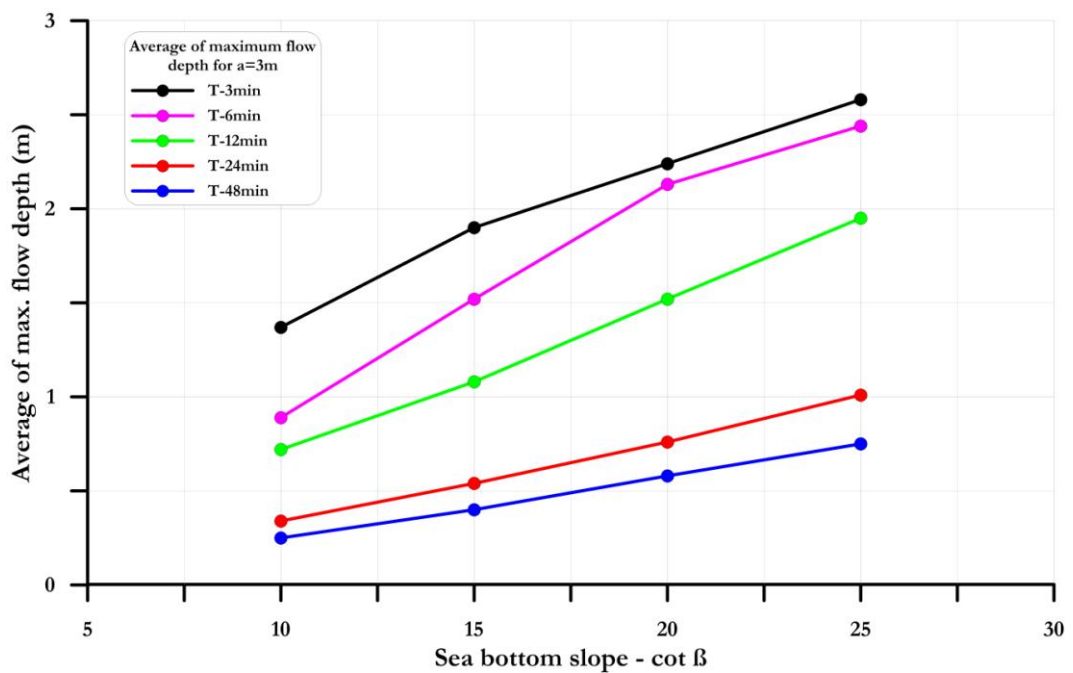


**Figure C.12:** The plot of average maximum flow depths with respect to bottom slope for the LEW of various wave periods with initial wave amplitude  $a= 3\text{m}$  on plain beach

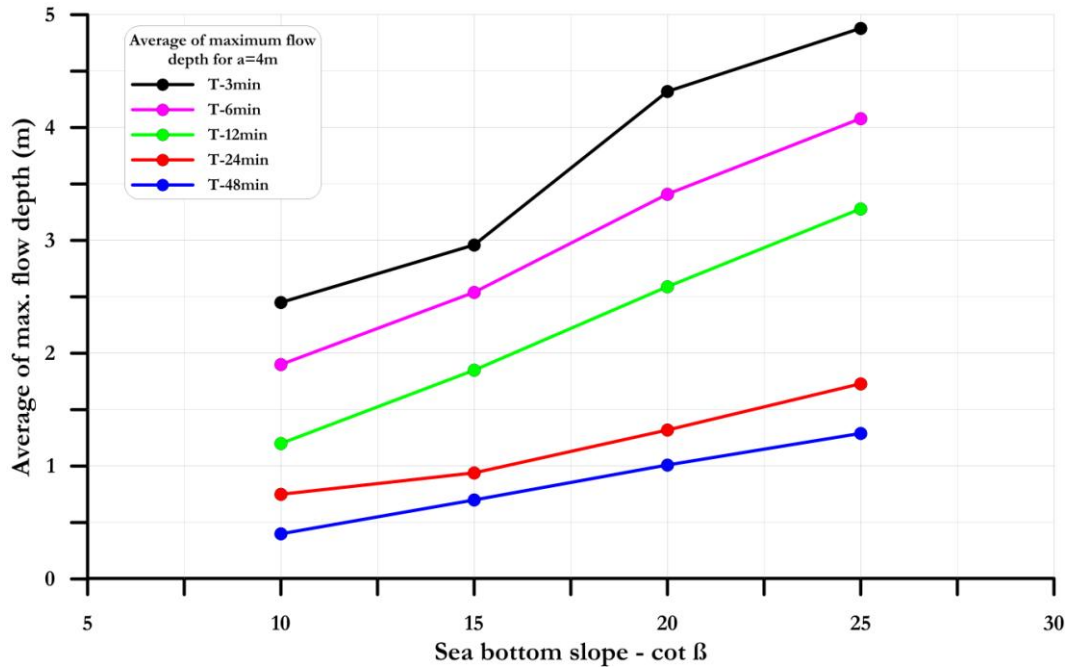


**Figure C.13:** The plot of average maximum flow depths with respect to bottom slope for the LEW of various wave periods with initial wave amplitude  $a= 4\text{m}$  on plain beach

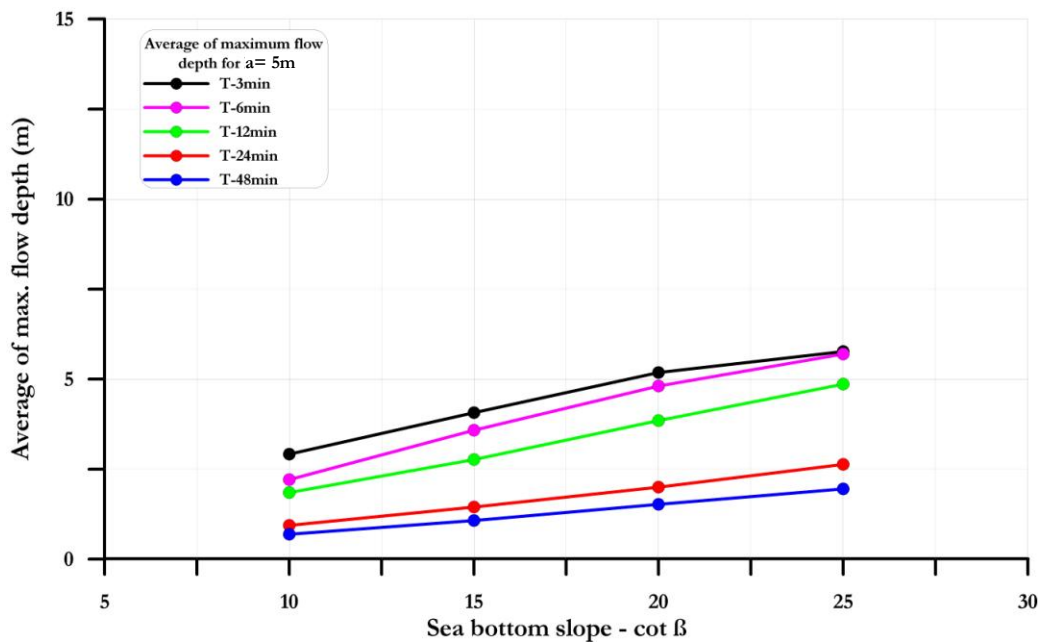


**Figure C.14:** The plot of average maximum flow depths with respect to bottom slope for the LEW of various wave periods with initial wave amplitude  $a= 5\text{m}$  on plain beach

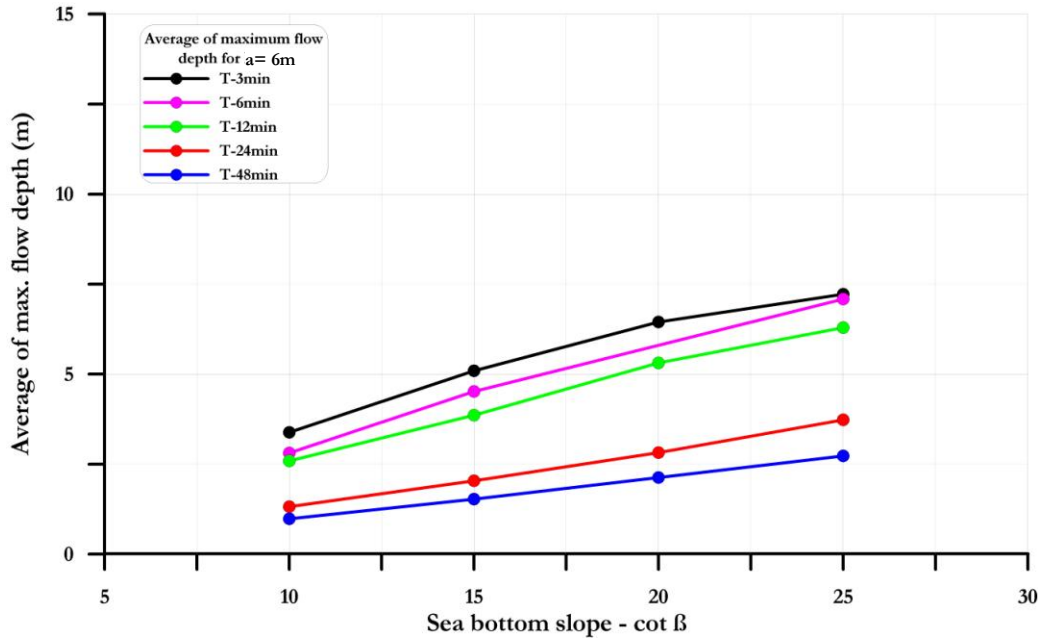


**Figure C.15:** The plot of average maximum flow depths with respect to bottom slope for the LEW of various wave periods with initial wave amplitude  $a=6\text{m}$  on plain beach

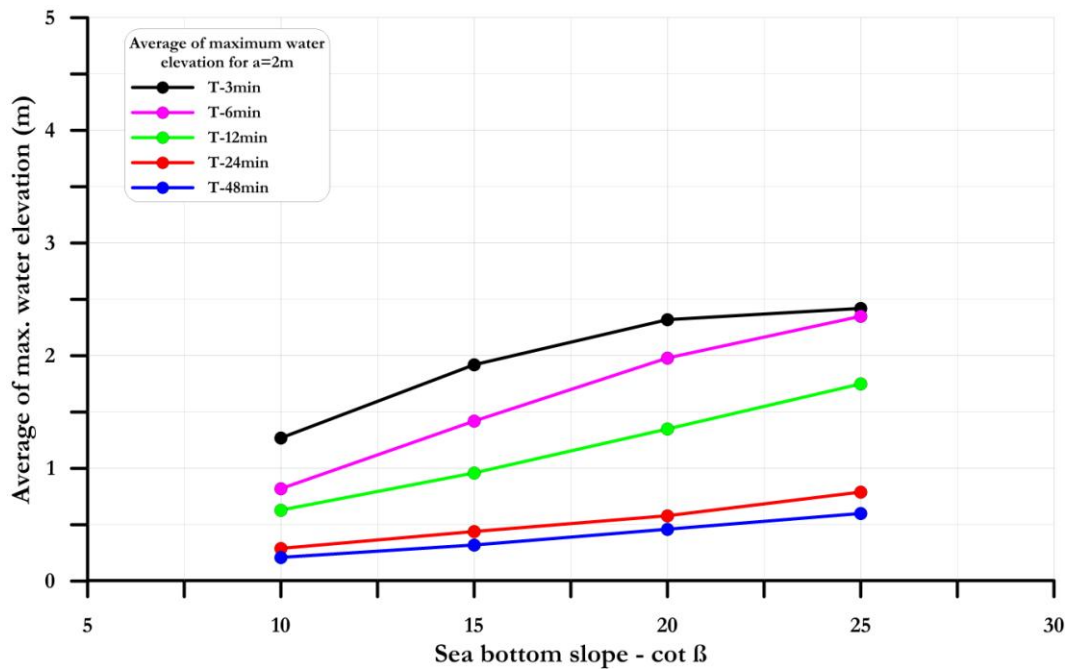


**Figure C.16:** The plot of average maximum water elevation with respect to bottom slope for the LEW of various wave periods with initial wave amplitude  $a=2\text{m}$  on plain beach

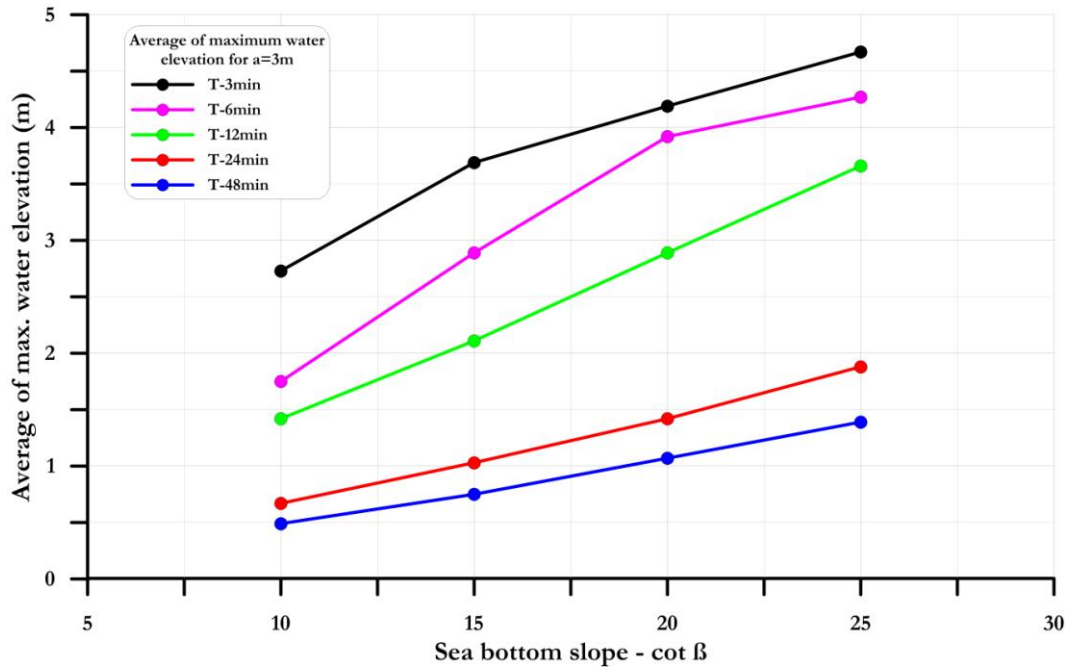


**Figure C.17:** The plot of average maximum water elevation with respect to bottom slope for the LEW of various wave periods with initial wave amplitude  $a= 3\text{m}$  on plain beach

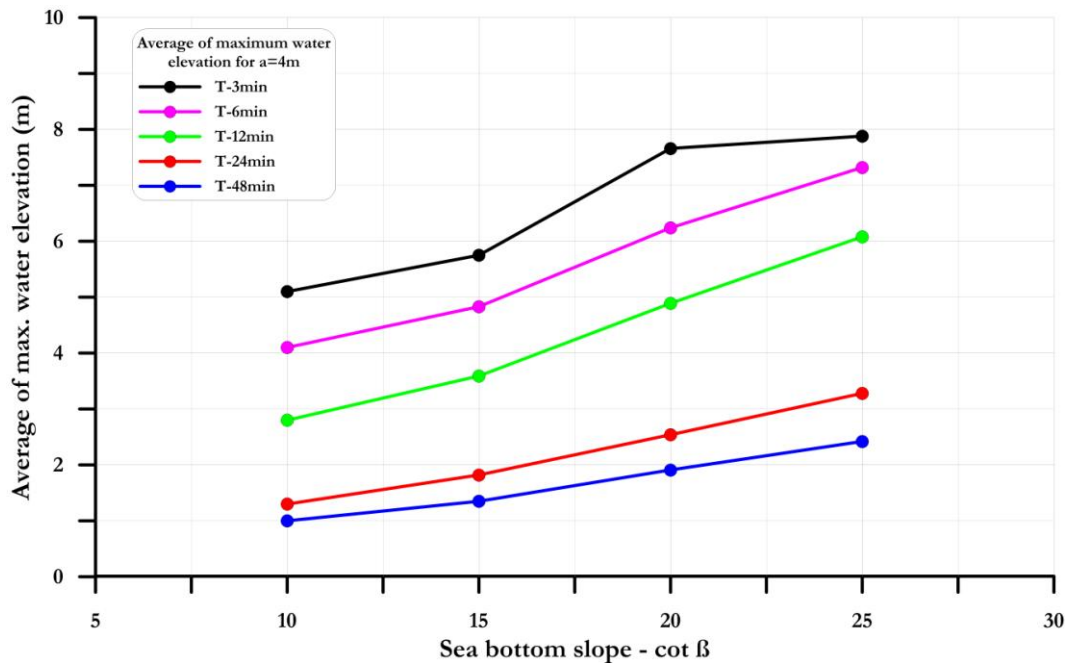


**Figure C.18:** The plot of average maximum water elevation with respect to bottom slope for the LEW of various wave periods with initial wave amplitude  $a= 4\text{m}$  on plain beach

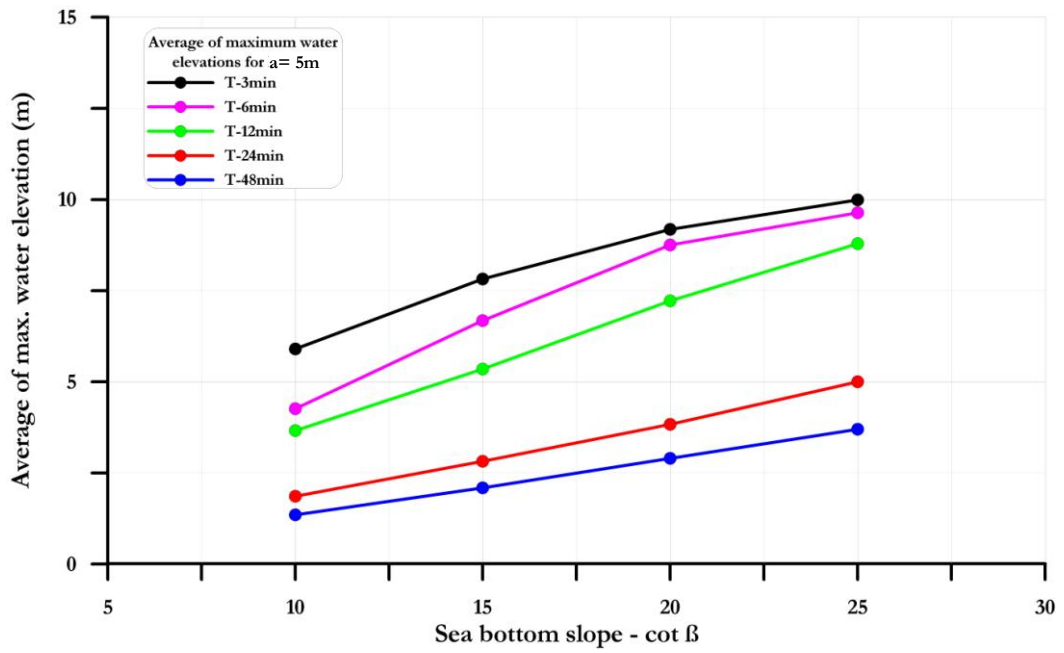


**Figure C.19:** The plot of average maximum water elevation with respect to bottom slope for the LEW of various wave periods with initial wave amplitude  $a = 5\text{m}$  on plain beach

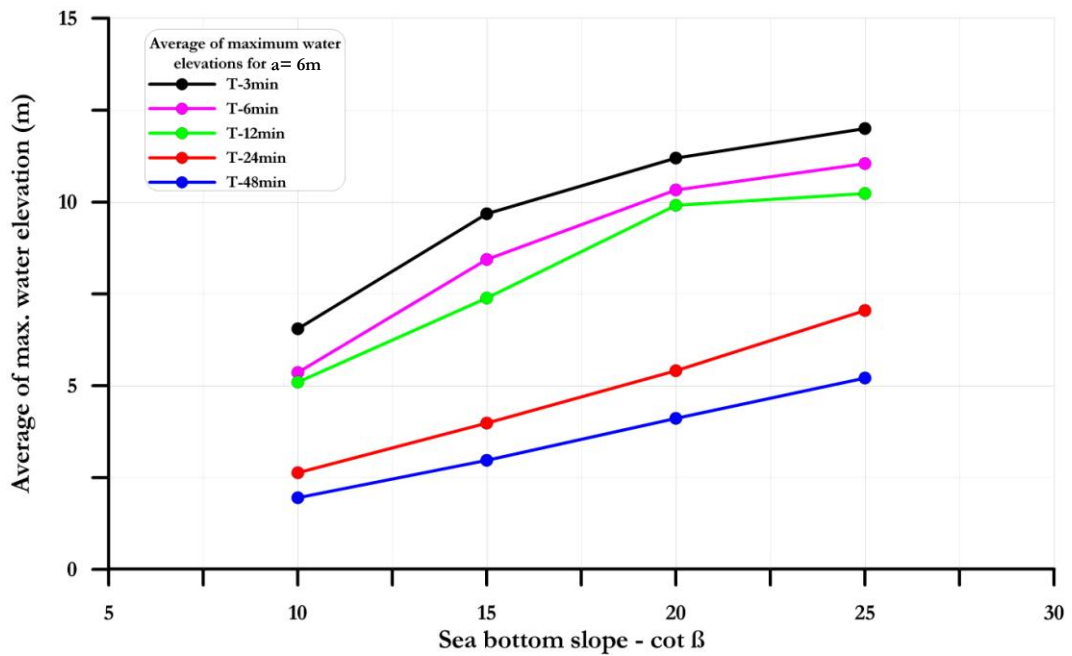


**Figure C.20:** The plot of average maximum water elevation with respect to bottom slope for the LEW of various wave periods with initial wave amplitude  $a = 6\text{m}$  on plain beach

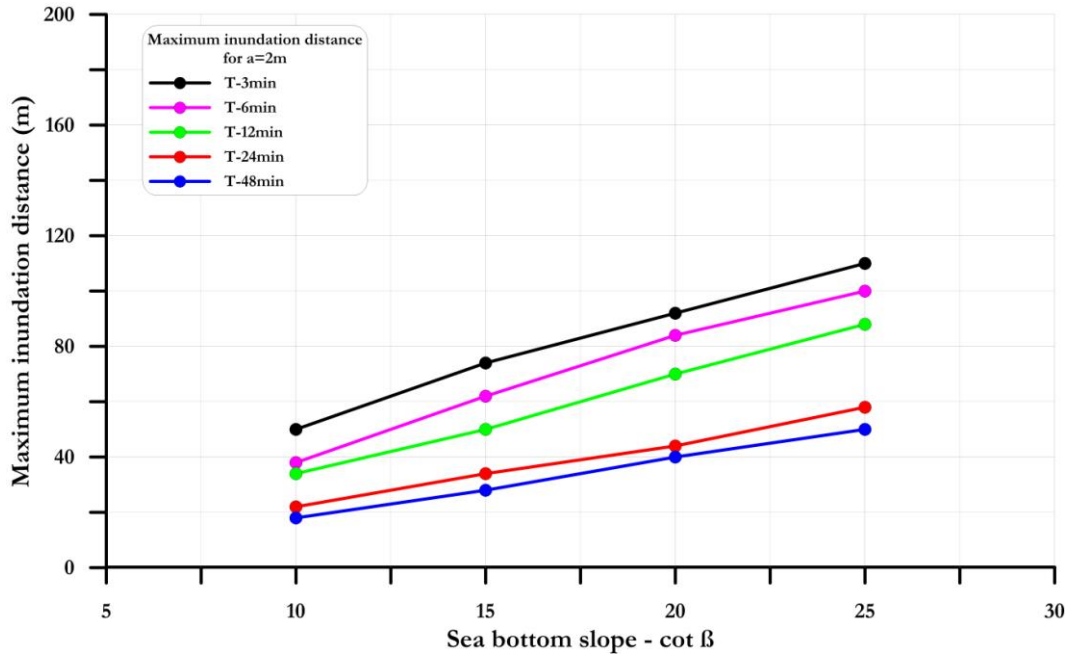


**Figure C.21:** The plot of maximum inundation distance with respect to bottom slope for the LEW of various wave periods with initial wave amplitude  $a= 2\text{m}$  on plain beach

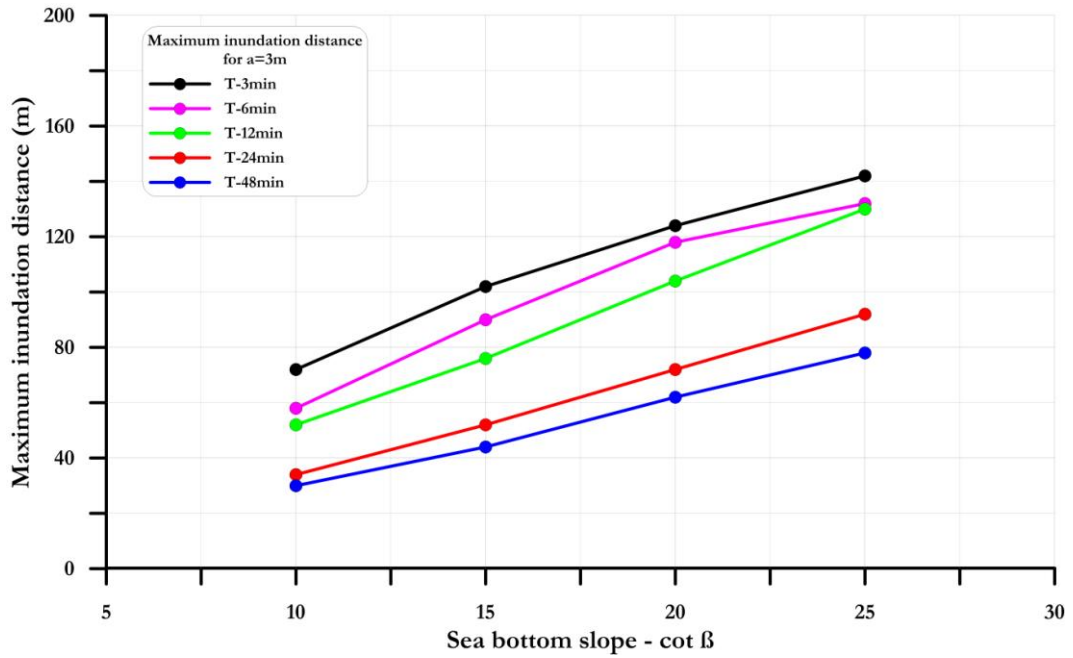


**Figure C.22:** The plot of maximum inundation distance with respect to bottom slope for the LEW of various wave periods with initial wave amplitude  $a= 3\text{m}$  on plain beach

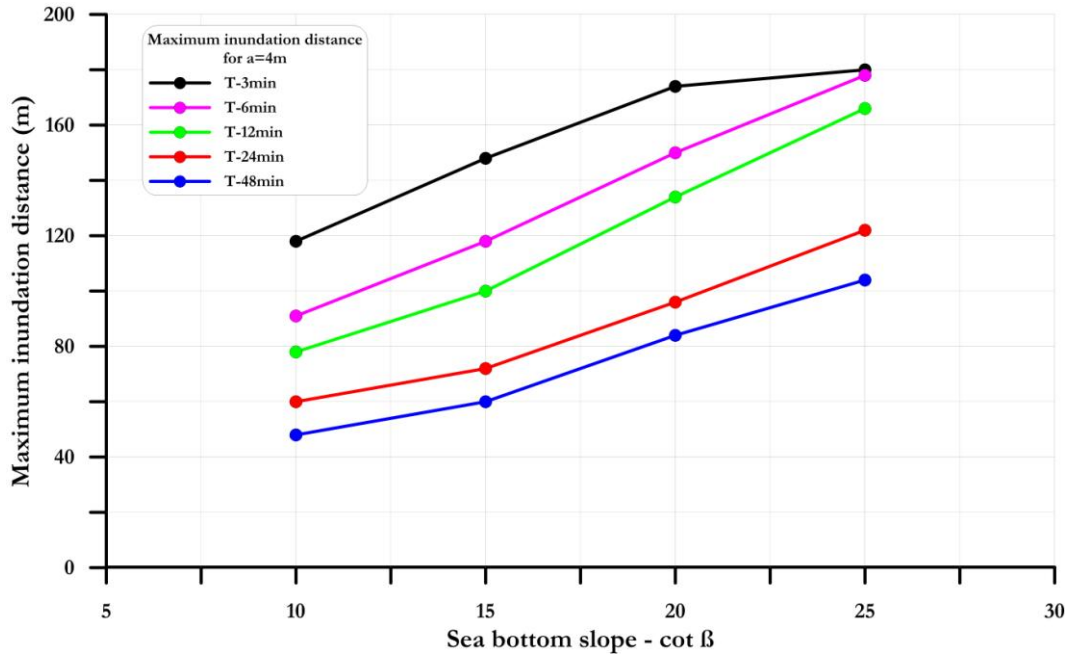


**Figure C.23:** The plot of maximum inundation distance with respect to bottom slope for the LEW of various wave periods with initial wave amplitude  $a= 4\text{m}$  on plain beach

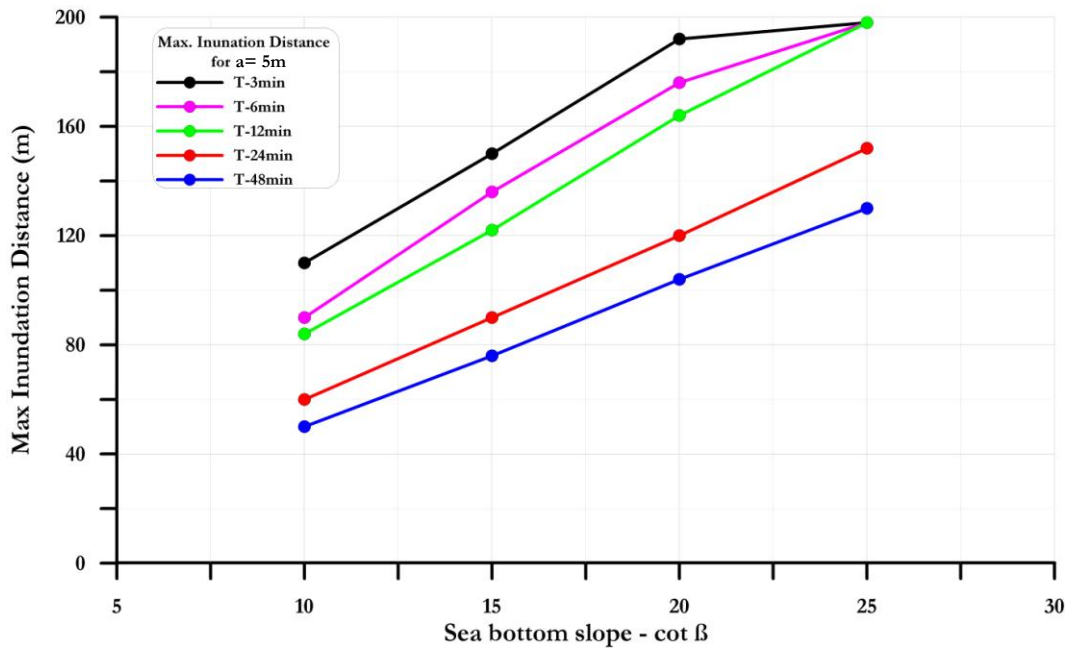


**Figure C.24:** The plot of maximum inundation distance with respect to bottom slope for the LEW of various wave periods with initial wave amplitude  $a= 5\text{m}$  on plain beach

# CURRICULUM VITAE

## PERSONAL INFORMATION

Surname, Name: Özer, Ceren  
Nationality: Turkish (TC)  
Date and Place of Birth: 8 January 1981, Ankara  
Marital Status: Single  
Phone: +90 312 210 54 36  
Fax: +90 312 210 18 00  
email: cceren@gmail.com

## EDUCATION

Degree	Institution	Year of Graduation
MS	METU Civil Engineering	2007
BS	METU Civil Engineering	2004
High School	Çankaya Atatürk Anatolian High School, Ankara	1999

## WORK EXPERIENCE

Year	Place	Enrollment
2011-present	METU Department of Civil Engineering Ocean Engineering Research Center	Scientific Project Specialist
2005-2011	METU Department of Civil Engineering	Research Assistant
2002 July-Aug	General Directorate of State Hydraulic Works, Department of Dams &Hydroelectric Power Plants	Intern Engineering Student
2001 July-Aug	BAG-KUR General Directorate	Intern Engineering Student

## FOREIGN LANGUAGES

Advanced English, Fair German

## PUBLICATIONS

1. Yalciner A.C., Suppasri A., Mas E., Kalligeris N., Necmioglu O., Imamura F., Ozer C., Zaitsev A., Ozel N.M., Synolakis C. (2012). *Field Survey on the Coastal Impacts of March 11, 2011 Great East Japan Tsunami*, J. of Pure Appl. Geophys., (in review)

2. Ozer, C., Yalciner, A. C. (2011). *Sensitivity Study of Hydrodynamic Parameters During Numerical Simulations of Tsunami Inundation*, J. of Pure Appl. Geophys., Springer Basel AG, DOI 10.1007/s00024-011-0290-6
3. Yalciner, A.C., Suppasri, A., Mas, E., Kalligeris, N., Necmioglu, O., Imamura, F., Ozer, C., Zaytsev, A., Ozel, N.M., Synolakis, C. (2011). *11 Mart 2011 Büyük Doğu Japonya Tsunamisinin Ardından Hasar Görmüş Kıyı Bölgelerinde Alan Çalışması*, Proceedings of 7th National Coastal Engineering Symposium, Prof. Dr. Yalçın Yüksel (Ed.), 77-86.
4. Ozer, C., Yalciner, A.C., Zaytsev, A. Pelinovsky E. (2011). *General View of Dispersion in Tsunami Modeling*, European Geosciences Union 2011 General Assembly, Geophysical Research Abstracts, Vol. 13, EGU2011-806-1
5. Yalciner A. C., Ozer C. (2011). *11 Mart 2011 Toboku-Kanto Depreşim Dalgası(Tsunamisi): Tsunamiden dünyaya Acı Bir Ders Daba*, an article about the numerical modeling of March 11, 2011 Great East Japan Tsunami and lessons learnt from that disaster, Tübitak Bilim-Teknik Dergisi (Popular Magazine) , April 2011, Year: 44, No: 521, pages 18-23.
6. Ozer C., Yalciner A. C. (2011). *Tsunami Bizî de Vurur mu?*, an article about March 11, 2011 Great East Japan Tsunami and tsunami risk in Turkey, Naviga (Popular Magazine) , April 2011, ISSN 1304 4311, pages 30-34.
7. Yalciner, A. C., Ozer, C., Karakus, H., Zaytsev, A., Guler, I. (2010). *Evaluation of Coastal Risk at Selected Sites Against Eastern Mediterranean Tsunamis*, Proceedings of 32<sup>nd</sup> International Conference on Coastal Engineering (ICCE 2010), Shanghai, China, June 30 – July 5, 2010
8. Zaytsev, A., Ozer, C., Pelinovsky, E., Yalciner, A.C., Chernov A. (2010). *On the Nonlinearity, Dispersion and Friction in Tsunami Modeling and Forecasting*, European Geosciences Union 2010 General Assembly, Geophysical Research Abstracts, Vol. 12, EGU2010-10512-1
9. Yalciner, A. C., Zahibo, N., Pelinovsky, E., Insel, I., Dilmen, D. I., Zaitsev, A., Chernov, A., Ozer, C. (2009). *Understanding the Possible Effects of Near and Far Field Tsunamis on Lesser Antilles by Numerical Modeling*, The Open Oceanography Journal, 2009, 3, pp. 67-69
10. Dilmen, D. I., Yalciner, A. C., Zaytsev, A., Chernov, A., Ozer, C., Insel, I.,Pelinovsky, E., Kurkin, A., Karakuş, H., Kanoğlu, U., Imamura, F. (2009). *CBS Tabanlı Tsunami Baskın Haritalarının Geliştirilmesi; Fethiye Örneği*, Proceedings of 62<sup>th</sup> Turkey Geology Congress, April 13-17, 2009.
11. Ozer, C., Karakus, H., Yalciner A. C. (2008). *Investigation of Hydrodynamic Demands of Tsunamis in Inundation Zone*, Proceedings of 7th International Conference on Coastal and Port Engineering in Developing Countries, Dubai, UAE, February 24-28, 2008

12. Yalciner A.C., Pelinovsky E., Zaytsev A., Kurkin A., Ozer C., Karakus H., Ozyurt G. (2007). *Modeling and Visualization of Tsunamis: Mediterranean Examples*, Tsunami and Nonlinear Waves, Anjan Kundu (Ed.), Springer, 2007, pp.273-283
13. Ozer C., Yalciner A.C. (2007). *Depreşim Dalgalarının Hidrodinamik Etki Düzeylerinin Araştırılması*, Proceedings of 6<sup>th</sup> National Coastal Engineering Symposium, Prof. Dr. Yalçın Arısoy (Ed.), 539-546.
14. Yalciner A. C.,Ozer C., Karakus H., Ozyurt G. (2005). *Understanding The Generation, Propagation, Near and Far Field Impacts of Tsunamis, Planning Strategies and Preparedness for Future Events*, The Course Notes of the Short Course on July, 11-12, 2005, for University Teknologi Malaysia, Kuala Lumpur, Malaysia, 140 pages.
15. Tuncay T., Tan O., Yolsal S., Yalciner A. C., Ozer C., Karakus H., Kuran U. (2005). *Bizde de Olur mu?*, an article about the tsunami risk in the Sea of Marmara in Turkey including technical reports after December 26th, 2004 Indian Ocean Tsunami, Tübitak Bilim-Teknik Dergisi (Popular Magazine), Jan. 2005, No: 446, pages 38-44.
16. Ozer C., (2007). *Investigation of Hydrodynamic Demands of Tsunamis in Inundation Zone*, M.Sc. Thesis, Middle East Technical University, Ankara, Turkey, 2007, 124 pages.

## **HOBBIES**

Scuba, sailing, swimming, traveling, music, movies, social responsibility projects